High-sensitivity analysis of the Cygnus region observed with VERITAS

Dissertation

zur Erlangung des akademischen Grades

doctor rerum naturalium
(Dr. rer. nat.)

im Fach: Physik
Spezialisierung: Experimentalphysik

eingereicht an der
Mathematisch-Naturwissenschaftlichen Fakultät
der Humboldt-Universität zu Berlin

von
M.Sc. Maria Krause

Präsident der Humboldt-Universität zu Berlin:
Prof. Dr.-Ing. Dr. Sabine Kunst

Dekan der Mathematisch-Naturwissenschaftlichen Fakultät:
Prof. Dr. Elmar Kulke

Gutachter: 1. Dr. Gernot Maier
2. Prof. Dr. Marek Kowalski
3. Prof. Dr. Petra Huentemeyer

Tag der mündlichen Prüfung: 17. März 2017

This thesis is dedicated to my parents
for their love, endless support
and encouragement.

Abstract

Cosmic accelerators produce high-energy particles which can generate γ-rays with energies larger than 100 GeV. Upon entering the Earth's atmosphere, these very energetic photons interact with atoms and molecules in the atmosphere and produce a growing cascade of secondary particles. Since the particles travel faster than the speed of light in the atmosphere, they emit Cherenkov radiation. The *VERITAS* observatory, consisting of four telescopes, is designed to detect Cherenkov radiation from cascades generated by photons with energies above 85 GeV.

Particle showers can be generated by photons or charged cosmic rays. Before applying any selection requirements, showers initiated by cosmic rays are about 10^3 times more common than those initiated by photons. This constitutes a vast amount of background events measured by *VERITAS*, limiting the sensitivity to γ-rays. To improve the separation power between γ-ray and cosmic-ray showers, an analysis technique based on Boosted Decision Trees (BDTs) is developed, dependent on the energy and zenith angle of the shower. Extensive tests are performed to study the discrimination capabilities of the BDT method using cosmic-ray data and Monte-Carlo simulations of γ-rays. Compared to the *VERITAS* standard analysis, the BDT method improves the sensitivity of detecting γ-rays.

The BDT method is applied to data obtained from observations of the Cygnus region, one of the most active star-forming regions of our Galaxy. It hosts numerous astrophysical objects capable of accelerating particles to extremely high energies, such as supernova remnants, pulsar wind nebula, binary systems, and associations of massive OB stars. The high density of potential sources and the information from multiwavelength observations led *VERITAS* to perform observations of the Cygnus region between April 2007 and June 2012. An area of 15° in Galactic longitude and 5° in Galactic latitude around the Cygnus region was scanned and about 295 h of data were collected. Four sources were detected in very-high-energy γ-rays: VER J2031+415, VER J2019+407, VER J2019+368, and VER J2016+371. They were analysed in detail and compared to possible counterparts measured at other wavelengths. The spectra of the three of the sources were fit to a power law. Two out of three spectra are consistent with those obtained in previous measurements, where the third one shows a softer spectral index than the published result. Finally, the greater sensitivity reached with the BDT method allowed the derivation of the most stringent upper limits to date on 50 potential γ-ray sources.

Kurzfassung

Kosmische Teilchenbeschleuniger, wie z.B. Supernovaüberreste, Pulsarwindnebel, binäre Systeme oder Assoziationen von massereichen OB Sternen, produzieren hochenergetische Teilchen, welche wiederum Gammastrahlung mit Energien größer als 100 GeV erzeugen. Treffen diese Photonen auf die Erdatmosphäre, so wechselwirken sie mit deren Atomen und Molekülen und produzieren dabei sekundäre Teilchen. Bewegen sich die Teilchen schneller als das Licht in der Atmosphäre, senden sie Tscherenkow-Strahlung aus. Mit dem *VERITAS*-Observatorium im Süden Arizonas, welches aus vier Teleskopen besteht, lassen sich die schwachen Lichtblitze der Tscherenkow-Strahlung von Photonen mit Energien oberhalb von 85 GeV nachweisen.

Die detektierten Teilchenschauer können sowohl durch Photonen als auch durch geladene Teilchen erzeugt werden. Letztere kommen etwa 10^3 mal häufiger vor als die durch Photonen erzeugten Teilchenschauer. Dies beeinflusst die Sensitivität des *VERITAS*-Experiments erheblich. Um diese gegenüber Gammastrahlung zu steigern, ist es notwendig, die Gamma/Hadron-Separation zu verbessern. In dieser Dissertation wurde eine Analysemethode, basierend auf Boosted Decision Trees (BDTs), entwickelt und für die Analyse der Daten des *VERITAS*-Observatoriums optimiert. Das große Potential zur Unterscheidung von Teilchenschauern der Photonen und der Hadronen wird anhand ausführlicher Tests und systematischer Studien mit Simulationen von Gammastrahlung und Beobachtungsdaten der kosmischen Strahlung verdeutlicht. Diese Studien werden sowohl energie- als auch zenitwinkelabhängig durchgeführt. Im Vergleich zur Standardanalyse kann die Sensitivität mit Hilfe der BDT Methode deutlich erhöht werden.

Die entwickelte und optimierte BDT Methode wird auf Beobachtungsdaten der Cygnus-Region angewandt. Diese ist eine der aktivsten sternbildenden Regionen unserer Galaxie und beherbergt eine Vielzahl von potentiellen kosmischen Teilchenbeschleunigern. Aufgrund der enormen Dichte an potentiellen Quellen sowie der hohen Wahrscheinlichkeit, neue Quellen zu detektieren und zu identifizieren, wurde die Cygnus-Region von April 2007 bis Juni 2012 mit *VERITAS* beobachtet. Hierbei wurde ein Bereich von 15° in galaktischer Länge und 5° in galaktischer Breite durchmustert. Die Beobachtungsdaten wurden mit einer für diese Himmelsregion optimierten Analysetechnik aufbereitet und ausgewertet. Vier Quellen hochenergetischer Gammastrahlung wurden detektiert: VER J2031+415, VER J2019+407, VER J2019+368 und VER J2016+371. Detaillierte spektrale Untersuchungen werden vorgestellt, gefolgt von einer Diskussion möglicher assoziierter Objekte in anderen Wellenlängenbereichen. Schließlich konnten mit Hilfe der verbesserten Sensitivität von *VERITAS* durch die BDT Methode niedrigere Obergrenzen für den Fluss der hochenergetischen Gammastrahlung von 50 potentiellen Gammastrahlungsquellen abgeleitet werden.

Table of Contents

Abstract **V**

Kurzfassung **VII**

1 Introduction **1**

2 Very high energy γ-rays **7**
2.1 Acceleration of cosmic rays . . . 8
2.2 Production mechanisms of VHE γ-rays . . . 10
2.3 Galactic sources of VHE γ-rays . . . 13
2.3.1 Supernova remnants . . . 13
2.3.2 Pulsars and pulsar wind nebula . . . 15
2.3.3 Compact binary systems . . . 17
2.3.4 Stellar clusters and stellar winds . . . 18
2.4 Extensive air showers . . . 19
2.4.1 Electromagnetic showers . . . 19
2.4.2 Hadronic showers . . . 20
2.4.3 Emission of Cherenkov light . . . 23
2.5 Imaging Atmospheric Cherenkov Technique . . . 24

3 The Very Energetic Radiation Imaging Telescope Array System **29**
3.1 The *VERITAS* instrument . . . 30
3.1.1 Telescope mechanics and optics . . . 30
3.1.2 Camera . . . 31
3.1.3 Trigger . . . 32
3.1.4 Data acquisition system . . . 34
3.1.5 The *VERITAS* upgrade in 2012 . . . 34
3.2 Calibrations . . . 35
3.3 The *VERITAS* data analysis . . . 36
3.3.1 Charge integration . . . 36
3.3.2 Image cleaning . . . 37
3.3.3 Image parametrisation . . . 37
3.3.4 Stereoscopic event reconstruction . . . 39
3.3.5 γ/hadron classification and event selection . . . 41
3.3.6 Signal extraction . . . 43
3.3.7 Limitations of current γ/hadron separation . . . 46

4 Improved γ/hadron classification using a multivariate analysis technique 49
4.1 γ/hadron discriminatory parameters . . . 50
4.2 Classification using Boosted Decision Trees . . . 56
4.2.1 Training phase . . . 56
4.2.2 Boosting . . . 57
4.3 Training and evaluation of the BDT method . . . 58
4.3.1 Choice of the training sample . . . 58
4.3.2 Training and test configurations . . . 60
4.3.3 Importance of the discriminant parameters . . . 61
4.3.4 Classifier output . . . 62
4.3.5 Definition of cuts for different source types . . . 64
4.4 Systematic studies using data/Monte-Carlo comparison . . . 65
4.5 Performance of the BDT analysis . . . 66
4.5.1 Angular resolution and energy bias . . . 66
4.5.2 Effective γ-ray collection area . . . 68
4.5.3 Classification power . . . 72
4.5.4 Sensitivity . . . 75
4.5.5 Spectral reconstruction . . . 77
4.5.6 Performance on non-standard datasets . . . 79
4.6 Conclusion and outlook . . . 80

5 The Cygnus region 83
5.1 Multiwavelength view of the Cygnus region . . . 84
5.2 *VERITAS* Cygnus sky survey from 2007 to 2008 . . . 86
5.3 The region of Cygnus X, Cygnus OB2, and the Cygnus Cocoon . . . 86
5.4 The region of Cygnus OB1 and MGRO J2019+37 . . . 89

6 VHE γ-ray observations of the Cygnus region with *VERITAS* 91
6.1 Survey analysis . . . 93
6.1.1 Division of the survey region . . . 93
6.1.2 Processing of individual observations . . . 93
6.1.3 Combination of individual observations . . . 95
6.1.4 Trial factor . . . 95
6.1.5 Estimation of the integral flux . . . 100
6.2 Results of the sky survey analysis . . . 101
6.2.1 Source detection . . . 101
6.2.2 The region of VER J2031+415 . . . 107
6.2.3 The region of γ-Cygni and VER J2019+407 . . . 111
6.2.4 The region of MGRO J2019+37 . . . 115

6.2.5 Limits on the VHE γ-ray emission 120

7 Summary and conclusions **135**

A Supplementary material for Chapter 4 **139**
A.1 Optimized training cut values of the Boosted Decision Trees 139
A.2 Response of the Boosted Decision Trees 140
A.3 Signal and background efficiencies after applying T and box cuts 144
A.4 Sensitivity of moderate cut configuration 146

B Supplementary material for Chapter 6 **147**
B.1 Division of the region of the Cygnus sky survey 147
B.2 List of exclusion regions of the Cygnus sky survey 148
B.3 Trial simulations 151
B.4 Skymaps of the Cygnus region 152
B.5 Spectral points 157
B.6 Upper limits on the flux 158

List of Figures **163**

List of Tables **167**

List of Abbreviations **169**

Bibliography **171**

Acknowledgement **191**

1

Introduction

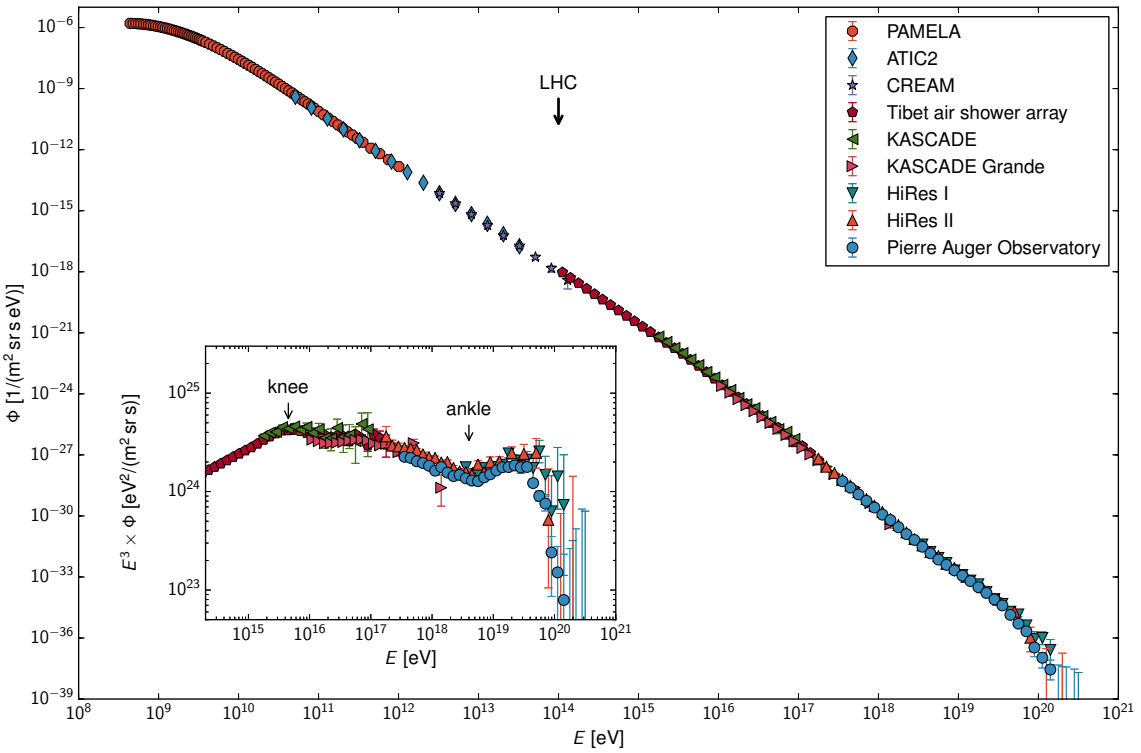

Figure 1.1: The energy spectrum of cosmic rays measured by different experiments in space, air, and on the ground. As a comparison, the currently maximum centre-of-mass energy reached by the LHC is marked. The inset box shows the flux of cosmic rays, Φ, multiplied by the energy, E, to the power of 3, which highlights the breaks in the spectrum above an energy of 10^{14} eV. The data are taken from Adriani et al. [2011]; Panov et al. [2007]; Yoon et al. [2011]; Amenomori et al. [2008]; Apel et al. [2012]; Abbasi et al. [2008]; Schulz [2013], and the figure is modified from Schellart [2015].

The fascination of *astroparticle physics* stems from the combination of the research of the most energetic elementary particles, forming the building blocks of matter on the smallest scale, with the research of largest objects in our universe. It combines the questions which mankind asked itself for hundreds of years: *Where do we come from? Where do cosmic rays come from? How do particles get accelerated to these high energies?*

The field of astroparticle physics was born in 1912 when Victor Hess measured the atmospheric ionisation as a function of altitude during several balloon flights. He discovered that the radiation increased with altitude and attributed this effect to a source of radiation entering the atmosphere from above. Cosmic rays had been discovered [Hess, 1912]. For this discovery, he was awarded the Nobel prize in 1936. Since then, a large number of experiments have precisely measured the energy spectrum of cosmic rays in different energy bands (Figure 1.1). Covering tens of decades in energy experimentally is only possible with multiple detection techniques. A complication of measuring cosmic rays is their interaction with nuclei in the Earth's atmosphere. The latter makes direct detection of cosmic rays on the ground impossible. At low energies ($<10^{11}$ eV), the large flux of particles allows for their direct detection by airborne or space experiments, such as satellites or balloons. However, the maximum payload of these instruments is limited and larger detector areas are needed to detect the low flux of particles of less than 1 particle/m^2/yr at larger energies. Therefore, ground-based experiments are used to detect cosmic rays with energies above 10^{11} eV. These experiments detect the cascade of secondary particles produced in the interaction between the primary particle and the atmosphere, called an *extensive air shower* (EAS).

The energy spectrum of cosmic rays is characterised by two distinct features, in particular the *knee* at an energy of about 4×10^{15} eV and the *ankle* at about 4×10^{18} eV. Below the knee, the spectrum follows a single power law

$$\frac{\mathrm{d}N}{\mathrm{d}E} \propto E^{-\Gamma}, \tag{1.1}$$

with a spectral index $\Gamma \approx 2.7$. Above the knee, the spectrum steepens to $\Gamma \approx 3.1$. At energies around the ankle, the spectrum flattens again. These features are depicted in the inset of Figure 1.1.

Although significant work has been done, the sources of cosmic rays and the origin of the spectral breaks remain unexplained. When searching for the sources of cosmic rays, one has to consider objects which are able to accelerate particles to a given energy. It is believed that the acceleration of particles is achieved via Fermi acceleration [Fermi, 1949; Blandford and Eichler, 1987] which involves magnetic fields as well as magnetic shocks. The latter have to accelerate particles several times until they reach the necessary energy. Based on these arguments, the maximum energy to which a source can accelerate particles is given by the *Hillas* criterion [Hillas, 1984]

$$E_{max} \approx \frac{Z \cdot \beta}{2} \left(\frac{B}{\mu\mathrm{G}}\right) \left(\frac{R}{\mathrm{pc}}\right), \tag{1.2}$$

with Z being the charge of the particle, β the velocity of the relativistic shock, B the magnetic field of the source in units of μG, and R the size of the shock region in pc. As supernova remnants (SNRs) are believed to produce shock fronts expanding in the interstellar medium (ISM) , they are a candidate for particle acceleration to energies around 10^{15} eV [Hillas, 1984]. Other plausible candidates to accelerate particles to these energies are for instance pulsars, pulsar wind nebulae

(PWNe), or binary systems. For the highest energies above the ankle ($\approx 10^{18}$ eV), extragalactic sources, e.g. active galactic nuclei (AGN) or γ-ray bursts, are plausible acceleration sites.

The search for sources of cosmic rays is hindered by the deflection of charged cosmic rays in the magnetic fields while propagating from the source to the Earth. When cosmic rays interact with molecular clouds or matter, e.g. around the sources, or with ambient photons from the cosmic microwave background, stellar photon fields or infrared emission from dust particles, etc., the resulting interactions will produce γ-rays and neutrinos. As both particles are uncharged they are not deflected in magnetic fields, pointing back to their origin. As by-products of the acceleration, these particles can directly trace the acceleration processes in astronomical objects. In addition, this can indicate which particles are accelerated in these sources. Only recently, a couple of neutrinos with energies above 10^{15} eV were detected by the IceCube experiment [Aartsen et al., 2013b] arguing for their origin in astrophysical sources [Aartsen et al., 2013a, 2014]. These particles are believed to carry important information about the acceleration processes and their sources as one needs very high energetic hadrons too create neutrinos with energies in the PeV (10^{15} eV) range as decay products.

γ-rays produced by the decay of the neutral pion, show the characteristic *pion bump* in the energy spectrum. Recently, first evidence for the acceleration of protons at SNR shocks producing γ-rays was confirmed by two SNRs, namely IC443 and W44 [Ackermann et al., 2013]. In addition, several shell-type SNRs have been reported as γ-ray emitters at TeV[1] energies, e.g. Tycho [Acciari et al., 2011], Cassiopeia A [Aharonian et al., 2001; Albert et al., 2007c; Acciari et al., 2010], and IC443 [Albert et al., 2007b; Acciari et al., 2009], indicating that these objects are able to accelerate cosmic rays. Furthermore, the detection of TeV γ-rays probe the high-energy end of the underlying parent particle distribution and can help to constrain the associated acceleration mechanism. In addition, recent studies showed that particles can be accelerated to even more than 10^{15} eV within the central 10 pc of our Galaxy originating from the supermassive black hole Sagittarius A* [Abramowski et al., 2016].

γ-rays can be efficiently produced in so-called giant molecular clouds. The latter are immediately connected with star-forming regions believed to be probable locations of cosmic-ray production in the Galaxy [Montmerle, 1979; Cassé and Paul, 1980]. Consequently, the search for TeV γ-rays from giant molecular clouds and star-forming regions is important to ascertain the possible existence of high-energy proton accelerators in our Galaxy.

Combined with observations at other wavelengths, studying the sky at very-high-energy (VHE) γ-rays (E>100 GeV) adds crucial information about the properties of the aforementioned objects. This branch of high energy astrophysics allows to study the origin of Galactic and extragalactic cosmic rays, as well as to investigate the mechanisms at work to accelerate cosmic rays to such high energies. Imaging Atmospheric Cherenkov Telescopes (IACTs) have established a discipline

[1] 1 TeV=10^{12} eV

to study astrophysical objects in this energy regime. The Very Energetic Radiation Imaging Telescope Array System (*VERITAS*) located in southern Arizona in the U.S.A. comprises four telescopes of the same architecture with a diameter of 12 m. With its location on the northern hemisphere it is well suited for the search of VHE γ-ray emission from extragalactic objects and northern Galactic regions such as the Cygnus region. This region of the Galaxy is a prime target to study VHE γ-ray emission. The distance of the Cygnus region to the Sun is about 1.7 kpc [Reipurth and Schneider, 2008], while the Galactic centre is about 8 kpc away. The Cygnus region contains a large number of astrophysical objects from which nonthermal emission at TeV energies has been observed. This region of the sky includes at least ten supernova remnants [Green, 2014], fourteen pulsars [Manchester et al., 2005], two high mass X-ray binary systems [Liu et al., 2000, 2001], and nine OB star associations [Uyaniker et al., 2001, and references therein]. Thus, this reveals the enormous potential of the Cygnus region to study the processes of acceleration and propagation of cosmic-ray particles through the emission of VHE γ-rays detectable on the Earth.

Until June 2016, *VERITAS* has detected 56 sources of Galactic and extragalactic origin. These sources emit VHE γ-rays at a flux level which made a detection in less than 140 h of observations per source possible. However, a larger amount of observation time is needed to establish weaker sources as VHE γ-ray emitters. The Crab Nebula is the so-called *standard* candle in VHE γ-ray astronomy with a flux of 1.8×10^{-11} photons/(cm^2 s) above 700 TeV [Hillas et al., 1998]. In comparison, the flux of γ-rays within the Cygnus region is measured to be about 4 % of the Crab Nebula flux above 200 GeV with an exposure time of 6 to 7 h taken in this region [Weinstein, 2009a; Ward, 2010]. To increase the sensitivity of IACTs, additional telescopes spread over a large area on the ground are needed. The future Cherenkov Telescope Array (*CTA*), starting operation in the next five to ten years, follows this approach [Acharya et al., 2013].

One method to increase the sensitivity of existing IACTs is to improve the rejection of background events. The development of an analysis technique based on the so-called *Boosted Decision Tree* method [Breiman et al., 1984] to distinguish between signal and background events is one of the main aims of this thesis and is addressed in the first part of this work. In the second part, the BDT method is applied to *VERITAS* data obtained from the Cygnus region.

This thesis is organised as follows:

- In Chapter 2, an introduction to the field of VHE γ-ray astronomy and the physics of extensive air showers is given. The differences between hadronic and electromagnetic showers are described in detail; together with information about the detection technique of IACTs.
- Chapter 3 describes *VERITAS*, including its calibration and data analysis scheme. This chapter concludes with the advantages and disadvantages of γ/hadron separation based on image parameters.
- In the fourth chapter, the development of the Boosted Decision Tree method used to analyse γ-ray data is presented. This chapter focuses on training and testing, as well as

the evaluation of the method's performance using γ-ray data obtained from observations of *VERITAS*.

- An overview of the history of observation of the Cygnus region, its objects, and their multiwavelength counterparts are presented in Chapter 5.
- The techniques employed to analyse the data taken with the *VERITAS* instrument of the Cygnus region are summarised in Chapter 6. In addition, it is shown in detail how to interprete the *VERITAS* dataset together with other multiwavelength observation.
- In the final chapter, the analyses and studies presented in this thesis are summarised and placed in a wider context.

2

Very high energy γ-rays

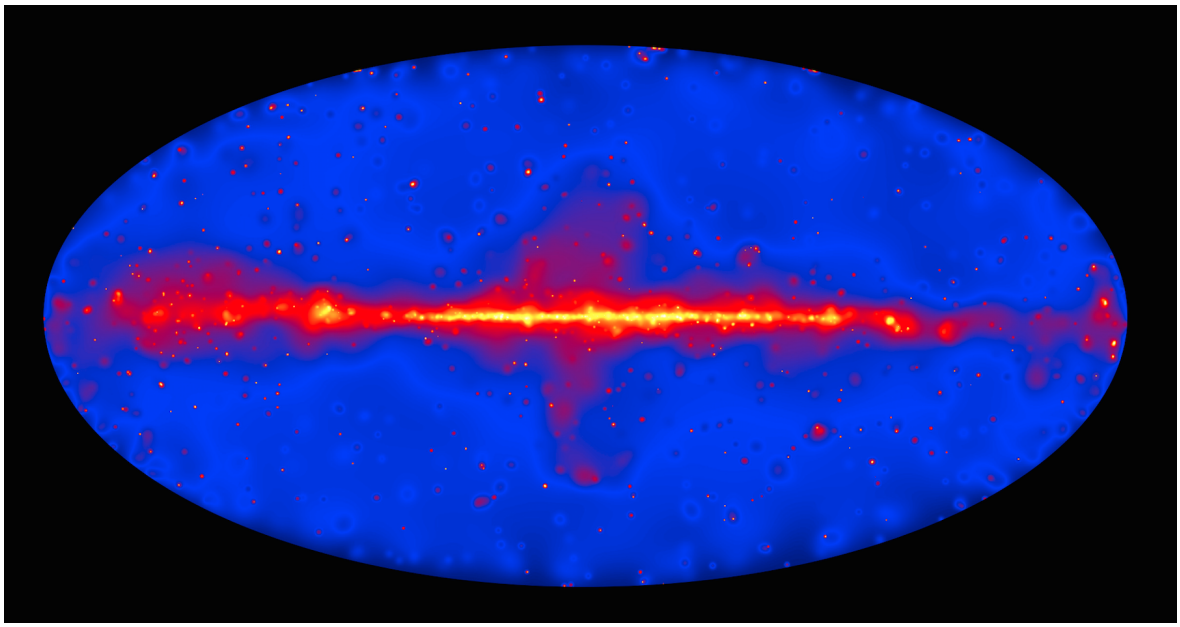

Figure 2.1: The entire γ-ray sky at energies above 50 GeV based on six years of data from the *Fermi*-LAT instrument [Ackermann et al., 2016]. Brighter colours indicate brighter γ-ray sources. Image credit: NASA/DOE/Fermi LAT collaboration.

Gamma rays are photons with energies $>10^5$ eV [Longair, 2011] up to multiple TeV. This broad energy range is the result of a wide variety of emission phenomena and studying photons over the full range requires a variety of detection techniques. High-energy γ-rays between 30 MeV and 100 GeV [Weekes, 1988] are detected by space-borne instruments like the Energetic Gamma Ray Experiment Telescope (*EGRET*) [Fichtel et al., 1983; Hughes et al., 1980], the *AGILE* instrument [Tavani et al., 2004] and the *Fermi* Large Area Telescope (*Fermi*-LAT) on board the Fermi Gamma-Ray Space Telescope. Figure 2.1 shows an image of the entire sky at γ-ray energies as seen by the *Fermi*-LAT instrument. Beyond this energy range, the flux of particles of astrophysical objects decreases steadily and the number of photons measured by the aforementioned instruments is limited by their detection area ($\mathcal{O}(1\,\mathrm{m}^2)$). This leads to the region of VHE γ-rays which is defined as energies larger than 10^{11} eV, up to about 10^{14} eV. This is about 10^{11} times more energetic than optical light. The sky in this energy range is explored by ground-based detectors.

In the following, the basic mechanisms for producing VHE γ-rays are introduced. Then, the characteristics of air showers, resulting from the interaction of VHE photons with the Earth's atmosphere, are briefly reviewed. This includes a discussion of the physical processes at work during the formation of an air shower induced by VHE γ-rays compared to the ones intiated by hadrons. Following this, the emission of Cherenkov light is discussed.

2.1 Acceleration of cosmic rays

In order to accelerate particles up to relativistic energies in astrophysical objects, there needs to be a mechanism for the transfer of energy to cosmic rays. Astrophysical shock fronts due to expanding shells of supernovae or relativistic outflows have long been considered as suitable sites for the acceleration of Galactic cosmic rays to TeV energies [Fermi, 1949; Bell, 1978a,b; Blandford and Ostriker, 1978; Blandford and Eichler, 1987]. The process for effective particle acceleration in a shock front is generally known as first-order Fermi acceleration and is illustrated in Figure 2.2. In the latter, a rapidly moving plasma collides with the ambient medium forming a shock. The shock front moves at speed U which is much smaller than the velocity of the high energy particles in the plasma of about 10^4 km/s [Prialnik, 2010]. In the rest frame of the shock, particles flowing across the shock from the upstream (e.g. into the ISM) to the downstream (e.g. the source-side of the outward flow) region can encounter magnetic instability which causes the particle to reflect back into the upstream region. The shocked material of the downstream region follows the shock at a velocity of $3/4 \cdot U$ in the case of an ideal gas [Longair, 2011]. The shock creates turbulences of the plasma in the up- and downstream regions which generates magnetic inhomogeneities. The charged particles are reflected by the magnetic field and cross the shock multiple times. Following this, the acceleration continues until the particle can escape the shock region. For each crossing, the particle gains an energy of $\Delta E = \xi E_0$ with $\xi \approx 4/3 \cdot U/c$. Thus, after k encounters, an injected particle with initial energy, E_0, obtains an energy of

$$E_k = E_0 \left(1 + \xi\right)^k . \tag{2.1}$$

If the probability of escape is denoted as P_{esc}, then the probability that the particle remains within the accelerating region after k encounters is $(1 - P_{esc})^k$. Thus, after k encounters the number of particles still participating in the acceleration process is

$$N_k = N_0 (P_{esc})^k . \tag{2.2}$$

The number of encounters required to reach an energy E is therefore

$$k = \frac{\ln\left(\frac{E_k}{E_0}\right)}{\ln\left(1 + \xi\right)} = \frac{\ln\left(\frac{N_k}{N_0}\right)}{\ln\left(P_{esc}\right)}, \tag{2.3}$$

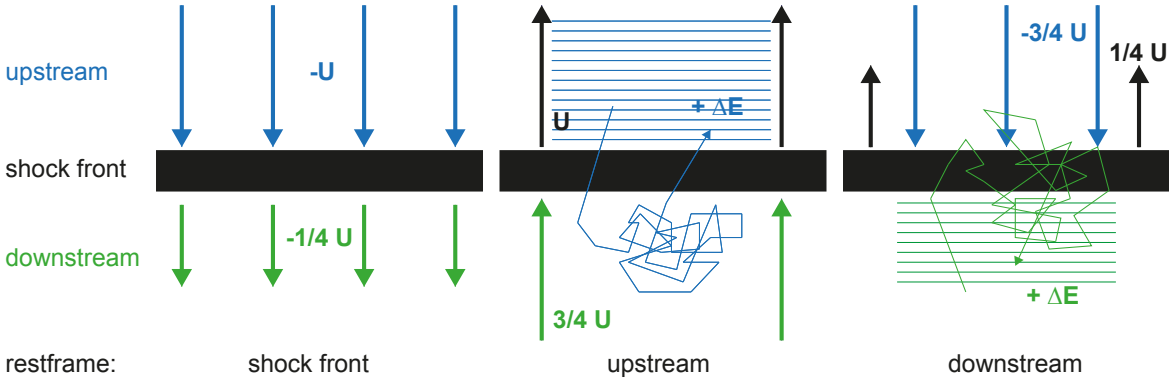

Figure 2.2: Schematic view of the acceleration of particles in the vicinity of a shock front propagating at a velocity, U, through the interstellar gas into an upstream medium. *Left:* The flow of interstellar gas in the vicinity of a shock front in the reference frame where the shock front is at rest. The upstream medium moves towards the shock front with velocity, U. The downstream medium follows with velocity, $1/4 \cdot U$, with respect to the shock front. *Middle:* The flow of gas as observed in the rest frame of the upstream medium. The particles in the upstream medium encounter gas of the downstream region moving with velocity $3/4 \cdot U$. They get scattered by magnetic turbulences behind the shock front and thereby gain energy, ΔE. *Right:* The flow of gas as observed in the rest frame of the downstream medium. The velocity distribution of the downstream region is isotropic. Particles diffusing from the shock to the upstream region encounter again gas moving towards the shock front with velocity $3/4 \cdot U$. Thus, the particles receive again an increase of energy ΔE when crossing the shock from downstream to upstream. Figure adapted from Funk [2005].

which leads to a power law of the form

$$\frac{N_k}{N_0} = \left(\frac{E_k}{E_0}\right)^{\frac{\ln P_{esc}}{\ln(1+\xi)}} . \tag{2.4}$$

Equation 2.4 can be translated to the number of particles, N, as a function of energy, E, over an energy interval, dE, given by

$$N(E)\mathrm{d}E = \text{constant} \times E^{-1+\frac{\ln P_{esc}}{\ln(1+\xi)}}\mathrm{d}E. \tag{2.5}$$

Thus, the spectral energy distribution depends on the probability of escape, P_{esc}, and the fractional energy gained per encounter, ξ. Following the argumentation from Bell [1978a], the differential energy spectrum resulting from diffusive shock acceleration of cosmic rays leads to a spectral index of $\Gamma \approx 2$. This is slightly harder than the spectrum of cosmic rays observed on Earth ($\Gamma \approx 2.7$ in Chapter 1). To overcome this discrepancy propagation effects of cosmic rays in the Galaxy have to be taken into account which softens the spectrum to ≈ 2.7. For a detailed discussion on the process of Fermi acceleration see Longair [2011].

2.2 Production mechanisms of VHE γ-rays

VHE γ-rays are produced primarily by three processes,

- hadronic interactions: relativistic hadrons create secondary products that decay and produce γ-rays;
- inverse Compton scattering: low energy photons are upscattered by relativistic electrons (e^-) or positrons (e^+) to produce VHE γ-rays;
- Bremsstrahlung: leptons (e.g. $\mathrm{e}^\pm$) experience a sharp retardation through their interactions with the Coulomb field of atomic nuclei, producing γ-rays.

This section summarises these processes. The reader is referred to Aharonian [2004] or Longair [2011] for an extensive description.

Hadronic interactions

Hadronic emission occurs when charged cosmic rays (primarily protons, but also heavier elements) interact with the ambient medium, e.g. the ISM consisting of neutral atoms, molecules, ions, and electrons; via nuclear interactions. During the first interaction of the primary particle, mesons, for example neutral or charged pions (π^0, $\pi^\pm$), and kaons (K^0, $K^\pm$), are produced, but also secondary nucleons (p, X) of the collision partners (p, N). In the next step, the secondary particles can either interact again after another interaction length or decay. The kaons and pions decay further according to

$$\begin{aligned} K^\pm &\rightarrow \mu^\pm + \overset{(-)}{\nu}_\mu \\ K^\pm &\rightarrow \pi^0 + \pi^\pm \\ K^0 &\rightarrow \pi^0 + \pi^0 \\ K^\pm &\rightarrow \pi^\pm + \pi^\mp \\ \pi^0 &\rightarrow \gamma\gamma \\ \pi^\pm &\rightarrow \mu^\pm + \overset{(-)}{\nu}_\mu \end{aligned} \tag{2.6}$$

and the muons according to

$$\mu^\pm \rightarrow e^\pm + \overset{(-)}{\nu}_e + \overset{(-)}{\nu}_\mu . \tag{2.7}$$

Here, the neutral pion with mass m_{π^0} =135 MeV/$c_0{}^2$ (c_0 – speed of light in vacuum) decays almost immediately after a livetime of about 8.5×10^{-17} s predominantly into two γ-rays. The energy spectrum of γ-rays produced via this channel reaches a maximum at about 67.5 MeV/$c_0{}^2$ in the centre-of-mass frame, also called the *pion bump*. Beyond this energy the spectrum decreases

smoothly. Where the spectrum of the incident particle follows a power law, the power-law index of the spectrum of γ-rays is close to that of the incident particle [Aharonian, 2004]. At low energies (below the pion bump) the production of γ-rays is heavily suppressed. The bump is characteristic of the decay of neutral pions, and difficult to explain by any other processes. Hence, it is a good indication for hadronic cosmic rays.

In addition to producing γ-rays, hadronic emission also produces neutrinos which, as part of the multimessenger approach to astrophysics, could provide significant evidence on the hadronic emission processes.

Inverse Compton scattering

The interaction of relativistic electrons with radiation fields through inverse Compton scattering is one of the most important processes in VHE astrophysics. This process is very efficient in the production of VHE γ-rays in many astrophysical sources, like AGN, SNRs and pulsars. In addition, it also occurs in the presence of ambient photons such as from the 2.7 K cosmic microwave background radiation, stellar photon fields, infrared emission from dust particles, etc. Relativistic electrons interact with low energy photons, upscattering them to VHE γ-rays. The probability of an interaction occurring depends upon the cross section, which depends on the energy of the incident photon. The total cross section is given by the Klein-Nishina formula [Longair, 2011]

$$\sigma_{KN} = \pi r_e^2 \frac{1}{x}\left\{\left[1 - \frac{2(x+1)}{x^2}\right]\ln(2x+1) + \frac{1}{2} + \frac{4}{x} - \frac{1}{2(2x+1)^2}\right\}, \tag{2.8}$$

where $x = \hbar\omega/m_e c_0^2$ and $r_e = e^2/(4\pi\epsilon_0 m_e c_0^2)$ is the classical electron radius with the permittivity of free space, ϵ_0, and the rest mass of the electron, m_e. For low-energy photons, i.e. $x \ll 1$, Equation 2.8 reduces to the Thomson cross section, $\sigma_T = 8\pi r_e^2/3$,

$$\sigma_{KN} = \frac{8\pi}{3} r_e^2 (1-2x) = \sigma_T (1-2x) \approx \sigma_T. \tag{2.9}$$

In the relativistic regime with $x \gg 1$, the Klein-Nishina cross section becomes

$$\sigma_{KN} = \pi r_e^2 \frac{1}{x}\left[\ln(2x) + \frac{1}{2}\right]. \tag{2.10}$$

In this energy regime, the scattered photons will carry away a large portion of the energy of the electron. The energy-loss rate of an electron with energy E passing through an isotropic field of photons with frequency ω_0 is given by Aharonian and Atoyan [1981] as

$$-\left(\frac{\mathrm{d}E}{\mathrm{d}t}\right) = \frac{\pi r_e^2 m_e^2 c^5}{\omega_0}\left(\ln\left(\frac{4E\omega_0}{(m_e c^2)^2}\right) - \frac{11}{6}\right). \tag{2.11}$$

Furthermore, the cross section decreases with increasing energy of the photon (Equation 2.10). Then, the spectrum of inverse Compton emission of an electron travelling through photons fields is determined following the derivation by Blumenthal and Gould [1970]

$$\frac{\mathrm{d}N}{\mathrm{d}t\mathrm{d}E} = \frac{2\pi r_e^2 m_e^2 c^3}{\gamma} \cdot \frac{N(E_\gamma)\,\mathrm{d}E_\gamma}{E_\gamma} \left[2q \ln q + (1+2q)(1-q) + \frac{\left(\Gamma_{E_\gamma} q\right)^2}{2\left((1+\Gamma_{E_\gamma} q\right)}(1-q) \right]. \tag{2.12}$$

Here, E_γ is the energy of the unscattered photon energy, N_{E_γ} the number density of photons, E the ratio of the upscattered photon energy E'_γ and the electron energy $E_e = \gamma m_e c^2$ given by $E = E'_\gamma/(\gamma m_e c^2)$. The dimensionless quantities Γ_{E_γ} and q are defined as

$$\Gamma_{E_\gamma} = \frac{4E_\gamma \gamma}{m_e c^2} \qquad\qquad q = \frac{E}{\Gamma_{E_\gamma}(1-E)}. \tag{2.13}$$

Bremsstrahlung

Charged particles emit radiation by deceleration in the Coulomb field of an atomic nucleus or an electron/positron. The maximum energy of the emitted photon is equal to the energy of the initial charged particle. Therefore, in case of a power-law distribution of the energy spectrum of the lepton, the photons produced via Bremsstrahlung show the same index of the distribution. The energy loss per cm of a relativistic particle of mass m and charge q by Bremsstrahlung [Bethe and Heitler, 1934] is given as

$$-\left(\frac{\mathrm{d}E}{\mathrm{d}x}\right) = 4\alpha\delta\frac{N_A}{A}(Z^2+Z)q^2\left(\frac{m_e}{m}\right)^2 r_e^2 E\left(\ln\left(\frac{183}{Z^{1/3}}\right)\right) \tag{2.14}$$

where Z and A are the atomic and mass number of the nucleus, δ the density of the material, and $\alpha = e^2/(4\pi\hbar\epsilon_0 c)$ the fine structure constant. Equation 2.14 clearly shows that the energy loss is directly proportional to the energy, E. It is important to note that the cross section, σ_{BS}, is proportional to Z^2 and that the total emission depends on the density of gas. Therefore, the bulk of the emission will happen in dense regions close to the sources of electrons. This process also plays an important role in the development of air showers. After a passage of one radiation length, X_0, the high-energy electron/positron loses all but $1/e$ of its energy E by Bremsstrahlung, given by

$$-\left(\frac{dE}{dx}\right) = \frac{E}{X_0}, \tag{2.15}$$

with the radiation length $X_0 \propto A/Z^2$. The radiation length in air is $36.664\,\mathrm{g/cm^2}$, while for hydrogen gas the radiation length is approximately $58\,\mathrm{g/cm^2}$ [Tsai, 1974].

2.3 Galactic sources of VHE γ-rays

Next to the mechanism to accelerate particles to very high energies, another aspect has to be considered to the question of cosmic-ray acceleration: What is the source of power for the accelerator? VHE γ-ray emission in our Galaxy, indicating environments that could also accelerate cosmic rays, is seen from the interactions of accelerated particles in various astrophysical objects such as SNRs [Reynolds, 2008], PWNe [Gaensler and Slane, 2006], and compact-object binary systems [Aharonian et al., 2005b]. In addition, colliding wind binaries (CWBs) and the sites of star formation are proposed sources of VHE γ-ray emission in the Milky Way [Abramowski et al., 2012a,b].

The flux of cosmic rays in the Galaxy can be derived as follows. The average density of cosmic rays in the Galactic disk, ρ_{CR}, is found to be $1\,\mathrm{eV/cm^3}$ [Wdowczyk and Wolfendale, 1989] and the volume of the disk is $V_D = \pi R^2 d \approx \pi(15\,\mathrm{kpc})^2(300\,\mathrm{pc}) \approx 7 \times 10^{66}\,\mathrm{cm^3}$ [Gaisser, 1990]. Thus, the energy input required to maintain the flux of cosmic rays is

$$L_{CR} = \frac{V_D \rho_{CR}}{\tau_{esc}} \approx 2 \times 10^{41}\,\mathrm{erg/s}. \tag{2.16}$$

Here, τ_{esc} is the average escape time of cosmic rays in the Galactic disk and assumed to be about $1.7 \times 10^7\,\mathrm{yr}$ [Stanev, 2010]. Thus, sources must have indicate a sufficiently large energy release in order to be a plausible candidate for the origin of cosmic rays.

Many source classes have been hypothesised as emitters of VHE γ-rays. Most of them have been detected by experiments in TeV astronomy. The Galactic plane including the Cygnus region contains many of these source classes which are exclusively related to evolutionary phases of stars, e.g. SNRs, PWNe, or compact binary systems. In the following, these are described along with the source class of CWBs.

2.3.1 Supernova remnants

Supernova remnants (SNRs) have long been proposed as potential sites to accelerate Galactic cosmic rays up to $10^{15}\,\mathrm{eV}$ [Zwicky, 1939]. SNRs are the results from the explosion of a star in a supernova. Supernova explosions are classified into two types based on their observed properties: *Type I* and *Type II*. Their main difference is the presence of hydrogen lines in the spectrum of the latter and their absence in the former [Prialnik, 2010]. Type I supernovae are related to the accretion of a binary companion star onto a white dwarf which is overloaded and undergoes an explosion. The remnant of these objects does not have a core. Due to strong gravity at the surface of the white dwarf, the object is compressed to very high densities and temperatures which fuses hydrogen into carbon and oxygen. Type II supernovae are associated with the gravitational collapse of a massive star which implodes and releases a shock-wave of ejecta into the surrounding

medium. They result in a black hole or a neutron star with a dipole magnetic field oriented with respect to the rotational axis. As the neutron star rotates, it emits radiation which is seen as pulsed emission. A rotating neutron star emitting pulsed radiation is called a pulsar.

Baade and Zwicky [1934] and Ginzburg and Syravatskii [1964] emphasised that the aforementioned power requirement (Equation 2.16) is suggestive of supernovae since the energy release of a supernova is about 10^{51} erg. With a supernova rate of one per 30 yr [Longair, 2011] the average energy release per supernova must be $L_{SN} \approx 10^{42}$ erg/s. This implies energetically it is quite feasible to account for the total energy density of cosmic rays with the assumption that they originate in supernova explosions.

VHE γ-rays are the tracers of particle acceleration of cosmic rays in SNRs. As a consequence, SNRs are high priority targets in the field of ground-based γ-ray astronomy. In shell-type SNRs, the material from the star is ejected into the surrounding ISM at very high velocity, up to 10^4 km/s. In this environment, particles undergo diffuse shock acceleration, as described in Section 2.1. Then, γ-ray emission can occur via accelerated electrons upscattering ambient photons by inverse Compton processes up to energies in the TeV regime [Hinton and Hofmann, 2009]. In addition, γ-rays can be emitted through accelerated protons interacting with ambient matter producing γ-rays via the π^0-decay (Equation 2.6). Theoretical expectations for the high-energy γ-ray emission of SNRs arising from hadronic interactions are given by Drury et al. [1994] as

$$\Phi_\gamma(>100\,\mathrm{MeV}) \approx 9 \times 10^{-11} f \left(\frac{E}{1\,\mathrm{TeV}}\right)^{-1.1} \left(\frac{E_{SN}}{10^{51}\,\mathrm{erg}}\right) \left(\frac{d}{1\,\mathrm{kpc}}\right)^{-2} \left(\frac{n}{1/\mathrm{cm}^3}\right) 1/(\mathrm{cm}^2\,\mathrm{s}), \tag{2.17}$$

where Φ_γ denotes the flux of γ-rays, f the fraction of the total supernova explosion energy, E_{SN}, converted into cosmic-ray energy, d the distance to the SNR, and n the density of the ambient medium. This formula assumes a power-law distribution of cosmic-ray energies with a typical differential spectral index of $\Gamma \approx 2.1$. The measurement of the spectrum of these objects at TeV energies can help to distinguish between the leptonic or hadronic origins of the emission. In case of hadronic acceleration, the γ-ray spectra of SNRs emitting at TeV energies are well described by a power-law function with an index of about 2 including a high-energy cutoff. In contrast, leptonic models tend to generate harder spectra at low energies ($<$1 TeV) with an index of 1.5 for γ-rays produced by inverse Compton scattering [Hinton and Hofmann, 2009]. However, by adjusting several model parameters such as the composition of the target radiation field, the leptonic model can mimic an E^2-spectrum. In addition, the separation between hadronic and leptonic models can be achieved by studying the morphology of the sources at X-ray and γ-ray wavelengths. The correlation between X-rays and γ-rays localized in the shell of an SNR seems to argue in favor of a leptonic origin of γ-rays [Hinton and Hofmann, 2009], especially when correlation with gas density is less pronounced.

2.3.2 Pulsars and pulsar wind nebula

A supernova explosion may create a *pulsar*; a rapidly rotating and highly magnetised neutron star surrounded by a rotating magnetosphere and a magnetic field axis that is misaligned with the rotation axis. Pulsars [Lyne and Graham-Smith, 2012], and their associated pulsar wind nebula (PWN) have long been investigated as VHE γ-ray sources [Gaensler and Slane, 2006]. The first VHE γ-ray source to be detected, the Crab Nebula [Weekes et al., 1989], is a PWN.

The various emission zones of a pulsar and a PWN are illustrated in Figure 2.3. Relativistic electrons and positrons are thought to be accelerated in the electromagnetic fields of the pulsar. The pulsed component of radiation is thought to originate from the pulsar magnetosphere. Synchrotron and curvature radiation is produced by electrons and positrons pulled from the surface of the neutron star by the strong rotating dipole magnetic field. This in turn emits electromagnetic radiation at a luminosity [Hinton and Hofmann, 2009]

$$\dot{E} \propto 3 \cdot 10^{33} B_{12}^2 P_{ms}^{-4} \mathrm{erg/s}, \tag{2.18}$$

where B_{12} is the magnetic field near the surface of the neutron star in units of 10^{12} G and P_{ms} is the period of the pulsar in milliseconds. Following this, the pulsar spins less rapidly as it loses energy to electromagnetic radiation. The central Crab pulsar has a spin-down luminosity of 5×10^{38} erg/s [Weekes, 2003]. The latter is predominantly produced by nonthermal processes due to a large magnetic field in the pulsar of about 10^8 to 10^{15} G [Gaensler and Slane, 2006]. The emitted electromagnetic radiation can undergo pair production in the magnetic field which in turn radiates again via synchrotron and curvature processes. The particle wind, called pulsar wind, interacts with the ambient medium generating a shock where particles are accelerated. This particle wind is replenished continuously by the pulsar as it converts its rotational energy into particle kinetic energy. If the pulsar is energetic enough, the outward energy flow is sufficient to provide high-energy particles in the surrounding nebula generating a PWN. Particles are accelerated to very high energies either by the expansion of the wind or at the shocks produced in collisions of the wind with the surrounding medium. These particles in turn can interact with magnetic and radiation fields. As a result, these electrons interact via inverse Compton scattering with lower-energy photons upscattering them to VHE photons. The relativistic particle wind of the pulsar terminates where the pressure of the wind is balanced by the pressure of the surrounding nebula. Beyond this wind termination, particles can be accelerated again leading to additional synchrotron emission and emission at TeV energies through inverse Compton scattering.

In contrast to the energy release of a supernova shock of about 10^{51} erg, the energy content of a PWN of order of 10^{49} erg is small. However, a large fraction of energy is carried by relativistic electrons with radiative livetimes of 10^3 to 10^4 yr [Hinton and Hofmann, 2009]. Therefore, kinetic energy is very efficiently converted into radiation. In addition, it is worth noting that after

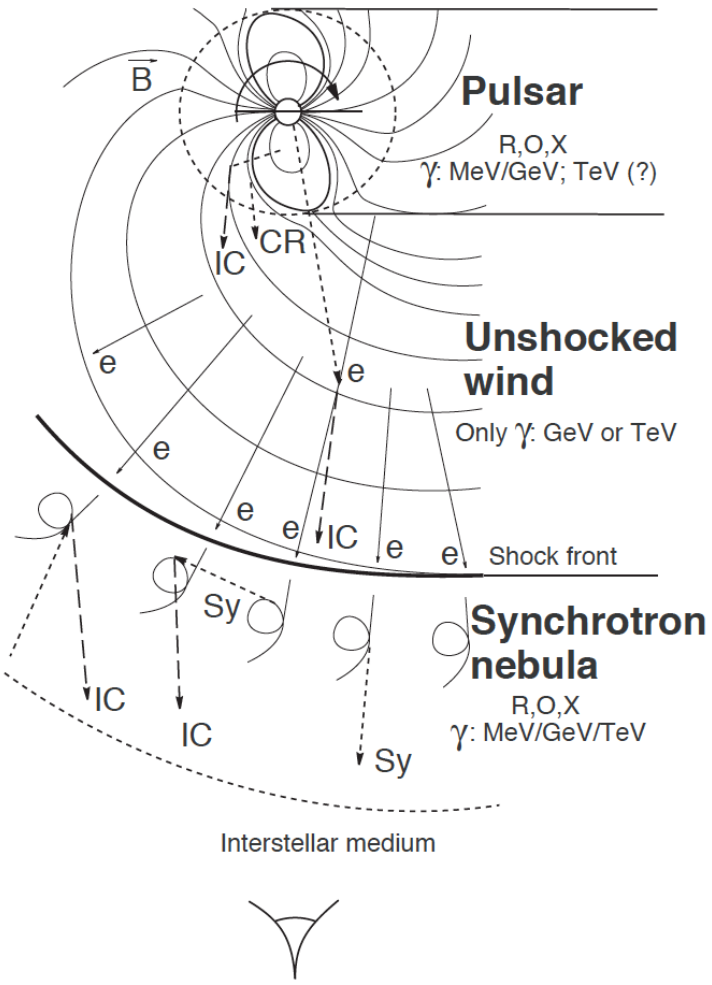

Figure 2.3: Sketch of the sites and various radiation mechanisms of nonthermal emission associated with PWNe. The inner region of the PWN emits radiation from the radio to γ-ray regime. The middle part is characterised by the particle wind which effectively emits γ-rays at GeV to TeV energies through inverse Compton scattering. The surrounding synchrotron nebula emits electromagnetic radiation from the radio to the TeV regime through synchrotron and inverse Compton scattering. Figure taken from Aharonian and Bogovalov [2003].

$\mathcal{O}(10^4\,\mathrm{yr})$ the deceleration of supernova shocks can no longer confine VHE particles leading to a cutoff in the spectrum at very high energies. But a pulsar may drive the PWN significantly longer resulting in a potential cutoff at higher energies.

Although, pulsars have been a subject of study for VHE γ-ray astronomy, most of their radiation is emitted at high energies. To date, only two pulsars are detected in the VHE regime: the Crab [Aliu et al., 2011] and the Vela pulsar [Max Planck Institute for Nuclear Physics, 2014; Stegmann, 2014]. In comparison, there are more than 30 PWN detected in this energy range [Wakely and Horan, 2016].

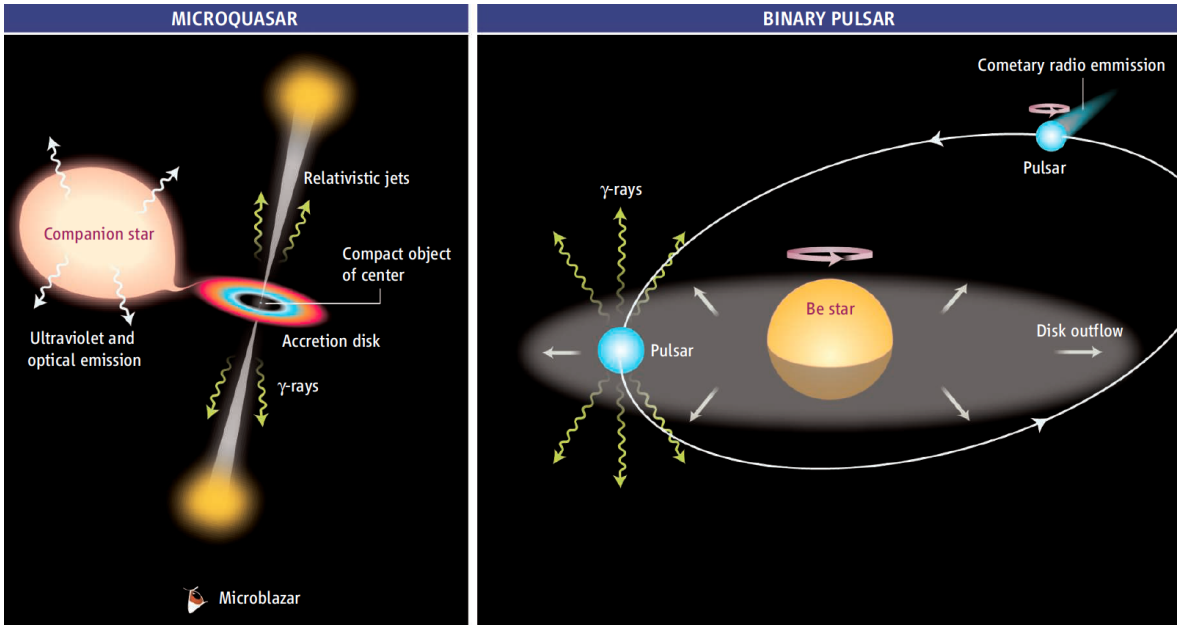

Figure 2.4: Models for VHE γ-rays from microquasars and binary pulsars. *Left:* Microquasars are powerd by a compact object via accretion of mass from a companion star. This produces jets which appear as microblazars if the jet is aligned with our line of sight. The energy of stellar photons is accelerated to TeV energies. *Right:* Pulsar winds are powered by the rotation of neutron stars. Interaction of the pulsar wind with the disk outflow might produce VHE γ-rays. Figure taken from Mirabel [2006].

2.3.3 Compact binary systems

A binary system is a system of two objects revolving around their common centre of mass. A compact object, such as a black hole, neutron star, or white dwarf, is gravitationally linked to a stellar companion. They are observed as dense environments with dense photon fields $\mathcal{O}(1\,\mathrm{eV/cm^3})$ of high frequency photons $\mathcal{O}(1\,\mathrm{eV})$ and high magnetic fields (mG to G) [Hinton and Hofmann, 2009].

Compact-object binary systems are separated into two categories: low-mass X-ray binaries [Liu et al., 2001] and high-mass X-ray binaries [Liu et al., 2000]. The former involve a donor star with smaller mass than their compact companion. The donor objects are characterised by their Roche-lobe overflow passing material onto the orbiting compact object. They emit large thermal X-ray radiation and are the brightest X-ray objects in the sky. The latter are described by a compact object orbiting a massive stellar companion, such as O, B, or Be stars. The stellar wind of the massive star collected by the compact object leads to strong X-ray emission. There are two mechanisms which explain the emission of VHE radiation from compact-binary objects, depicted in Figure 2.4. In the first model, particles are accelerated in a relativistic jet formed by accretion onto the compact object. They are classified as *microquasars* [Mirabel and Rodríguez,

1994, 1999; Mirabel, 2006, 2007]. These objects can emit VHE γ-rays by scattering of ambient photons by shock-accelerated electrons via inverse Compton scattering. Observations have shown that the kinetic power of jets from microquasars may be larger than 10^{39} erg/s [Gallo et al., 2005]. In addition, microquasar jets trigger shocks where electrons are accelerated up to TeV energies [Corbel et al., 2005] which then may lead to VHE γ-ray emission.

Different from microquasars are so-called binary pulsars. These objects pair an energetic pulsar with a main-sequence star. Their emission is driven by interaction between the pulsar wind and the stellar wind from the main-sequence companion, with acceleration at the termination shock of the wind. The γ-ray emission is produced by inverse Compton scattering of electrons from the pulsar wind on the stellar photons.

Both scenarios are expected to provide periodic emission from either outbursts of relativistic jets in the case of microquasars or emission at periastron, i.e. when the orbital path of the compact object is closest to the stellar companion, for the binary-pulsar scenario.

It is worth noting that there are over 300 low-mass and high-mass X-ray binary systems listed in recent catalogues [Liu et al., 2006, 2007]. In comparison, at the time of writing there are five binary systems with secure detections at VHE γ-rays: PSR B1259-63 [Aharonian et al., 2005a], LS 5039 [Aharonian, 2005], LS I $+61^{\circ}303$ [Albert et al., 2006; Acciari et al., 2008], HESS J0632+057 [Aharonian et al., 2007b], 1FGL J1018.6-5856 [Ackermann et al., 2012b; Abramowski et al., 2015]. In addition, HESS J1832-093 [Abramowski et al., 2014; Eger et al., 2016] is proposed to have a binary nature.

2.3.4 Stellar clusters and stellar winds

All known Galactic sources of VHE γ-rays are associated with massive star formation [Hinton and Hofmann, 2009]. Both the end points of the massive stellar lifecycles, SNRs and pulsars, and high-mass X-ray binaries are TeV emitters. Therefore, it might be possible that massive stars are able to accelerate particle to TeV energies even in the absence of a compact object. Particle acceleration might occur at the shock fronts formed by colliding stellar winds in a binary system of two massive stars. These CWBs consist of a Wolf-Rayet star ($M_{WR} \geq 20 M_{\odot}$ [Reimer et al., 2006]) with an OB star ($M_{OB} \geq 16 M_{\odot}$ [Prialnik, 2010]) companion or a Wolf-Rayet star with another Wolf-Rayet star companion. Shocks are expected to form at the collision boundary of both stellar winds with resulting acceleration of particles to high energies via diffusive shock acceleration. In the vicinity of a massive star, the surrounding ISM is blown off either because of the strong wind or due to the explosion of the star. In particular, the combined effects from supernova explosions and stellar winds from OB associations produce quite large cavities filled with gas, called *superbubbles* [Parizot et al., 2004]. An example of such an effect is the Cygnus superbubble [Uyaniker et al., 2001]. Moreover, particles can be injected by young OB stars

and subsequently get accelerated by the shock wave of a supernova explosion in its surrounding [Montmerle, 1979; Cassé and Paul, 1980; Voelk and Forman, 1982].

In addition, several binary systems have been studied as potential sites for VHE particle acceleration, e.g. WR140 [Pittard and Dougherty, 2006] and η Carina [Abramowski et al., 2012b]. But so far, no unambiguous VHE detection from CWBs was found. In contrast, extended VHE γ-ray emission has been detected from the vicinity of the young massive stellar clusters Westerlund 1 [Abramowski et al., 2012a] and Westerlund 2 [Aharonian et al., 2007a]. This emission can be powered by stellar winds within the cluster. Other objects of interests can be found in the Cygnus region. As an example, the association of massive stars of Cygnus OB2 within the Cygnus region has been proposed as a counterpart of the unidentified source within the Galactic plane discovered by the High Energy Gamma Ray Astronomy Experiment (*HEGRA*) [Aharonian et al., 2002a]. However, as all known γ-ray sources of the Galactic plane are associated with high-mass star formation, it is possible that this emission is associated with a single PWN.

2.4 Extensive air showers

As a high-energy particle, e.g. cosmic-ray nucleus or a photon, enters the Earth's atmosphere, it interacts with molecules and atoms in the air, and creates secondary particles. These secondary particles in turn interact again with the atmospheric nuclei generating a cascade of particles, a so-called *extensive air shower* (EAS). Depending on the type of the primary particle, the induced EAS has different components. If a photon strikes the atmosphere, it pair-produces electrons and positrons generating an electromagnetic shower. On the other hand, a cosmic-ray nucleus interacts via the strong force, generating a hadronic shower, including a hadronic core, a muonic component, and electromagnetic subshowers. The basic properties of both types of EASs are reviewed in the following. Furthermore, the emission of Cherenkov light by charged particles moving faster than the speed of light in air is described.

2.4.1 Electromagnetic showers

An electromagnetic air shower initiated by a VHE photon starts with the production of an electron-positron pair within the Coulomb field of an atmospheric nucleus, called *pair production*. The produced high-energy leptons undergo Bremsstrahlung in the presence of a Coulomb field of an atomic nucleus and radiate γ-rays. The characteristic amount of matter traversed for these related interactions is the radiation length, X_0, measured in g/cm^2. The radiation length in air for electrons/positrons is $X_0 = 36.664\,\mathrm{g/cm^2}$ [Tsai, 1974]. The first interaction typically takes place after one radiation length of the atmosphere, at an altitude of about 20 km. As $X_{0,\gamma} = \frac{9}{7} X_{0,e^\pm}$ [Gaisser, 1990; Grieder, 2010], electromagnetic cascades triggered by electrons/positrons or photons reveal

a similar shape due to the underlying process. However, the first interaction of electrons/positrons is slightly higher in the atmosphere compared to γ-rays. This fact makes the showers distinguishable. This discrimination could be important by the identification of γ-ray-induced showers over lepton-induced showers [Maier, 2007].

The process of pair production of γ-rays and the resultant leptons emitting γ-rays repeats itself through the atmosphere until the mean energy of the particle drops below the critical energy, E_c, of about 84 MeV [Rossi and Greisen, 1941; Grieder, 2010]. A particle cascade is developed. At the critical energy, the energy loss via ionisation of air molecules dominates over the creation of particles via Bremsstrahlung and pair production. At this point, the shower maximum, X_{max}, is reached, the number of particles diminishes.

A simple model describing the development of electromagnetic air showers was presented by Rossi and Greisen [1941] and Heitler [1954]. This is used to derive the basic properties of electromagnetic air shower development [Matthews, 2005],

- The number of secondary particles, N_p, increases exponentially until the shower maximum is reached.
- The maximum number of particles, $N_{p_{max}}$, is proportional to the energy of the primary particle, E_0,
$$N_{p_{max}} = \exp\left(\frac{X_{max}}{X_0}\right) = \frac{E_0}{E_c}. \tag{2.19}$$
- The depth of the shower maximum,X_{max}, is proportional to the logarithm of the energy of the primary particle, E_0,
$$\begin{aligned} E(X_{max}) &= E_0 \cdot \exp\left(\frac{X_{max}}{X_0}\right) \equiv E_c, \\ X_{max} &= \ln\left(\frac{E_0}{E_c}\right) X_0. \end{aligned} \tag{2.20}$$

2.4.2 Hadronic showers

In contrast to electromagnetic showers, a high-energy cosmic-ray particle like a proton enters the Earth's atmosphere, interacting with the nuclei of air molecules via the strong force and initiating a hadronic air shower. The air shower consists of three components: the hadronic core, a muonic component, and electromagnetic subshowers, as depicted in Figure 2.5. In some cases, most of the primary energy is transferred into a neutral pion in one of the first interactions. Its decay into two γ-rays (Equation 2.6) leads to the development of an electromagnetic component. The photons in turn initiate electromagnetic subshowers through production of electron-positron pairs. Even if the incident particle is of hadronic origin electromagnetic subshowers are generated. This is relevant in the context of γ/hadron identification.

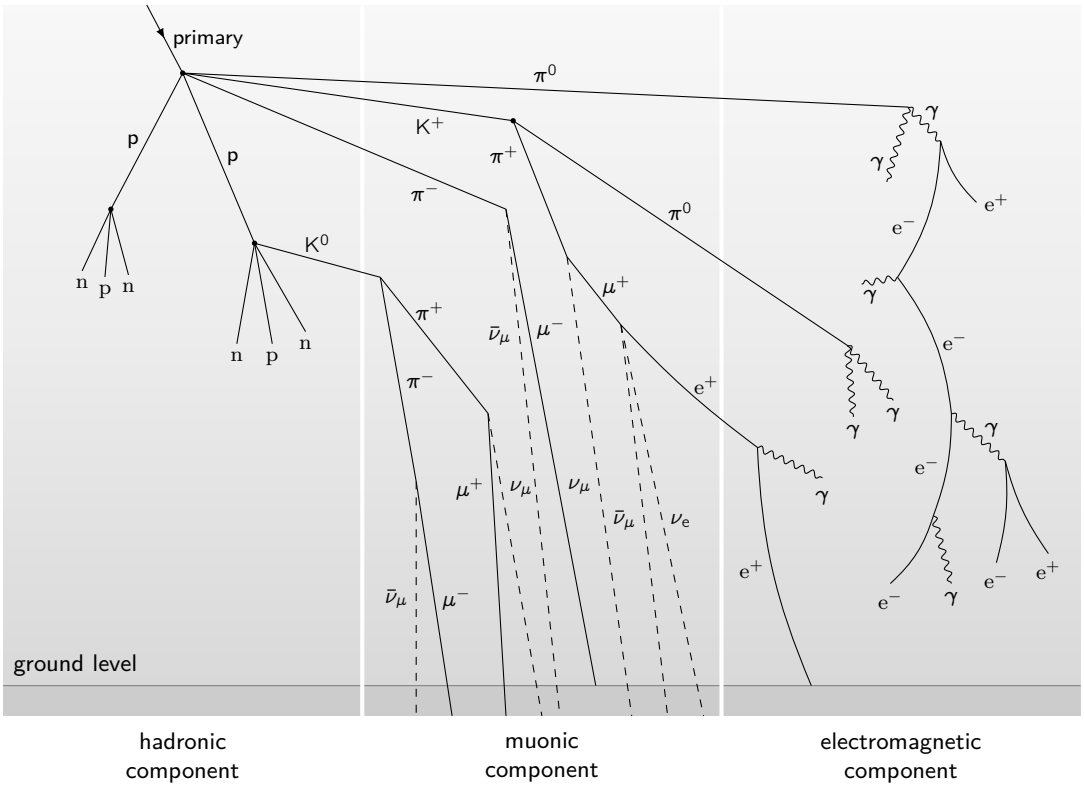

Figure 2.5: Sketch of the longitudinal development of an extensive air shower induced by a primary particle. The shower includes the hadronic, muonic, and electromagnetic component as well as neutrinos. Figure adapted from Lafebre [2008].

As the core of an hadronic cascade consists of products of hadronic interactions (e.g. kaons, pions, neutrons), the fraction of energy that goes into electromagnetic subshowers, which are mainly responsible for the emission of Cherenkov light, varies with energy from about 40 % at 50 GeV to >60 % at 1 TeV [Leroy and Rancoita, 2016, and references therein]. The typical light yield of Cherenkov light (Section 2.4.3) from pure electromagnetic showers is about two to three times larger than that from cosmic-ray-induced showers [Weekes, 2003].

Hadronic and electromagnetic cascades show distinct properties [Jelley and Porter, 1963; Hillas, 1996; Weekes, 2003; Grieder, 2010] which are characteristic for the interaction processes at work during their formation. They are described in the following:

- The nuclear interaction length of hadrons in air is typically larger than the radiation length of photons. Thus, hadrons penetrate deeper into the atmosphere than γ-rays or cosmic-ray electrons/positrons resulting in a larger depth of the shower maximum, X_{max}.
- The secondary particles of hadronic showers receive a high transverse momentum, e.g. by inelastic scattering and decay processes. This leads to a larger lateral extension compared to electromagnetic showers where the lateral development is determined by elastic multi-

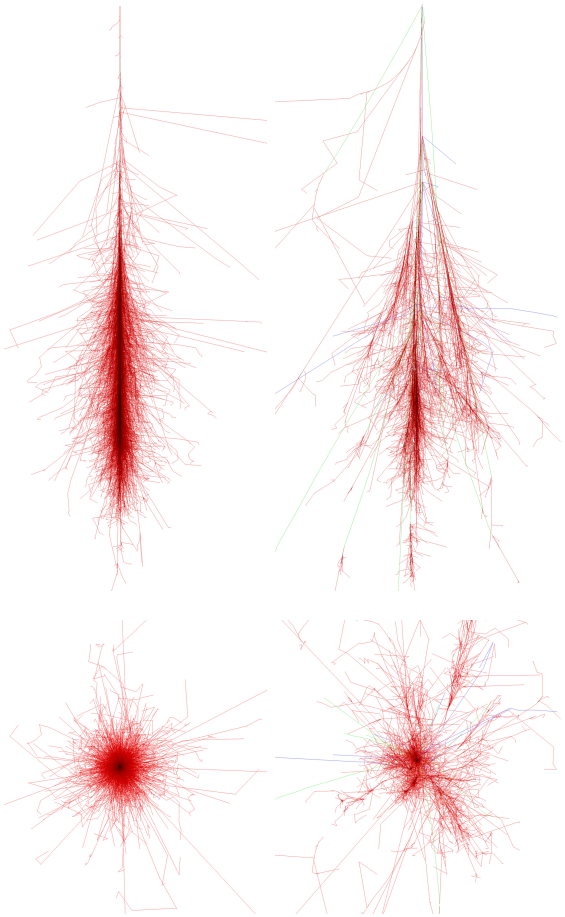

Figure 2.6: Simulated air showers initiated by a primary photon (*left*) and proton (*right*) with an energy of 100 GeV and entering the Earth's atmosphere at a zenith angle of 0°. The upper plots illustrate the longitudinal development. The first interaction height is fixed to 30 km. The lower plots demonstrate the lateral extension with a spread of ±5 km around the shower core. Colours represent the tracks of the following particles: electrons/positrons/photons (red), muons (green) and hadrons (blue). Figures taken from Schmidt [2005].

ple Coulomb scattering of electrons/positrons. The mean scattering angle of high-energy electrons/positrons with an energy close to the critical energy is smaller and thus, the electromagnetic lateral spread is small.

- While hadronic showers develop through complex multiparticle processes, electromagnetic showers undergo three-particle processes, e.g. Bremsstrahlung and pair production. The former results in larger fluctuations in the structure of hadronic showers which are more scattered and geometrically larger than electromagnetic showers. Moreover, hadronic cascades consist of a less pronounced radial symmetry with respect to the shower axis, as for instance depicted in Figure 2.6.

These differences in the development of air showers are used to discriminate between γ-ray- and hadronic-induced showers.

2.4.3 Emission of Cherenkov light

At VHE energies the majority of secondary charged particles in an air shower travels with a velocity, v, exceeding the phase velocity of light, c, in air. These particles emit Cherenkov light [Cherenkov, 1934] in a narrow cone with angle Θ_C with respect to the primary particle path as illustrated Figure 2.7:

$$\cos\Theta_C = \frac{1}{\beta n_r}, \tag{2.21}$$

where n_r is the refractive index of the medium the particle travels through. This equation has important implications,

- As $\cos\Theta_C < 1$, the threshold velocity below which no radiation is produced is given by $\beta > 1/n_r$. The minimum energy of a particle to produce Cherenkov radiation depends on the mass of the particle, m_0, and the refractive index, n_r,

$$E_{min} = \gamma_{min} m_0 c^2 = \frac{m_0 c^2}{\sqrt{\left(1 - \frac{1}{n_r^2}\right)}}. \tag{2.22}$$

- If $\beta \simeq 1$ or $v \simeq c$, the maximum angle of emission, $\Theta_{C_{max}}$ (*Cherenkov angle*), is reached

$$\Theta_{C_{max}} = \arccos\left(\frac{1}{n_r}\right). \tag{2.23}$$

The number of produced Cherenkov photons by a charged particle per unit length, x, and per unit wavelength, λ, is computed by the Frank-Tamm-formula [Tamm and Frank, 1937]

$$\frac{d^2N}{dx\,d\lambda} = 2\pi\alpha z^2 \cdot \frac{1}{\lambda^2}\left(1 - \frac{1}{\beta^2 n_r^2(\lambda)}\right) \tag{2.24}$$

with α being the fine structure constant and z the charge of the particle. When crossing the atmosphere, shower particles cross a medium that continuously changes its refractive index, n_r, on the way to ground. Following the assumption of an isothermic atmosphere [Hillas, 1982] with an initial refractive index of $n_{r_0} = 2.9 \times 10^{-4}$, a scale height of $h_0 = 7250\,\mathrm{m}$, and a height at sea level, h, the refractive index can be approximated by

$$n_r(h) = 1 + n_{r_0} \cdot \exp\left(-\frac{h}{h_0}\right). \tag{2.25}$$

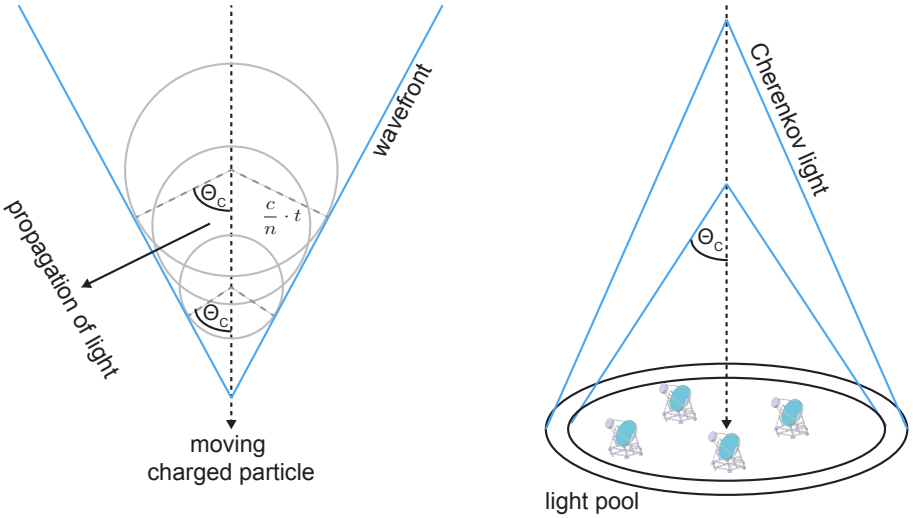

Figure 2.7: Schematic diagram of the Cherenkov radiation emitted by a charged relativistic particle moving along the z-axis. The Cherenkov radiation is emitted under the angle Θ_C producing a light pool of Cherenkov photons on ground. The scheme illustrates the direction of propagation of the Cherenkov photons and the instantaneous position of the wavefront. Figure adapted from Grieder [2010].

If the height, h, decreases, the refractive index, n_r, increases as the density of air increases and the Cherenkov angle, Θ_C, decreases according to Equation 2.21. The light cone of γ-ray showers characterised by a homogeneous light distribution in a ring with radius between 80 and 120 m [Aharonian et al., 2008] around the shower axis is called the *Cherenkov light pool*. Beyond the radius of this light pool, the number of Cherenkov photons drops exponentially. For hadronic showers the situation is different. Secondary particles receive a higher transverse momentum which makes these showers more widely spread. The emission of Cherenkov light by the electromagnetic subshowers exhibit larger fluctuations. Moreover, there is an additional component of Cherenkov light on ground. This arises from muons reaching the ground with sufficient energy to produce Cherenkov radiation in a cone around their path. Another crucial difference is the fact that the front of Cherenkov photons emitted by an electromagnetic cascade arrives at ground within 2 to 5 ns [Grieder, 2010] while hadronic showers have a wider time spread of 10 to 15 ns due to electromagnetic subshowers and larger transverse momentum. These differences are used in IACT experiments to discriminate between cosmic-ray- and γ-ray-induced air showers.

2.5 Imaging Atmospheric Cherenkov Technique

As the Earth's atmosphere is opaque to high-energy photons, the most direct approach to study the γ-ray sky is to send detectors into space. However, the detector area of satellites becomes

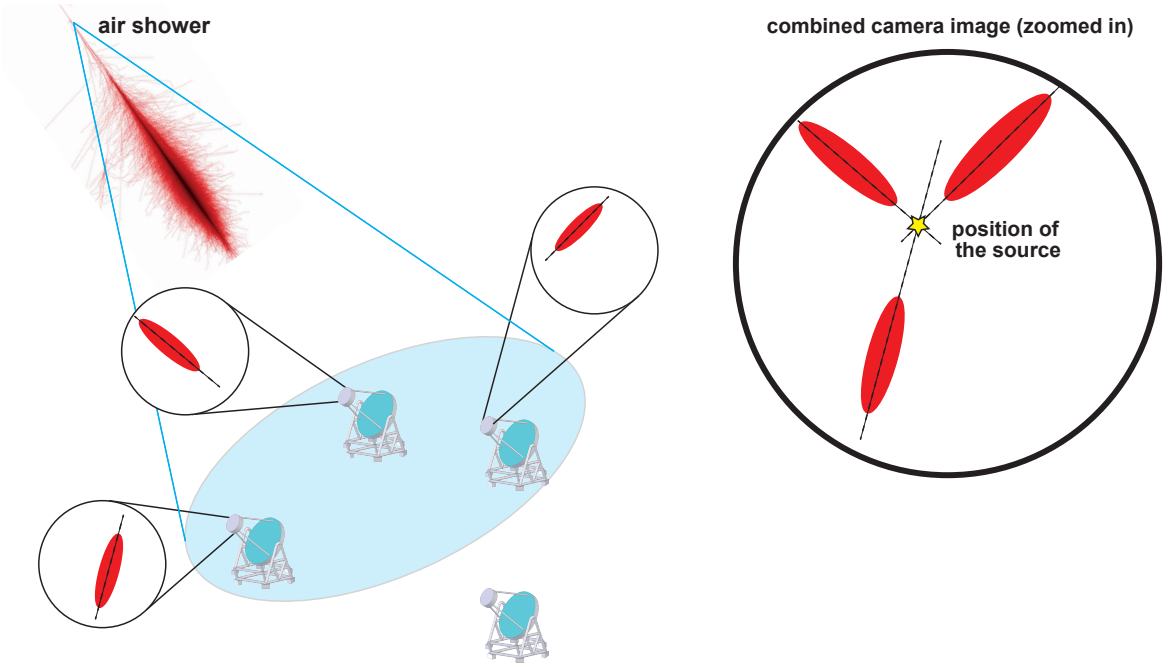

Figure 2.8: Illustration of the detection principle of γ-rays with the imaging atmospheric Cherenkov technique. Multiple telescope array images are used to detect the air shower. The intersection point (yellow star) of the major axes of the three red image represents the position of the source in the camera. Figure adapted from Guenette [2010].

too small to measure γ-rays at energies in the VHE regime as their flux decreases dramatically dependent on energy. To study the universe at these energies, detectors with huge collection areas are required, e.g. IACT experiments. They measure the Cherenkov light produced by air showers in the atmosphere. Galbraith and Jelley [1953] first reported on imaging atmospheric Cherenkov detectors using the Earth's atmosphere as a calorimeter to sample the Cherenkov light. The pioneering instrument in this field was the *Whipple* telescope located on Mount Hopkins in the U.S.A. [Weekes et al., 1989]. The detection principle requires a large mirror to collect the Cherenkov light and fast photon detectors to record them. The Cherenkov light of the air shower is focused around the direction of the incident primary particle illuminating an area of about 120 m in radius on the ground. The mirrors reflect the Cherenkov light onto an array of fast photon-detectors. As Cherenkov photons arrive within a very short time interval, fast photon detectors and electronics are required to discriminate Cherenkov light from fluctuations of the night sky background (NSB). Photomultiplier tubes (PMTs) are currently the most efficient light sensors for IACT cameras. In addition, a larger mirror area leads to a larger collection area for the detection of Cherenkov photons and to a lower energy threshold of the system compared to arrays with smaller mirror areas.

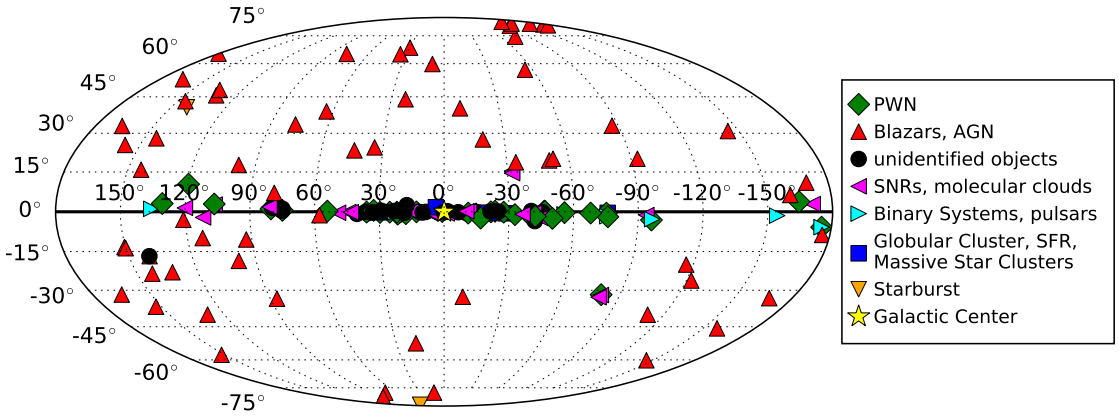

Figure 2.9: Skymap of sources of VHE γ-rays. The positions of all known VHE γ-ray sources emitting at TeV energies, detected by IACTs [Wakely and Horan, 2008] are shown in a Mollweide projection of the sky in Galactic coordinates. The source positions are taken from Wakely and Horan [2016].

Because of the high background induced by cosmic-ray showers, a large collection area of the telescope cannot provide adequate sensitivity for effective studies of cosmic γ-rays [Aharonian et al., 2008]. Therefore, ground-based detectors should be able to suppress hadronic-induced air showers. The discrimination between γ-ray- and cosmic-ray-induced showers is based on shower shape parameters. In the stereoscopic approach, the IACT technique is combined with multiple telescopes to image the air shower from different viewing angles [Kohnle et al., 1996]. The telescopes are spaced by about 100 m. This is large enough to provide a sufficient baseline for stereoscopic measurements but small enough that several telescopes are positioned within the Cherenkov light pool, as illustrated in Figure 2.7. This improves the reconstruction of the detected γ-ray showers and the rejection of hadronic showers compared to measurements with a single telescope. In addition, a coincidence requirement is applied to reject single-telescope triggers caused by the NSB, or by cosmic-ray muons with impact points close to the telescope mirror. Using a stereoscopic measurement approach, as depicted in Figure 2.8, the source position in the camera is more accurately reconstructed.

Present instruments in the field of ground-based γ-ray astronomy are aimed to be sensitive to photons with energies above about 50 to 100 GeV. The three major experiments using the IACT technique are the High Energy Stereoscopic System (*H.E.S.S.*) in Namibia [Aharonian et al., 2006b], the Major Atmospheric Gamma Imaging Cherenkov Telescopes (*MAGIC*) on the Canary island of La Palma [Aleksić et al., 2016a,b], and *VERITAS* in the U.S.A. These instruments have a typical duty cycle of about 10 % (approximately 1000 h/yr) as faint Cherenkov light from air showers cannot be detected during daylight. The number of known γ-ray emitters at very high energies detected by IACTs currently exceeds 170 sources [Wakely and Horan, 2008]. These are of Galactic and extragalactic origin, as depicted in Figure 2.9. Source types of Galactic objects

are believed to be SNRs, pulsars, PWNe, binary systems, and stellar winds interacting with the ISM. In addition, unidentified sources without any obvious counterpart at other wavelengths, as well as the Galactic centre, have been shown to emit VHE γ-rays in our Galaxy. Furthermore, starburst galaxies, AGN, and γ-ray bursts contribute to the amount of γ-ray emission seen from outside our Galaxy [Degrange and Fontaine, 2015]. The 56 sources detected by *VERITAS* until 2016 include 21 Galactic sources, and 35 sources of extragalactic origin.

Having introduced the acceleration of cosmic rays and the production mechanisms of γ-rays, this chapter further described the population of potential classes of VHE γ-ray emitters in the Galactic plane. It concluded with the physics of extensive air showers and their detection via IACTs. The following chapter will focus on the description of the Very Energetic Radiation Imaging Telescope Array System (*VERITAS*) and its current analysis approach of VHE γ-ray data is presented.

3

The Very Energetic Radiation Imaging Telescope Array System

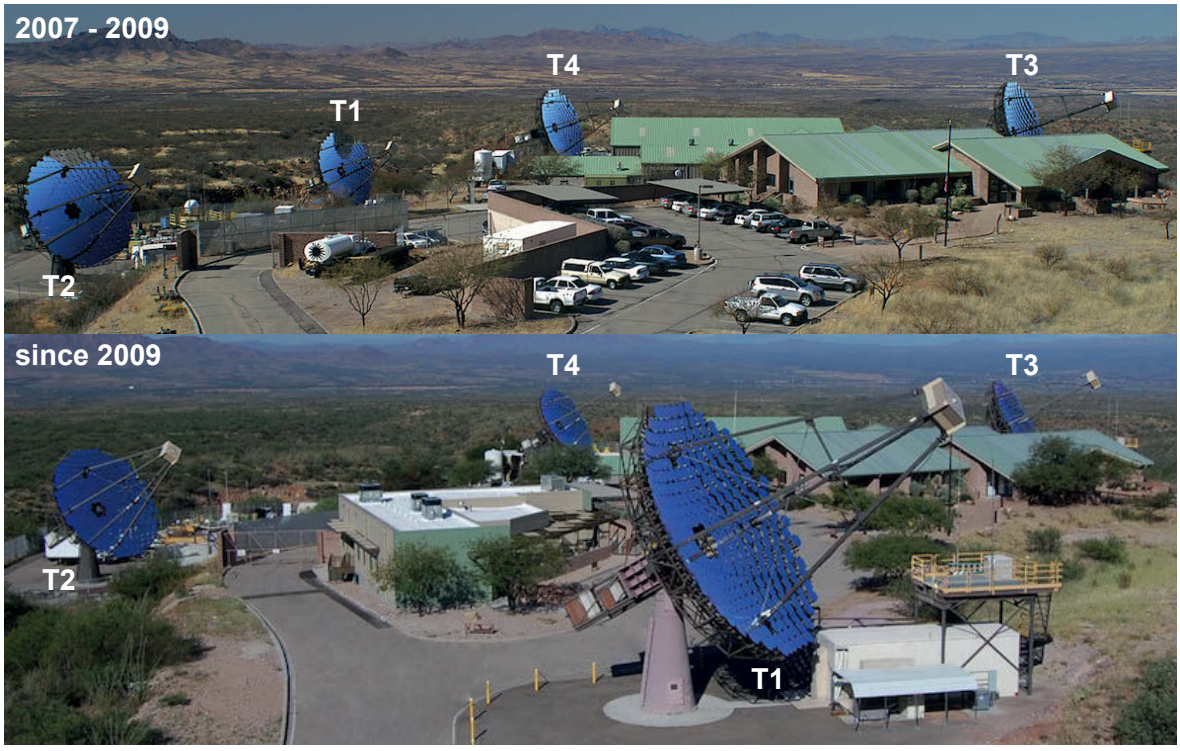

Figure 3.1: The *VERITAS* array before (top) and after summer 2009 (bottom). The relocation of telescope T1 in summer 2009 led to a relatively uniform array layout. The distance between two telescopes is about 100 m. Image credit: *VERITAS* collaboration.

In February 2005, the first atmospheric Cherenkov telescope of the **V**ery **E**nergetic **R**adiation **I**maging **T**elescope **A**rray **S**ystem (*VERITAS*) started operating [Holder et al., 2006]. *VERITAS* is located at the basecamp of the Fred Lawrence Whipple Observatory in southern Arizona, U.S.A. (31°40′30.21″N, 110°57′7.77″W) at an elevation of 1270 m. The array layout is shown in Figure 3.1. The construction of the full array of four telescopes with a diameter of 12 m was completed in 2007 [Holder et al., 2009]. The full array reaches an angular resolution of about 0.1° at 1 TeV, whereas each telescope covers a field of view of approximately 3.5°. *VERITAS* is designed to study astrophysical sources within an energy range from 100 GeV to over 30 TeV

[Holder et al., 2009]. Since the completion of the array the sensitivity of *VERITAS* has steadily increased, mainly due to two major hardware upgrades, but also as a results of a number of smaller hardware and software improvements. The first major improvement took place in summer 2009 with the relocation of telescope 1. It was moved in order to make the array more symmetric, increasing the overall sensitivity by approximately 30 % [Perkins and Maier, 2009]. The second major upgrade was conducted in 2012 with the replacement of all PMTs with high-quantum-efficiency devices, and an improvement of the trigger system [Kieda, 2013].

From here, the period before the relocation of telescope 1 (2007/09/01 – 2009/08/31) is referred to as V4, the period after the relocation of telescope 1 and before the camera upgrade (2009/09/01 – 2012/08/31) as V5, and the period after the camera upgrade (2012/09/01 – present) as V6. Note that an observing season spans the months of September to the following July, after which the array is shut down until the following September to allow for the Arizona monsoons. This thesis focuses on data taken between April 2007 and June 2012. Therefore, the description of the *VERITAS* instrument in this chapter concentrates on the telescope array before the second major upgrade.

In this chapter, the principle of operation of the *VERITAS* instrument including the mechanical and optical structure is introduced. Next, the trigger algorithm used to detect light coming from potential γ-ray-initiated air showers is described, and the *VERITAS* analysis is presented in detail. Finally, the challenge of separating hadronic-induced showers from VHE photon induced showers is discussed. Here, the selection criteria which have been proven to be very efficient at reducing this background are highlighted.

3.1 The *VERITAS* instrument

VERITAS consists of four identical telescopes. Each one is comprised of four major units; the optical support structure and mirror, the camera, the trigger system, and the data acquisition system.

3.1.1 Telescope mechanics and optics

Each telescope, as illustrated in Figure 3.2, consists of an altitude-over-azimuth positioner supporting a tubular steel optical support structure (OSS) [Holder et al., 2006]. The maximum slew speed is about $1\,^{\circ}/\mathrm{s}$. The telescope follows a Davis-Cotton design [Davies and Cotton, 1957] with a focal length of 12 m. At the focus of the reflector the camera is mounted on a quadropod. The camera load is directed by a mechanical bypass onto a set of counterweights at the back of the OSS. The reflector mounted onto the OSS comprises 345 hexagonal, aluminised mirror facets [Roache et al., 2007]. Each facet has an area of $0.322\,\mathrm{m}^2$ resulting in a total mirror area

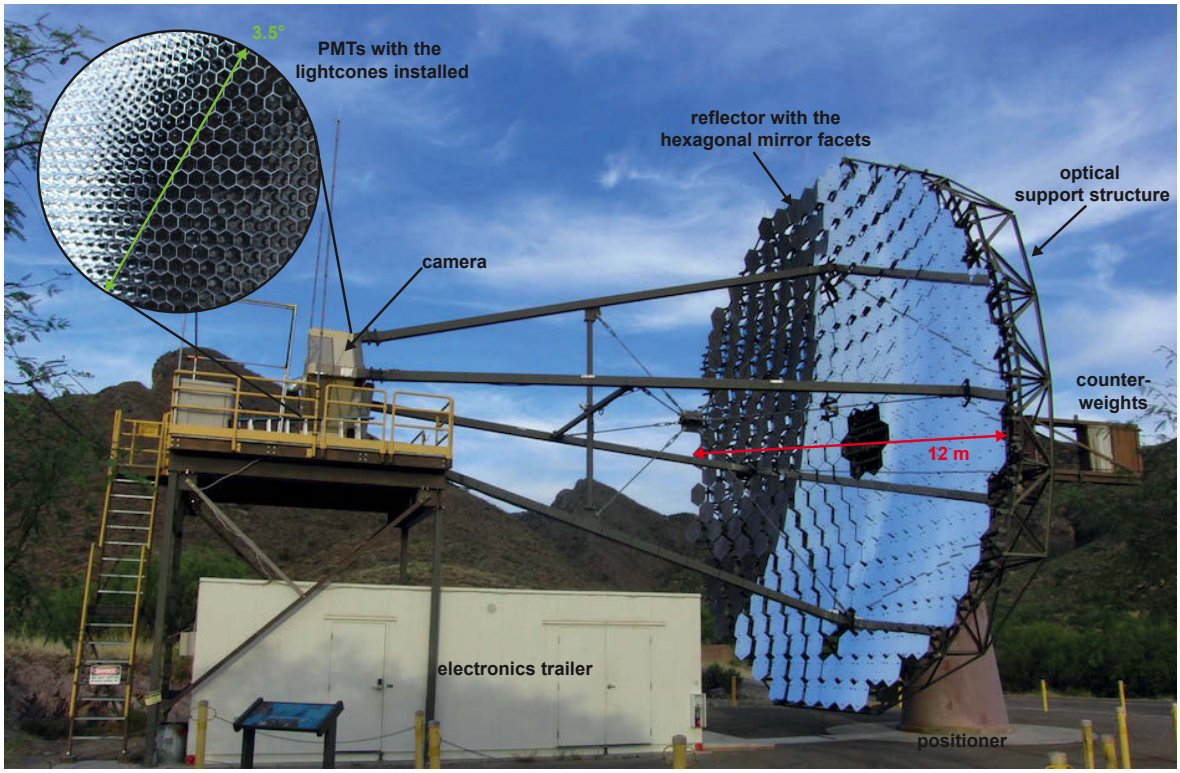

Figure 3.2: A single *VERITAS* telescope (T1) with the different telescope components indicated.

of about 110 m^2. Due to the load of the OSS, each mirror facet moves by a small amount due to gravity. The latter distorts with variations in zenith angle pointing resulting in possible pointing inaccuracies and in an increase of the point spread function (PSF) [Toner et al., 2007]. The PSF describes the response of an imaging system to a point source of light at infinity. This distortion is measured on a regular basis by performing an alignment of each mirror facet when placing a CCD camera at the focus of the optical system facing the reflector [McCann et al., 2010]. The 80 % containment radius of the optical PSF of *VERITAS* is typically less than 0.05° at operational elevations [McCann et al., 2010].

3.1.2 Camera

At the focus of each reflector, a camera with 499 PMTs is located (Figure 3.2). Until autumn 2012, the photon sensors were Photonis XP2970/22 29 mm diameter PMTs (Section 3.1.5). The PMTs are UV-sensitive with a quantum efficiency of 25 % at wavelengths relevant for Cherenkov images of about 320 nm [Nagai et al., 2007]. They are spaced by 0.15° giving a total aperture of the camera system of 3.5° [Holder et al., 2006; Nagai et al., 2007]. In front of each PMT, a Winston-type light concentrator [Jordan and Krennrich, 2004; Nagai et al., 2007] is installed which reduces the dead space between the pixels, increases the collecting area, and reduces the amount

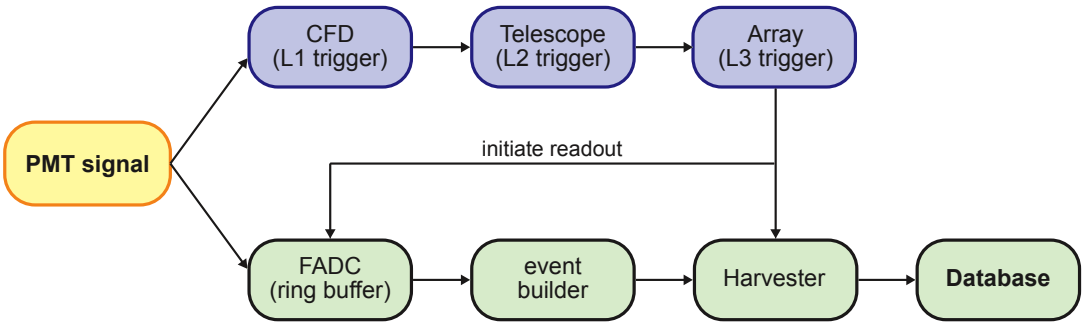

Figure 3.3: A simplified schematic view of the *VERITAS* trigger and DAQ system. The signal from the PMT is sent to the three-level trigger system (upper blue part). A copy of these signals is fed into the DAQ system (lower green part). Here, the signal gets digitized and buffered until the readout is initiated by the L3 trigger at which point events are assembled. Finally, the data are written to a database and archived.

of background light entering the PMT. The PMTs are powered with a multichannel power supply which allows individual control of each unit. They operate at a nominal gain of approximately 2×10^5 [Holder et al., 2006]. The PMTs are connected to high-speed preamplifiers boosting the signal again by a factor of 6.6. In addition, the preamplifier provides a direct DC output for anode-current monitoring purposes [Nagai et al., 2007] to protect the PMT from additional light sources such as bright stars. The signal from the preamplifiers is transmitted to the trigger electronics [Weinstein, 2007] and the data acquisition (DAQ) system [Hays, 2007] as illustrated in Figure 3.3.

3.1.3 Trigger

The *VERITAS* trigger system receives the signal from the preamplifiers. It is designed to trigger only on light coming from potential γ-ray-initiated air showers, rather than from fluctuations in the NSB, or from single muons from cosmic-ray showers. The trigger has three hierarchical conditions, which are described in detail in Weinstein [2007], as shown in Figure 3.3.

The first trigger level acts at the single pixel level (L1). Each PMT is equipped with a constant fraction discriminator (CFD) [Hall et al., 2003] to reduce the coincidence resolving time and hence, lower the energy threshold. The CFD produces a 10 ns output pulse if the sum of the voltages of the PMT pulse and a time-delayed copy crosses a certain threshold. In addition, each CFD is equipped with a rate feed-back which adjusts the CFD trigger rate when the NSB level changes.

The second trigger level is at the camera level (L2). The criterion of the pattern trigger is satisfied if three adjacent pixel surpass the L1 trigger within a time window of about 6 ns [Holder et al., 2006]. This trigger level is aimed to reject fluctuations due to NSB and PMT afterpulsing, and to select compact Cherenkov light images.

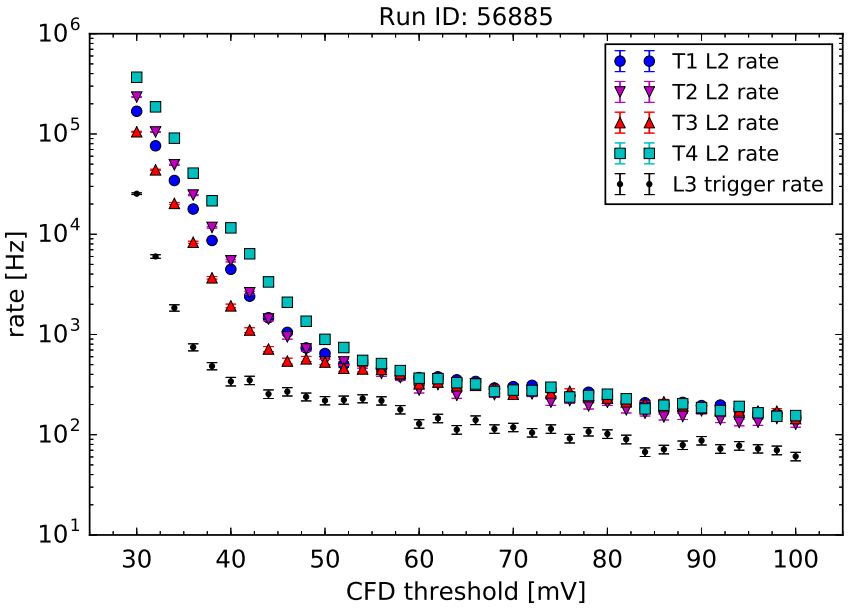

Figure 3.4: An example of a *VERITAS* bias curve taken under dark sky conditions. The trigger rates depend on the PMT discriminator voltage settings (CFD threshold) which varies between 30 and 100 mV. The black dots indicate the array trigger (L3 trigger) rate and the colours represent the L2 rates of the individual telescopes. Where no error bars are visible, the uncertainties are smaller than the size of the symbols.

The final trigger level is the array level trigger (L3). This trigger mainly rejects local muons by requiring a trigger on multiple telescopes in the array. In most cases, these particles are only able to trigger a single telescope, due to the limited size of their light pool. The L2 trigger from at least two telescopes within 50 ns is required. The latter ensures a stereoscopic view of the event. Due to the close proximity of about 35 m between telescopes 1 and 4 before summer 2009, and to the accidental trigger on events produced by local muons, an analysis cut was included to reject events that only triggered these two telescopes [Perkins and Maier, 2009]. When the L3 trigger occurs, a logical signal is sent back to all four telescopes to initiate the readout of the buffer by the DAQ system (Section 3.1.4). During the readout time, no additional trigger can be accepted. This introduces a dead time to the system, which is about 10 % at a L3 trigger rate of 225 Hz [Weinstein, 2007].

In order to set the trigger levels for the best trigger conditions (low energy threshold, low contribution from the NSB, stable trigger rates), bias curves (Figure 3.4) are taken. Trigger rates at the camera level (L2) of each telescope, and at the array level (L3) are recorded by the system depending on the CFD trigger threshold. If the trigger threshold is too low, the triggers are dominated by the NSB fluctuations. This decreases dramatically as the trigger threshold rises. Above a certain threshold the triggers are dominated by cosmic and γ-rays. At this point, the trigger rate decreases more slowly. The optimal CFD threshold is found at the inflection point

where the trigger rate contributions of both components (NSB and cosmic rays) are equal [Lin, 2015]. However, air showers initiated by low-energy γ-rays tend to be smaller and fainter than high-energy ones. Therefore, they are more likely to be seen at lower CFD thresholds. The lower the CFD threshold, the lower the energy threshold of the whole instrument. As the NSB level depends on the brightness of the sky, the optimal CFD threshold depends on different factors, such as weather conditions, intensity of star light in the field of view, and the intensity of moonlight.

3.1.4 Data acquisition system

The data acquisition (DAQ) system of *VERITAS* employs a 500 megasample per second flash analog-to-digital converter (FADC) at each telescope [Hays, 2007]. These FADCs continuously digitize the analog PMT signal at a rate of 2 ns/sample. Then, this is stored to a ring buffer for 32 µs while awaiting the L3 trigger signal. When an L3 trigger is received, the DAQ system reads out a section (2007-2012: 16 samples) of this buffer for each PMT signal. Then, the digitised signals are sent to a telescope-level event builder, where complete events are integrated, tested and passed to the array-level data harvester machine. The harvester combines the event information of the telescope-level into array-level information such as time and event number. Finally, this is stored into a custom *VERITAS* data format and saved to disk for offline data analysis. In addition, all observing conditions such as trigger settings, voltage values, and weather conditions, as well as target information, observation mode, and any comments from the observers, are recorded to the database.

3.1.5 The *VERITAS* upgrade in 2012

As mentioned at the beginning of the chapter, *VERITAS* underwent a major upgrade in summer 2012 when the PMTs in each camera were replaced to lower the energy threshold and to improve the overall sensitivity of *VERITAS* [Kieda, 2011; Otte, 2011; Kieda, 2013]. The pre-upgrade PMTs of type Photonis XP2970 were substituted by Hamamatsu R10560-100-20 PMTs.

The main advantage of the new PMTs is the larger photon-detection efficiency. They measure on average about 23 % more Cherenkov photons than the previous type of PMTs. This leads towards a higher light yield of about 35 %. Another benefit of the new PMTs of Hamamatsu is their narrower pulse shape of about 40 % compared to the Photonis ones [Otte, 2011]. This discriminates the Cherenkov light of air showers from fluctuations of the NSB better. In addition, the signal-to-noise ratio is improved by narrowing the summation window of the trace analysis.

Additionally, the trigger system of *VERITAS* was upgraded [Zitzer, 2013]. The reduced coincidence gate width at the camera level from 6 ns to about 3 ns improved the rejection of the NSB, permitting a reduction of the energy threshold at the trigger level.

The upgrade of the trigger and the camera system with high-quantum efficiency PMTs reduces the energy threshold from about 100 GeV before the upgrade to about 85 GeV now [Park, 2015]. Currently, *VERITAS* can detect a 1 % Crab Nebula-like source with 5σ in about 25 hours [Park, 2015].

As mentioned above, this thesis focuses on data taken between April 2007 and June 2012. Therefore, the description of the *VERITAS* analysis in the following concentrates on the telescope array before this upgrade.

3.2 Calibrations

The digital information originating from the primary data including FADC traces and trigger information have to be translated into a calibrated form. Calibrations are determined while commissioning, monitored, and adjusted periodically during the lifetime of the experiment.

The absolute gain of the PMTs is determined with a nitrogen laser with a wavelength of 337 nm and a pulse length of 4 ns [Hanna, 2007]. A laser run lasting for 5 min is taken each night monitoring the gain evolution and checking for problems of the camera. Diffusers at the end of the PMTs provide a uniform and simultaneous illumination of the camera. The pulses are used for flat fielding the response of the channels. If the RMS of the relative gain distribution exceeds about 10 %, the high voltage of the single PMTs is adjusted to achieve the same relative gain in each channel. As all pixels have about the same relative gain, trigger rates are expected to be similar in all pixels.

The same laser run which is used for the flat fielding of the camera provides a measurement of the time delays between each channel. These channel-to-channel variations arise from different cable length and electronic delays. This correction is applied in the data analysis. Since January 2010, each *VERITAS* telescope has been equipped with an LED-based flasher system. Since then, the time of a calibration run was shortened to about 2 min. Full details of the method of analysing the information of the flasher run are given in Hanna et al. [2010].

The individual PMT rates are large due to the NSB. Every point in the sky has essentially a different NSB. Therefore, the noise is monitored by recording the fluctuations in all PMTs. The value of the output signal of the PMT where no Cherenkov light is detected is called the *pedestal* [Daniel, 2007]. Pedestal events are artificially triggered at a frequency of 1 Hz, and are averaged every three minutes for each pixel. They are used in turn to calibrate the total charge in a pixel. This baseline measurement of the pixel in the absence of Cherenkov light is a useful diagnostic tool to remove problematic pixels from data taking and analysis.

In addition to the calibration of the camera system, the weather conditions are continuously monitored. The atmosphere is an integral part of the detector and Cherenkov telescopes are

sensitive to various weather conditions due to the presence of atmospheric particles and clouds. To monitor the sky quality, the sky temperature is measured by infrared pyrometers. A rise in temperature adverts to clouds and haze, as water vapors and droplets in the field of view of the pyrometer act as infrared emitters. All information is logged into a database, facilitating the correct interpretation of the scientific results.

3.3 The *VERITAS* data analysis

The analysis of VHE γ-ray data begins with a data file containing the information pertaining to the events in the data run. The purpose of the analysis is to estimate the spectrum or the morphology from a source in the sky. This section deals with the standard data analysis framework of *VERITAS*, specifically the analysis software package *eventDisplay*[1] [Daniel, 2007]. The following steps are discussed: calibration and image processing, background reduction, γ/hadron separation, and signal extraction.

3.3.1 Charge integration

The total charge in each pixel is obtained by integrating the FADC trace over a selected time window. It is measured in digital counts (dc). Two typical FADC traces are shown in Figure 3.5. The left panel shows a typical pulse shape of a PMT signal arising from Cherenkov photons. It is characterised by a fast rise to a peak value, and a slight decay back to the baseline value, the pedestal. The arrival time of the signal is identified by the time T_0, where the trace rises to half its maximum value. This value is corrected for the relative time delays between the pixels. The right panel in Figure 3.5 shows a typical shape where no Cherenkov light is detected. It is characterised by fluctuations around the pedestal value. The method of charge integration as used in the *VERITAS* analysis package *eventDisplay* follows the double-pass approach [Holder, 2005]. In the first step, the charge and arrival time are calculated by integrating the FADC trace with a wide integration window (typically 16 ns). Following this, the image is cleaned and parametrised as described in Section 3.3.2 and Section 3.3.3, and the arrival time T_0 is determined. In the second step, a smaller integration window (typically 6 samples with a sample width of 2 ns) is applied to increase the signal-to-noise ratio. The starting position of this short integration window is obtained by a fit of the temporal shower development along the major axis of the image, after it is parametrised. The slope of the fit function, the time gradient, determines the starting point. Finally, the charge is obtained by subtracting the pedestal value for the same integration window, and the relative gain is applied to calibrate the charge.

[1] https://znwiki3.ifh.de/CTA/Eventdisplay%20Software

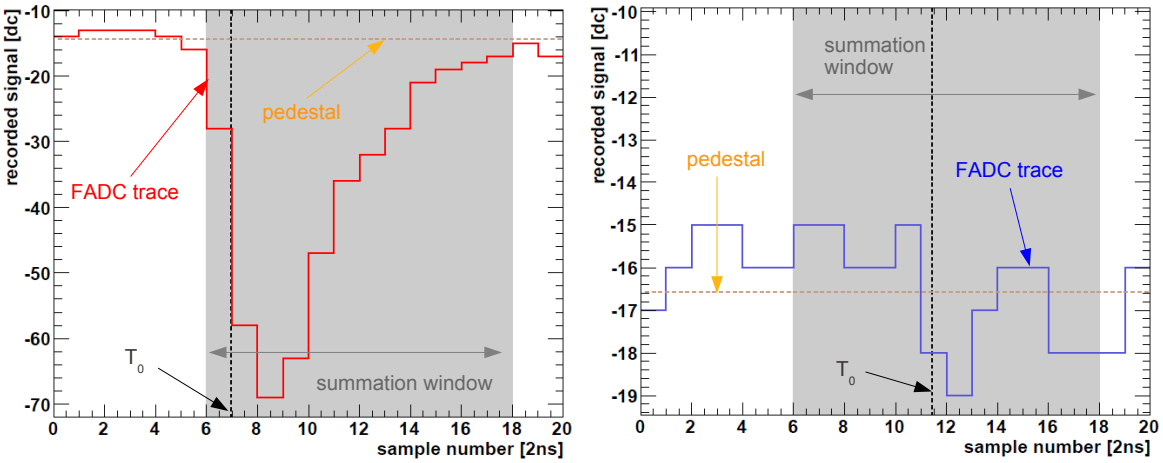

Figure 3.5: *Left:* A trace from a single channel that has received a significant signal of Cherenkov photons. The 12 sample (1 sample equivalent to 2 ns) window has been placed to integrate the bulk of the trace whilst excluding background fluctuations (grey shaded area). The trace is offset from zero by a pedestal of about −16 dc (orange dashed line). *Right:* The FADC trace in the absence of Cherenkov photons fluctuates around the pedestal. The black dashed line demonstrates the arrival time, T_0. Figure adapted from Prokoph [2013].

3.3.2 Image cleaning

After the charge in each pixel is determined, image cleaning follows [Bond et al., 2003; Daniel, 2007]. This removes background fluctuations from the event and assists to identify if the air shower was initiated by a γ-ray or a cosmic ray. Pixels with an integrated charge greater than five times their pedestal standard deviation are identified as picture pixels. Any neighbouring pixel of these pixels producing an integrated charge greater than 2.5 times their pedestal variations are identified as boundary pixels. If a pixel has passed cleaning but no boundary pixel adjacent, it is removed. The remaining picture and boundary pixels define the image of the Cherenkov shower.

3.3.3 Image parametrisation

The recorded image is a two-dimensional projection of an air shower resembling an ellipse. At this stage in the analysis, the image is parametrised, where the image parameters are extracted according to the moment analysis [Hillas, 1985]. The parameters are listed in Table 3.1 and illustrated in Figure 3.6. The equations used to derive the so-called Hillas parameters are outlined in Fegan [1997]. Then, the extracted parameters are used to determine the source position of the shower and the energy of the primary particle. They are also used for γ/hadron separation [Fegan, 1997].

parameter	description
size	The integrated charge or total intensity of the light content of the shower, denoted as s.
width	The RMS spread of the light along the minor axis of the elliptical image, denoted as w.
length	The RMS spread of the light along the major axis of the elliptical image, denoted as l.
distance	The distance from the centroid of the image to the centre of the field of view of the camera.
centroid	The coordinates of the centre-of-gravity of the image, denoted as C.
loss	The fraction of the charge of the image on the edge of the camera. It is used to remove strongly truncated images at the camera edge.

Table 3.1: Definition of image shape parameters.

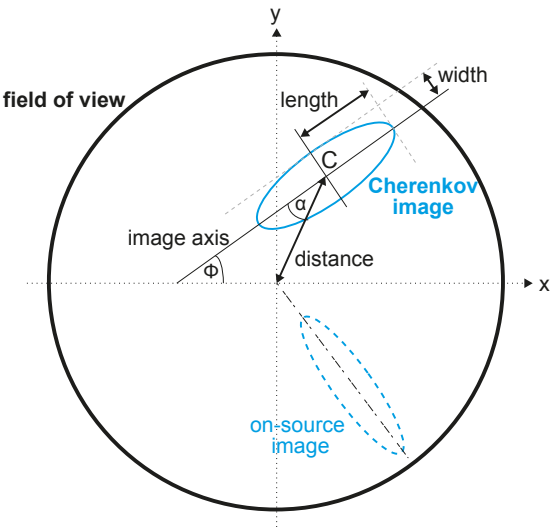

Figure 3.6: Basic image parameters of an air Cherenkov image used to select photon-initiated showers and discriminate against hadron-initiated showers. The black solid circle demonstrates the field of view of the telescope camera. The blue solid ellipse represents pixel image contours, whereas C is the centroid of the image. The blue dashed ellipse indicates the shape of an *on-source Cherenkov image*, where the extension of the major axis intercepts with the centre of the field of view.

3.3.4 Stereoscopic event reconstruction

After all individual telescope images are cleaned and the image parameters are determined, the images are combined to reconstruct the shower. As a first step, quality cuts are applied to the images itself to remove images that will be problematic to reconstruct, e.g. they are too small or too close to the edge of the camera and mostly truncated. These cuts include a minimum number of picture/boundary pixels ($N_{pix} \geq 5$), a minimum image size ($s > 400\,\mathrm{dc}$), a maximum loss value ($loss < 0.2$), and a minimum number of three telescope images.

Arrival direction and position of the shower core

Showers develop along the original direction of the initiated particle. For each shower image the origin of the shower is located on the major axis of the image ellipse. The direction of the event is reconstructed by following algorithm 1 of Hofmann et al. [1999]. Here, multiple images of the showers are overlaid in a single camera, as depicted in Figure 2.8, and the intersection point of the major axes for each pair of two images is calculated. To identify where the γ-ray originated, the weighted average of the intersection points is taken into account. These weights include the angle between two image axes, the image size, and the ratio of image width-over-length. Thus, brighter and more elongated images receive higher weights.

Similarly the position of the shower core on the ground can be determined. The latter describes the location on the ground where the γ-ray would have landed, if it had not been absorbed in the atmosphere. The image axes are projected onto a plane perpendicular to the telescope pointing direction. The shower planes intersect the ground in a straight line, on which the shower core must be located. Then, the core position is determined by minimising the distances from each major axis to the position of the source taking the weighted average of the intersection of all axes into account. At this point, the impact parameter, R, which is the distance between the telescope and the shower core in the plane perpendicular to the shower arrival direction, can be determined. The latter is an important parameter for the analysis when estimating the energy of the primary particle initiating the air shower.

Emission height

In addition to the direction and the position of the core of the shower, the emission height, h_{em}, is calculated [Aharonian et al., 1997]. The emission height is estimated for each combination of two telescopes (pair-wise). The final value is the mean of all telescope pairs weighted by their corresponding image size. Furthermore, the $\chi^2_{h_{em}}$-value of the emission height of each pair of two telescope events is determined. Both parameters can be used to efficiently reject background events, as charged cosmic rays and muons penetrate deeper into the atmosphere than γ-rays.

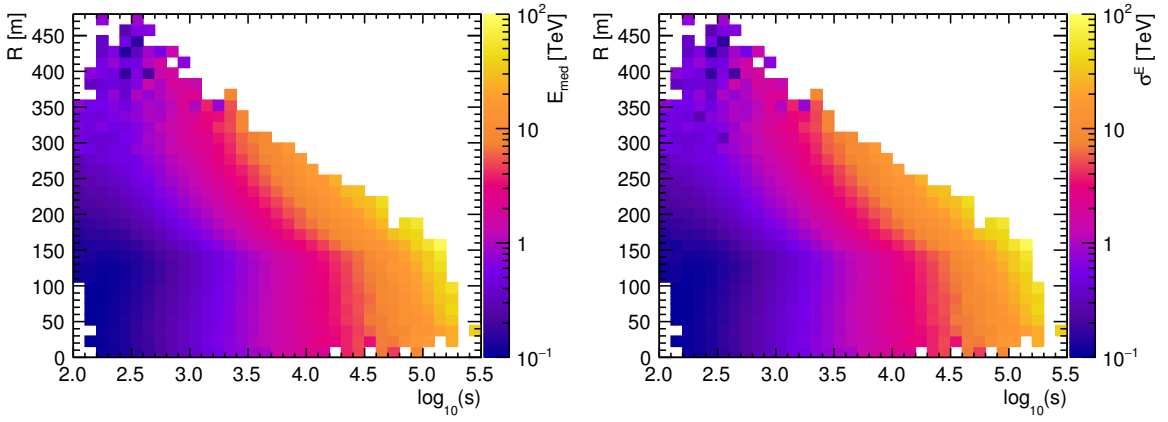

Figure 3.7: A lookup table for the median, E_{med} (*left*), and 90 %-width value, σ_i^E (*right*), as used for the reconstruction of the energy of the event, E. Tables are produced from MC simulations as a function of impact parameter, R, and image size, s.

Position of the shower core

The shower core describes the location on the ground where the γ-ray would have landed, if it had not been absorbed in the atmosphere.

Energy

The last parameter to be extracted from the shower images is the energy, E. This is linked to the total charge contained in the image, s, and to the impact parameter, R. Showers close to the telescope appear bigger in the camera, while showers further away show up smaller. Furthermore, the reconstructed energy also depends on the observing conditions, such as the distance from the position of the source to the centre of the camera (*wobble offset*, δ), zenith and azimuth angles, and the NSB. The energy is estimated using Monte-Carlo (MC) simulations of γ-ray induced showers at a wide range of zenith angles, wobble offsets, and NSB levels. These are used to produce reference tables, called *lookup tables*. They are filled with the median, E_{med}, and the 90 %-width, σ^E, values of the energy, E, as a function of R and s. An example for a fixed shower direction and level of NSB is shown in Figure 3.7. For each telescope image, an energy estimate, E_i, is derived. As the simulations are performed in finite steps of zenith angle, wobble offset, and NSB level, the estimated value is obtained by interpolating between the results from different tables. The reconstructed energy of the event E is computed by averaging over the energy estimated from N telescopes, calculated over the square of the 90 %-width value σ_i^E;

$$E = \frac{\sum_{i=1}^{N} \frac{E_i}{\left(\sigma_i^E\right)^2}}{\sum_{i=1}^{N} \frac{1}{\left(\sigma_i^E\right)^2}}. \tag{3.1}$$

In addition, the χ^2_E-value of the energy estimation is derived as

$$\chi^2_E = \frac{1}{N-1} \sum_{i=1}^{N} \left(\frac{E - E_i}{\left(\sigma_i^E\right)^2} \right). \tag{3.2}$$

The latter is used as part of the γ/hadron separation procedure, as the energy estimated from individual images differ from the average energy much more for irregular hadronic showers, than for regular compact γ-ray images.

3.3.5 γ/hadron classification and event selection

Until this stage of the analysis, direction and energy of the showers are reconstructed. The challenge remains to effectively remove the isotropic cosmic-ray-like events from γ-ray-like events. The hadronic background is a factor $\mathcal{O}(10^3)$ larger than the number of γ-rays emitted by astrophysical objects. The typical parameters to identify cosmic-ray-like and γ-ray-like events are image shape parameters (Table 3.1).

Shower-shape parameters

The shower shape depends on the observing parameters (zenith angle, wobble offset), the distance to the telescope, and the energy. A single shower viewed from different sides can have a different shape in each telescope. To discriminate the dominant component of hadron-induced showers with a broader and irregular shape from the more elliptically shaped γ-rays, *eventDisplay* follows the approach as described in Krawczynski et al. [2006]. This uses the parameters *mean reduced scaled width*, denoted as $MRSW$, and *mean reduced scaled length*, $MRSL$. Both parameters depend on the energy of the primary particle, the impact parameter, and the NSB. Therefore, lookup tables based on γ-ray MC simulations are used, similar to the lookup tables applied to the energy reconstruction. The lookup tables are filled with the median, $\hat{w}(R,s)$, and the 90 %-width values of the expected image width, $\sigma_{w_{MC}}(R,s)$, as a function of image size, s, and impact parameter, R. Finally, the image width for individual telescope images, w_i, are combined in a weighted average for an array of telescopes with multiple images per event. The same applies for the expected length of the image, respectively. They are derived as

$$MRSW = \frac{1}{N_{images}} \sum_{i=0}^{N_{images}} \left(\frac{w_i - \hat{w}(R,s)}{\sigma_{w_{MC}}(R,s)} \right) \cdot \left(\frac{\hat{w}(R,s)}{\sigma_{w_{MC}}(R,s)} \right)^2 \tag{3.3}$$

and

$$MRSL = \frac{1}{N_{images}} \sum_{i=0}^{N_{images}} \left(\frac{l_i - \hat{l}(R,s)}{\sigma_{l_{MC}}(R,s)} \right) \cdot \left(\frac{\hat{l}(R,s)}{\sigma_{l_{MC}}(R,s)} \right)^2. \tag{3.4}$$

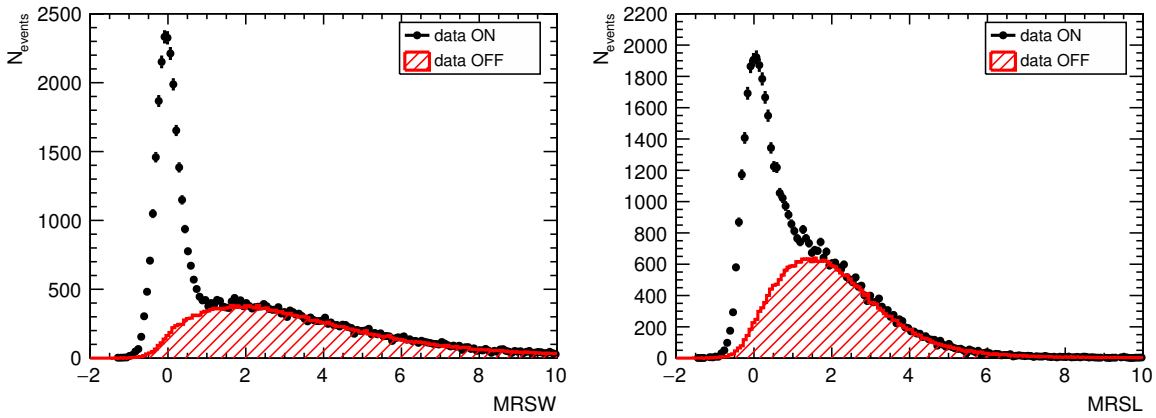

Figure 3.8: Event distribution of the mean reduced scaled width, *MRSW* (*left*), and the length, *MRSL* (*right*), as obtained from an analysis of the Crab Nebula. The black points show all reconstructed events in the `ON` region which arise from γ-ray-like events. The red curves show events from the `OFF` regions arising from background events.

By this definition, both parameters are centred on zero and Gaussian distributed for γ-ray-induced air showers. Because hadronic showers are less compact and more irregular, their images are longer and wider than γ-ray showers as demonstrated in Figure 3.8. By averaging over the number of telescopes recording an image, N_{images}, the analysis benefits from several advantages. The statistical fluctuations of the image shape parameters are taken into account in the estimation of the *MRSW* and *MRSL*. Furthermore, hadronic showers which look from one side like an electromagnetic cascade and from the other side like an hadronic cascade, can be effectively suppressed.

Event selection

The selection of γ-ray like events in *eventDisplay* is performed in a *preselection* phase, followed by the reconstruction of the direction and the shower properties. The preselection criteria are,

- A cut on the minimum size of the image is applied, which guarantees that showers can be properly reconstructed.
- Showers, which arrived too far from the telescopes ($>$350 m), are discarded because the major axes of their images are almost parallel. This results in a large uncertainty in the reconstructed location of the core of the shower.
- The maximum distance between the centroid of the image and the camera centre is set to 1.5°. This rejects images that are truncated close to the camera edge resulting in a mis-reconstructed shower direction and an underestimated primary particle energy because a large part of the charge of the image could be located outside of the field of view.

The direction is reconstructed for all events, which are detected in at least three telescopes. They also have to fulfill the preselection requirements. Then, the shower shape parameters are estimated. They reveal a separation power between γ-ray- and cosmic-ray-induced air showers. A single cut on the $MRSW$ and $MRSL$ effectively reduces the hadronic contribution. As cosmic rays arrive isotropically on Earth, a cut on the distance between the assumed source position and the reconstructed shower direction can further suppress hadronic background for point-like sources.

VERITAS defines three types of cuts which are generated for the majority of the sources. They are called *soft*, *moderate*, and *hard*. They are optimised depending on their source strength and spectral index, Γ, of the energy distribution $dN/dE \propto E^{-\Gamma}$ to obtain the maximum significance per observation time. *Soft* selection criteria are primarily for sources with a spectral index of $\geq$3.0. They are characterised by a low size cut. Thus, the energy threshold is low and more γ-ray statistics are available at the cost of a lower signal-to-noise ratio. *Hard* selection criteria are applied for sources with a hard spectral index of about $\leq$2.0 or weak sources. A large size cut is used. These cuts result in a smaller PSF and a better signal-to-noise ratio at the expense of a higher energy threshold and lower γ-ray statistics [Park, 2015]. In addition, there are *moderate* selection criteria which is a compromise between the other two sets of cuts and used for the majority of the sources.

3.3.6 Signal extraction

Even after using the aforementioned cuts to identify γ-ray-like events, an irreducible background remains which must be considered in the analysis. This background mainly arises from electron- and positron-induced air showers, and from cosmic rays, which appear like γ-rays [Maier and Knapp, 2007]. To account for this, the reconstructed shower direction for each γ-ray-like event is added into a skymap. Observations are taken with telescopes pointing at a certain distance (usually about 0.5°) away from the source in four cardinal directions (north, east, south, west). Then, the background is estimated from regions in the field of view which do not overlap with the source. Within the skymap two regions are defined: the ON region and the OFF region. These are used to compute the VHE γ-ray excess, N_{excess}, from the expected source region by

$$N_{excess} = N_{\mathrm{ON}} - \alpha N_{\mathrm{OFF}}, \tag{3.5}$$

where N_{ON} and N_{OFF} represent the number of events in the ON and OFF region, respectively. The factor ,α, is used to account for the difference in area and camera acceptance between these regions. The ON region is described by a circular region of radius θ_{cut} centred on the candidate source position. For point sources, this value is similar to the PSF of the telescope system and about 0.089°, while it is about 0.223° for slightly extended sources. The definition of the OFF

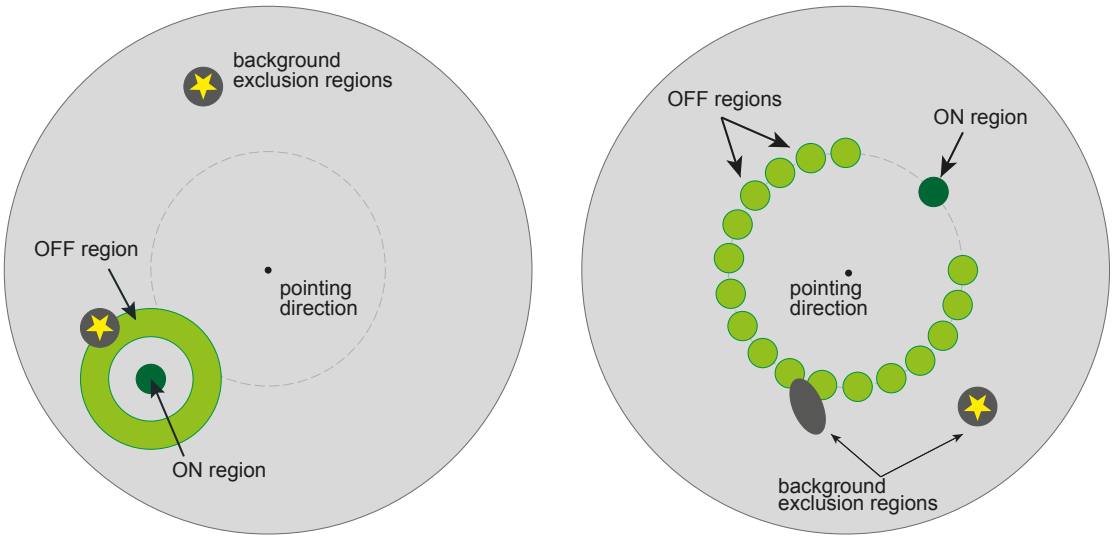

Figure 3.9: The two background analysis methods: ring background model (*left*) and reflected region model (*right*). The light green regions are used to estimate the background. There are positioned to avoid the potential source, bright stars or any other sources that could affect the flux in this region. The dark green region is used to determine the ON counts.

region is more complicated. There are several different methods; the two applied in this thesis will be described next. The first one is the *ring background model* (left panel Figure 3.9) where the background is estimated by a ring of given radius and width concentric around the ON region. To reduce the effect of statistical fluctuations in the background sample, a large area of the OFF region is selected. The radii of the ring are chosen so that the OFF region does not overlap with the ON region, to avoid double count of the events. As shown in the left panel of Figure 3.9, the response of the OFF region is no longer the same as in the ON region, because each position inside the ring lies at a different distance from the centre of the camera. Thus, it is necessary to model the response of the camera carefully, called *camera acceptance*. The correction factor, α, is computed by the ratio of the area modified with the camera acceptance, ϵ_γ;

$$\alpha = \frac{\int_{\mathrm{ON}} \epsilon_\gamma(\Psi_x, \Psi_y, \vartheta, t) \mathrm{d}\Psi_x \mathrm{d}\Psi_y \mathrm{d}\vartheta \mathrm{d}t}{\int_{\mathrm{OFF}} \epsilon_\gamma(\Psi_x, \Psi_y, \vartheta, t) \mathrm{d}\Psi_x \mathrm{d}\Psi_y \mathrm{d}\vartheta \mathrm{d}t}. \tag{3.6}$$

The camera acceptance is obtained from γ-ray-like events and depends on the zenith angle, ϑ, and the exposure time ,t. In addition, it varies within the field of view of the camera system. The position in the field of view is defined in two rectangular directions, Ψ_x and Ψ_y.

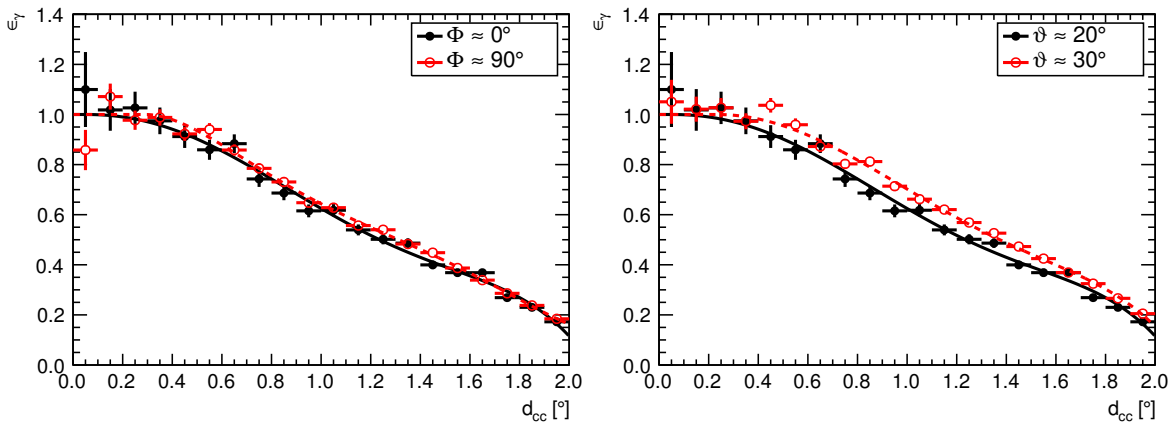

Figure 3.10: Camera acceptance curve of the *VERITAS* camera as obtained from γ-ray-like events as a function of distance to the camera centre, d_{cc}, in degrees. The solid and dashed lines represent the fit to the corresponding data points. *Left:* Two camera acceptance curves for γ-ray-like events arriving from the north (black, filled circles), and the east (red, open circles). *Right:* Two camera acceptance curves for two different zenith angles of observations (black, filled circles: 20°; red, open circles: 30°). It is assumed, that the acceptance in the camera is radially symmetric.

As the exposure time is the same for both ON and OFF region and the change of the zenith angles during a single observation is negligible with about 2° to 3°, Equation 3.6 can be simplified to

$$\alpha = \frac{\int_{\mathrm{ON}} \epsilon_\gamma(\Psi_x,\Psi_y)\mathrm{d}\Psi_x\mathrm{d}\Psi_y}{\int_{\mathrm{OFF}} \epsilon_\gamma(\Psi_x,\Psi_y)\mathrm{d}\Psi_x\mathrm{d}\Psi_y}. \tag{3.7}$$

Figure 3.10 shows a typical curve of the camera acceptance of *VERITAS* for two different azimuth (left) and zenith angles (right) of observation. This demonstrates that different observing conditions have to be considered in the analysis. In addition, the camera acceptance also depends on the energy [Funk, 2005], and the azimuth angle, Ψ_{az}. It is important to note that these dependencies could introduce systematic uncertainties in the analysis.

The second method to estimate the background is called the *reflected region model* (right panel of Figure 3.9). OFF regions are defined as circles with the same radius as the ON region. Both ON and OFF regions are placed at an equal distance to the telescope pointing position, the *wobble offset*. In this model it is assumed that the γ-ray acceptance correction is radially symmetric and there is no need for a correction of the acceptance of the camera.

To avoid possible under- or overestimation of the background, regions around known γ-ray emitters and bright stars (star magnitude in the visual band smaller than 6.5) are excluded, as they produce additional noise in the camera. Finally, the significance of detection of a single observation, S, is

calculated according to equation 17 in Li and Ma [1983];

$$S = \sqrt{2\left\{N_{\mathrm{ON}} \ln\left[\frac{1+\alpha}{\alpha}\left(\frac{N_{\mathrm{ON}}}{N_{\mathrm{ON}}+N_{\mathrm{OFF}}}\right)\right] + N_{\mathrm{OFF}} \ln\left[(1+\alpha)\left(\frac{N_{\mathrm{OFF}}}{N_{\mathrm{ON}}+N_{\mathrm{OFF}}}\right)\right]\right\}}. \tag{3.8}$$

The commonly accepted threshold, required to consider a source as detected, is a statistical significance of five standard deviations (5σ), written as $\sigma \geq 5$. In the absence of a signal, the function S follows a normal distribution with a standard deviation, $\sigma_G = 1$, and mean, $\mu_G = 0$. If multiple observations of the same pointing are combined, the correction factor, α, is the same and $N_{\mathrm{ON}} = \sum N_{\mathrm{ON}}^{(i)}$ and $N_{\mathrm{OFF}} = \sum N_{\mathrm{OFF}}^{(i)}$. However, if multiple observations, N_{obs}, with different pointings are combined, α may vary due to different exclusion regions in the field of view for different wobble offsets. To account for this, a generalised form of Equation 3.8 is used [Aharonian et al., 2004];

$$S = \sqrt{2}\left\{\sum_{i}^{N_{obs}} N_{\mathrm{ON}}^{(i)} \ln\left[\left(\frac{\sum_{i=1}^{N_{obs}} N_{\mathrm{ON}}^{(i)}}{\sum_{i=1}^{N_{obs}} \frac{\alpha_i}{1+\alpha_i} N_{\mathrm{ON}}^{(i)} + N_{\mathrm{OFF}}^{(i)}}\right)\right] + \sum_{i}^{N_{obs}} N_{\mathrm{OFF}}^{(i)} \ln\left[\left(\frac{\sum_{i}^{N_{obs}} N_{\mathrm{OFF}}^{(i)}}{\sum_{i}^{N_{obs}} \frac{1}{1+\alpha_i} N_{\mathrm{ON}}^{(i)} + N_{\mathrm{OFF}}^{(i)}}\right)\right]\right\}^{1/2}. \tag{3.9}$$

3.3.7 Limitations of current γ/hadron separation

The aforementioned shower shape parameters (Section 3.3.5) are proven to effectively reduce the cosmic-ray background independent of the observing conditions and the energy of the primary particle. These image parameters employ global shower properties, such as width and length of the image. On the other hand, stereoscopic information are not fully considered by these parameters. The information stored in the image shape parameters is not sufficient to distinguish cosmic-ray showers, having a substantial part of its energy in the electromagnetic part, from γ-ray showers. While the moment analysis utilizes the two-dimensional shape of the recorded image of the EAS in the camera for shower reconstruction and γ/hadron classification, multivariate classification algorithms (MVAs) use the multidimensional observable space rather than each observable separately [Mitchell, 1997; Behnke et al., 2013]. Individual cuts of each observable are not able to exploit possible correlations among different observables. A signal event that looks as background-like in only a single observable will inevitably be misclassified as a background event in a cut-based analysis. On the other hand, it might very well be correctly classified with the MVA. This method is able to compensate for this one background-like feature by exploiting all other observables that might indicate a signal event.

Chapter 4 introduces a classification technique using this and other parameters. They are combined in a multivariate analysis using boosted decision trees [Breiman et al., 1984]. This method is applied to the data obtained from the *VERITAS* experiment. Finally, the potential to separate photon-induced showers from hadronic ones is demonstrated.

4

Improved γ/hadron classification using a multivariate analysis technique

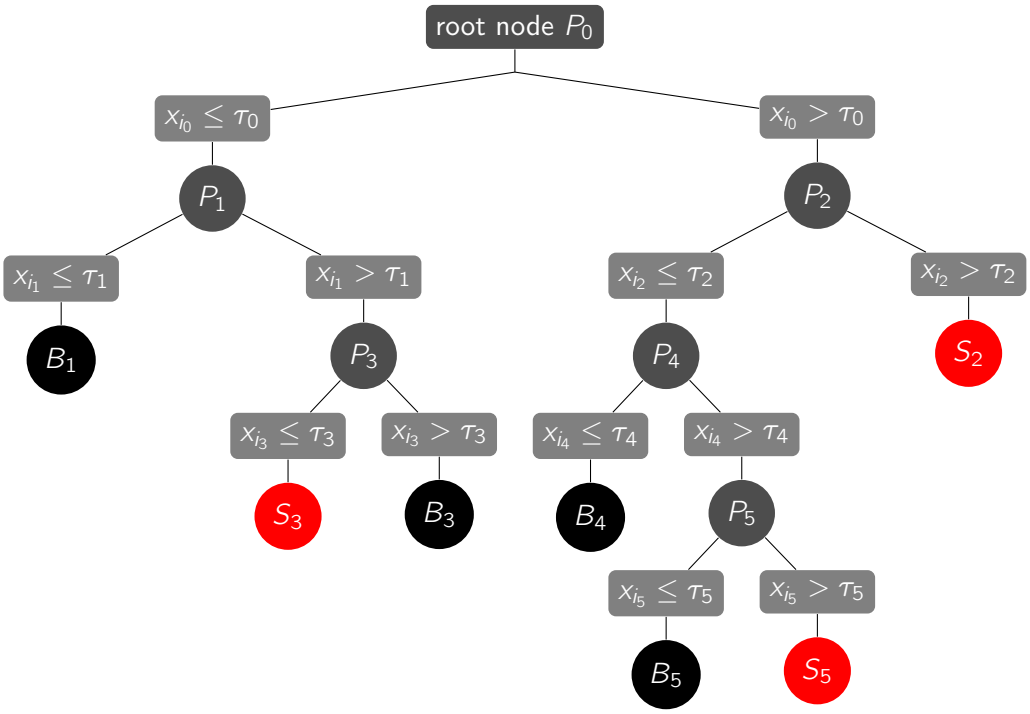

Figure 4.1: Sketch of the development of a decision tree. An event described by a set of parameters, P_i (i=0...5), is classified by sorting it through the tree. At each node it undergoes a binary split criterion, τ_j, on one of its parameters, x_{i_j}, until it ends up in a terminal node. The leaf returns the classification of the event marking it as either signal (S) or background (B).

As described in Chapter 3, one step in a typical data analysis is to select the events of interest. Already before, several classifications have been performed on the basis of *raw* event observables such as trigger conditions, or the direction of arrival. In this chapter, one refers to an event which is classified as either signal or background. In comparison to the classical multidimensional

rectangular cut selection, multivariate analysis techniques such as Random Forests (RFs) and Boosted Decision Trees (BDTs) have been studied and successfully applied to existing IACT experiments recently [Albert et al., 2008a; Ohm et al., 2009; Becherini et al., 2011; Aleksić et al., 2012]. These methods use the statistical distributions of events in the space of observable to decide the class membership of a particular event as either signal or background. This is achieved by combining the information of all observables of an event into one single variable, T. The variable is in turn used to decide if the event is selected as signal, or rejected as a background event, depending on whether the variable crosses a previously set threshold or not.

In this thesis, a so-called supervised machine learning algorithm [Behnke et al., 2013] is used, in particular the BDT method integrated in the Toolkit for Multivariate Data Analysis (TMVA) package [Hoecker et al., 2007] of ROOT [Brun and Rademakers, 1997]. It can be applied for γ/hadron classification and to the study of VHE γ-ray sources. The objective is to detect γ-ray showers in the presence of a hugely dominant background of hadronic showers, which must be rejected with very high efficiency while keeping γ-rays if the signal-to-noise ratio of the detection process is to be improved. In practice, by far the most predominant source of trigger events in Cherenkov detectors arises from the hadronic background dominated itself by protons.

The method focuses on performance studies of a decision-tree based γ/hadron classification to study VHE γ-ray sources observed by *VERITAS*. The parameters chosen to discriminate γ-rays from cosmic rays are introduced in Section 4.1 while the details of the MVA using BDTs are described in Section 4.2 followed by a discussion of their training and evaluation (Section 4.3). The stability of the method is tested through comparison of MC simulations and real γ-ray data in Section 4.4. Finally, in Section 4.5 the performance and sensitivity of the BDT method is evaluated using MC simulations and through the application to *VERITAS* data.

4.1 γ/hadron discriminatory parameters

EASs can be described by a series of properties that differ, on average, between the signal γ-rays and the background cosmic-rays, referred to in the following as *classification parameters*. The Hillas parameters encode information about the shape of the image of the air shower (Section 3.3.3). The great potential in γ/hadron classification using these parameters was shown by Fegan [1997]. In the *VERITAS* standard analysis, a classical rectangular cut selection is applied, where cuts on the shower shape parameters *MRSL* and *MRSW* are utilised to discriminate cosmic rays from γ-rays. Their separation potential is illustrated in Figure 4.2(a) where the distribution of γ-rays from MC simulations and cosmic rays from `OFF` data are shown. As illustrated, this so-called *box cuts* approach suppresses a large fraction of charged cosmic rays. However, they apparently do not fully explore the available information stored in the two parameters. For instance, a cut on *MRSW* as a function of *MRSL* could already improve the separation. MVAs using BDTs

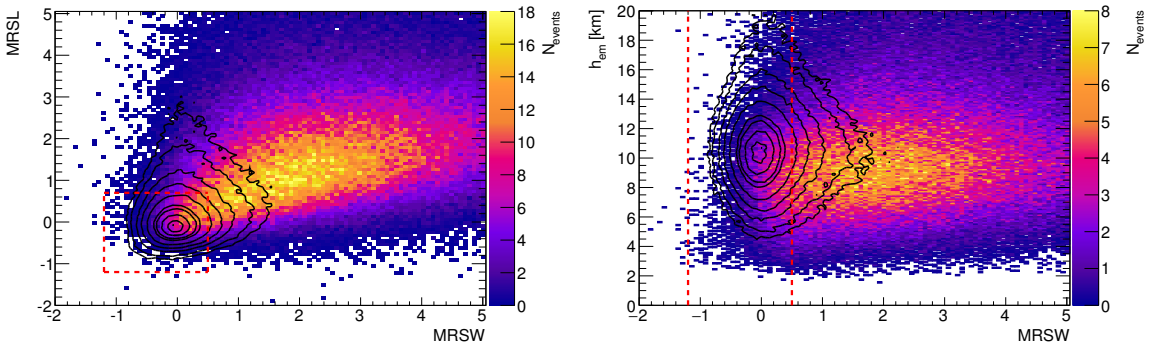

(a) (b)

Figure 4.2: Comparison of the distributions of mean reduces scaled width, *MRSL*, vs. mean reduced scaled length, *MRSW*, (*left*) and emission height, h_{em}, vs. *MRSW* (*right*). The color scale represents the number of hadronic cosmic rays, N_{events}, within a zenith angle range from 15° to 25°. The black contours demonstrate γ-rays of MC simulations at a zenith angle of 20°. The dashed red lines indicate the shower shape cuts as used in the *VERITAS* standard analysis to select γ-ray-like events.

consider these non-linear correlations between the parameters, that cannot be achieved with an event selection based on simple box cuts.

In addition to these two parameters, additional shower parameters for γ/hadron identification are used, such as the height of the Cherenkov emission, h_{em}, the spread of the energy estimation, χ^2_E, or the distance between the centre of the array and the position of the shower on the ground, d_{core}. These variables take advantage of the stereoscopic approach and are defined as the average value over all telescopes considered for reconstruction, referred by the term of *multiplicity*. To summarise, the variables utilised for γ/hadron classification applied in this thesis are,

- the shower shape parameters *MRSW* and *MRSL* as introduced in Section 3.3.5 characterising the measured width and length of an image of given size, s, and impact parameter, R;
- the height of the Cherenkov emission, h_{em} referred to the actual thickness traversed by the shower, and the spread of the reconstructed emission height per shower, $\chi^2_{h_{em}}$;
- the spread of the energy estimation of the primary particle, χ^2_E, over all participating telescopes;
- the distance, d_{core}, between the centre of the array ($X_{0_{array}}$, $Y_{0_{array}}$) and the reconstructed position of the shower on the ground (X_{core}, Y_{core}).

Figure 4.3 illustrates the distribution of the aforementioned classifying variables using a sample of γ-rays from MC simulations and cosmic rays from `OFF` data. The energies of the primary particle are chosen to be between 0.08 TeV and 0.32 TeV, as well as at zenith angles of observations

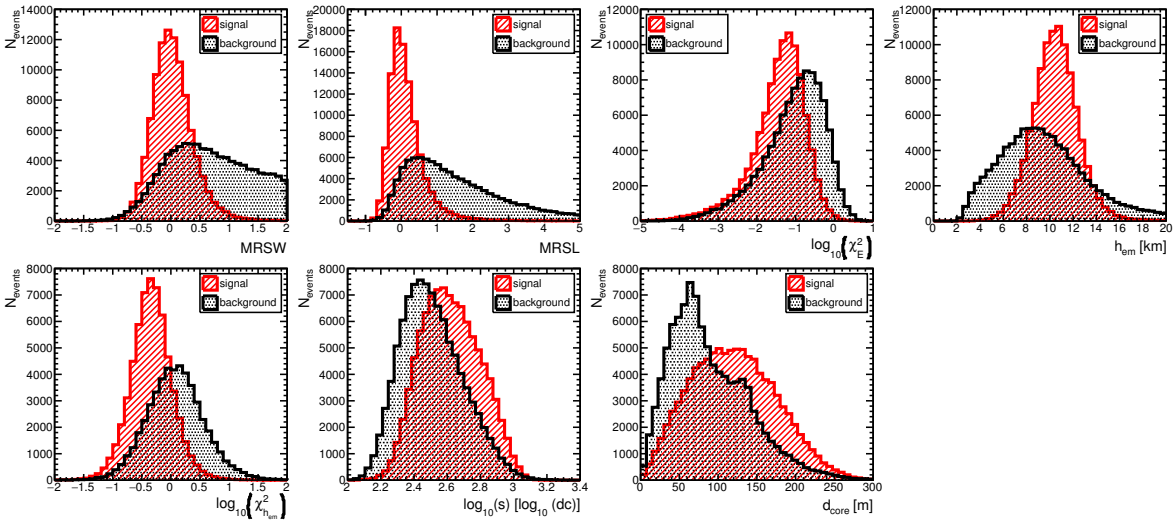

Figure 4.3: Distribution of the classifying variables with γ/hadron classification potential for MC γ-rays (red, hashed) and cosmic rays from OFF data (black, dotted) with reconstructed energies from 0.08 TeV to 0.32 TeV and zenith angles of observation between 0° and 22.5°.

between 0° and 22.5°. It is clearly visible that all parameters show their power for γ/hadron classification. Thus, this can be utilised for background rejection in the analysis.

In addition, Figure 4.4 and Figure 4.5 depict the dependence of the classification variables *MRSW*, *MRSL*, $\log_{10}\chi^2_E$, h_{em}, and d_{core} for MC γ-rays and OFF data on reconstructed energy and zenith angle.

The former figure illustrates a stable evolution of MC γ-rays for the parameters *MRSW* and *MRSL*. Contrary to this behaviour the distributions of the OFF data are stable for *MRSL* but show strong variations for *MRSW* with increasing energy. The latter is the result of the large transverse momentum given to pions in strong interactions [Hillas, 1996]. Similar to their dependence on energy, the classification parameters *MRSW* and *MRSL* show a rather stable characteristic for γ-ray-induced EASs over all zenith angles of observation (Figure 4.5). In comparison, the distribution of *MRSW* for hadron-induced particle cascades varies with larger zenith angles as showers have to travel a longer path through the Earth's atmosphere until they reach the detector. This leads to larger fluctuations in the shower and in general a larger width of the images.

As introduced in the previous chapter (Section 3.3.4), the energy of the primary particle is reconstructed for each telescope individually. Then, the parameter χ^2_E of the energy estimation is the average spread over all participating telescopes. Due to the irregular structure of an hadronic air shower caused by inelastic scattering and decay processes, such as the production of charged pions, the energy, E, may result in different reconstructed values for telescopes seeing the shower from different viewing angles. Irregularities in the shape of the shower image lead to a larger spread in

the reconstructed energy for cosmic-ray-induced air showers, as demonstrated in the third row of Figure 4.4 and Figure 4.5. In addition, showers at low energies exhibit larger fluctuations in the recorded images.

The height of the Cherenkov emission, h_{em}, is estimated for all pairs of two telescope events and combined into an average weighted by the size of the image, whereas $\chi^2_{h_{em}}$ is the value of the height of emission of each pair of two telescope events. As depicted in the fourth row of Figure 4.4 and Figure 4.5, the parameter h_{em} is especially a powerful parameter at low energies and large zenith angles. In contrast to γ-ray showers, the distribution of h_{em} for hadron-induced EASs is generally wider as they show much larger shower-to-shower fluctuations. Consequently, the spread of the reconstructed emission height for each shower, $\chi^2_{h_{em}}$, is larger for cosmic rays compared to VHE γ-rays. The latter is also illustrated in Figure 4.2(b), where the larger spread for cosmic rays is clearly visible. It is worth noting that events at small emission heights are mainly caused by muon detections [Maier and Knapp, 2007]. In addition, the radiation length of hadrons is generally larger compared to the radiation length of electrons/positrons and photons (Section 2.4.1 and Section 2.4.2). As a consequence, hadronic showers penetrate deeper into the atmosphere, resulting on average in a smaller height of the Cherenkov emission, h_{em}. Furthermore, the height of the shower maximum of EASs induced by electromagnetic processes tend to increase with larger zenith angle as showers have to travel a longer path through the atmosphere. On the other hand, the behaviour is opposite for hadron-induced showers where h_{em} decreases with increasing zenith angle. It is worth noting that the bulk of hadron-induced showers towards smaller values of h_{em} at large zenith angles, as shown in Figure 4.5, might result from poorly reconstructed events which are located further out of the array, arrived at low zenith angles, or are initiated by primary particles with low energies.

As cosmic rays arrive isotropically on Earth, a cut on the distance, d_{core}, between the centre of the array ($X_{0_{array}}$, $Y_{0_{array}}$) and the reconstructed position on the ground (X_{core}, Y_{core}) can efficiently suppress the hadronic background. This parameter is mainly used to exclude events which are badly reconstructed, e.g. events at large distances from the centre of the array. It is worth noting that this parameter is generally smaller for cosmic rays than for γ-rays. Furthermore, the distribution of cosmic rays tends to be wider.

The results of these studies show that parameters with effective γ/hadron classification power depend partially on energy and zenith angle. Consequently, this behaviour has to be taken into account when developing an improved algorithm for γ/hadron classification with a stable response on γ-ray events over the whole parameter space of the instrument, compared to the current rectangular approach on cut selection. The aforementioned dependencies will influence the classifier response as well. Therefore, a training of the BDTs in bands of energy and zenith angle is suggested to achieve the best performance. *VERITAS* operates in the energy range from about 80 GeV to $>$ 30 TeV, and performs observations at zenith angles between 0° and about

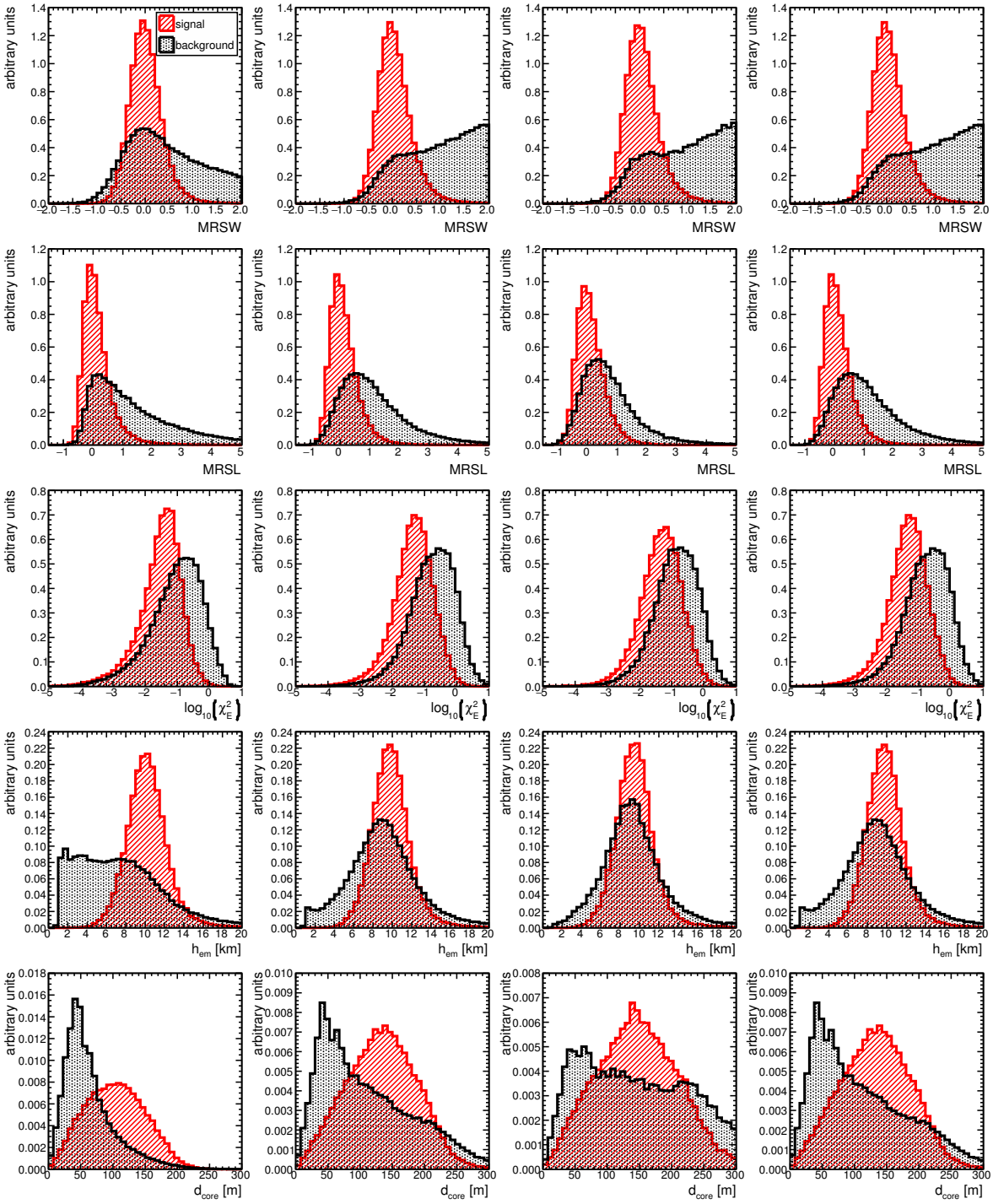

Figure 4.4: Energy dependence of the input variables *MRSW*, *MRSL*, $\log_{10}\chi^2_E$, h_{em}, and d_{core} used for the discrimination between γ-ray- and hadron-induced EASs for γ-rays from MC (red, hashed) and cosmic rays from OFF data (black, dotted). The distributions are shown for events in the zenith angle range between 0° and 22.5°. The energy increases from the first to the fourth column: 0.08 TeV to 0.32 TeV, 0.32 TeV to 0.5 TeV, 0.5 TeV to 1 TeV, and >1 TeV.

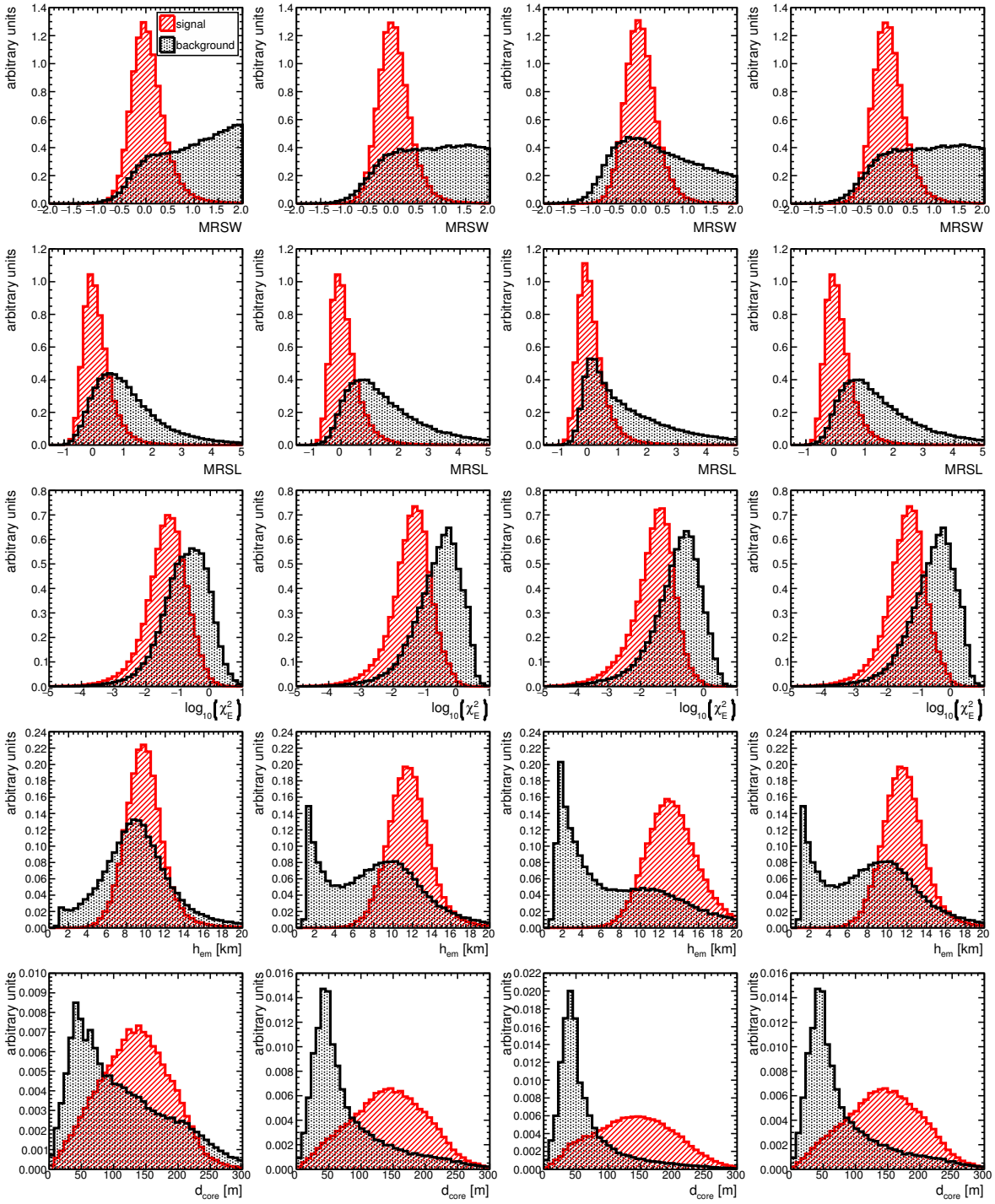

Figure 4.5: Zenith angle dependence of the input variables *MRSW*, *MRSL*, $\log_{10}\chi^2_E$, h_{em}, and d_{core} used for the discrimination between γ-ray- and hadron-induced EASs for γ-rays from MC (red, hashed) and cosmic rays from OFF data (black, dotted). The distributions are shown for events with reconstructed energies between 0.5 TeV and 1 TeV. The zenith angle of observation rises from the first to the fourth column: 0° to 22.5°, 22.5° to 32.5°, 32.5° to 42.5°, and 42.5° to 75°.

60°. Accordingly, the dynamical range of the training of the BDTs, described in the next section, is performed in four energy bins (0.08 TeV to 0.32 TeV, 0.32 TeV to 0.5 TeV, 0.5 TeV to 1 TeV, and >1 TeV) and four zenith angle bins (0° to 22.5°, 22.5° to 32.5°, 32.5° to 42.5°, and >42.5°). These bands are chosen such that there is sufficient statistics available for the training process. At the same time, it was guaranteed that the distributions of the input parameters does not change significantly within the corresponding bin. In the highest energy and zenith angle bin, the bin size must be substantially larger than the other bins. This is a consequence of the limited statistics available of charged cosmic rays resulting from different energy spectra of γ-rays and cosmic rays with spectral indices of $\Gamma_\gamma \approx 2.0$ and $\Gamma_{CR} \approx 2.7$, respectively. Thus, in the following the training of the BDTs as performed for each energy and zenith angle band is introduced.

4.2 Classification using Boosted Decision Trees

BDTs are based on simpler objects, decision trees. Decision trees are tree-structured elements consisting of a series of binary splits using the aforementioned classification parameters. They start with a *root* node and are built up of repeating splits and nodes down to the final nodes (*leaf*). A set of nodes and splits resulting in a leaf is called a *branch*. An event is classified according to the class label of the leaf at the end of the tree branch in which it ends up.

4.2.1 Training phase

Individual decision trees are trained by splitting the training sample, N_{train}, which is comprised of a sample of signal, N_S, and background, N_B, events. The type of an event is denoted by Y_i:

$$Y_i = \begin{cases} +1 & \text{if event } i \text{ is signal-like;} \\ -1 & \text{if event } i \text{ is background-like} \end{cases} . \tag{4.1}$$

Starting from the root node using the whole training sample, the number of events of the signal training sample is normalised to the number of events of the background training sample. Thus, all events of the signal sample have the same weight, $\omega_i(S)$, and all events of the background sample have the same weight, $\omega_i(B)$. Then, a classifying variable and the corresponding cut value that provides the best separation of the sample at this node is determined. This criterion is found by computing the *Gini* index, G,

$$G = \left(\sum_{i=1}^{N} \omega_i \right) p(1-p), \tag{4.2}$$

where p is the signal purity defined as the fraction of weight of a leaf due to signal events and ω_i is the weight of event i. The best split classifying variable and their corresponding cut value are determined by comparing the separation index before and after the split. Taking the difference between them results in the separation gain, G_{sep}, which is maximal for the best splitting parameter,

$$max(G_{sep}) = G_{parent} - G_{right-node} - G_{left-node}. \tag{4.3}$$

The best split is then performed in order to split the training sample into two daughter nodes, for which the whole process is re-iterated. The entire process is then repeated until the number of events in a leaf is smaller than a predefined value, or the signal-to-background purity of a leaf exceeds a predefined value. However, decision trees are very sensitive to statistical fluctuations in the training sample. To overcome this problem, an iterative method is used to stabilise its performance, the *boosting* algorithm [Schapire, 1990; Freund, 1995; Freund and Schapire, 1999]. This process combines many different decision trees to form a *forest*.

4.2.2 Boosting

At the beginning, a classifier is trained with events that have the same weight, ω_i, and the tree is built as described above. For the next training iteration, a modified training sample with larger weight on previously misclassified events is used. Trees are trained with data samples that are derived from training events by reweighting the events according to the adaptive boosting (*AdaBoost*) algorithm [Freund and Schapire, 1997; Schapire and Singer, 1990]. In general, an event is classified by the variable ξ_{t_i};

$$\xi_{t_i} = \begin{cases} +1 & \text{if event } i \text{ is classified as a signal event in tree } t; \\ -1 & \text{if event } i \text{ is classified as a background event} \end{cases} \tag{4.4}$$

Comparing this with Equation 4.1, a misclassified event is defined by $Y_i \neq \xi_{t_i}$, i.e. a signal event arrived in a background leaf or a background event is classified into a signal leaf. These events get a higher weight via multiplication by the boost factor, α_t. For the AdaBoost method, this parameter is computed by

$$\alpha_t = \beta_{ada} \cdot \ln\left(\frac{1-\epsilon_t}{\epsilon_t}\right), \tag{4.5}$$

where the parameter β_{ada} is the user-specified learning rate of the tree. The weighted fraction of misclassified events in the previous tree t_{i-1}, ϵ_t, is computed by

$$\epsilon_t = \frac{\sum\limits_{Y_i \neq \xi_{t_i}} \omega_i}{\sum\limits_{i=1}^{N} \omega_i}. \tag{4.6}$$

The weight of a misclassified event is thus given by

$$\omega_i = \omega_i' \cdot \exp \alpha_t, \tag{4.7}$$

where ω_i' is the weight of the event, i, in the previous tree. The re-weighting forces the training of the next tree to focus on events which are not classified correctly in the previous iteration. For the purposes of normalisation, all events of the previous tree are reweighted by

$$\omega_i = \frac{\omega_i'}{\sum\limits_{Y_i \neq \xi_{t_i}} (\omega_i' \cdot \exp \alpha_t) + \sum\limits_{Y_i = \xi_{t_i}} \omega_i'}. \tag{4.8}$$

4.3 Training and evaluation of the BDT method

After the introduction of the basic classification algorithm of the BDTs, this section focuses on the training and evaluation of the BDT classifiers using *VERITAS* data by mean of the aforementioned classifying variables. For the studies presented in this thesis, the TMVA version 4.2.0[1] and the ROOT version 5.34.14[2] are used. At the beginning, the training set as used for the BDT training is presented. As this study leads to a specific design of the decision trees, differing somewhat from the default options of the BDT procedure as implemented in the TMVA package, they are described in detail. Finally, the response of the classifier is tested and the importance of the discriminant parameters for various observational conditions is examined.

4.3.1 Choice of the training sample

The BDTs are trained with known signal and background samples. The former consists of γ-ray showers produced by MC simulations with CORSIKA [Heck et al., 1998; Heck, 2016]. They are simulated at zenith angles from 0° to 65° and energies between 30 GeV and 200 TeV for point-like sources at a fixed wobble offset of 0.5°. The lower energy boundary increases up to 100 GeV for zenith angles above 55°. The simulated γ-rays follow an energy distribution $dN/dE \propto E^{-\Gamma}$ with $\Gamma = 2.0$. Taking advantage of the large set of available *VERITAS* data as a background sample, the use of time-consuming hadron simulations can be avoided. The data are collected under good weather conditions, with all four telescopes operational, and taken in wobble mode, with the centre of the camera offset from the source by 0.5°. In order to avoid contamination of the background sample with badly-reconstructed γ-rays, only events with a shower direction of $>$0.22° from the known source position are used.

[1] http://tmva.sourceforge.net
[2] https://root.cern.ch

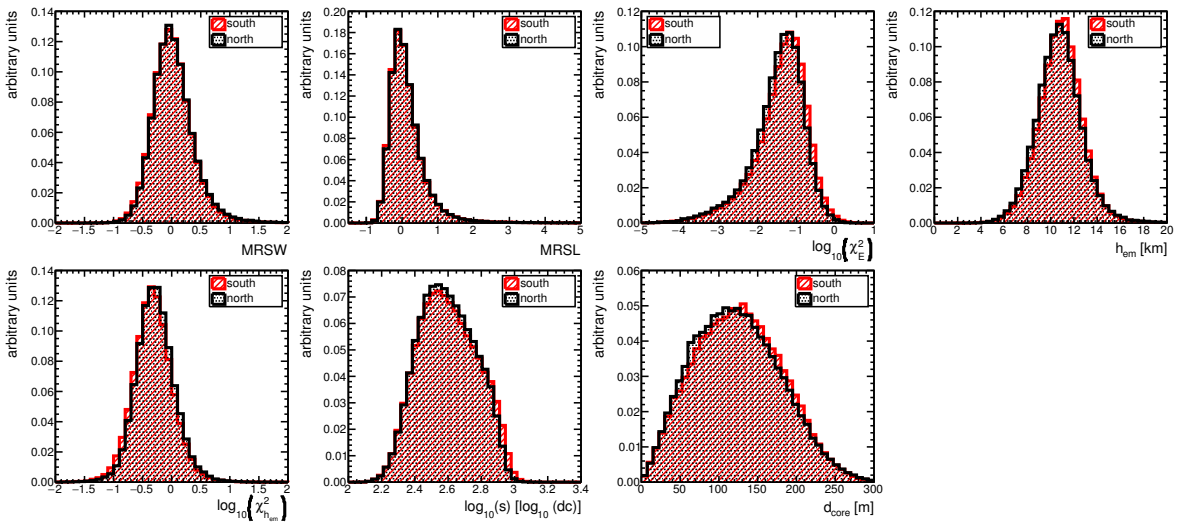

Figure 4.6: Distribution of the classifying variables with γ/hadron classification potential for MC γ-rays arriving from the southern (red, hashed) and northern (black, dotted) direction at zenith angles of observation of about 20°.

Note that the NSB light levels observed in data vary substantially depending on the location of the source in relation to the Galactic plane. Since the NSB level impacts the distributions of the parameters *MRSW* and size, *s*, it is necessary to train the BDTs over the full range of NSB levels observed in data. Therefore, a mix of Galactic (high NSB level) and extragalactic (low NSB level) observations taken at various zenith angles using regions of the camera which do not contain any known γ-ray source, are used for the background training sample. The NSB levels in simulation are selected to match the range of NSB levels found in the background sample. The Earth's geomagnetic field affects the shower development, as do atmospheric conditions. Thus, it is expected that the shower parameters will vary with the azimuth angle of observation. As their effect on the shower development is expected to be small (Figure 4.6) compared to the influence of the energy and zenith angle, separate trainings were not performed for observations of northern versus southern sources. However, this should be part of future studies, but is beyond the scope of this thesis.

As well as for the *VERITAS* standard analysis using the *box cuts* method, *preselection* requirements are made on the parameters *MRSW* (-2.0 $<$ *MRSW* $<$ 2.0), *MRSL* (-2.0 $<$ *MRSL* $<$ 2.0), and the distance between the centre of gravity of the image and the camera centre of 0.78°. The latter one reduces the image truncation at the edge of the camera, while the former two requirements remove trivially classifiable background events reducing the background sample to events that are difficult to distinguish from γ-rays. Consequently, these cuts assure good shower reconstruction.

parameter	test values
MaxDepth	3, 10, 25, 50, 75 and 100
nEventsMin	20, 25, 50, 100 and 200
NTrees	50, 100, 150, 200, 300, 500, 700, 1000 and 2000

Table 4.1: Different values of the parameters used to construct the architecture of the BDTs and to test their performance.

4.3.2 Training and test configurations

The changes in the *VERITAS* array (Section 3.1) impact the training parameter distributions, necessitating three separate BDT trainings that use signal and background samples from the appropriate time periods. A set of bins in zenith angle and energy are defined for the training/test phases for each of the telescope array configurations. In order to maximise the separation between the signal and background response distributions, the values defining the tree architecture of the specific parameter environment as used in this thesis are tuned. Ideally, the chosen parameters should give minimal overtraining and good separation between signal and background distribution for all training configurations (all energy and zenith angle bins, and three array configurations).

The effect of varying the number of trees, the minimum leaf size, and the maximum training depth of the trees is studied. Several values of the parameters, as summarised in Table 4.1, are tested, and the effect on the BDT response examined. During the development of this analysis, it was observed that the discrimination between γ-rays and cosmic rays is enhanced when allowing the tree to develop quite deeply and then cutting back the branches with an optimal *PruneStrength*. Pruning reduces statistical fluctuations by removing insignificant branches [Breiman et al., 1984]. Within this thesis, a prune strength of -1 is chosen enabling an automatic pruning of the trees. This means that at each step of the tree, the current quality of the tree is calculated and finally, it will be cut at the minimum of the tree quality. Deeper trees have the advantage that all training variables are used. Then, pruning is necessary to stabilise performance when growing deeper trees. For this reason, in this analysis the splitting of the tree can be carried out up to a maximum depth of the tree (*MaxDepth*) of 50 node layers. However, the sequence of separation is stopped once a minimum number of 100 events has been reached in a node, called *nEventsMin*.

During the development of this analysis method, it has been observed that an instability in performance, meaning more overtraining of the trees, occurs when the number of requested trees composing a forest, N_{Trees}, is too low. The separation between the signal and background response distributions was similar in all energy and zenith angle bands between 200 trees and 1000 trees (*NTrees*). Therefore, a value of $NTrees = 200$ is used to reduce computing time.

Given the total number of signal and background events available for a specific bin, the number of events to be used during the training phase was set to 2×10^5. This provides enough events in

parameter	option
NTrees	200
BoostType	AdaBoost
AdaBoostBeta	1.0
SeparationType	GiniIndex
nEventsMin	100
PruneMethod	CostComplexity
PruneStrength	-1
MaxDepth	50
nTrain_Signal	200000
nTrain_Background	200000
nTest_Signal	nTrain_Signal
nTest_Background	nTrain_Background

Table 4.2: Parameters used to construct the architecture of the BDTs applied for the discrimination procedure presented in Section 4.2. The description of the parameters follows the notation as provided in the TMVA package.

each training bin reducing statistical fluctuations and therefore, stabilising the overall performance. Finally, the number of events during the test phase is again 2×10^5 but independent of the training sample. The result of the tuning of the BDT configuration is summarised in Table 4.2. However, one has to note that the training parameters found in this study might still not be the most optimal ones. Further investigations of the latter might even improve the analysis method presented here but is beyond of the scope of this thesis.

4.3.3 Importance of the discriminant parameters

As presented in Figure 4.3 and Figure 4.4, each classifying variable shows potential to distinguish γ-rays from cosmic rays dependent on energy and zenith angle. This characteristic is reflected in the difference of the importance of the variables for building the BDTs. The importance of a classifying parameter is examined by ranking the classification parameters according to the frequency with which they are used in the splitting of the decision tree nodes. It is weighted by the square of the separation gain according to Equation 4.3 and the number of events corresponding to each daughter node [Hoecker et al., 2007]. Figure 4.7 illustrates the relative importance of the input classification variables dependent on zenith angle and reconstructed energy. As the distribution of each parameter depends on zenith angle and energy, it is likely that a certain variable is important at low energies whereas it shows little classification power at large energies, and vice versa. From the left panel of Figure 4.7 it can be observed that the variable *MSRW* is the most important classification parameter at energies between $\approx$400 GeV and $\approx$4 TeV. Below a few hundred GeV γ-ray- and EASs induced by muons arising from hadronic interactions look

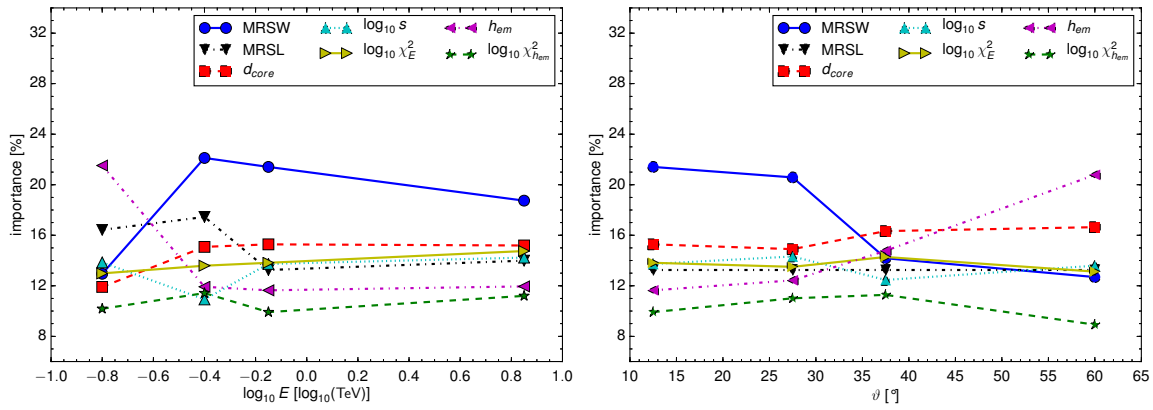

Figure 4.7: Relative importance of the training parameters as a function of mean reconstructed energy, E, at zenith angles of observation, ϑ, between 0° and 22.5° (*left*), and as a function of mean zenith angle of observation for reconstructed energies from 0.5 TeV to 1 TeV (*right*).

very similar [Maier and Knapp, 2007]. Thus, it is very challenging to discriminate these showers using only the shape of the Cherenkov light image in the camera. The height of the Cherenkov light emission, h_{em}, adds important information about the nature of the primary particle and can be used to distinguish between cosmic rays and γ-rays at low energies, as can be observed in the left panel of Figure 4.7. For events with reconstructed energies above 4 TeV, the parameter $\log_{10} \chi^2_E$ becomes increasingly important for the classification. Particle cascades induced by γ-rays show a regular structure whereas hadron-induced EASs show large fluctuations during the shower development leading to a larger spread in reconstructed energy between the telescopes. The right panel of Figure 4.7 presents the development of the relative importance of the classification parameters for events with energies between 0.5 TeV and 1 TeV. It is obvious that the importance of the parameter h_{em} increases with zenith angle leading to an increased energy threshold of the telescope system [Sommers and Elbert, 1987].

4.3.4 Classifier output

At the final stage of the BDT procedure the forest of N_{Tree} trees is combined together resulting in a single classifier output value, T, given by the weighted behaviour of the individual decision trees;

$$\mathrm{T}_i = \sum_{t=1}^{N_{Tree}} \alpha_t \xi_{t_i}, \tag{4.9}$$

where α_t is the boost factor and ξ_{t_i} the weighted fraction of the misclassified events according to Equation 4.5 and Equation 4.6, respectively. The response of the classifier from the training phase is tested for all zenith angle and energy bands to evaluate the global performance of this

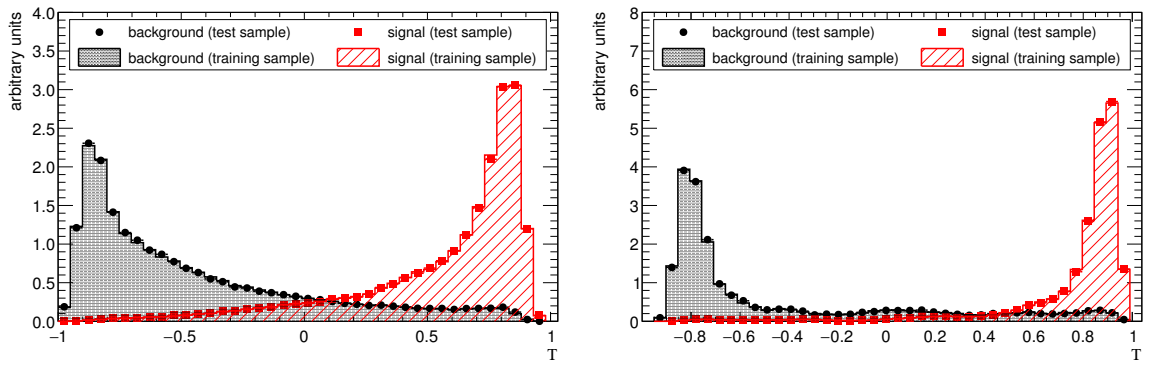

(a) (b)

Figure 4.8: BDT response, T, for an independent test sample of known signal and background composition. Events in the sample have energies between 0.08 TeV to 0.32 TeV *(a)* and $>$1 TeV *(b)* and zenith angles of 0° to 22.5°.

MVA. This is done with an independent set of events and compared with the training classifier distribution. This comparison is depicted in Figure 4.8 for events with a reconstructed energy $>$1 TeV and zenith angle of observation between 0° and 22.5°. The agreement between the testing and the training sample is evaluated by the Kolomogorov-Smirnov (KS) test, with values between 0 and 1, on the shape of the two resulting distributions. This test is an important check on the reliability of the classification behaviour of signal to background events. If the statistical test of compatibility fails, meaning a result of the KS test of ≈ 0, the reliability of the analysis results cannot be guaranteed. This means that the performance of the training is not reproduced by an independent dataset. This in turn can be influenced by a too small dataset. As an example, the result of the metric is 0.113 for the signal and 0.305 for the background sample, shown in Figure 4.8(b). In general, the classification shows several characteristic features over the whole parameter space,

- At low energies (Figure 4.8(a)), a significant amount of signal events is located in the background regime of the BDT output and vice versa. This effect is also seen for large zenith angles of observation. At high energies the effect is less pronounced.
- The shape of the distribution changes with energy and zenith angle band from a broad behaviour at low energies (large zenith angles) to a narrower shape at high energies (small zenith angles).

The distributions of the BDT response for all energy and zenith angle bands are shown in Section A.2. To summarise, the signal and background distributions look different depending on the energy and the zenith angle band. This argues for energy and zenith angle dependent cuts on T in the analysis to make the γ/hadron classification independent of these quantities. The determination of the cut value is discussed in the following.

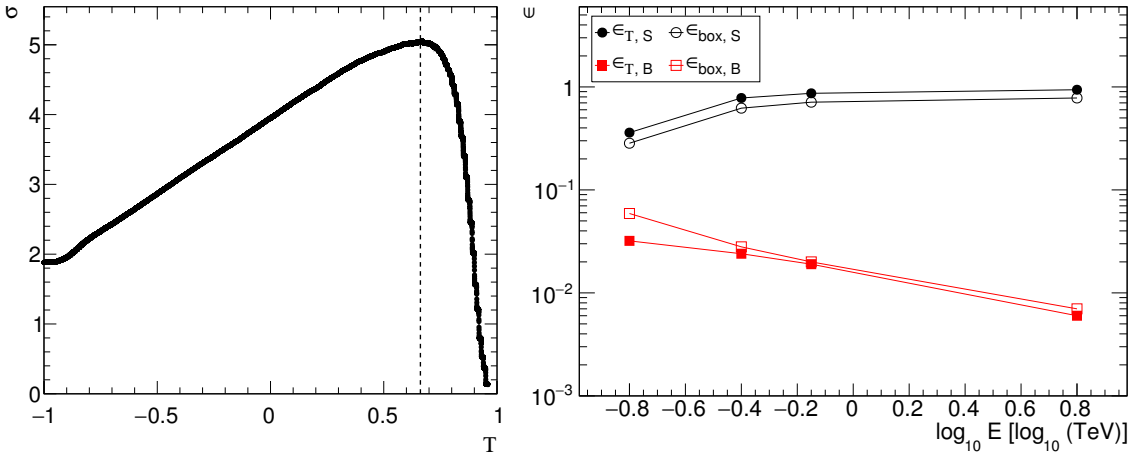

(a) (b)

Figure 4.9: *(a)* Significance, σ, as a function of T for events with energies between 0.08 TeV to 0.32 TeV and zenith angles between 0° and 22.5°. The vertical dashed line indicates T_{sel}. *(b)* Signal (black circles) and background (red squares) efficiency, ϵ, as a function of energy, E, after applying the optimal selection T_{sel} (filled symbols) and the box cuts (open symbols), for zenith angles of 0° to 22.5°. The uncertainties of the efficiency are smaller than the size of the symbols.

4.3.5 Definition of cuts for different source types

As seen in Figure 4.8, the probability density distribution of observables for signal and background events overlap. Thus, there are regions in the phase space where one can find both signal and background events. This leads to unavoidable errors in the decisions made to classify the events such as misclassifying a background event as signal. An optimal selection requirement, T_{sel}, on the BDT response must be determined in each energy and zenith angle band, such that events with T above (below) T_{sel} are considered as γ-rays (cosmic rays). However, it is not sufficient to simply choose the classification that gives the smallest number of misclassification. The optimisation of the final cut values is rather done by maximising the significance of the signal. This is based on the γ-ray efficiencies as a function of energy in order to optimise the detection sensitivity for sources with different fluxes. γ-ray selection cuts are optimised for two combinations of source strength and source spectra, for strong and weak sources as well as for moderate and hard sources. The optimal value of T_{sel} is determined by assuming a source with a minimum strength necessary to be detected at the 5σ confidence level calculated according to Equation 3.8 with at least 10 signal events. As T_{sel} depends on the required observation time and source strength, the optimisation is performed for a fixed observation time for moderate and hard spectrum sources. Signal and background selection efficiencies as a function of T_{sel} are scaled by realistic signal and background rates extracted from observations of the Crab Nebula

after applying the preselection requirements (Section 4.3.1), multiplied by an assumed observation time. The resulting curves give the number of signal and background events in each energy and zenith angle band as a function of T_{sel}. The detection significance is calculated, and the value of T_{sel} at the maximum significance is selected, as illustrated in Figure 4.9(a). The T_{sel} cut values which correspond to the T cuts of the moderate and hard configuration as used in this thesis are summarised in Table A.1. Furthermore, Figure 4.9(b) shows the signal and background efficiencies as a function of energy after applying the optimal selection T_{sel}, for zenith angles between 0° and 22.5°. They are calculated based on γ-ray events from MC simulations and background events from data using

$$\epsilon_S = \frac{N^S_{Y_i=\xi_{t_i}}}{N^S_{tot}}, \qquad \epsilon_B = \frac{N^B_{Y_i=\xi_{t_i}}}{N^B_{tot}}, \tag{4.10}$$

Here, N^S_{tot} is the total number of all γ-ray events from MC simulations, N^B_{tot} the total number of background events from data, $N^{S,B}_{Y_i=\xi_{t_i}}$ the number of correctly classified events (see Equation 4.1 and Equation 4.4) from the sample of signal and background events. The filled black (red) symbols show the signal (background) efficiency after applying the optimised T cuts. As energy increases, it is possible to retain much of the signal (>35 %) while suppressing the majority of the background (90%) for this range of zenith angles. In contrast, the open black (red) symbols indicate the signal (background) efficiency using the box cuts. As demonstrated, these cuts retain less signal (>30 %) than the T cuts while suppressing a comparable amount of background events. The uncertainty on the efficiency, ϵ, is approximated by $1/\sqrt{N}$. For a complete overview of signal and background efficiencies for all energy and zenith angle bands see Section A.3.

4.4 Systematic studies using data/Monte-Carlo comparison

To test the method of the BDT algorithm and evaluate its inherent systematic uncertainties, the consistency of the BDT response is validated by comparing the distributions for simulated γ-rays to a dataset from the Crab Nebula. This validation is necessary as the training of the BDT is performed using γ-rays from MC simulations and one has to assure that the classification does not differ when applied to real γ-ray events. The dataset used in the following is based on observations of the Crab Nebula from 2010 and 2011. The data comprise a total livetime of 71 h (dead-time corrected) with zenith angles smaller than 20°. In the following, the VHE γ-ray excess obtained from data of the Crab Nebula with a wobble offset of 0.5° are compared to the prediction as obtained from MC simulations at a fixed zenith angle of 20° and a wobble offset of 0.5°. Figure 4.10 represents an energy-dependent comparison between VHE γ-ray excess events (Equation 3.5) and simulated γ-rays. The agreement between data and MC simulations demonstrates the consistent behaviour of simulated and real γ-ray events. The cumulative distribution

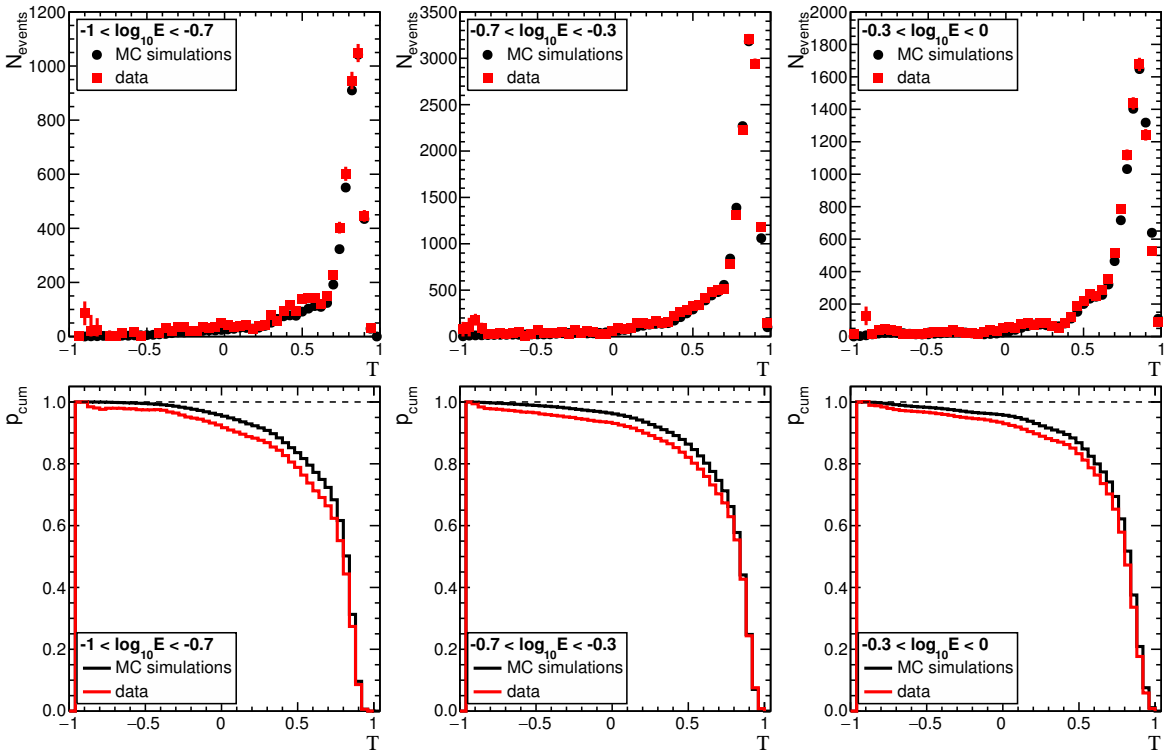

Figure 4.10: *Top:* BDT response, T, for MC simulations of γ-rays (black circles) and VHE γ-ray excess events (red squares) of the Crab Nebula using data from 2010 to 2011. *Bottom:* Probability, p_{cum}, of classifying an event as signal at a given value T for γ-ray events from MC (black) and VHE γ-ray excess events (red).

function, as depicted in the three lower plots of Figure 4.10, demonstrates a slight disagreement between data and MC simulations indicating a systematic uncertainty of $<10\,\%$ to $15\,\%$ on the calculation of the flux of a source.

4.5 Performance of the BDT analysis

Depending on the γ-ray selection cuts of the analysis, basic parameters like the energy threshold, the PSF, or the effective γ-ray collection area change. This section compares the basic performance of several parameters of the telescope system between the *VERITAS* standard analysis and the analysis using the optimised T cuts.

4.5.1 Angular resolution and energy bias

The angular resolution is very important for the sensitivity of the instrument for point sources. In addition, it is crucial for morphology studies of extended VHE γ-ray sources and their associations

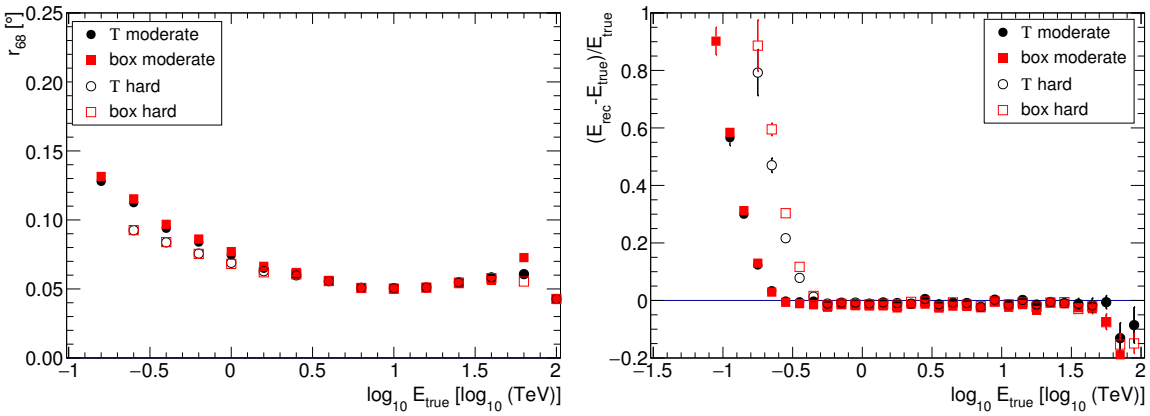

(a) (b)

Figure 4.11: *(a)* Angular resolution, r_{68}, as a function of simulated energy, E_{true}, for γ-rays from MC at a zenith angle of 20° and a wobble offset of 0.5° for the cuts applied in the *VERITAS* standard analysis and in the T analysis, as well as for the moderate and hard configuration, respectively. *(b)* Energy bias as a function of simulated energy, E_{true}, for γ-rays from MC at a zenith angle of 20° and a wobble offset of 0.5 for the cuts applied in the *VERITAS* standard analysis and in the T analysis, as well as for the moderate and hard configuration, respectively.

with astrophysical objects known from other wavelengths. The angular resolution is defined as the distance from the source which contains 68 % of all reconstructed γ-ray events simulated at a certain position on the sky at a given zenith angle and wobble offset. Figure 4.11(a) depicts the evolution in terms of angular resolution, r_{68}, as a function of simulated energy, E_{true}, for the analysis using T and box cuts. It can be observed that the angular resolution obtained with the T analysis is consistent with the one achieved from the *VERITAS* standard analysis. The energy of VHE γ-rays impinging the Earth's atmosphere and creating EASs is reconstructed according to the procedure described in Section 3.3.4. Its uncertainty is defined as the relative difference between the true MC energy and the reconstructed energy of the event $\delta E = (E_{rec} - E_{true})/E_{true}$, called *energy bias*. Figure 4.11(b) depicts the distribution of the energy bias as a function of simulated energy. The energy bias is shown for two sets of cuts, as well as for T and the *VERITAS* standard analysis, for a zenith angle of 20°, a wobble offset of 0.5°, and a spectral index of 1.5. For energies close to the threshold, a large positive bias occurs due to the cut on the image amplitude. Thus, events with reconstructed energies larger than the true energy are most likely to be selected. Conversely, a negative bias at high energies is visible which is attributed to several affects such as less statistics available in this energy range, or badly reconstructed events for high-energy showers due to truncation of the image.

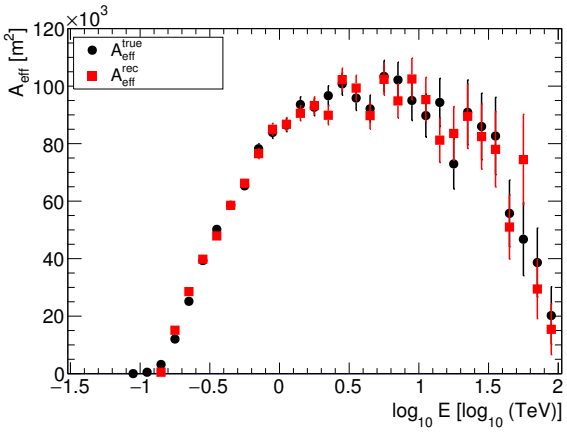

Figure 4.12: Effective areas, A_{eff}, as a function of true MC (black circles) and reconstructed (red squares) energy, E, for a medium zenith angle of 20°, a wobble offset of 0.5°, and cuts based on the BDT algorithm for γ/hadron separation.

4.5.2 Effective γ-ray collection area

The effective collection area describes the efficiency of the instrument to detect γ-rays. It depends on several parameters,

- the energy, E, of the primary particle;
- the zenith angle, ϑ, of the primary particle, which changes the distance between the shower maximum in the atmosphere and the detector;
- the azimuth angle, Ψ_{az}, of the telescope pointing, which reflects the orientation of the shower with respect to the Earth's magnetic field;
- the pointing offset from the source position, δ, which is determined by the pointing direction of the instrument.

Effective areas with different offsets, δ, can be obtained from the same simulated EASs. It is worth noting that for the location of the *VERITAS* instrument, minimum influence of the geomagnetic field is expected to occur for EASs developing in the South [Krause, 2011]. The effective area can be expressed as

$$\tilde{A}_{eff} = 2\pi \int_0^\infty p_\gamma(E, \vartheta, \Psi_{az}, \delta, R) R dR, \tag{4.11}$$

with the impact parameter, R, and the probability of a γ-ray shower to be detected and pass all event selection cuts, p_γ. The detection sensitivity is derived from MC simulations using γ-rays which are fully propagated through the whole analysis chain as applied to data (Section 3.3). The probability p_γ is evaluated by calculating the ratio of the number of γ-rays detected and passing all event selection cuts, N_γ, to the total number of simulated γ-rays, N_{γ_0}, at different energies,

configuration	ϑ	size (min)	E_{th}
		dc	GeV
T moderate	20°	400	≈220
	40°	400	≈360
box moderate	20°	400	≈180
	40°	400	≈360
T hard	20°	900	≈350
	40°	900	≈710
box hard	20°	1000	≈350
	40°	1000	≈710

Table 4.3: Energy threshold, E_{th}, of the T analysis for a Crab-Nebula-like source with spectral index $\Gamma = 2.4$, different cut configurations hard and moderate, as well zenith angles, ϑ, of 20° and 40°. The energy threshold is defined as the energy where the effective area achieves 10 % of its maximum value. The systematic uncertainty on the energy scale is estimated to be ±20 %.

E,

$$A_{eff}(E, \vartheta, \Psi_{az}, \delta) = \tilde{A}_{eff}\,(R = R_0)\,\frac{N_\gamma(E, \vartheta, \Psi_{az}, \delta)}{N_{\gamma_0}(E, \vartheta, \Psi_{az}, \delta)}. \tag{4.12}$$

Here, $\tilde{A}_{eff}\,(R = R_0) = (\pi R_0^2)$ with $R_0 = 750\,\mathrm{m}$ is the area over which the impact points of the primary particle are simulated. Figure 4.12 shows the effective areas determined using Equation 4.12 after applying all selection cuts for a zenith angle of 20° and a wobble offset of 0.5° as a function of reconstructed and simulated energy. The two effective areas appear very similar characterised by a sharp rise at low energies towards a turnover. The energy threshold, E_{th}, is defined as the energy where the effective area achieves 10 % of the plateau value. The corresponding values for different cut configurations and zenith angles of observation are listed in Table 4.3. At low energies, the effective area is limited by the amount of Cherenkov light reaching the detector and by a cut on the amplitude of the Cherenkov light image in the camera. This can be understood in terms of shower development. Low-energy showers develop early in the atmosphere and create much less Cherenkov light than showers at higher energies. At energies larger than the energy threshold, the effective area increases slowly until the maximum is reached around 4 TeV (E_{max}). For energies larger than E_{max}, the effective area decreases gradually due to distant high-energy events producing images located far away from the camera centre. At very low and very high energies, the curves of the effective area versus reconstructed and simulated energy deviate as the energy bias becomes large. Effective areas are calculated for a distinct set of azimuth angle Ψ_{az}, zenith angle ϑ, and wobble offset δ. To obtain the effective area for an arbitrary set of (ϑ, , and) as well as NSB level, a linear interpolation in $\cos\vartheta$, δ, and NSB level is performed. Because of the increasing dependence of the effective area on azimuth angle, the

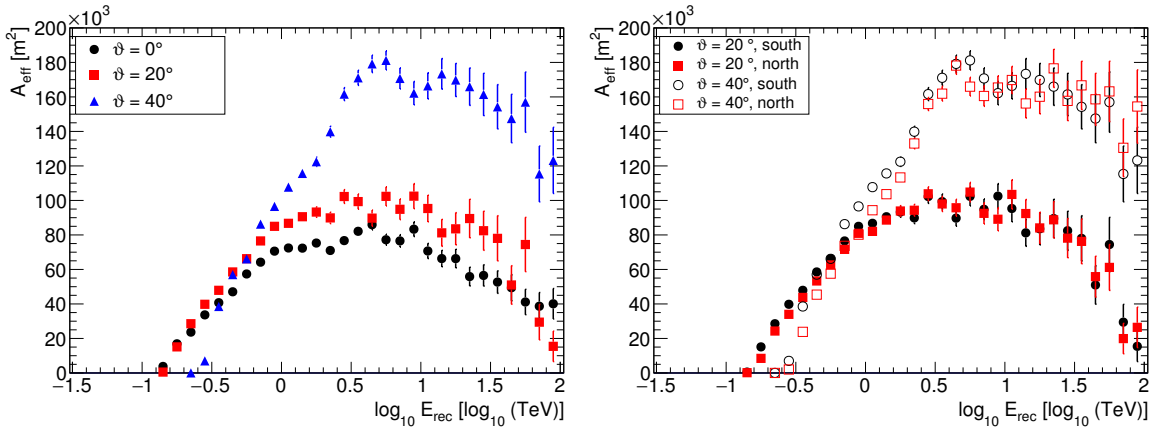

(a) (b)

Figure 4.13: *(a)* Effective areas, A_{eff}, as a function of reconstructed energy, E_{rec}, for various zenith angles, ϑ. The azimuth angle and the wobble offset are fixed to $\Psi_{az} = 0°$ and $\delta = 0.5°$, respectively. *(b)* Effective areas, A_{eff}, for two different zenith angles, ϑ, versus reconstructed energy, E_{rec}, and for azimuth angles of 0° (north) and 180° (south).

latter are calculated for different azimuth angles. Note that effective areas are only valid for the analysis configuration used in this step, including the γ-ray selection cuts, and the size of the ON source region. Two different kinds of effective areas based on the ON region are used: point-source effective areas and extended-source effective areas. Effective areas for point sources are calculated with a value of the ON region, θ_{int}, optimised for analysis of a point source. The size of the ON region is typically smaller than the size of the point source which is influenced by the limited angular resolution of the instrument. As a consequence, the flux of the source calculated using these effective areas corresponds to the point source and not just the emission inside the ON region. On the other hand, extended-source effective areas are estimated with a larger ON region than the angular resolution of the instrument but do not include the correction factor of the flux calculation. Thus, the flux calculated with these effective areas corresponds only to the emission within the ON region chosen for the source analysis.

Figure 4.13 and Figure 4.14 represent some effective areas to illustrate their basic dependencies on azimuth and zenith angle, as well as on the chosen configuration of the analysis cuts. Figure 4.13(a) shows the effective area as a function of reconstructed energy of the shower for a typical zenith angle of 0°, 20°, and 40°, and a wobble offset of 0.5°. As the light has to travel a longer path through the atmosphere for large zenith angles, the probability of photons to get absorbed is much higher than for smaller zenith angles. Therefore, larger effective areas result from showers at large zenith angles as showers will spread Cherenkov photons over a larger area but with reduced intensity [Sommers and Elbert, 1987].

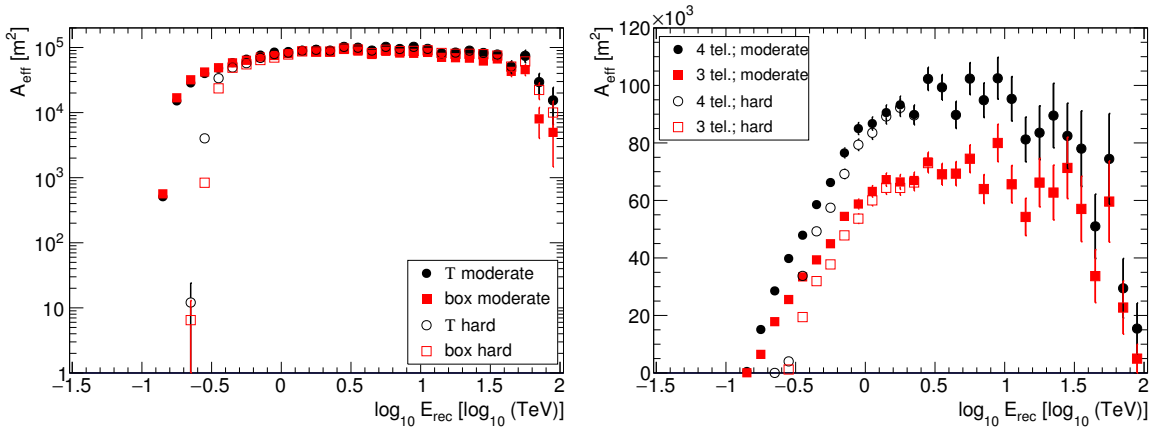

(a) (b)

Figure 4.14: *(a)* Effective areas, A_{eff} as a function of reconstructed energy, E_{rec}, for γ-rays from MC at a zenith angle of 20° and a wobble offset of 0.5° for the cuts applied in the *VERITAS* standard analysis and in the BDT analysis, as well as for moderate and hard configurations, respectively. *(b)* Effective areas, A_{eff}, obtained for a zenith angle of 20°, and a wobble offset of 0.5° for the hard and the moderate configuration based on the BDT method using the full *VERITAS* array of four telescopes (4 tel.) and excluding one telescope (3 tel.).

Figure 4.13(b) depicts the effective areas for azimuth angles of 0° and 180°, and two different zenith angles of 20° and 40°. An azimuth angle of 0° represents the pointing direction of the *VERITAS* instrument north. It is clearly visible that the effective areas are larger for $\Psi_{az} = 0°$ than for $\Psi_{az} = 180°$. This is caused by the orientation of the Earth's magnetic field relative to the direction of the shower development. At the site of the *VERITAS* observatory, the angle between the magnetic field lines and shower axis is larger when pointing north. Electrons and positrons created during the development of EASs are deflected in opposite direction with respect to the geomagnetic field due to the Lorentz force.

The effective area of γ-ray from MC as obtained for T cuts and standard box cuts is illustrated in Figure 4.14(a). The ratios of the effective areas obtained from box and T selection cuts are shown in Figure 4.15. For small energies $E \leq 500$ GeV in the moderate configuration the effective area for T cuts is in general slightly smaller compared to the effective area as achieved with the box cuts. In addition, the effective area of the hard configuration of the T cuts is larger over the whole range of energies compared to the box cuts. Furthermore, the energy threshold for hard cuts is increased which is mainly caused by 400 dc required per shower image by the moderate cuts compared to 900 dc or 1000 dc for hard cuts (Table 4.3). Moreover, Figure 4.14(b) illustrates the dependency on the number of operating telescopes. In case, where one of the telescopes of the *VERITAS* instrument has a technical problem, the array is operated with only three telescopes. This decreases the effective area by about 20 % to 30 % for energies above the trigger threshold.

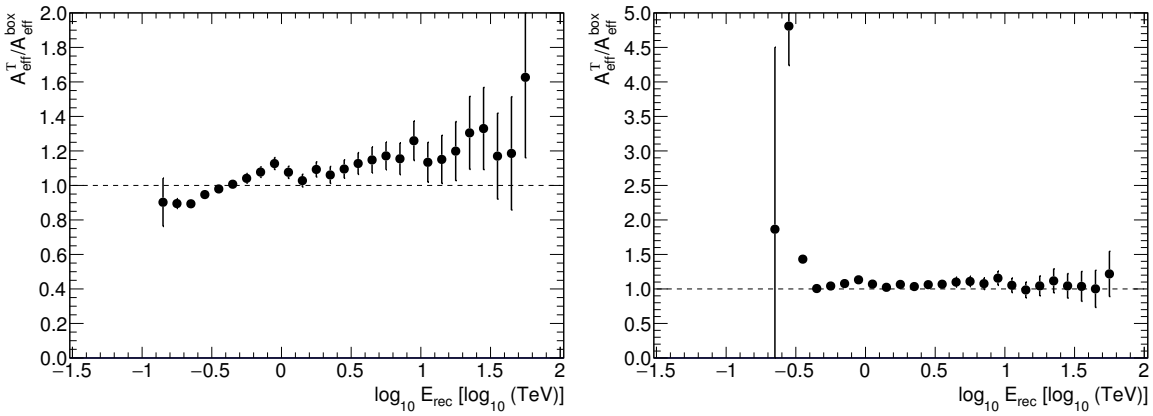

(a) (b)

Figure 4.15: Ratio of the effective areas, $A_{eff}^{\mathrm{T}}/A_{eff}^{box}$ as a function of reconstructed energy, E_{rec}, for γ-rays from MC at a zenith angle of 20° and a wobble offset of 0.5°. *(a)* For moderate cuts. *(b)* For hard cuts.

4.5.3 Classification power

A parameter commonly used in astronomy to quantify the effectiveness of particular analysis cuts is the quality factor, q, [Bugayov et al., 2002] defined as

$$q = \frac{\epsilon_{\gamma}}{\sqrt{\epsilon_{\mathrm{CR}}}}, \tag{4.13}$$

with $\epsilon_i = \hat{N}_i/N_i$ and i refers to either γ-rays or cosmic rays (CR). $\hat{N}_i$ and N_i are the number of events after and before applying the selection criteria. Then, the ratio between the quality factors computed for analysis cuts using the BDT and the box cuts method is calculated by

$$\frac{q_{\mathrm{T}}}{q_{\mathrm{box}}} = \frac{\epsilon_{\gamma_{\mathrm{T}}}}{\sqrt{\epsilon_{\mathrm{CR}_{\mathrm{T}}}}} \cdot \frac{\sqrt{\epsilon_{\mathrm{CR}_{\mathrm{box}}}}}{\epsilon_{\gamma_{\mathrm{box}}}} \tag{4.14}$$

with the uncertainty determined using Equation 4.13 as

$$\delta q_j = \sqrt{\frac{N_{\mathrm{CR}} \cdot \hat{N}_{\gamma} \cdot (N_{\gamma} - \hat{N}_{\gamma})}{\hat{N}_{\mathrm{CR}} \cdot N_{\gamma}^3} + \frac{\hat{N}_{\gamma} \cdot (N_{\mathrm{CR}} - \hat{N}_{\mathrm{CR}})}{4 \cdot N_{\gamma} \cdot \hat{N}_{\mathrm{CR}}^2}}, \tag{4.15}$$

where j refers to either BDT or box cuts. The final uncertainty is then estimated by

$$\delta q' = \sqrt{\left(\frac{\delta q_{\mathrm{T}}}{q_{\mathrm{box}}}\right)^2 + \left(-\frac{q_{\mathrm{T}} \cdot \delta q_{\mathrm{box}}}{q_{\mathrm{box}}^2}\right)^2}. \tag{4.16}$$

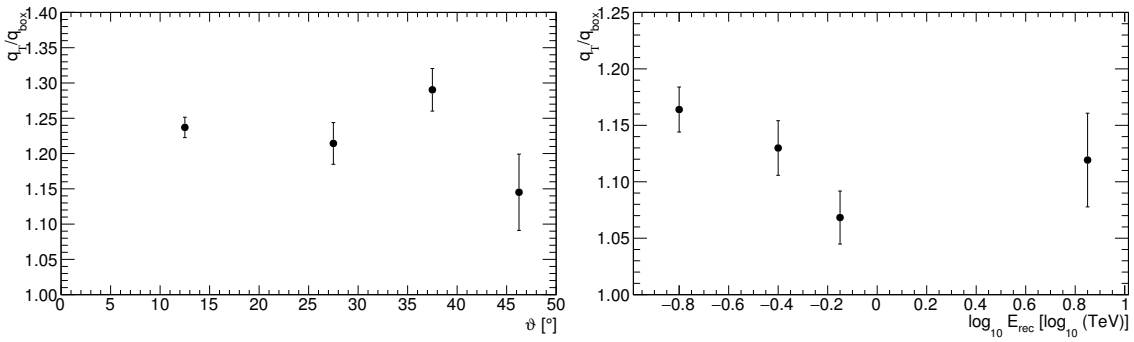

Figure 4.16: Ratio of the quality factor, defined as q_{T}/q_{box} versus zenith angle (*left*) and reconstructed energy (*right*). The quality factor for the BDT analysis, q_{T}, is compared to the *VERITAS* standard analysis, q_{box}. The values of q are determined using the cut efficiencies for γ-rays from MC simulations and background events from `OFF` data in the specific range of zenith angle, ϑ, and reconstructed energy, E_{rec}.

Figure 4.16 demonstrates the dependence of $q_{\mathrm{T}}/q_{\mathrm{box}}$ on the zenith angle and reconstructed energy after the selection criteria were applied to the dataset. The ratio illustrates that the training in bands of energy and zenith angle results in a stable improvement of γ/hadron classification power throughout the parameter space for analysis cuts using the BDT method compared to standard box cuts.

The classification power of the available cuts can be also checked by studying the distribution of signal and background events according to each classifying variable, as shown in Figure 4.17. Evidently, the distributions of the variables *MRSW* and *MRSL* differ significantly between events classified correctly by the T cuts but not by the box cuts, compared to events correctly classified by the box but not by the T selection cuts. The optimised T selection cuts take events into account which are excluded when box cuts are applied, as the latter filter events by mainly two criteria: -1.2$<$*MRSW*$<$0.5 and -1.2$<$*MRSL*$<$0.7. Thus, γ-ray events which appear larger in the camera due to their energy or impact parameter are excluded by these cuts, whereas the events are correctly classified by the T analysis. Especially, it is obvious from the distribution of the variable *MRSW* in Figure 4.17 that there are more events with *MRSW*$<$0.5 classified correctly by the T cuts than by the box cuts. This may be caused by events with a small emission height ($<$6 km) which are excluded by the box cuts but accepted by the T cuts. To sum up, signal events with properties falling outside the ranges of the box cuts are thus classified as background events by the *VERITAS* standard analysis whereas they are identified correctly by the T cuts.

Based on these distributions, their signal efficiency, ϵ_S, and purity, η_S can be considered. The signal efficiency and purity of the T analysis are compared to the efficiency and purity for all events which are correctly classified according to the box cuts method, and the other way around.

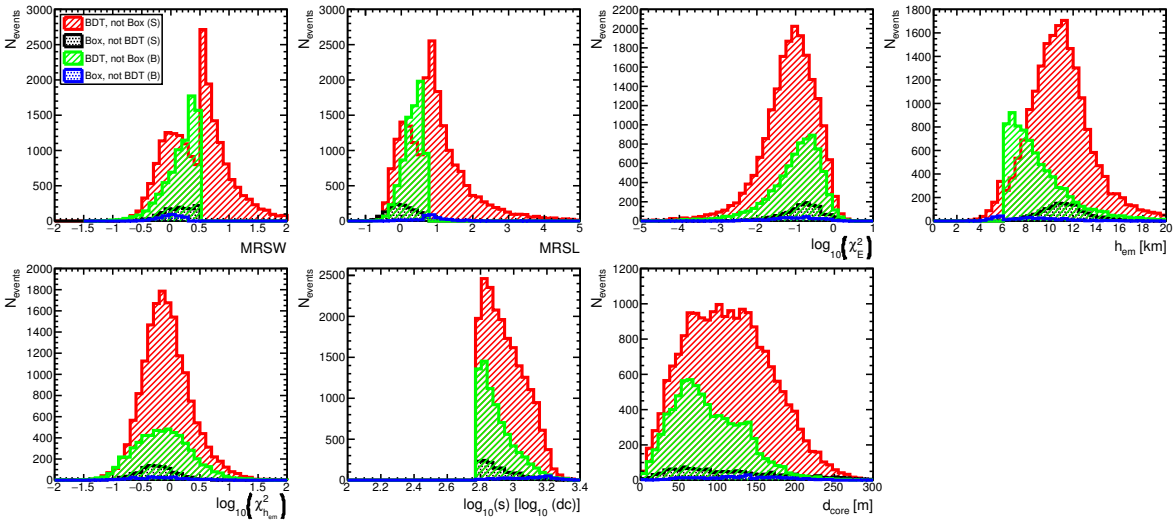

Figure 4.17: Distribution of the classifying variables for events after applying the T and box cuts using MC simulations of γ-rays at about $\vartheta = 20°$ and an energy from 0.32 TeV to 0.50 TeV. Data of the Crab Nebula in the same range of energy and zenith angle are used. The striped areas show the distribution of events which did not passed the box cuts but where correctly classified by the T selection cuts. The dotted areas show the distribution of events not passing the T selection cuts but correctly classified by the box cuts.

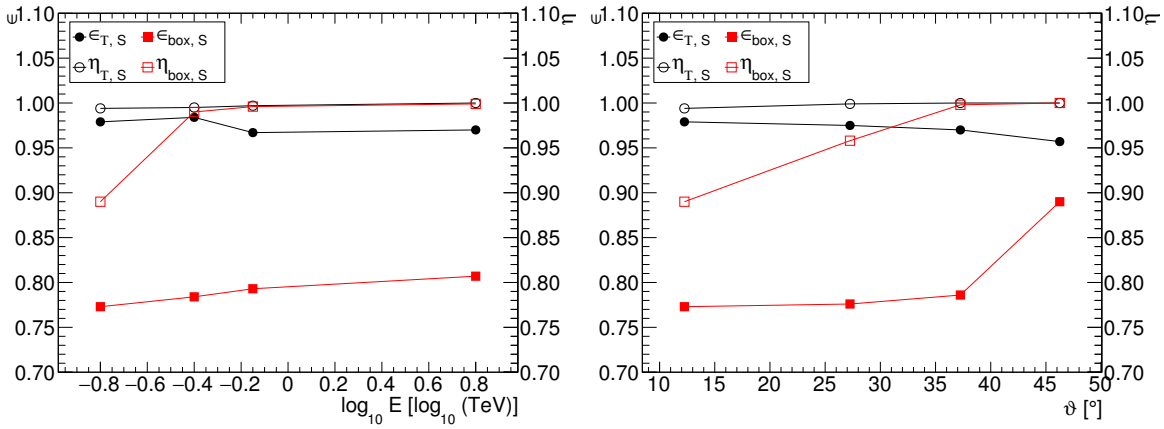

(a) (b)

Figure 4.18: Signal efficiency (black filled circle), $\epsilon_{T,S}$, and purity (black open circle), $\eta_{T,S}$, after applying the optimal selection T_{sel} for events correctly classified by the box cuts. The red squares represent the efficiency (filled), $\epsilon_{box,S}$, and purity (open), $\eta_{box,S}$, after applying the box cuts for events correctly classified by the T analysis. The uncertainties are smaller than the size of the symbols. *(a)* As a function of reconstructed energy, E, for events with zenith angle, ϑ, between 0° and 22.5°. *(b)* As a function of zenith angle, ϑ, for events with energies between 0.08 TeV to 0.32 TeV.

Here, the signal efficiency is calculated according to Equation 4.10. The purity is given as follows

$$\eta_S = \frac{N^S_{Y_i=\xi_{t_i}}}{N^S_{tot} + N^B_{tot}}, \tag{4.17}$$

where N^S_{tot} is the total number of all γ-ray events from MC simulations, N^B_{tot} the total number of background events from data, $N^S_{Y_i=\xi_{t_i}}$ the number of correctly classified events (see Equation 4.1 and Equation 4.4) from the sample of signal events. Figure 4.18 presents the signal efficiency and purity after applying the optimal selection T_{sel} to events correctly classified by the box cuts. In addition, the efficiency and purity after applying the box cuts to events correctly classified by the T analysis are shown. As can be seen, the purity of both box cuts and T analysis are comparable, while the efficiency is higher for the T analysis ($>$90 %) compared to the box cuts method ($>$70 %) throughout the whole parameter space. This demonstrates that the optimised γ/hadron separation using the BDTs outperforms the box cuts by about 20 % to 30 %. The uncertainty on the efficiency and purity is approximated by $1/\sqrt{N}$. To summarise, this demonstrates that the correlation of the classification variables used to discriminate between signal and background events should be taken into account, as done for the T selection cuts.

4.5.4 Sensitivity

A benchmark test of the BDT performance compared to the standard box analysis for the moderate and hard configuration is accomplished by analysing data of the Crab Nebula. Data taken at low zenith angles (ϑ<20°) are used in order to allow comparison of the two methods at the lowest energies. The differential flux sensitivity is defined as the lowest flux in a given energy bin which results in a significant detection after a certain observation time. The results are shown in Figure 4.19. Sensitivity improvements can be seen across the entire energy range, with the most significant improvements of about 10 % to 20 % at energies below 1 TeV.

Table 4.4 lists a comparison between observation time required to detect a point-like VHE γ-ray source with a flux between 1 % and 100 % of the flux of the Crab Nebula [Hillas et al., 1998] for a hard spectrum source with an approximated energy threshold as listed in Table 4.3, and different array configurations. The cuts are applied to Crab Nebula data taken at zenith angles smaller than 20°. The T cuts show better sensitivity over a wide range of source strengths. The required observation time for the T analysis is up to 25 % (V4 array configuration), 20 % (V5), and 20 % (V6) less compared to the *VERITAS* standard analysis. The comparison between observation time required to detect a point-like VHE γ-ray source using a moderate spectrum source is shown in Section A.4. In addition to the aforementioned tests, the performance of the proposed analysis has been tested on a set of different *VERITAS* sources obtained from the reflected-region background model. The results obtained for a sample of four sources are presented in Table 4.5 and compared to the box cuts analysis. There are three extragalactic sources, Markarian 501,

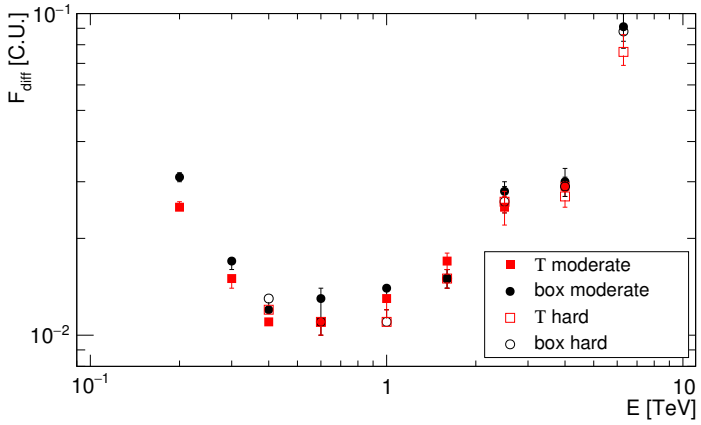

Figure 4.19: Differential flux sensitivity of T cuts versus standard *VERITAS* cut selection for low zenith angle ($\vartheta < 20°$) data of Crab Nebula with about 42 h observation time.

array configuration	$\Phi(E)$	t_{box}	t_{T}
	C.U.		
V4	1	3.50 min	3.20 min
	0.30	11.80 min	10.50 min
	0.10	45.60 min	37.30 min
	0.05	2.20 h	1.80 h
	0.03	5.20 h	4.00 h
	0.01	36.50 h	27.50 h
V5	1	2.60 min	2.50 min
	0.30	8.80 min	8.20 min
	0.10	34.60 min	29.90 min
	0.05	1.60 h	1.40 h
	0.03	3.60 h	3.00 h
	0.01	24.50 h	20.00 h
V6	1	2.10 min	2.10 min
	0.30	7.20 min	6.90 min
	0.10	33.40 min	29.30 min
	0.05	1.70 h	1.40 h
	0.03	3.90 h	3.20 h
	0.01	28.40 h	22.30 h

Table 4.4: Observation time required for a detection of a point-like VHE γ-ray source with a flux between 1 % and 100 % of the flux of the Crab Nebula in Crab Units (C.U.) for a hard spectrum source with an approximated energy threshold as listed in Table 4.3 and different *VERITAS* array configurations. The uncertainties of observation time are about 2 to 4 %.

source	ϑ	t_{obs}	analysis	N_{ON}	αN_{OFF}	N_γ	N_{bkg}	S
		h				1/min	1/min	
IC443	14	10.8	box	2597	2266	0.505 ± 0.085	3.485 ± 0.110	6.1
			T	2682	2226	0.691 ± 0.086	3.430 ± 0.109	8.4
Markarian 501	15	20.8	box	2937	703	1.793 ± 0.044	0.562 ± 0.009	55.2
			T	2590	405	1.753 ± 0.041	0.324 ± 0.007	62.3
M87	28	31.4	box	215	130	0.045 ± 0.008	0.069 ± 0.002	6.2
			T	199	104	0.051 ± 0.008	0.055 ± 0.002	7.5
RGB J0710+591	40	21.7	box	140	120	0.030 ± 0.010	0.078 ± 0.003	3.3
			T	110	67	0.033 ± 0.008	0.051 ± 0.003	4.4

Table 4.5: Performance of the applied cuts on some *VERITAS* sources. For each, the results obtained with the analysis using box cuts are shown in the first line and results obtained with the optimised T analysis presented in this thesis are shown just below. For IC443 and Markarian 501, the moderate cut configuration is used, whereas for M87 and RGB J0710+591, hard configuration is applied. ϑ is the mean zenith angle of observation, t_{obs} the observation time, N_{ON} represents the total number of events around the source position in the sky, N_{OFF} represents the normalised number of background events, N_γ is the rate of γ-ray-like events per minute, N_{bkg} is the rate of background events per minute, and S is the significance of the detection. The normalisation factor, α, depends on the observation conditions of the source and varies between 0.16 and 0.20 for the presented sample.

M87 and RGB J0710+591, together with a Galactic source, the SNR IC443. The observed main trend is that the T analysis yields to a better performance for all studied sources. Even through the number of ON events, N_{ON}, is reduced for three out of four sources, the number of OFF events, N_{OFF}, decreases significantly using the T analysis up to a factor of about 1.02 to 1.7. The gain in sensitivity of the T analysis over the box cuts analysis shown here, corresponds to a reduction of the observation time by factor 1.13 to 1.38. In more detail, the improvement of the BDT method in sensitivity gives a gain in significance compared to the box cuts method of $>$1.13 for all tested sources.

4.5.5 Spectral reconstruction

The applicability of the BDT method for the spectral analysis of VHE γ-ray sources is tested in the following. Together with the morphology of a VHE γ-ray source, the energy spectrum of the emitted γ-rays provide valuable information on the acceleration mechanism at work in astrophysical objects. Consequently, one of the key quantities to study VHE γ-rays is the differential energy spectrum of the VHE γ-ray source. This study verifies that no spectral features are introduced with the T analysis. This is of particular concern given that the selection on the BDT response is

optimised in each energy and zenith angle band individually, leading to 16 different values, T_{sel}. The differential energy spectrum is defined as the number of photons detected from the source, N_γ, per unit area $\mathrm{d}A$, unit time $\mathrm{d}t$ and unit energy $\mathrm{d}E$,

$$\Phi(E) = \frac{\mathrm{d}N_\gamma}{\mathrm{d}A\mathrm{d}t\mathrm{d}E}. \tag{4.18}$$

The quantity which is measured by *VERITAS* and directly related to the γ-ray spectrum of the source is the differential γ-ray rate after event selection and background subtraction, N_{obs}, in bins of reconstructed energy, E_j^{rec},

$$N_{obs}(E_j^{rec}) = \frac{\mathrm{d}N_\gamma}{\mathrm{d}t\mathrm{d}E_{rec}} = \int_{t_0}^{t_1} \mathrm{d}t \int_0^\infty p(E_j^{rec}|E) A_{eff}(E,\vartheta,\Psi_{az},\delta)\epsilon_D(t)\frac{\mathrm{d}N\gamma}{\mathrm{d}A\mathrm{d}t\mathrm{d}E}\mathrm{d}E, \tag{4.19}$$

where $dN_\gamma/(\mathrm{d}A\mathrm{d}t\mathrm{d}E) = \Phi(E)$ is the source spectrum to be determined (Equation 4.18). The first integral represents the time of observation between t_0 and t_1, taking into account the dead time of the detector included in the factor $\epsilon_D(t)$. The probability density function (PDF) $p(E_j^{rec}|E)$ describes the probability of a γ-ray with energy E to be reconstructed to have an energy E_{rec}. It depends on the zenith angle, the azimuth angle, and the wobble offset, and is estimated via MC simulations. The effective collection area of the instrument is calculated according to Equation 4.12. To obtain the underlying source spectrum, the energy smearing and the energy bias, described by the PDF are combined with the effective area, $A_{eff}(E_{rec})$. To correctly account for the migration in energy caused by the reconstruction bias, the MC γ-rays have to be produced following a typical assumed source spectrum. Then, the actual source spectrum is calculated according to

$$\Phi(E_{rec}) = \frac{1}{A_{eff}(E_{rec},\vartheta,\Psi_{az},\delta)}\frac{\mathrm{d}N_\gamma}{\mathrm{d}t\mathrm{d}E_{rec}}. \tag{4.20}$$

To produce the differential photon spectrum of a source, the flux is determined in energy bins whereas each bin width is minimal the energy resolution of the instrument. The basic requirements used within this thesis to generate a spectral point are a statistical significance (Equation 3.8) of at least 2σ. Otherwise an upper limit is calculated according to Rolke et al. [2005] to represent the flux measurements. The differential source spectrum is obtained by fitting a power law to the discrete flux measurements and the associated uncertainty. As a consistency check, the spectral results are shown for the Crab Nebula. The dataset used to derive the differential energy spectrum comprises a total livetime of about 42 h taken at zenith angles between 10° and 30°. Figure 4.20 shows the differential energy spectrum of the Crab Nebula as obtained for the BDT analysis compared to the box cuts analysis. The differential flux points differ by less than 1σ between the analysis methods for all points, as illustrated by the residuals in the lower panel. The latter indicates the consistency between the spectral analysis applying T or box cuts.

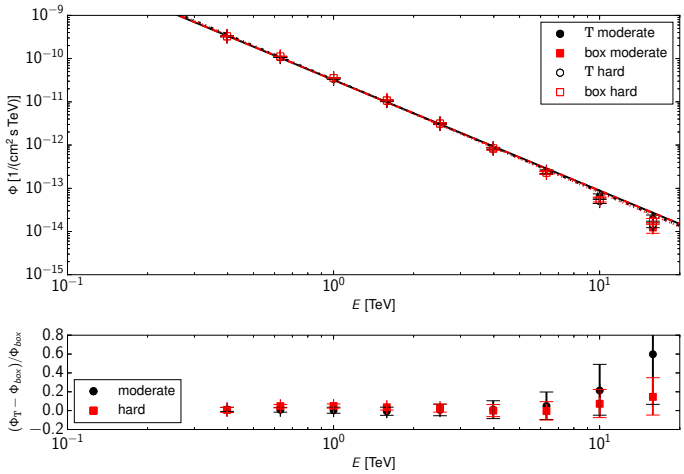

Figure 4.20: Differential energy spectrum and residuals of the Crab Nebula as obtained with the standard *VERITAS* and the T cuts using the moderate and hard configuration. The dashed red line denotes the fit of a power law to the T spectrum, whereas the solid black line denotes the fit of a power law to the spectrum obtained with standard *VERITAS* cuts.

4.5.6 Performance on non-standard datasets

As discussed in Section 4.3.1, the BDTs are trained with data which does not overlap the source region taken with all four telescopes of *VERITAS* operational and at a wobble offset of 0.5°. The γ-rays are simulated according to these conditions. It is thus necessary to test the sensitivity of the BDT analysis on datasets taken with larger wobble offsets and with only three telescopes available. Consequently, the performance of the T analysis is tested on observations of the Crab Nebula with wobble offsets of 0.7°, 1.0°, and 1.3° taken at zenith angles between 15° and 25°. The data analysis is done for the BDT and the standard *VERITAS* cuts using the moderate configuration. The results are shown in Table 4.6. An improvement in significance and γ-ray rate compared to the *VERITAS* standard analysis is observed regardless of the wobble offset of the data. Furthermore, the last row demonstrates the performance of the T cuts and the box cuts analysis on Crab Nebula data taken with only three telescopes operational. While the γ-ray rate increases by about 25 % for the BDT analysis compared to the *VERITAS* standard analysis, the background rate is comparable leading to larger significance. These results illustrate an improvement over the whole parameter space regardless of the wobble offset and the telescope configuration when using the T cuts. However, a dedicated training in bins of wobble offsets could still increase the sensitivity of the analysis but is beyond the scope of this thesis.

δ	N_{tel}	$\sigma_{\mathrm{T}}/\sigma_{box}$	$N_{\gamma,box}$	$N_{\gamma,\mathrm{T}}$	$N_{bkg,box}$	$N_{bkg,\mathrm{T}}$
			1/min	1/min	1/min	1/min
0.5°	4	1.05	7.45±0.06	7.44±0.06	0.44±0.01	0.28±0.01
0.7°	4	1.08	7.57±0.22	8.44±0.23	0.57±0.06	0.54±0.05
1.0°	4	1.14	4.97±0.17	5.92±0.19	0.45±0.05	0.42±0.04
1.3°	4	1.14	2.90±0.13	3.33±0.14	0.29±0.04	0.24±0.04
0.5°	3	1.15	3.03±0.11	3.80±0.12	0.17±0.03	0.17±0.03

Table 4.6: Sensitivity of the T analysis using a training configuration at wobble offset, δ, of 0.5° and four telescopes operating applied to data of the Crab Nebula taken at different wobble offsets different number of telescopes, N_{tel}, operating. The significances (σ), the γ-ray rate (N_{γ}), and the background rate (N_{bkg}) are compared between the BDT and the *VERITAS* standard analysis.

4.6 Conclusion and outlook

In this chapter, a new analysis method is presented, based on an MVA approach optimised for the detection of faint-sources observed with the *VERITAS* instrument. This method is developed so as to be easily applied to data obtained from future IACT experiments such as *CTA*.

A number of BDT classifiers have been defined, in order to take into account the different classes of data, with bins in zenith angle and energy. Applying the analysis to real data, several configurations have been defined so as to allow cut optimisation for different expected source characteristics (point and extended) in order to study their morphology. The consistency of the new method is validated by comparing the BDT response with that for real γ-ray excess from the Crab Nebula and additional Galactic and extragalactic sources as measured with *VERITAS*. In addition, the optimised T cuts have proven to achieve a 20 % to 25 % gain in sensitivity and observation time compared to the box cuts. As a final consistency check, the spectrum of the Crab Nebula as derived by the presented BDT method is compared to that obtained by *VERITAS* using the box cuts. Both spectra show excellent compatibility. Overall, the BDT method increases the sensitivity over a large variety of sources taken with different observing conditions.

Beyond the classifying variables used in this work, parameters which describe the properties of the intrinsic image are sensitive to different shower properties [Lemoine-Goumard et al., 2006]. These parameters could improve the BDT classification. In addition, recently several campaigns [de Naurois and Rolland, 2009; Parsons and Hinton, 2014] studied the reconstruction of the shower parameters by comparing the raw shower image in a camera with the predictions obtained from simulations on a pixel-by-pixel level. The development of this reconstruction method for the application to *VERITAS* data is currently ongoing [Vincent, 2015]. The inclusion of these

parameters into the BDT training could improve the sensitivity of the analysis but is beyond the scope of this thesis.

This chapter described the training, testing, and evaluation of a new method for γ/hadron separation using a method based on boosted decision trees. The method has proven to be efficient for various VHE γ-ray sources. In the following chapter, the Cygnus region of our Galaxy is introduced in detail. Afterwards, the newly optimised T cuts will be applied to data from the Cygnus region taken by *VERITAS*.

5

The Cygnus region

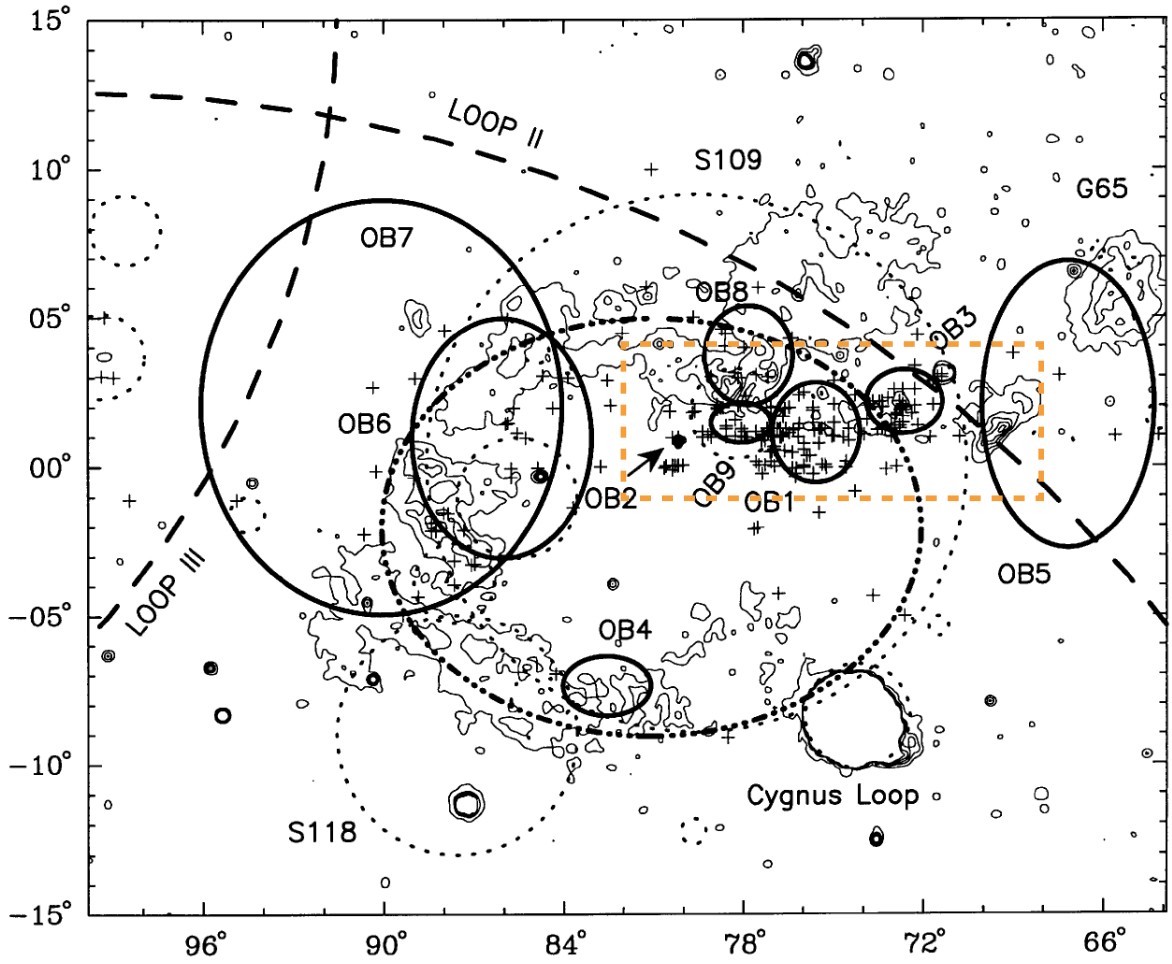

Figure 5.1: Map of the Cygnus region in Galactic coordinates. The thick dashed-dotted ellipse shows the location of the Cygnus superbubble. Solid ellipses indicate the approximate position and extent of the OB associations. Thick dashed lines present the boundaries of the radio loops *Loop II* and *Loop III*. Plus signs mark the positions of stars. Dotted circles show the prominent HII regions *S109* and *S118*. Thin line contours denote the X-ray image taken with the satellite ROSAT. The orange dashed rectangle represents the area of the *VERITAS* sky survey of the Cygnus region. Figure adapted from Uyaniker et al. [2001].

The Cygnus region is one of the brightest and most active regions in the northern sky, and a place of ongoing star formation, including the Cygnus X complex. It consists of nine OB associations with a total stellar mass as high as $10^6 M_\odot$ [Reipurth and Schneider, 2008] and a total kinetic stellar wind energy input of $\geq 10^{39}$ erg/s [Lozinskaya et al., 2002]. This corresponds to a small fraction of the kinetic energy input by SNRs in the entire Galaxy (Section 2.3.1). The best studied OB association within the Cygnus region to date is the OB2 association. It contains more than 2600 OB-type stars, 100 O stars, and 3 Wolf-Rayet stars [Reipurth and Schneider, 2008, and references therein]. In comparison, the Carina nebula seen from the southern hemisphere contains more than 66 O-type stars [Feinstein, 1995; Smith, 2006]. Therefore, the Cygnus region is the largest known star-forming region outside the Galactic centre. It also contains more than 20 HII regions [Uyaniker et al., 2001]. Furthermore, it has been pointed out that molecular clouds in the Cygnus X region are connected and partly show evidence of interaction with massive OB associations [Schneider et al., 2006; Ackermann et al., 2012a].

The Cygnus region can be seen as a small scale version of a whole galaxy, harbouring a wealth of objects, attested by >10 SNRs [Green, 2014], >14 pulsars [Manchester et al., 2005], PWNe, HII regions, Wolf-Rayet binary systems, nine OB associations, microquasars, dense molecular clouds, and a superbubble. Besides, Acero et al. [2015] reported on more than 60 γ-ray sources detected with *Fermi*-LAT, whereas 16 sources are related to the region of the Cygnus cocoon. Therefore, it is a promising area to address questions related to origin and acceleration mechanism of particles in massive star-forming regions. In addition to the aforementioned properties of the Cygnus region, its special appearance has been attested by a total interstellar mass of $8^{+5}_{-1} \times 10^6 M_\odot$ at a distance of 1.4 kpc based on measurements of HI, HII and H_2 emissivities detected by *Fermi*-LAT in γ-rays [Ackermann et al., 2012a]. In comparison, the total interstellar mass of HI, HII and H_2 in the entire Galaxy amounts to about $4.9 \times 10^9 M_\odot$ [Draine, 2011].

In this chapter, the Cygnus region and its view at multiple wavelengths is introduced with the focus on observations and published results in the VHE γ-ray regime.

5.1 Multiwavelength view of the Cygnus region

Owing to the richness of star formation and the close proximity to the solar sytem of 1 to 2 kpc [Uyaniker et al., 2001], the Cygnus region is an area in our galaxy well studied at a broad range of wavelengths. It is covered in radio and sub-mm lines by the Canadian Galactic Plane Survey (CGPS) [Taylor et al., 2003] and the Giant Metrewave Radio Telescope [Paredes et al., 2007], in infrared by the MSX survey, the *Spitzer* Cygnus Legacy Project [Benjamin et al., 2003; Churchwell et al., 2009; Beerer et al., 2010; Kraemer et al., 2010], and the survey of Cygnus X of the *Herschel Space Observatory* [Schneider et al., 2016]. Moreover, it was observed in X-rays by *Chandra* and its Cygnus OB2 Legacy Project [Butt et al., 2003, 2006; Wright and Drake, 2009; Wright et al.,

2010], *XMM-Newton* [Horns et al., 2007], and *Suzaku* [Murakami et al., 2011]. The $10^\circ \times 10^\circ$ region around Cygnus X-1 was surveyed in the γ-ray regime by *INTEGRAL* [Jourdain et al., 2011; Krivonos et al., 2012].

This provides a dynamic multiwavelength context in which a survey of the Cygnus region taken at VHE γ-rays benefits from information gathered at other wavelengths. This information may then be used for source identification and interpretation of measurements. Survey studies were performed previously by IACT experiments at other regions of the Galaxy. The *HEGRA* instrument was the first system of IACTs that conducted a systematic survey of the Galactic plane at very high energies [Aharonian et al., 2002b]. The dataset covered about 115 h of quality-selected observation time, distributed over the Galactic Plane from the Galactic centre to the Cygnus region ($-2^\circ<l<85^\circ$, $-2^\circ<b<2^\circ$). Due to the location of *HEGRA* on the northern hemisphere, the Galactic centre region could only be observed at large zenith angles. Thus, northern IACTs operate with a greatly increased energy threshold. The *HEGRA* survey provided flux upper limits on many potential VHE γ-ray sources with values ranging from 7 % C.U. to several C.U.

The *H.E.S.S.* survey of the Galactic plane was the first survey to be conducted with currently operating IACTs. The location of the instrument on the southern hemisphere results in much better observing conditions for searches in the inner part of the Galactic plane. The initial survey was performed between May and July 2004 in a range of Galactic coordinates of $-30^\circ<l<30^\circ$ and $-3^\circ<b<3^\circ$ [Aharonian et al., 2006a]. A flux sensitivity down to 2 % of the Crab Nebula flux at these energies was reached. During this survey, 17 new sources of VHE γ-ray emission were detected. An extension of the *H.E.S.S.* survey was carried out after 2004 with extended limits to encompass longitudes between 60° and 275° [Chaves, 2011]. This expanded the catalogue of VHE γ-ray sources of *H.E.S.S.* to about 52. In addition, the extension of the Galactic plane survey until 2013 led to 77 source detections in the TeV energy regime [Deil et al., 2015].

The success of these surveys led to the conduction of a survey of the Galactic Plane with *VERITAS* at northern longitudes not covered by *H.E.S.S.* Thus, the Cygnus region was surveyed between April 2007 and October 2008 spanning 15° Galactic longitudes and 5° in Galactic latitudes [Weinstein, 2009b]. This is described in more detail in the next section. In addition, the *Milagro* and the Tibet air-shower array with their wide field of view of about 1 sr (*Milagro*) and 2 sr (Tibet air-shower array) [Amenomori et al., 2007] performed large-scale surveys of this region. In 2007, the *Milagro* experiment published results of five years of observations of the Cygnus region [Abdo et al., 2007a,b]. This revealed a new source of VHE emission, MGRO J2019+37, with an extent of $0.32^\circ \pm 0.12^\circ$. In addition, diffuse emission which might be explained by several unresolved sources in the Cygnus region was revealed. Following this, *VERITAS*, with its better angular resolution and lower energy threshold, could resolve the emission and lead to detection of new sources. Several γ-ray sources of this region were detected as well by high-energy instruments such as *HEGRA* [Aharonian et al., 2005c], *EGRET* [Hartman et al., 1999], *Fermi*-LAT [Abdo

et al., 2009d], *Milagro* [Abdo et al., 2007b], and *ARGO-YBJ* [Bartoli et al., 2012], discussed in more detail below.

5.2 *VERITAS* Cygnus sky survey from 2007 to 2008

VERITAS surveyed the Cygnus region between $67^\circ < l < 82^\circ$ and $-1^\circ < b < 4^\circ$ from April 2007 to October 2008. Starting at the *VERITAS* commisioning phase, the survey continued over the following three observing seasons. During the first observing season 2006/2007, the survey was conducted with the three-telescope array consisting of T1, T2, and T3 (Figure 3.1). The remaining seasons, 2007/2008 and 2008/2009, utilised the full array consisting of all four telescopes.

This first analysis of the initial survey until October 2008 [Ward, 2010] comprises approximately 104 h of quality-selected data. The data were analysed in a blind-search followed by additional targeted observations of regions with a significance larger than 4σ until December 2008. In total, 130 h of quality-selected data have been collected to that time. Following the analysis of these data, further independent observations took place between Autumn 2009 and June 2012. Analysis of these datasets reached a sensitivity of about 4 % of the Crab Nebula flux above 200 GeV at 99 % confidence level (CL) [Weinstein, 2009a] and resulted in the detection of VER J2019+407 [Aliu et al., 2013] and the previously known VHE γ-ray sources TeV J2032+4130 [Aliu et al., 2014a] and MGRO J2019+37 [Aliu et al., 2014b].

5.3 The region of Cygnus X, Cygnus OB2, and the Cygnus Cocoon

The Cygnus X complex is one of the brightest regions in the sky at almost all wavelengths. However, in optical light this region looks almost completely dark due to a band of non-luminous molecular dust clouds which absorbs radiation at these wavelengths. This massive star-forming region hosts a large number of sources and source types. This includes the star association OB2, the SNR G78.2+2.1, a cocoon of accelerated cosmic rays seen by *Fermi*-LAT, the VHE source TeV J2032+4130, and the microquasar Cygnus X-3. An overview of this area at infrared wavelengths obtained with the *Herschel Space Observatory* is shown in Figure 5.2.

TeV J2032+4130 was discovered by *HEGRA* as the first source emitting VHE γ-rays with no obvious counterpart at any other wavelength [Aharonian et al., 2002a]. This detection was confirmed by *Whipple* [Konopelko et al., 2007]. Furthermore, *MAGIC* [Albert et al., 2008b] observed this source and reported an upper limit on the γ-ray flux of $(4.5 \pm 0.3_{stat} \pm 0.35_{sys}) \times 10^{-13}\,\mathrm{erg/(cm^2\,s)}$. As the position of the source is coincident with the OB association, Cygnus OB2, and located north of the microquasar Cygnus X-3, it was suggested that these

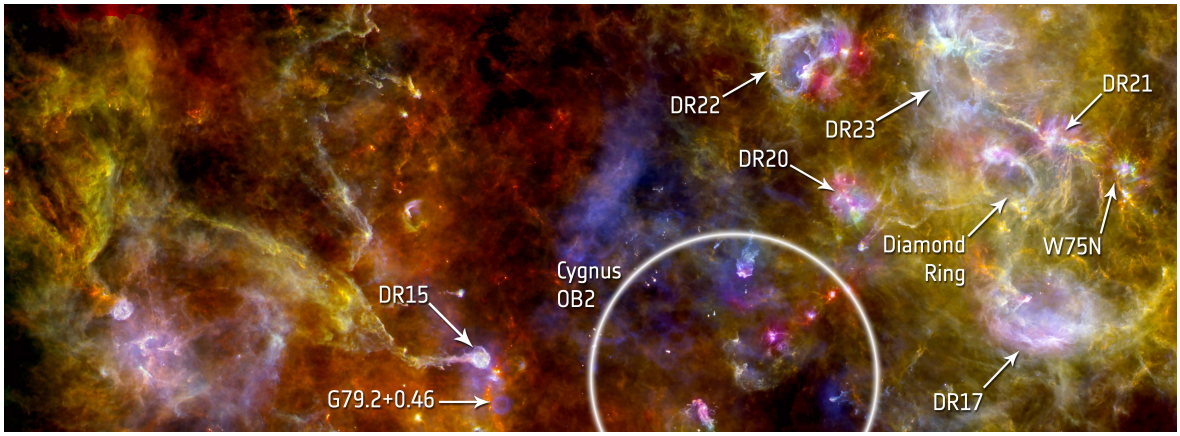

Figure 5.2: Infrared image of the star-forming region Cygnus X as seen by the *Herschel Space Observatory*. The image spans about $6^\circ \times 2^\circ$ ($\approx$500 ly) and depicts prominent regions such as the massive stellar cluster Cygnus OB2 and W75N, the bright regions associated with the formation of massive stars such as DR21 or the Diamond Ring, as well as the nebula G79.2+0.46. Image credit: ESA/Herschel/PACS/SPIRE/HOBYS Consortium.

two sources could be the origin of VHE γ-rays [Aharonian et al., 2002a]. Later, the previously unknown γ-ray pulsar PSR J2032+4127 was discovered by *Fermi*-LAT at 0.7° away from the TeV source with a period of 143 ms and a spin-down luminosity of 2.63×10^{35} erg/s [Abdo et al., 2009a]. Following this, a possible connection between TeV J2032+4130 and PSR J2032+4127 was proposed. This was strengthened by the detection of X-ray emission spatially coincident with TeV J2032+4130 [Murakami et al., 2011]. As a consequence of these results, *VERITAS* [Aliu et al., 2014a] carried out 48.2 h of observations of this source (Figure 5.3(a)). The γ-ray flux above 1 TeV was found to be $(2.35 \pm 0.55) \times 10^{-12}/(\mathrm{cm}^2\,\mathrm{s})$. The relationship of the source to other sources in this region, in particular the Cygnus cocoon detected by *Fermi*-LAT discussed below, is still under investigation. Inside the Cygnus region, TeV J2032+4130 is the only source spatially coincident with an OB association, in particular the OB2 region. The available stellar wind energy in OB2 makes this region a prime target to study the theory of particle acceleration inside stellar winds. γ-ray emission in the vicinity of the SNR G78.2+2.1, also known as γ-Cygni [Higgs et al., 1977], was first detected by the *EGRET* instrument [Thompson et al., 1995]. *Fermi*-LAT discovered a bright γ-ray pulsar, PSR J2021+4026, at the centre of the remnant [Abdo et al., 2010a,b] and measured extended γ-ray emission on the scale of about 0.5° above 10 GeV [Lande et al., 2012]. VHE γ-rays detected by *VERITAS* from the region of γ-Cygni are shown in Figure 5.3(b). Further observations or high-sensitivity analysis could improve the understanding of the VHE γ-ray emission from this source, especially in terms of its relationship to emission seen at other wavelengths.

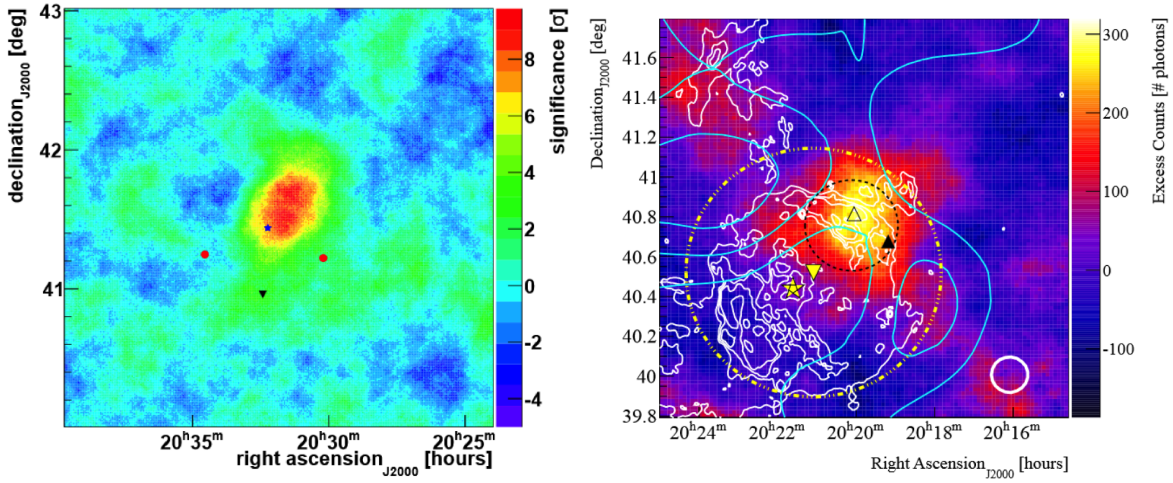

(a) (b)

Figure 5.3: *(a)* VHE γ-rays of the region around TeV J2032+4130 as obtained during observations with the *VERITAS* instrument. The position of Cygnus X-3 and PSR J2032+4127 are represented by a black inverted triangle and a blue star, respectively. The red circles indicate the pointing positions of the telescopes during observation. Figure taken from Aliu et al. [2014a]. *(b)* Emission of TeV γ-rays of VER J2019+407 overlaid with the radio contours of the CGPS at 1420 GHz. Also shown are the γ-ray pulsar PSR J2021+4026 (yellow star), 1FGL J2020.0+4049 and 2FGL J2019.1+4040 (black open and filled triangle). The cyan contours show the emission from the Cygnus cocoon detected by *Fermi*-LAT. Figure taken from Aliu et al. [2013].

A cocoon of accelerated cosmic rays was proposed to be a source of hard excess of γ-rays measured by *Fermi*-LAT above 1 GeV [Ackermann et al., 2011], also known as the Cygnus cocoon. Its angular size spans about 2° between the region of Cygnus OB2, TeV J2032+4130, and the SNR G78.2+2.1. Abdo et al. [2012] propose spatial coincidence of the cocoon with MGRO J2031+41. Initially, this source was associated with TeV J2032+4130 but this raises issues related to the flux of the *Milagro* source which is about 10 times larger than the detected flux obtained with IACT measurements. Furthermore, the *ARGO-YBJ* collaboration reported on the emission of ARGO J2031+4157 that matches the extension of the Cygnus cocoon [Bartoli et al., 2014]. The latter bridges the spectrum in the GeV energy range measured by *Fermi*-LAT with that of MGRO J2031+41. As a consequence, this reinforces the interpretation of three sources as a result of interactions of energetic particles flooding the Cygnus X region. In addition, enhanced radio and X-ray emission is seen in this direction. G78.2+2.1 is positioned near the Cygnus cocoon which also shows VHE γ-ray emission [Abdo et al., 2007a; Bartoli et al., 2014]. This demonstrates that the SNR could be a source of at least part of the high energy particles seen in the cocoon.

The identification of the counterpart of TeV J2032+4130 in radio, optical, infrared, or X-ray wavelengths, would improve our understanding of the emission processes at very high energies. In

addition, it would solve the long-standing problem of the unidentified VHE γ-ray source, as well as the correlation between the TeV extended emission seen by *Milagro* and *ARGO-YBJ*, and the Cygnus cocoon.

The first emitting microquasar at GeV γ-rays seen by *AGILE* [Tavani et al., 2009] and *Fermi*-LAT [Abdo et al., 2009b], Cygnus X-3, allows to explore nonthermal processes associated with the formation of relativistic jets from accreting black holes. The latter could have important consequences in high-energy and very-high-energy physics, potentially shedding light on whether hadronic processes are involved in γ-ray emission. The orbital light curve indicates the region of GeV emission could potentially be separated from a binary system. This is either caused by jets and the formation of internal shocks, or from re-collimation shocks when the jet interacts with dense winds from the Wolf-Rayet stellar companion. This scenario is currently invoked to explain the GeV emission from blazars which argues in favour of the jet of Cygnus X-3 pointing towards our line of sight. Currently, the spectrum at very high energies is unconstrained. So far, upper limits on the VHE γ-ray emission were set by *VERITAS* and *MAGIC* but no detection was confirmed.

5.4 The region of Cygnus OB1 and MGRO J2019+37

Since its discovery at γ-ray energies, MGRO J2019+37 [Abdo et al., 2007b] has been the subject of studies about its nature. The bright region with a flux level of 80% of the Crab Nebula flux at 20 TeV overlaps with several SNRs, HII regions, Wolf-Rayet stars, high-energy γ-ray sources, and a hard X-ray transient. *VERITAS* was able to disentangle this extended source into two emitting regions: a point source and an extended source [Aliu et al., 2014b].

The former, VER J2016+371, is suggested to be associated with the SNR CTB 87 (G74.9+1.2) and based on X-ray and radio morphologies. CTB 87 is likely a PWN. In addition, Saha [2016] reported on a source in the vicinity of VER J2016+371 detected at GeV energies by *Fermi*-LAT suggesting a likely counterpart of this VHE source at GeV energies.

The extended source found by *VERITAS*, called VER J2019+368, can be tentatively associated with the young and energetic radio and γ-ray pulsar PSR J2021+3651 and its nebula, SNR G75.1+0.2 [Abdo et al., 2007b]. Its age and spin-down luminosity are found to be 17 kyr and 3.38×10^{36} erg/s, respectively [Abdo et al., 2009c]. It is possible that a single accelerator cannot power the entire multi-TeV source. Following this, the massive star-forming region associated with the HII region *Sharpless* 104 (*Sh* 2-104) was suggested to contribute to the VHE γ-ray emission through wind collisions or interactions of protostar jets with the surrounding medium [Torres et al., 2004]. In addition, particle acceleration in shocks driven by winds from Wolf-Rayet stars in the young cluster Ber87 in the Cygnus OB1 association was also proposed as origin of the VHE γ-rays [Bednarek, 2007].

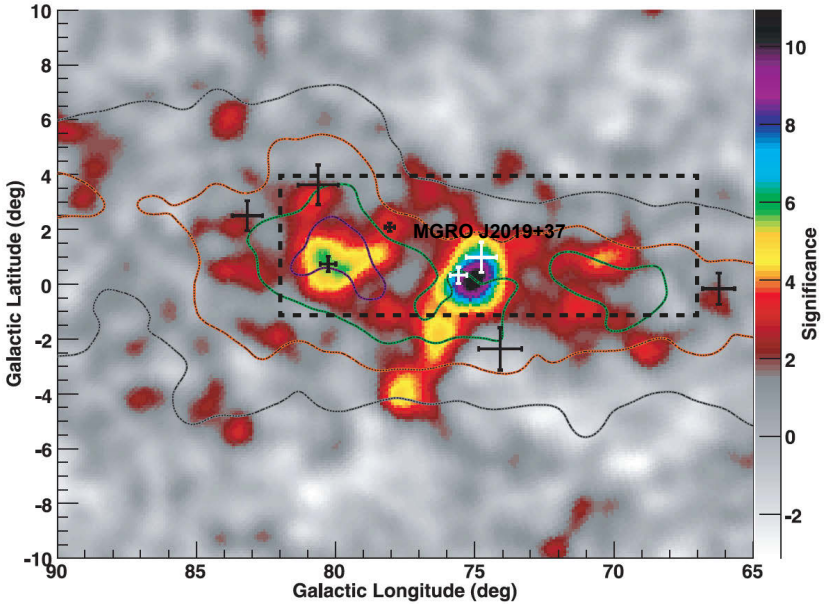

Figure 5.4: Cygnus region as seen by the *Milagro* experiment. The contours show the matter density in this region and the crosses present the position of *EGRET* sources with their corresponding uncertainties. The black dashed rectangle shows the region of the *VERITAS* sky survey of the Cygnus region. Figure adapted from Abdo et al. [2007a].

Having introduced the Cygnus region, including its extensive multiwavelength observations ranging from the radio to the VHE γ-ray regime, the following chapter focuses on the analysis of observations of it taken by *VERITAS*. The survey observations and the dedicated follow-up observations were analysed separately before. In this thesis, a combined analysis of the full dataset is performed. The larger amount of data, comprising about 295 h, allows to investigate the emission of VHE γ-rays from this region in greater detail. To understand the underlying physical processes in this region, it is important to study their individual astrophysical objects. Thus, a systematic study of these objects is performed using the multivariate analysis method presented in Chapter 4.

6

VHE γ-ray observations of the Cygnus region with *VERITAS*

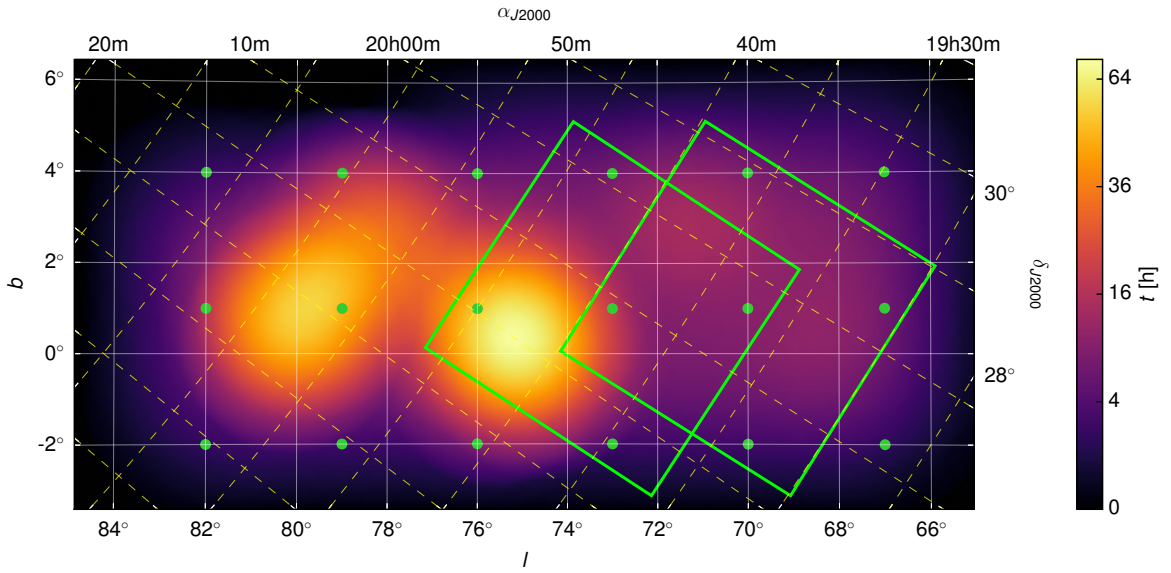

Figure 6.1: The region of the Cygnus sky survey in Galactic (longitude, l, and latitude, b) and equatorial (right ascension, α_{J2000}, and declination, δ_{J2000}) coordinates. The green points represent the central positions of the fields, used for the analysis with the *eventDisplay* package version `v480b`. Two fields are shown as green squares and each field has a size of $6° \times 6°$ in equatorial coordinates. The colour scale represents the acceptance-corrected, accumulated observation time, t.

The *VERITAS* sky survey of the Cygnus region took place between April 2007 and October 2008 and spanned an area from 67° to 82° in Galactic longitude and from $-1°$ to 4° in Galactic latitude. Runs were taken at pointed positions with a spacing of 0.8° in longitudinal and 1° in latitudinal direction. An exposure time of approximately one hour per grid point was taken, where each hour was broken into observation runs of 20 min each. The base survey resulted in a relative uniform exposure of about 6 h.

Runs were selected based on weather and hardware conditions. About 130 h of quality-selected data were taken in survey mode. An additional 165 h were taken to follow-up. In total, about

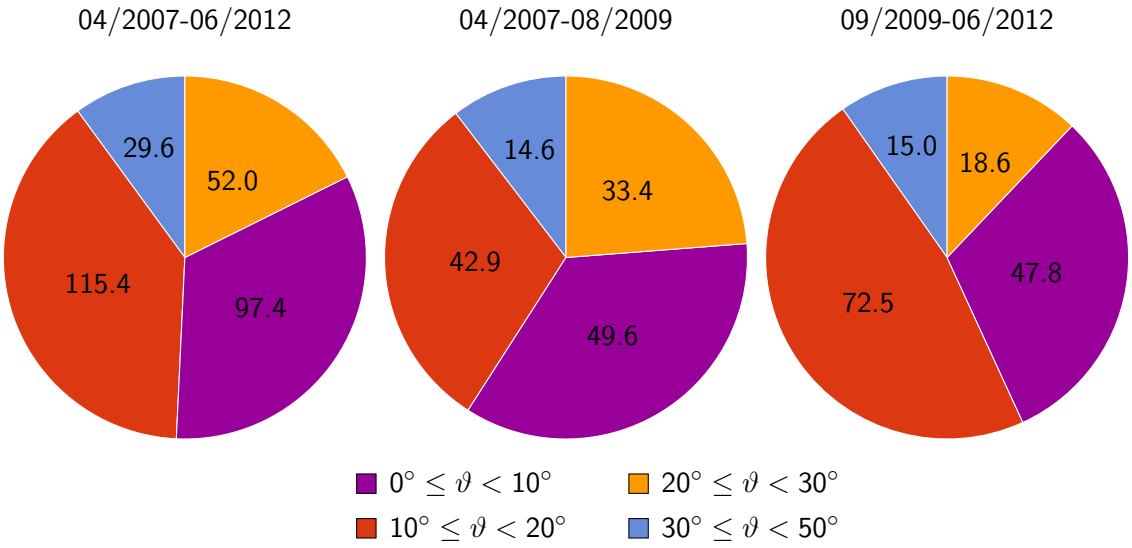

Figure 6.2: Distribution of observation time in hours for different periods of time and different ranges of zenith angle, ϑ. *Left:* Full dataset containing observations from 04/2007 to 06/2012. *Middle:* Observations taken with the V4 array configuration of *VERITAS* (04/2007 to 08/2009). *Right:* Observations taken with the V5 array configuration of *VERITAS* (09/2009-06/2012).

295 h of observations were taken within the area of the sky survey, 273 h of which classified as good quality. Figure 6.1 shows the exposure time spent on the Cygnus region. The regions of enhanced exposure are due to follow-up targeted observations.

Figure 6.2 shows the distributions of zenith angle for the whole dataset dependent on array configuration. To conduct observations with the best performance of the instrument, the observations have to be carried out close to zenith. However, depending on the declination of the region of interest, the culmination of the Cygnus region occurs at the *VERITAS* site at larger zenith angles. The mean zenith angle of all observations is 20°. From the total ∼295 h of observation time, ∼141 h (47.7 %) were taken with the V4 array configuration from 2007 until summer 2009, whereas ∼154 h (52.3 %) of observations were conducted with the V5 array configuration after telescope T1 was moved. The majority of the runs were conducted at low zenith angles (ϑ<20°), covering ∼213 h of the total observing time.

The much larger *VERITAS* dataset that is now available from the Cygnus region and the improved analysis methods dedicated to the detection of faint γ-ray emission allow us to reconsider the characterisation of this emission in the Cygnus region.

6.1 Survey analysis

The *VERITAS* sky survey of the Cygnus region yielded a large amount of data, about 295 h, taken in 945 separate runs spanning five observing seasons from 2007 to 2012. The dataset contains observations taken with three and four telescopes of *VERITAS*. In combination with the distribution of observations over a large area on the sky, the analysis gets very complex. For this purpose, an analysis chain was developed, as described in the following, which can be separated between run-wise operations and the combination of their results afterwards.

6.1.1 Division of the survey region

In order to analyse a large region of the sky with the size of this survey, the region was divided into different fields. For this, the extension of the exposure map analysis as shown in Figure 6.1 is used. The field was divided into 18 regions. The distance of the central position of two maps was set to 3° in longitudinal and latitudinal direction, respectively. As the results are presented in equatorial coordinates, the central positions of each field were converted into right ascension, α_{J2000}, and declination, δ_{J2000}. They are listed together with the corresponding Galactic coordinates in Table B.1. Each field spanned an area of 3°×3°. Therefore, the fields overlap to ensure that no gaps are present when analysing the survey region.

6.1.2 Processing of individual observations

For each field, individual runs were analysed with the raw counts map centred on the central position of the corresponding field. These maps contain all events passing the event selection cuts and have a bin size of 0.025°. This is significantly smaller than the PSF of the *VERITAS* instrument (Section 4.5.1) but large enough to reduce the trial factor of the analysis, as described in detail below. For γ/hadron cuts, moderate and hard T selection cuts (Chapter 4) were used. This was chosen apriori based on the average spectral index of VHE γ-ray sources in the Galactic plane reported by Wakely and Horan [2016], as shown in Figure 6.3(a). The average index is found to be about 2.4. This was confirmed by the *H.E.S.S.* and the *Milagro* sky survey [Aharonian et al., 2006a; Abdo et al., 2007b]. For each grid point in the scan region, the number of signal events in the ON region, N_{ON}, was calculated by summing all events within a circle of radius $\theta_{int} = 0.09°$ for the search of point sources and $\theta_{int} = 0.22°$ for the search of slightly extended sources. These cuts were selected based on the angular resolution of *VERITAS*. The cut for extended-source searches was chosen apriori and is optimal for the detection of γ-ray sources with average size of Galactic SNRs [Green, 2014] of about 0.2°, as shown in Figure 6.3(b). The background level, N_{OFF}, was estimated by using the ring background model, as described in Section 3.3.6. This method was chosen as the exposure of the field of view is not the same at each point and thus, the

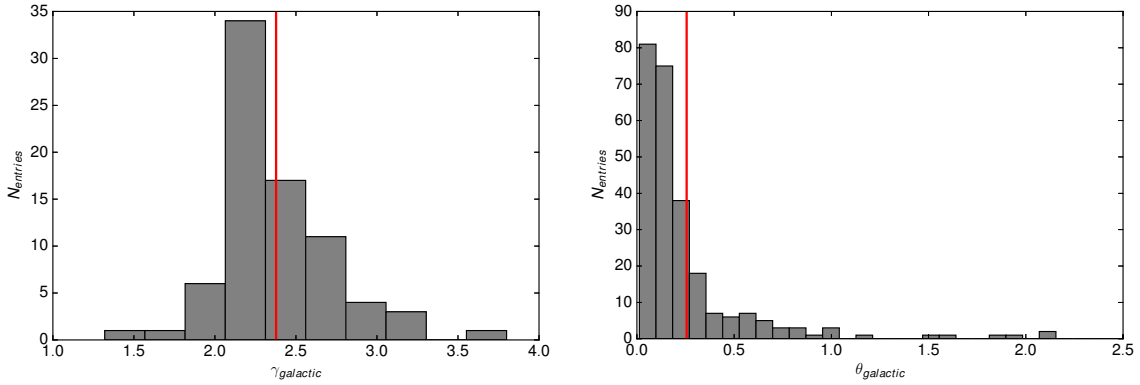

(a) (b)

Figure 6.3: *(a)* Distribution of spectral indices $\gamma_{galactic}$, as listed in Wakely and Horan [2016]. The red line presents the average spectral index of about 2.4. *(b)* Extension of Galactic SNRs $\theta_{galactic}$, as listed in Green [2014]. The red line presents the average size of Galactic SNRs and is about 0.2°.

analysis set	θ_{int}	θ^2_{int}	r	r_w	r_{in}	r_{out}	κ
point	0.09°	$0.008^{\circ 2}$	0.6°	0.13°	0.53°	0.67°	20
extended	0.22°	$0.050^{\circ 2}$	0.825°	0.35°	0.65°	1.00°	11.55

Table 6.1: Analysis parameters used to generate the significance maps to search for VHE γ-ray sources. The radius of the ON region is denoted by θ_{int}, r denotes the mean radius of the ring from which the background level is estimated. The width of the ring, the inner, and the outer ring radius are indicated as r_w, r_{in}, and r_{out}, respectively. The ratio of the area between the OFF and the ON region is denoted by κ.

reflected region method, used for the estimation of the background to compute the significance, is inappropriate. The parameters used to estimate the background level are summarised in Table 6.1. The ring radius of 0.6°, used for the search of point sources, was increased to 0.825° for the search of extended sources and the ratio of the area set to 11.55 apriori to avoid overlapping of the ON and OFF region for the extended-source search. Because each grid point inside the ring lies at a different distance from the centre of the camera, it is necessary to take the response of the camera into account. The correction factor, α, is computed from the ratio of the area of the ON and the OFF region modified by the camera acceptance, according to Equation 3.7. Images which are too close to the edge of the camera and mostly truncated are removed from the analysis apriori. To avoid systematic effects related to the camera acceptance curve at these larger distances from the camera centre, only events detected within 1.5° of the pointing direction of the instrument are considered. The acceptance maps are filled by rotating a one-dimensional acceptance template around the observing position (Figure 3.10). The template was obtained from survey runs taken

with all four telescopes binned in zenith angle ranges from 0° to 20°, 20° to 30°, and 30° to 40°. The acceptance map therefore contains similar zenith and azimuth angles, and NSB levels as the observing runs. In addition, a fourth map is generated indicating the positions and extension of known VHE γ-ray sources and stars with magnitude in the visual band smaller than 6.5. The map is shown in Figure B.1 and excluded stars are listed in Table B.3. This map of exclusion regions is used as a mask and no background estimate is taken from a region marked within the map. From the ON counts (N_{ON}), the background level (N_{OFF}), and the correction factor (α) for each grid point in the map, a statistical significance, S, can be determined according to Equation 3.8. Thus, each grid point is tested for the existence of a γ-ray source at its position, resulting in a significance map.

6.1.3 Combination of individual observations

In the next step, the maps from each individual observation falling into one field of the skymap are added up to large maps encompassing the field. To minimise binning effects during this process, the bin size of the fields is set to the bin size of the run-wise maps (0.025°). The raw counts map, the ON and the OFF region are merely added. However, the correction factor has to be scaled to account for different times of observation,

$$\alpha_{\mathrm{norm}} = \frac{\alpha_{\mathrm{ON}}}{\alpha_{\mathrm{OFF}}} = \frac{\sum_{i=1}^{N_{obs}} \frac{\alpha_i}{1+\alpha_i} \left(\sum_{i=1}^{N_{obs}} N_{\mathrm{ON}\,i} + \sum_{i=1}^{N_{obs}} N_{\mathrm{OFF}\,i} \right)}{\sum_{i=1}^{N_{obs}} \frac{1}{1+\alpha_i} \left(\sum_{i=1}^{N_{obs}} N_{\mathrm{ON}\,i} + \sum_{i=1}^{N_{obs}} N_{\mathrm{OFF}\,i} \right)} = \frac{\sum_{i=1}^{N_{obs}} \frac{\alpha_i}{1+\alpha_i} \left(N_{\mathrm{ON}\,i} + N_{\mathrm{OFF}\,i} \right)}{\sum_{i=1}^{N_{obs}} \frac{1}{1+\alpha_i} \left(N_{\mathrm{ON}\,i} + N_{\mathrm{OFF}\,i} \right)}, \tag{6.1}$$

where N_{obs} denotes the total number of combined observations. Following this, the significance is calculated according to Equation 3.9 with the correction factor as given above.

6.1.4 Trial factor

The analysis of the survey region was done during a blind-search for the presence of a γ-ray signal over cosmic-ray background at any location in the region. Thus, a large number of statistical trials, X_T, is introduced. The significance S as stated in the maps shown in Figure 6.8 and Figure 6.9 denotes the probability p_{pre} before accounting for these trials. In the absence of signal, the significance follows a normal distribution with p given as

$$p = \frac{1}{\sqrt{2\pi}} \int_{-\infty}^{S} \exp\left(-\frac{x^2}{2}\right) \mathrm{d}x. \tag{6.2}$$

Assuming the hypothesis that no γ-ray signal is present, each location in the map is tested using the ring background model (Section 3.3.6). As each position on the sky is tested across the entire observation region, the likeliness of measuring an upward fluctuation with high statistical significance increases. Since the significance maps contain a large number of test positions, the significance has to be corrected by a trial factor, X_T [Gross and Vitells, 2010]. The statistical significance of measurement before any adjustment is known as *pre-trial* significance, S_{pre}, and with the adjusted significances as *post-trial* significance, S_{post}. Following the approach from Gross and Vitells [2010], the probability, p_{post} of finding a signal with a *post-trial* significance, S_{post}, can be determined by

$$p_{post} = X_T \cdot p_{pre}, \tag{6.3}$$

where p_{pre} denotes the probability of finding a signal with a *pre-trial* significance, S_{pre} at any location in the survey area. Following the approach from Ward [2010], an expression for the trial factor is found by describing the search for a γ-ray like signal as a simple failure/success test at each position in the sky [Leo, 1994], where the probability is distributed according to the Binomial probability function

$$p_n = \frac{N!}{n!(N-n)!} p_{pre}^n (1-p_{pre})^{N-n}. \tag{6.4}$$

The quantity p_n denotes the probability of observing n successes in N attempts. Following this, the probability of observing more than n successes in N attempts, $p_{n\geq 1}$, is given by

$$p_{post} := p_{n\geq 1} = \sum_{n=1}^{N} \frac{N!}{n!(N-n)!} p_{pre}^n (1-p_{pre})^{N-n} = 1-(1-p_{pre})^N. \tag{6.5}$$

For larger values of N, meaning more trials, the likeliness of observing this success increases. From Equation 6.3 and Equation 6.5, the trial factor, X_T, can be calculated by

$$X_T = \frac{p_{post}}{p_{pre}} = \frac{1-(1-p_{pre})^N}{p_{pre}}. \tag{6.6}$$

It follows from this equation and first order Taylor series that for small probabilities, p_{pre}, and uncorrelated grid points in the map, the trial factor X_T would be exactly equal to the number of tested positions (= number of bins in skymap). However, in the analysis presented here the significances are correlated by the ON region through the summation of events within the θ_{int}^2 circle and by the background determination using the OFF region through the summation within the ring, as illustrated in Figure 6.4. Therefore, it is not possible to derive the correct trial factor analytically. It is evident that the trial factor must be between the most optimistic value, $X_{T,min}$, determined by how many times the θ_{int}^2 circle fits into the survey region and the most conservative approach, $X_{T,max}$, determined by the number of trial positions. For analyses using the integration radius suitable for a point-source search ($\theta_{int} = 0.09$), $X_{T,min}$ is approximately 7860, while for an extended-source search ($\theta_{int} = 0.22$), $X_{T,min}$ is about 1270. The trial factor

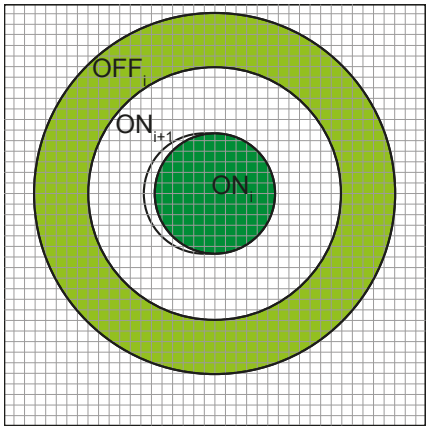

Figure 6.4: Schematic description of the correlation between adjacent grid points. The light-grey squares show the grid positions, the two circles show two adjacent ON regions and the light-green ring shows the background region for the dark-green ON regions. Thus, the significances calculated for neighbouring grid positions are highly correlated.

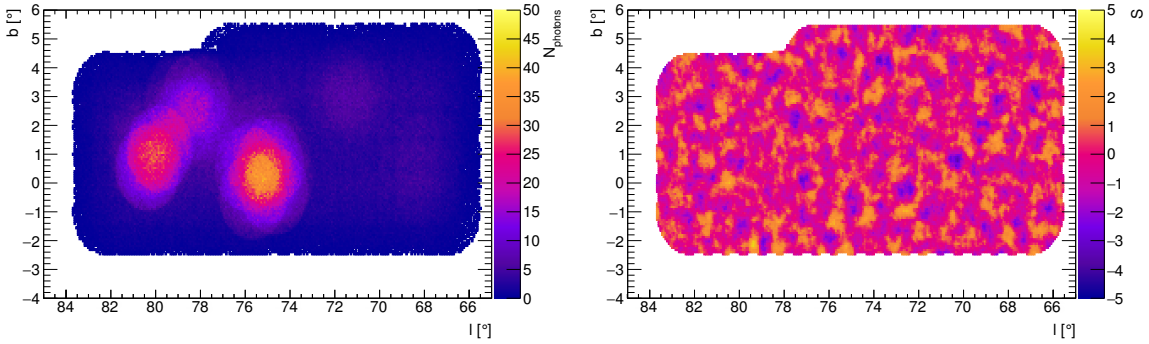

Figure 6.5: Pseudo-random raw γ-ray counts ($N_{photons}$) map and significance (S) map obtained from the MC simulations. A region of $20^\circ \times 10^\circ$ in Galactic coordinates was simulated with a grid size of $0.025^\circ \times 0.025^\circ$.

was estimated using MC simulations of the *VERITAS* survey observations. For each simulation a ring background analysis of the dataset was performed. A pseudo-random raw γ-ray counts map of the Cygnus region was sampled based on the acceptance curve, exposure time, and number of events obtained from the original raw counts map. The acceptance map was produced from data. Each map spanned an area of 20° in Galactic longitude and 10° in Galactic latitude, covering the whole survey region, divided into bins of size $0.025^\circ \times 0.025^\circ$. Thus, the maximum value of the trial factor, $X_{\mathcal{T},max}$, is 320000. No sources of γ-rays were simulated in this MC campaign. An analysis using the ring background model was carried out on this map and simulated significance maps were generated, as shown in Figure 6.5. The process was repeated 1.5×10^6 times for both point and extended analyses. After each simulation, the significance value of a fixed reference bin in the skymap and the maximum significance value located anywhere within the entire search

region were recorded. These distributions are shown in Figure 6.6. In case of the random-bin distribution, this fit is described by a Gaussian distribution with mean μ_G and standard deviation σ_G,

$$f_{Gauss}(x, c_G, \sigma_G, \mu_G) = c_G \cdot \frac{1}{\sqrt{2\pi}\sigma_G} \exp\left(-\frac{1}{2}\left(\frac{x-\mu_G}{\sigma_G}\right)^2\right). \tag{6.7}$$

Here, c_G denotes a constant value used for normalisation. The distribution of the significances of the maximum bin is best described by an extreme-value distribution, in this case a modified Gumbel function is used, with the location parameter μ_M, the scale parameter β_M, and a constant c_M given as

$$f_{Gumbel}(x^2, c_M, \beta_M, \mu_M) = \frac{c_M}{\beta_M} \cdot \exp\left(-\frac{x^2-\mu_M}{\beta_M}\right) \cdot \exp\left(-\exp\left(-\frac{x^2-\mu_M}{\beta_M}\right)\right). \tag{6.8}$$

The results of the fit are listed in Table 6.2. The cumulative probability details the right-sided probabilities for both distributions with increasing significance, S. These probabilities were calculated by integrating the fits of the distribution using

$$F_{CDF}(x) = \int_{x_0}^{\infty} f(x)dx, \tag{6.9}$$

where $f(x)$ is either the distribution described in Equation 6.7 or Equation 6.8. Then, the ratio of the probabilities for both distributions at a specific significance can be calculated, indicating a value for the effective trial factor, X_T (Equation 6.6). Figure 6.7(a) shows the trial factor as a function of pre-trial significance, S_{pre}. As can be seen, the trial factor increases with increasing significance, but it is always significantly smaller than the number of bins in the skymap reflecting the correlation of both the signal, due to the size of the `ON` region relative to the grid spacing, and the background, due to the size of the `OFF` region. The extended-source analysis has a smaller X_T than the point-source analysis reflecting the higher level of correlation of the `ON` region. The dependence of the post-trial significance on the pre-trial significance is shown in Figure 6.7(b). Below a pre-trial significance of about 4.3 the post-trial significance is zero since a fluctuation of this magnitude is expected in every observation. It is essential to note that in this case a pre-trial significance of at least about 7 is necessary to obtain a significant detection post-trial, i.e. $S_{post} > 5$. If an agglomeration of bins exceeds 5σ, the detection of a new VHE γ-ray source is regarded as solid.

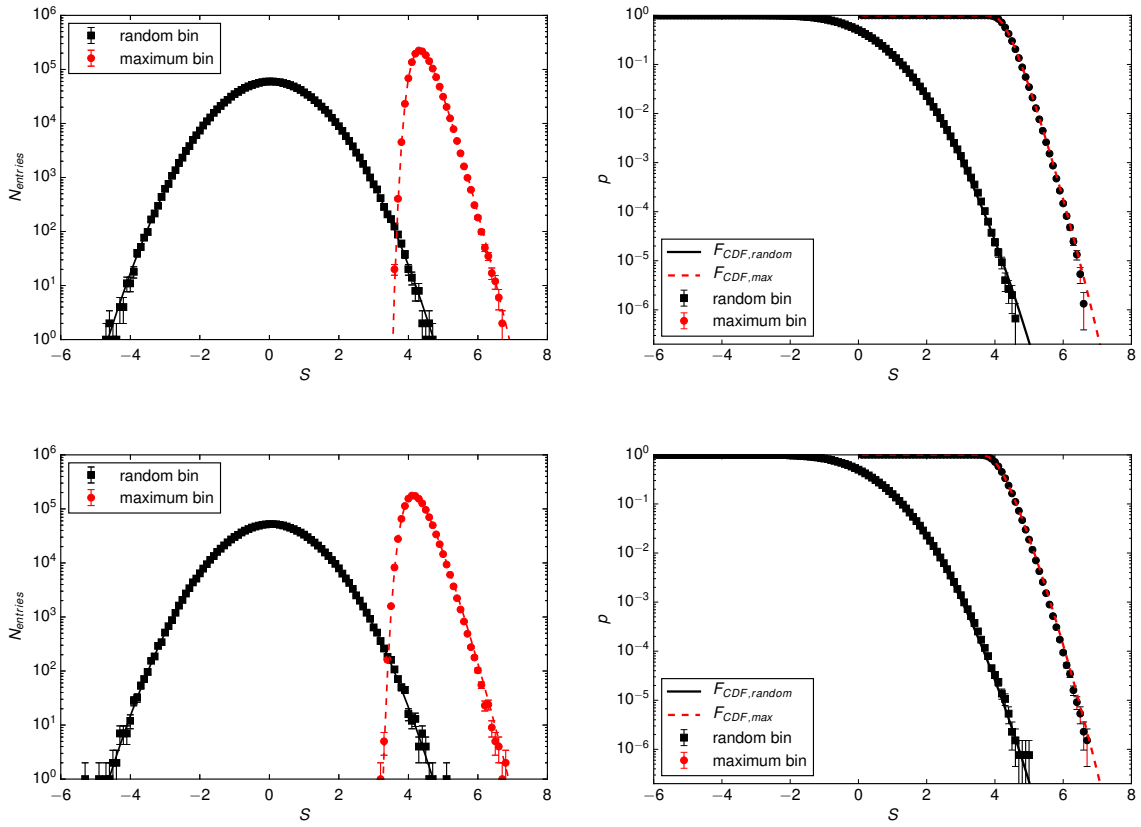

Figure 6.6: *Left:* Distributions of significances, S, for MC simulations of the survey from the maximum (red, circles) and random (black, squares) bin for both point (top) and extended (bottom) source analyses. The black solid line represents the Gaussian fit (Equation 6.7), the red dashed line the fit to the distribution of the maximum bin (Equation 6.8). *Right:* The cumulative probability, p, curves as calculated from the distributions of the significances using Equation 6.9.

	point source	extended source
random bin	$c_G = 1.499 \times 10^5 \pm 54$ $\sigma_G = 0.9996 \pm 4 \times 10^{-4}$ $\mu_G = 4.27 \times 10^{-2} \pm 4 \times 10^{-4}$	$c_G = 1.312 \times 10^5 \pm 50$ $\sigma_G = 1.007 \pm 4 \times 10^{-4}$ $\mu_G = 4.80 \times 10^{-4} \pm 4 \times 10^{-4}$
maximum bin	$c_M = 1.332 \times 10^6 \pm 765$ $\beta_M = 2.180 \pm 0.001$ $\mu_M = 18.682 \pm 0.001$	$c_M = 1.120 \times 10^6 \pm 1110$ $\beta_M = 2.317 \pm 0.003$ $\mu_M = 17.103 \pm 0.003$

Table 6.2: The fit results to the distributions of significances from the survey simulations for point and extended analyses. The formulas describing the distribution of the random and the maximum bin are given in Equation 6.7 and Equation 6.8, respectively.

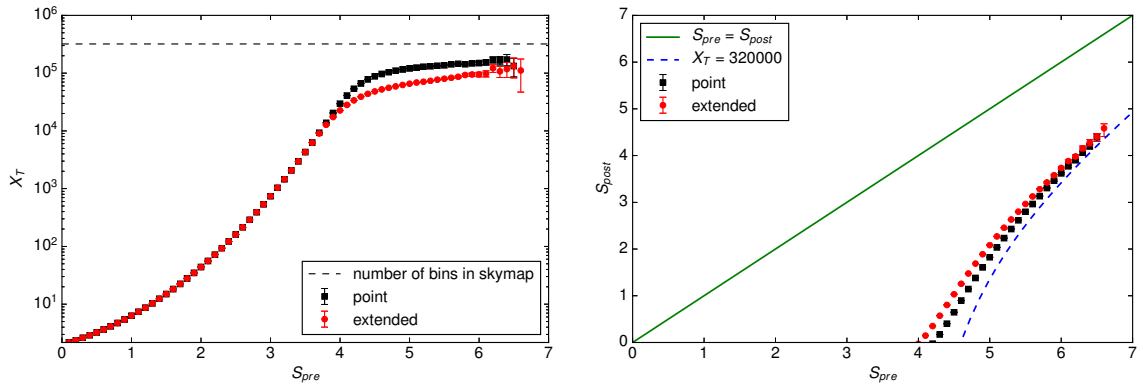

(a) (b)

Figure 6.7: *(a)* Trial factor, X_T, as a function of pre-trial significance, S_{pre}, for point (black, squares) and extended (red, circles) source analyses. The black dashed line presents the total number of bins in the skymap of the whole Cygnus region observed with *VERITAS*. *(b)* The post-trial significance, S_{post}, as a function of pre-trial significance, S_{pre}, for point and extended source analyses. The green solid line shows the behaviour in case $S_{pre} = S_{post}$, and the blue dashed line represents the dependency in case of a maximum value of the trial factor of 320000. Below $S_{pre} \approx 4.3$ the post-trial significance is zero, i.e. a fluctuation of this magnitude is expected for every observation.

6.1.5 Estimation of the integral flux

The significance is not a physical quantity of the characteristic of the astrophysical object which can be easily compared to other results. The most interesting measurement is flux, representing the actual brightness of the object and described as the number of photons detected per second and per unit detection area. If no detection above a post-trial significance of 5σ is found, an upper limit on the flux is estimated. To do this, the upper limit on the γ-ray flux from an upper limit of the number of events, a spectral assumption, and an energy range over which the upper limit is calculated, are required. The assumed energy spectrum with an index Γ is expressed as

$$\frac{\mathrm{d}N}{\mathrm{d}E} = N_0 \left(\frac{E}{E_0} \right)^{-\Gamma}, \tag{6.10}$$

where N_0 is the normalisation constant and E_0 a given normalisation energy. Following this, an upper limit on the number of excess events, N^{UL}_{excess}, is determined following the formalism of Rolke et al. [2005] (method 4) at 95 % confidence level. The normalisation of the flux integral, N_0, is then given as

$$N_0 = \frac{N^{UL}_{excess}}{\langle A_{eff} \rangle \cdot t}, \tag{6.11}$$

where $\langle A_{eff} \rangle$ is the average effective γ-ray collection area over the whole range of energy, weighted by the assumed energy spectrum with index Γ. The dead-time corrected time of observation is denoted as t. Then, the integral upper limit on the energy flux, Φ^{UL}, between energies E_{min} and E_{max}, is calculated as

$$\begin{aligned} \Phi^{UL} &= \int_{E_{min}}^{E_{max}} \frac{\mathrm{d}N}{\mathrm{d}E} \mathrm{d}E = \int_{E_{min}}^{E_{max}} N_0 \left(\frac{E}{E_0} \right)^{-\Gamma} \mathrm{d}E \\ &= N_0 \cdot \frac{1}{1-\Gamma} \cdot \frac{1}{E_0^{-\Gamma}} \cdot \left(E_{max}^{-\Gamma+1} - E_{min}^{-\Gamma+1} \right) \\ &= \frac{N_{excess}^{UL}}{\langle A_{eff} \rangle \cdot t} \cdot \frac{1}{1-\Gamma} \cdot \frac{1}{E_0^{-\Gamma}} \cdot \left(E_{max}^{-\Gamma+1} - E_{min}^{-\Gamma+1} \right). \end{aligned} \tag{6.12}$$

6.2 Results of the sky survey analysis

The data were taken with observations targeted on a grid pattern which are necessary to cover the whole sky survey region. The significance maps obtained for each field using the ring background model are presented in this section. For each field, the distribution of significances from each map was plotted in a one-dimensional histogram and known VHE γ-ray emitters and bright stars were removed in an attempt to discover additional sources. In the presence of a new source in the survey area, an excess towards high significances is expected. In the absence of a new source, the distribution is expected to follow a normal distribution with mean $\mu = 0$ and standard deviation $\sigma = 1$.

Where possible, the reconstructed differential energy spectra are fitted with a power law and the resulting index is compared to previous measurements. The spectral analysis was conducted using the reflected region model negating the requirement for a correction due to the camera acceptance. As the latter varies with energy, the reflected region method is the preferred method for spectral analyses. In order to evaluate all possible counterparts to the observed sources, some of the significance maps derived here are overlaid with measurements from other instruments at various wavelengths. The combination of the individual studies for each object should lead to a better understanding of the nature of these objects.

In addition, other candidate VHE γ-ray sources in the Cygnus region are investigated and upper limits on their VHE γ-ray flux are derived.

6.2.1 Source detection

The significance maps for each field of the Cygnus sky survey obtained using hard cuts are shown in Figure 6.8 and Figure 6.9. The maps are produced with the parameter sets listed in Table 6.1.

For visibility, the colour scale was saturated at 7σ (pre-trial), which corresponds to about 5σ post-trial. The maps produced with moderate cuts can be found in Section B.4.

It should be noted that the S values in these maps are significances before accounting for the trial factor. The examination of the maps clearly show four locations of relatively strong γ-ray excess which exist at varying levels of positive significance. These correspond to the objects discussed in Chapter 5, VER J2031+415, VER J2019+407, VER J2019+368, and VER J2016+371. The significance maps have been searched for further candidate sources of γ-rays requiring a minimum significance of 6.8σ, corresponding to 5σ after accounting for all trials. No evidence for additional sources above threshold was found. The individual VHE γ-ray sources and other individual regions of interest are addressed in greater detail below.

Figure 6.10 and Figure 6.11 show the histograms of the significances of the maps generated with hard T cuts. In each figure, the green histogram represents the distribution of the significances without any source exclusion. The cyan histogram shows the distribution after removal of known VHE γ-ray emitters and bright stars. The resulting distributions are consistent with a pure background model in all regions. Each histogram is fitted with a normal distribution and no significant deviations between the data and the fit are observed, indicating that there are no additional bright sources.

In order to confirm the results presented here, an independent secondary analysis was conducted with the *VEGAS* software package [Cogan, 2007] as part of an ongoing analysis [VERITAS collaboration, in preparation]. The resulting significance map of this analysis is shown in Figure 6.12.

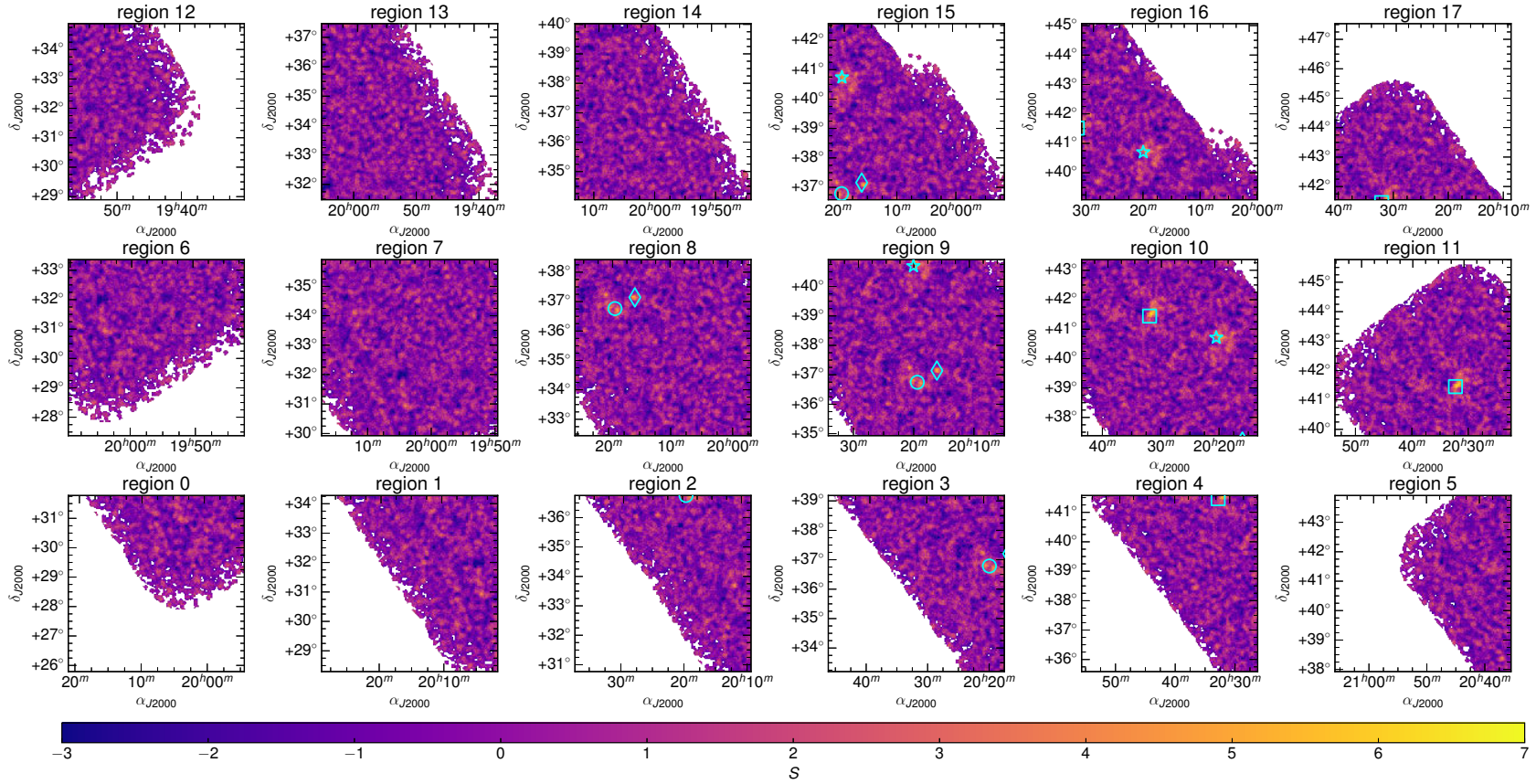

Figure 6.8: Significance maps of the *VERITAS* Cygnus sky survey region for the search of point sources. The counts of the ON region are summed from a circle of radius $\theta_{int} = 0.09^\circ$ around each bin. The γ/hadron separation was done using hard T cuts. The colour scale is saturated at 7σ for visibility. The following objects are also plotted: VER J2031+415 (square), VER J2019+407 (star), VER J2016+371 (diamond), VER J2019+368 (circle).

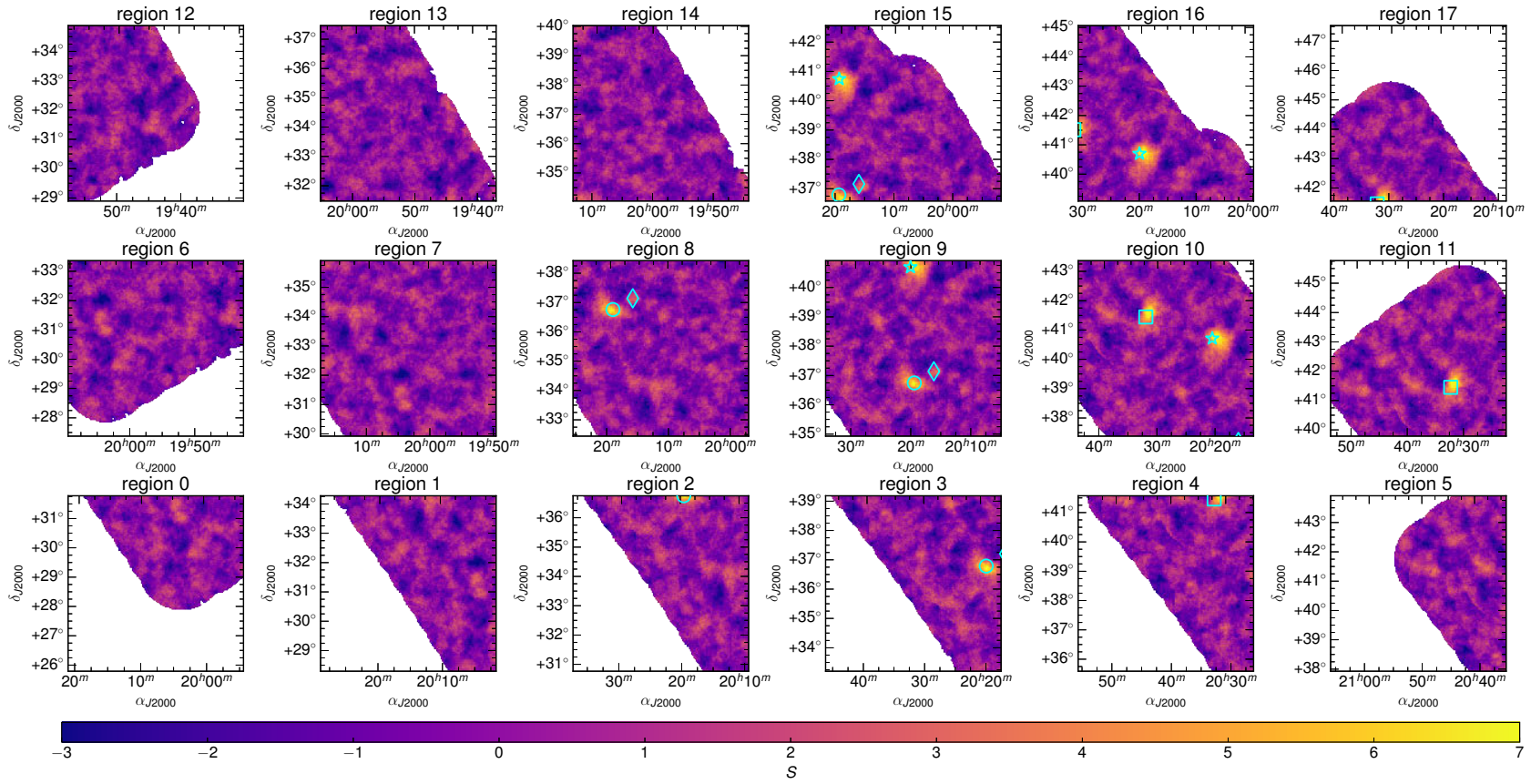

Figure 6.9: Significance maps of the *VERITAS* Cygnus sky survey region for the search of extended sources. The counts of the ON region are summed from a circle of radius $\theta_{int} = 0.22^{\circ}$ around each bin. The γ/hadron separation was done using hard T cuts. The colour scale is saturated at 7σ for visibility. The following objects are also plotted: VER J2031+415 (square), VER J2019+407 (star), VER J2016+371 (diamond), VER J2019+368 (circle).

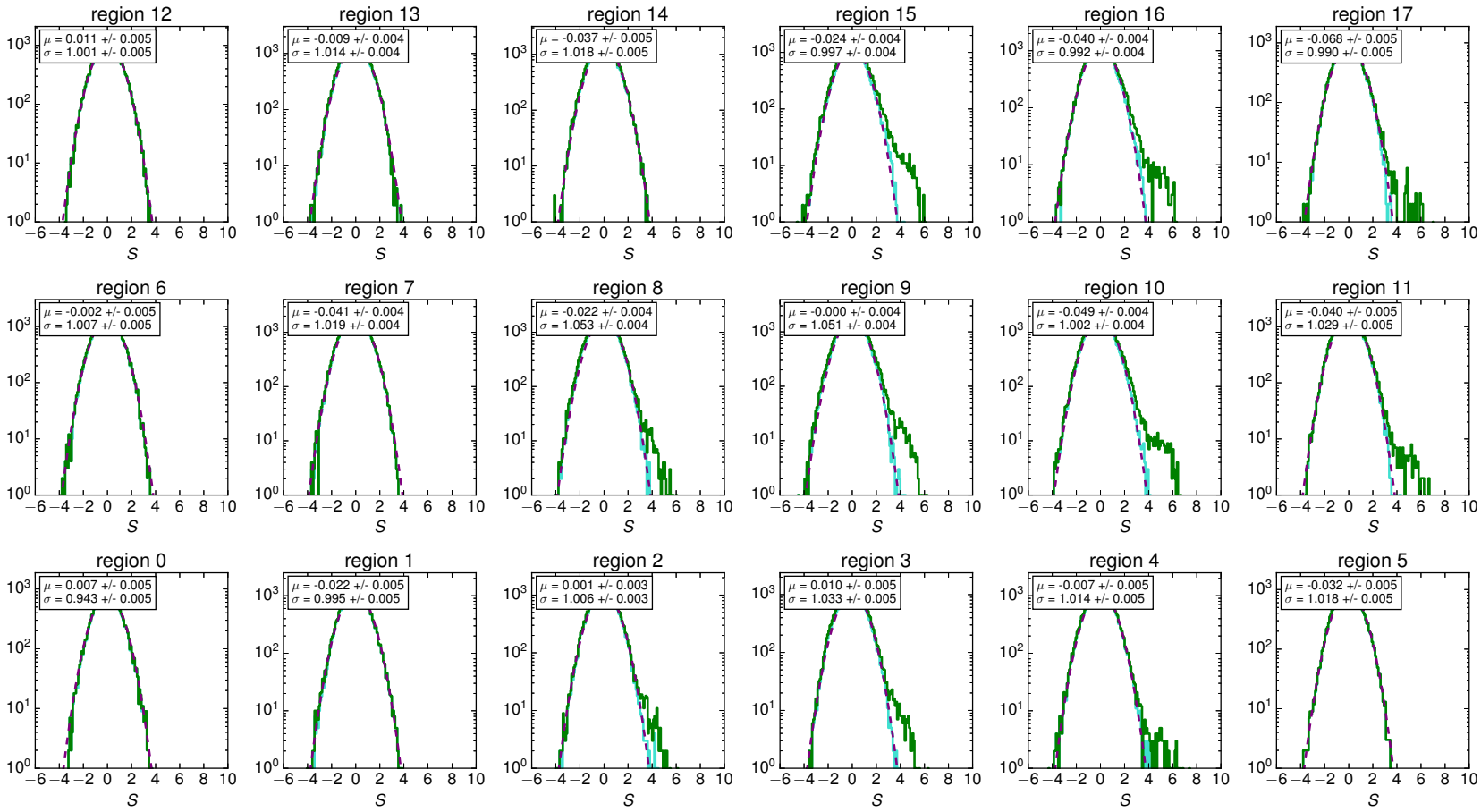

Figure 6.10: Distributions of the significances, S, of the bins. The eighteen histograms correspond to each region of Figure 6.8 generated with hard cuts and an integration radius of $\theta_{int} = 0.09°$. The green histogram represents the distribution of the significances without any exclusion regions. The cyan histogram shows the distribution after removal of known VHE γ-ray emitters and bright stars with a magnitude in the visual band smaller than 6.5 (Section B.2). The dashed magenta line shows the fit of the latter histogram with a normal distribution of mean μ and standard deviation σ, denoted in the upper left box of each canvas.

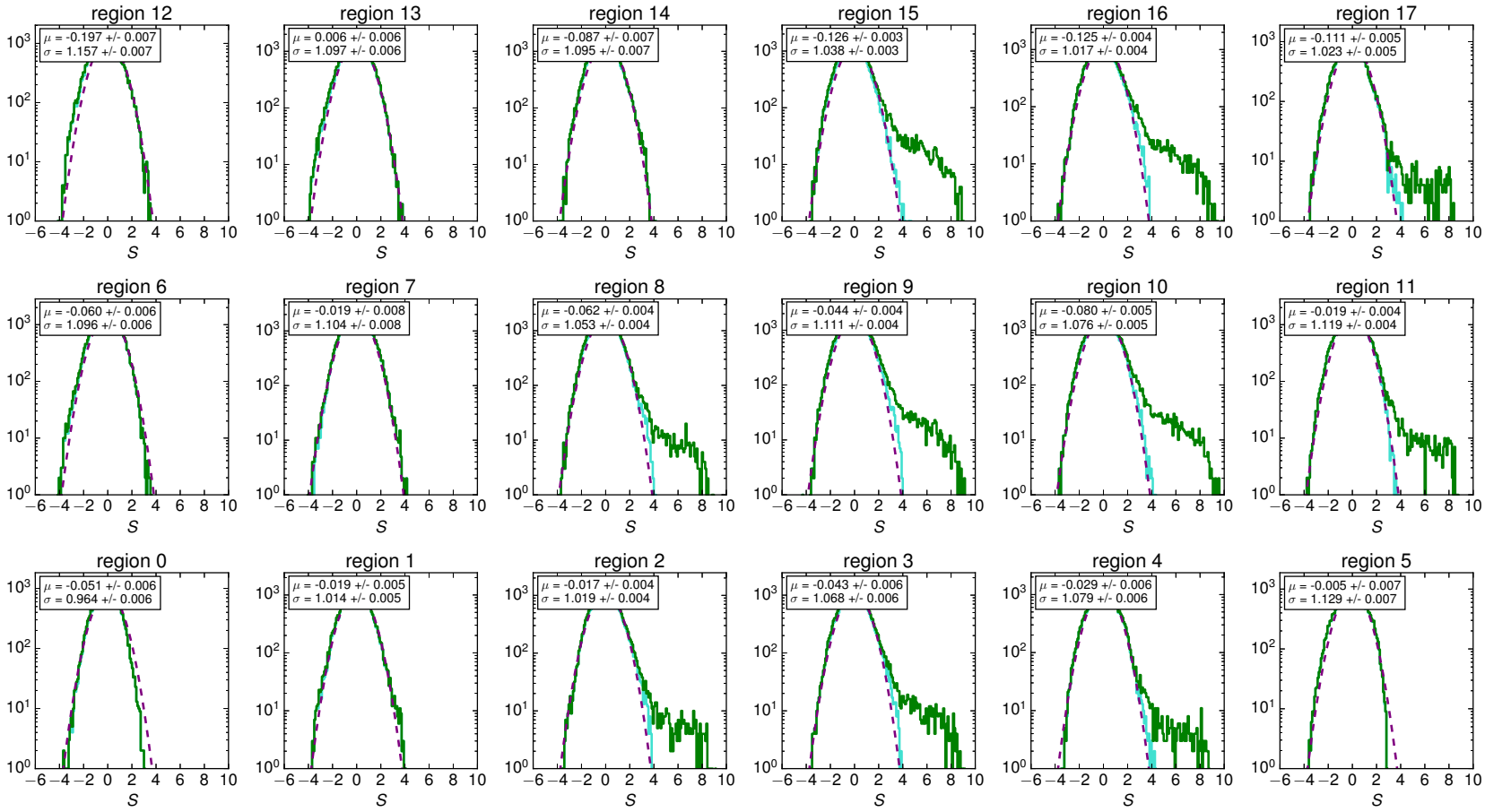

Figure 6.11: Distributions of the significances, S, of the bins. The eighteen histograms correspond to each region of Figure 6.8 generated with hard cuts and an integration radius of $\theta_{int} = 0.22°$. The green histogram represents the distribution of the significances without any exclusion regions. The cyan histogram shows the distribution after removal of known VHE γ-ray emitters and bright stars with a magnitude in the visual band smaller than 6.5 (Section B.2).The dashed magenta line shows the fit of the latter histogram with a normal distribution of mean μ and standard deviation σ, denoted in the upper left box of each canvas.

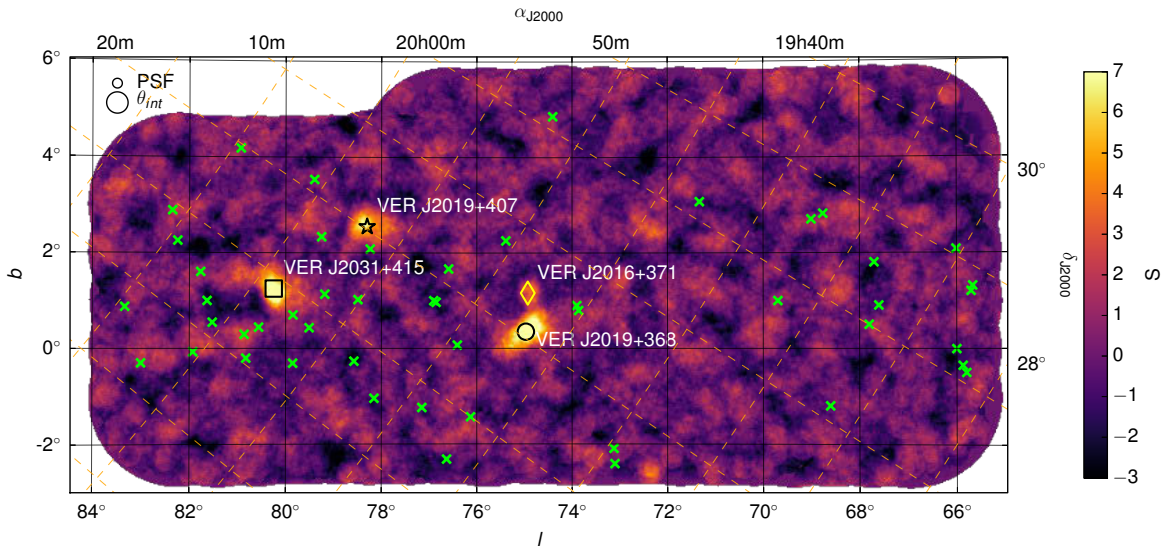

Figure 6.12: The region of the Cygnus sky survey in Galactic (longitude, l, and latitude, b) and equatorial (right ascension, α_{J2000}, and declination, δ_{J2000}) coordinates using the second analysis package, *VEGAS* [Cogan, 2007]. The colour scale is saturated at 7σ for visibility. The green crosses show the positions of the objects considered for the search of VHE γ-ray emission (Section 6.2.5). The following objects are also plotted: VER J2031+415 (square), VER J2019+407 (star), VER J2016+371 (diamond), VER J2019+368 (circle).

6.2.2 The region of VER J2031+415

The analysis of VER J2031+415 associated with the first unidentified VHE γ-ray source TeV J2032+4130, observed for about 61.1 h (dead-time corrected) at an average zenith angle of 18.5° resulted in 1086 events recorded in the source region and 7119 events in the selected background region. This yields a peak-significance of 8.6σ using the integration radius optimised for the search of an extended source, $\theta_{int} = 0.22°$. Figure 6.13(a) shows the significance map obtained with a PSF for the analysis of 0.08°. The map is smoothed with a two-dimensional top-hat function of radius 0.22° in order to reduce statistical fluctuations. In addition, the significance contours of MGRO J2031+41 [Abdo et al., 2007b] are overlaid on the significance map. The significance distribution is shown in Figure 6.13(b). After removal of the sources, no additional source is observed.

Since the discovery of TeV J2032+4130 by *HEGRA* [Aharonian et al., 2005c], multiple observations were taken in order to identify potential counterparts to this source at other wavelengths. During the large-scale survey of the *Milagro* water Cherenkov detector, an extended source MGRO J2031+41 was detected. The *Milagro* flux was derived over an area of $3° \times 3°$. The object VER J2031+415 was detected using a smaller integration radius of 0.22°. Therefore,

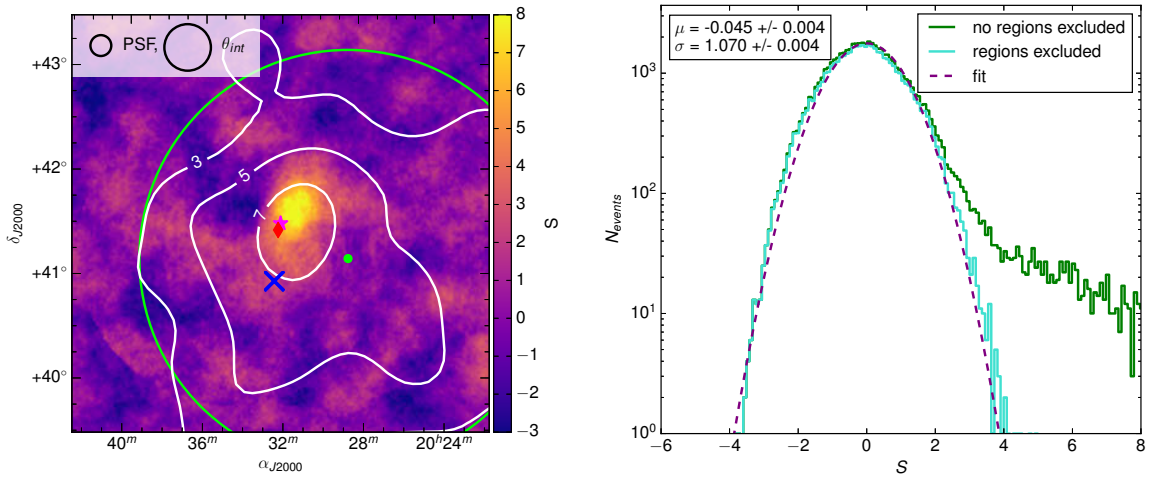

(a) (b)

Figure 6.13: *(a)* VHE γ-ray significance map of the region surrounding VER J2031+415 (magenta star). Overlaid are the *Milagro* [Abdo et al., 2007b] contours of 3, 4, 5, 6, and 7σ. The blue cross represents the location of Cygnus X-3 and the red diamond is the position of 3FGL J2032.2+4126. The centre of the *Fermi*-LAT detection of the Cygnus cocoon is shown as a green circle together with its approximate extension. *(b)* The significance distribution of the results obtained from *VERITAS* before (green) and after (cyan) excluding known VHE γ-ray emitters and stars. The dashed magenta line shows the fit of the latter histogram with a normal distribution of mean μ and standard deviation σ.

MGRO J2031+41 is probably composed of objects other than VER J2031+415, e.g. the extended emission of the Cygnus cocoon measured by *Fermi*-LAT [Ackermann et al., 2011]. In fact, the *ARGO-YBJ* experiment confirmed the measurements from *Milagro* [Bartoli et al., 2012], detecting the source ARGO J2031+4157, which they later identified with the emission of the Cygnus cocoon [Bartoli et al., 2014].

The spectrum obtained from the analysis is shown in Figure 6.14 compared with available measurements from *HEGRA*, *MAGIC*, and *ARGO-YBJ*. The differential energy spectrum is fitted with both a power law, defined in Equation 6.10, and a curved power law given as

$$\frac{\mathrm{d}N}{\mathrm{d}E} = N_0 \left(\frac{E}{E_0} \right)^{-\Gamma+\beta\cdot\frac{E}{E_0}}, \tag{6.13}$$

where Γ denotes the spectral index, N_0 the normalisation, E_0 the normalisation of the energy, and β a parameter describing the curvature of the power law. The parameters obtained from the fit of the power law are $N_0 = (0.54 \pm 0.09_{stat}) \times 10^{-12}/(\mathrm{TeV\,cm^2\,s})$ at 1 TeV and $\Gamma = 2.20 \pm 0.12_{stat}$ with $\chi^2/n_{df} = 6.42/5 = 1.3$. The parameters obtained for the best fit curved power law are

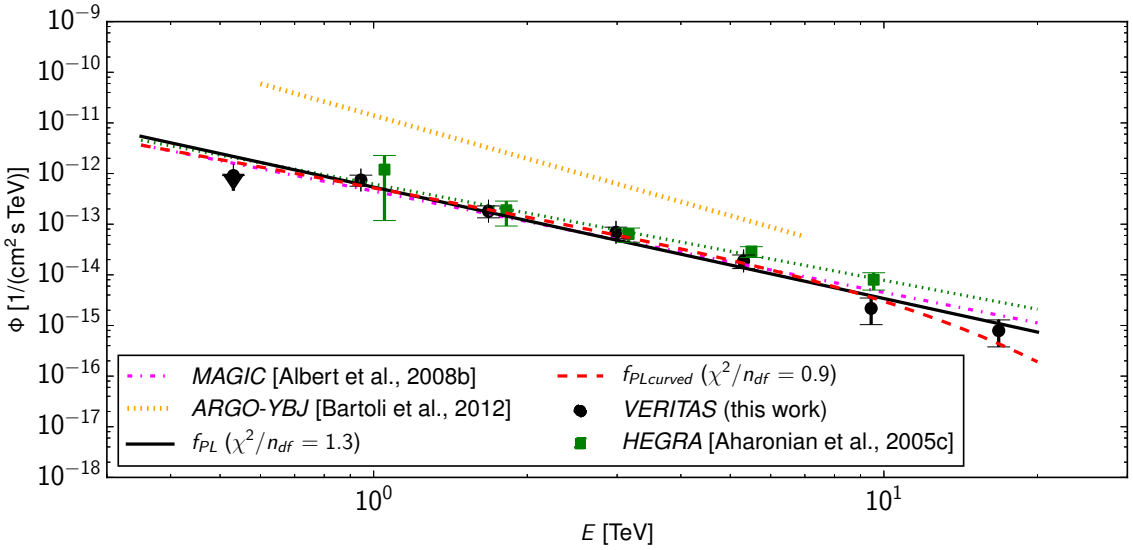

Figure 6.14: Differential energy spectra from sources in the region around VER J2031+415. Black circles represent the results obtained by the *VERITAS* analysis using hard T cuts and the extended integration region ($\theta_{int} = 0.22°$). The black solid line represents the best power-law fit, f_{PL}, and the red dashed line shows the best curved power-law fit, $f_{PLcurved}$. Green squares show the results on TeV J2032+4130 obtained by *HEGRA* [Aharonian et al., 2005c]. The green dotted line is the power-law fit to the *HEGRA* results. The energy spectrum obtained from *MAGIC* [Albert et al., 2008b] (dashed-dotted, magenta) and from *ARGO-YBJ* [Bartoli et al., 2012] (dotted, orange) are also shown. Downward triangles represent upper limits on the flux.

found to be $N_0 = (0.52 \pm 0.10_{stat}) \times 10^{-12}/(\mathrm{TeV\,cm^2\,s})$ at 1 TeV, $\Gamma = 1.84 \pm 0.29_{stat}$, and $\beta = -0.04 \pm 0.03$ with $\chi^2/n_{df} = 3.61/4 = 0.9$. An F-test gives a chance probability of 0.85 (1.44σ) that the curved power law is preferred over the simple power law. It is therefore concluded that the *VERITAS* spectrum above 400 GeV is well described by a power law.

The total integral flux of photons above 600 GeV was derived to be $(1.11 \pm 0.14_{stat}) \times 10^{-12}/(\mathrm{cm^2\,s})$, corresponding to about 2 % of the Crab Nebula flux. The flux values of Figure 6.14 are listed in Table B.4.

The spectral indices derived by both *HEGRA*, and *MAGIC*, and previously by *VERITAS*, are consistent with the one derived here,

- this work: $2.20 \pm 0.12_{stat}$;
- *HEGRA* [Aharonian et al., 2005c]: $1.90 \pm 0.10_{stat}$;
- *MAGIC* [Albert et al., 2008b]: $2.00 \pm 0.30_{stat}$;
- *VERITAS* [Aliu et al., 2014a]: $2.10 \pm 0.14_{stat}$.

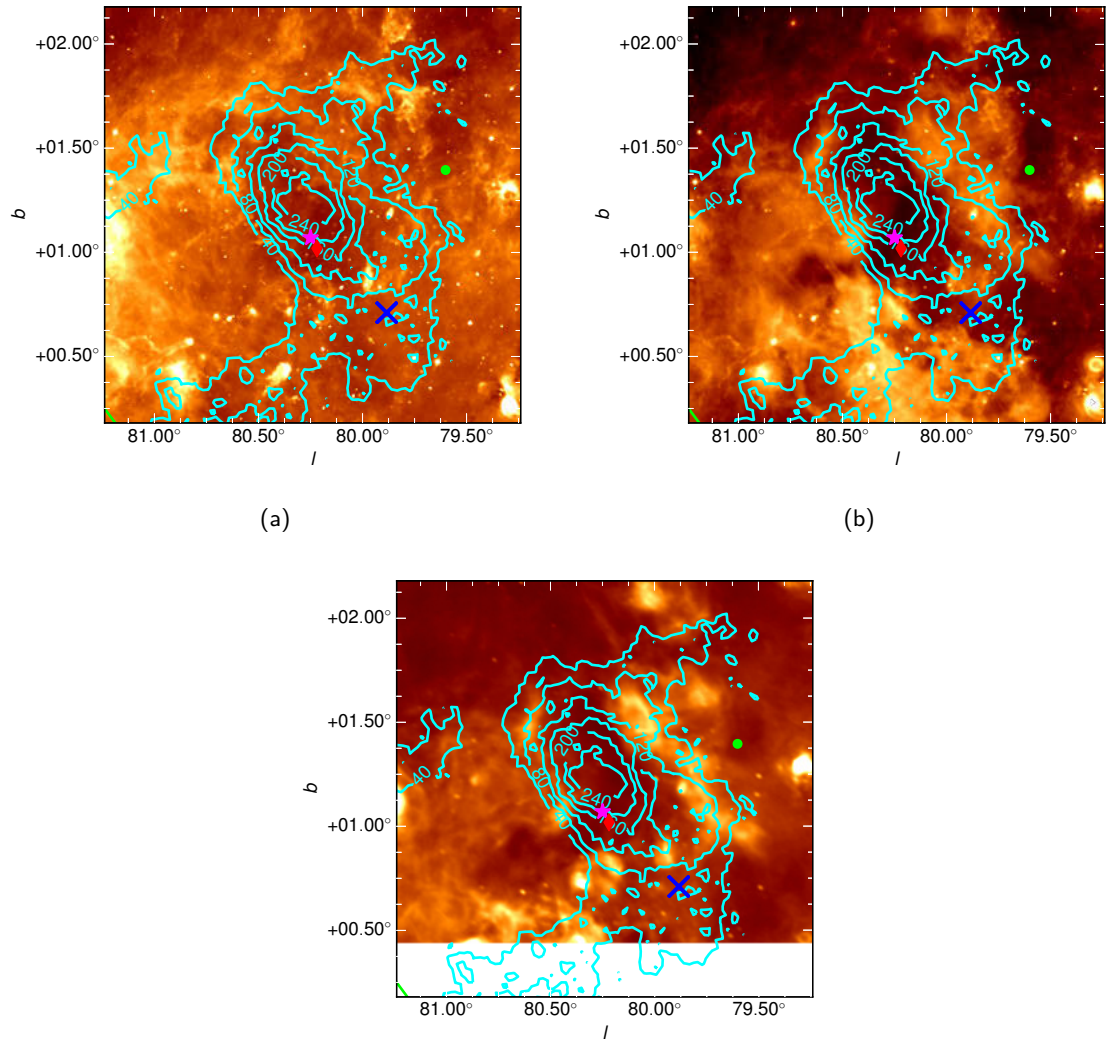

Figure 6.15: VER J2031+415 and its vinicity in infrared and radio wavelengths. *(a) Spitzer* MIPS 24 µm image [Rieke et al., 2004; Beerer et al., 2010]. *(b) Spitzer* IRAC 8 µm image. *(c)* CGPS at 1420 GHz image [Taylor et al., 2003]. All images show the *VERITAS* excess contours at levels of 40, 80, 120, 160, 200, and 240 counts. Also plotted are the objects mentioned in Figure 6.13.

However, the observations obtained by *ARGO-YBJ* resulted in a significantly softer spectral index of 2.60 ± 0.30 [Bartoli et al., 2014]. One has to note that this experiment operates at energies (10^{11}<E<10^{16} eV) comparable to those of existing IACTs, but their measured extension is much larger.

Figure 6.15 shows multiwavelength images of VER J2031+415 and its vicinity. The images are overlaid with the γ-ray excess contours obtained here. The infrared emission of the *Spitzer Space*

Telescope and the radio emission of the CGPS, are dominated by bright diffuse emission, leading to complex structures. The latter is caused by star-forming activity taking place in the complex of Cygnus X.

A number of hypotheses were suggested for the source of the VHE γ-ray emission in the region of the Cygnus OB2 star association. As noted in Aliu et al. [2014a], the γ-ray emission happens to be confined within a rare void surrounded by many massive stars. In particular, there are between 80 and 120 O stars and about 1200 OB star members reported in this region [Knödlseder, 2000; Comerón et al., 2002; Comerón and Pasquali, 2012]. The total mechanical stellar wind energy of $\geq 10^{39}$ erg/s from the Cygnus OB2 association [Lozinskaya et al., 2002] could accelerate Galactic cosmic rays up to 10^{15} eV [Cassé and Paul, 1980; Butt et al., 2003]. This should in turn be enough to power the VHE γ-ray emission.

However, it should be noted that almost all of the massive stars are located outside of the region of γ-ray emission. Aliu et al. [2014a] argue that it is plausible that an explosion of a supernova within the OB2 association and its remnant expand into the surrounding medium. If the supernova occurred about 30 000 yr ago, its shell could have grown much larger and become fainter. Therefore, the VHE γ-ray emission could come from a PWN powered by PSR J2032+4127 with a spin-down luminosity of 2.7×10^{35} erg/s. In this case, a spectral cutoff not too far from 10 TeV should be seen. However, the energy spectrum shown in Figure 6.14 does not indicate a cutoff up to 20 TeV, weakening the argument in favor of a PWN scenario.

Lyne et al. [2015] propose a binary nature of PSR J2032+4127 with a $15 M_{\odot}$ Be star. The authors argue that this object might not be powerful enough to cause the entire VHE γ-ray emission. They note that in case the γ-ray emission resulted from the proper motion of this binary system with an orbital period of about 20 and 30 yr, then the increased age will lead to a smaller transverse velocity of <30 km/s. This is smaller than 51 km/s estimated by Aliu et al. [2014a]. The closest distance between the pulsar and its companion star is expected to occur in end 2017 or early 2018 [Ho et al., 2017; Lyne et al., 2015]. Observations during this period could help to investigate the origin of the γ-ray emission.

6.2.3 The region of γ-Cygni and VER J2019+407

VER J2019+407 was observed for about 37.1 h (dead-time corrected) at an average zenith angle of 24.1°. Its analysis resulted in 729 events recorded in the source region of radius $\theta_{int} = 0.22°$ and 3022 in the selected background region. This yields a significance of 9.7σ at the previously reported *VERITAS* position of VER J2019+407 [Aliu et al., 2013]. Figure 6.16(a) shows the significance map of VER J2019+407 and its vicinity. The γ-ray PSF for the analysis is 0.08° and the map is smoothed with a two-dimensional top-hat function corresponding to the source integration radius of 0.22°. As can be seen, VER J2019+407 is extended beyond the PSF of

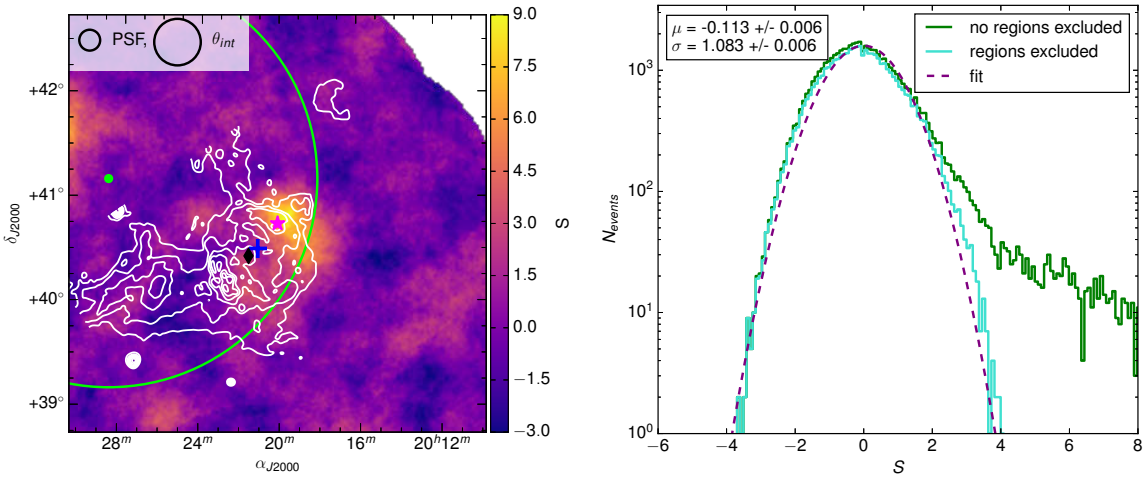

(a) (b)

Figure 6.16: *(a)* VHE γ-ray significance map of the region surrounding VER J2019+407 (magenta star), along with nearby pulsars and SNRs which were considered as possible counterparts. The blue plus-sign marks the location of the *Fermi*-LAT source 3FGL J2021+4031e associated with γ-Cygni and the black diamond is the location of the central γ-ray pulsar PSR J2021+4026. The centre of the *Fermi* detection of the Cygnus cocoon is shown as a green circle together with its approximate extension. The white contours show the radio emission detected from the CGPS at 1420 MHz (with eight logarithmically spaced levels at brightness temperatures from 20 K to 150 K) [Taylor et al., 2003]. The colour scale indicates significances S. *(b)* The significance distribution of the results obtained from *VERITAS* before (green) and after (cyan) excluding known VHE γ-ray emitters and stars. The dashed magenta line shows the fit of the latter histogram with a normal distribution of mean μ and standard deviation σ.

the instrument. The location of the γ-ray pulsar PSR J2021+4026 (γ-Cygni) associated with 3FGL J2021.5+4026 is also shown. The VHE γ-ray source is identified at the northwest rim of the SNR G78.2+2.1, associated with the γ-Cygni pulsar. The emission at very high energies is in good agreement across the whole remnant as mapped by the radio emission from the CGPS. Figure 6.16(b) shows the significance distribution, indicating that there is no additional VHE γ-ray emission after removal of the sources.

Figure 6.17 shows the energy spectrum obtained from the analysis, fitted with both a power law (Equation 6.10) and a curved power law (Equation 6.13). The parameters obtained for the power-law function are $N_0 = (1.47 \pm 0.14_{stat}) \times 10^{-12}/(\text{TeV cm}^2\,\text{s})$ at 1 TeV and $\Gamma = 2.96 \pm 0.17_{stat}$ with $\chi^2/n_{df} = 3.28/3 = 1.1$. The best fit curved power law is described by the parameters $N_0 = (1.50 \pm 0.16_{stat}) \times 10^{-12}/(\text{TeV cm}^2\,\text{s})$ at 1 TeV, $\Gamma = 2.81 \pm 0.35_{stat}$, and $\beta = -0.05 \pm 0.12$ with $\chi^2/n_{df} = 3.04/2 = 1.5$. An F-test gives a chance probability of 0.27 (0.35σ) that the curved

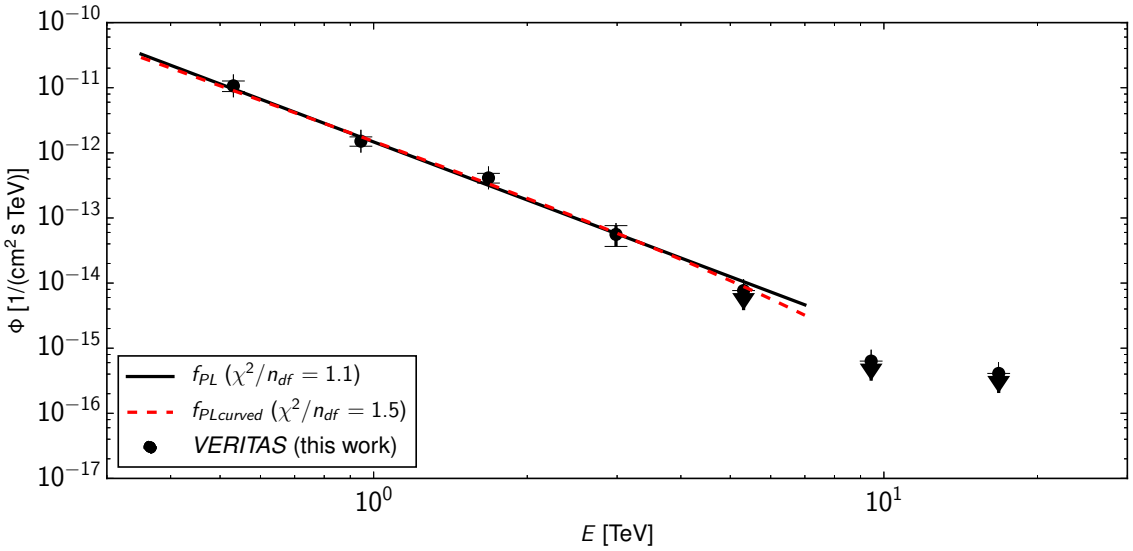

Figure 6.17: Differential energy spectrum of VER J2019+407. Black circles represent the results obtained by the *VERITAS* analysis using hard T cuts and the extended integration region ($\theta_{int} = 0.22°$). The black solid line represents the best power-law fit, f_{PL}, whereas the red dashed line shows the best fit assuming a curved power law, $f_{PLcurved}$. Downward triangles represent upper limits on the flux.

power law is preferred over the simple power law. Thus, the *VERITAS* spectrum above 500 GeV is well described by a power law with spectral index $2.96 \pm 0.17_{stat}$. This value is significantly softer than the previously reported spectrum by *VERITAS* with an index of $2.37 \pm 0.14_{stat} \pm 0.20_{sys}$ [Aliu et al., 2013]. The difference could be explained by the fact that the previous analysis used only a subset of the data included in this analysis. Previously, only data taken with all four telescopes between September and November 2009 were included, resulting in a total livetime of about 18.6 h. The analysis presented in this thesis uses a more extended dataset, including data taken during the sky survey and additional observations until June 2012. This includes several observations performed with three telescopes.

The total integral flux of photons above 600 GeV is $(2.09 \pm 0.21_{stat}) \times 10^{-12}/(\mathrm{cm}^2\,\mathrm{s})$, corresponding to about 5 % of the Crab Nebula flux. The values of the flux points of Figure 6.17 are listed in Table B.5.

Several hypotheses were suggested for the origin of the VHE γ-ray emission. Aliu et al. [2013] proposed that the VHE γ-ray emission seen at the location of VER J2019+407 might arise from the PWN scenario powered by PSR J2021+4026, associated with 3FGL J2021+4031e. The spin-down luminosity of the pulsar of about 10^{35} erg/s might be enough to power this emission.

However, this scenario is unlikely as there is no VHE γ-ray emission seen at the pulsar's position. It might be possible that VER J2019+407 is still a PWN but from an unknown pulsar situated in the line of sight of the SNR and therefore not seen in our direction.

The agreement between the VHE γ-ray emission and the radio continuum can be best explained by the generation of shocks due to the interaction of the supernova ejecta and the surrounding medium. The HI shell surrounding the SNR G78.2+2.1 moves with an expansion velocity of about 10 km/s [Lozinskaya et al., 2000]. The interaction of the HI shell with the supernova shock might drive a shock into the shell of density $2.5/\mathrm{cm}^3$, which would lead to a reverse shock. Both shocks can result in emission seen in radio, X-rays, and γ-rays. These shocks can produce VHE γ-rays via inverse Compton scattering of boosted electrons or hadronic interactions of accelerated nuclei. Assuming that the flux of photons at TeV energies arises from hadronic processes, the expected γ-ray flux above the given threshold energy can be calculated according to Equation 2.17. To obtain an integral flux above 600 GeV mentioned above, the following parameters were assumed:

- a distance to the object $d = 1.7$ kpc which is consistent with the approximated distance of the Cygnus region;
- a total energy of the supernova explosion $E_{SN} = 10^{51}$ erg;
- a fraction $f \approx 0.1$ of the total energy converted into cosmic rays.

Subsequently, one obtains a minimum density of the ambient medium of $0.38/\mathrm{cm}^3$. Note that this calculation is based on the total flux of photons integrated over the entire shell of the SNR, while the VHE γ-ray emission is only observed in a small portion of the shell of the SNR in radio wavelengths. As a consequence, only a fraction of the total supernova energy would participate in shock acceleration leading to VHE γ-ray emission.

Fraija and Araya [2016] identified that above 15 GeV, the emission detected by *Fermi*-LAT originates from the same region as the VHE emission previously detected by *VERITAS*. The *Fermi*-LAT emission presented by the authors in the southern shell of the remnant has a softer spectrum at GeV energies than the northern part of the remnant and thus it may not be strong enough for detection by *VERITAS*. Deeper observations, in particular with the lower energy threshold following the camera upgrade of *VERITAS* in 2012, may clarify this.

The SNR G78.2+2.1 is about 2.4° away from the centre of the Cygnus OB2 star association. An extended emission between these objects was detected by *Fermi*-LAT, over an area of about 50 pc at energies from 1 GeV to 100 GeV, known as the Cygnus cocoon [Ackermann et al., 2011]. However, it is very difficult to draw conclusions of the relationship between the SNR and the Cygnus cocoon based on the analysis presented in this thesis alone. γ-ray emission on the scale of the extension of the Cygnus cocoon cannot be detected using the ring background model. This would need additional new analysis methods optimised for highly extended sources using a maximum likelihood model fitting of data obtained from IACT measurements [Knödlseder et al., 2016].

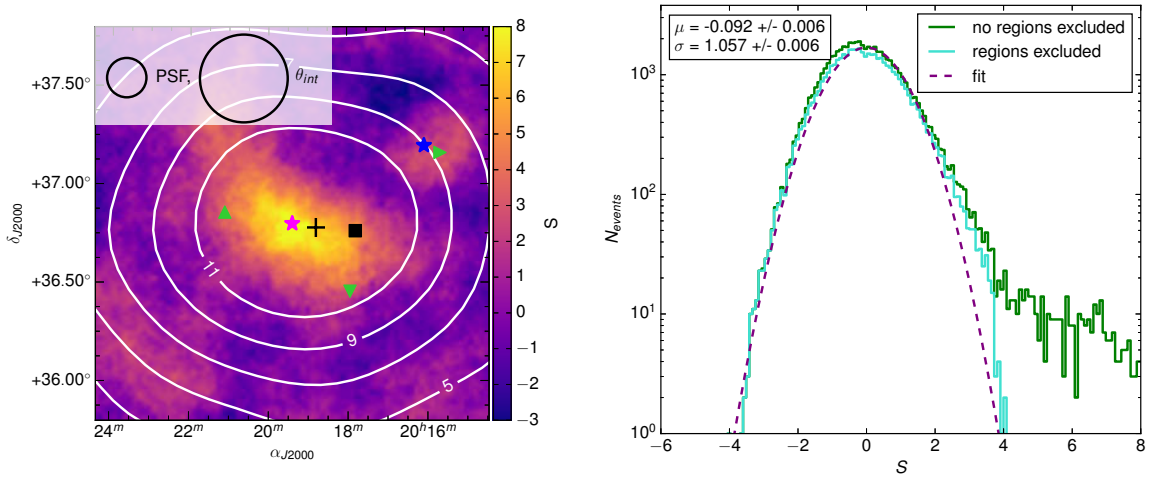

(a) (b)

Figure 6.18: *(a)* VHE γ-ray significance map of the region surrounding VER J2019+368 (magenta star). Overlaid are the *Milagro* [Abdo et al., 2007b] contours of 5, 7, 9, and 11σ. Also plotted are the locations of VER J2016+371 (blue star), IGR J20188+3647 (black plus-sign), 3FGL J2015.6+3709 (green $\triangleright$), 3FGL J2017.9+3627 (green $\triangledown$), 3FGL J2021.1+3651 (green $\triangle$), and *Sh* 2-104 (black square). *(b)* The significance distribution of the results obtained from *VERITAS* before (green) and after (cyan) excluding known VHE γ-ray emitters and stars. The dashed magenta line shows the fit of the latter histogram with a normal distribution of mean μ and standard deviation σ.

6.2.4 The region of MGRO J2019+37

The extended emission of MGRO 2019+37 was disentangled into a point source, VER J2016+371, and an extended source, VER J2019+368, in a previous analysis campaign [Aliu et al., 2014b]. In the following, both sources are studied in detail.

Results of VER J2019+368

The analysis of VER J2019+368 includes observations of about 81.4 h (dead-time corrected) at an average zenith angle of 19.3°, resulting in 1390 events recorded in the source region and 7018 events in the selected background region. This yields a peak-significance of 8.8σ using the integration radius optimised for an extended source, $\theta_{int} = 0.22°$. Figure 6.18(a) shows the significance map obtained with a PSF for the analysis of 0.08°, smoothed with a two-dimensional top-hat function of radius θ_{int}. As well, the significance contours of MGRO J2019+37 [Abdo et al., 2007b] are shown. Figure 6.18(b) shows the significance distribution. After removal of the sources, no additional significant excess of VHE γ-ray emission is observed.

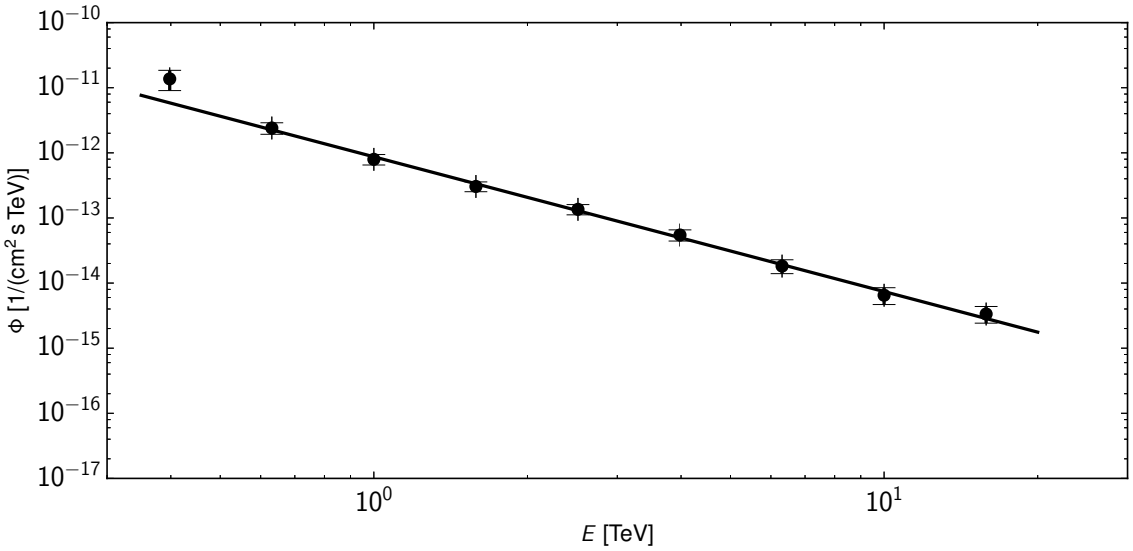

Figure 6.19: Differential energy spectrum of VER J2019+368. Black circles represent the results obtained by the *VERITAS* analysis using hard T cuts and the extended integration region ($\theta_{int} = 0.22°$). The black solid line represents the best power-law fit.

The spectrum obtained from the analysis is shown in Figure 6.19. The differential energy spectrum above 300 GeV is well described by a power law (Equation 6.10) with a normalisation $N_0 = (0.87 \pm 0.09_{stat}) \times 10^{-12}/(\text{TeV cm}^2\,\text{s})$ at 1 TeV and an index $\Gamma = 2.07 \pm 0.08_{stat}$ with $\chi^2/n_{df} = 4.30/7 = 0.6$. No evidence for a curvature in the spectrum could be found. This spectrum is softer than the previously reported spectrum by *VERITAS* [Aliu et al., 2014b]. However, it should be noted that the previously reported spectrum was produced with a significantly larger integration radius of 0.50° rather than 0.22°.

The total integral flux of photons above 600 GeV is $(1.49 \pm 0.12_{stat}) \times 10^{-12}/(\text{cm}^2\,\text{s})$ corresponding to about 3 % of the Crab Nebula flux. Results of the spectral calculation are listed in Table B.6.

Aliu et al. [2014b] stated that VER J2019+368 coincidences well with the central region of MGRO J2019+37 and is the main contributor to the extended emission. The potential *Fermi*-LAT counterparts to the extended VHE γ-ray emission are both 3FGL J2017.9+3627 and 3FGL J2021.1+3651 [Abdo et al., 2013]. While the former is associated with the pulsar PSR J2017+3625 discovered by the Einstein@Home distributed computing pulsar project [Anderson et al., 2006; Gotthelf et al., 2016; Clark et al., 2017, and reference therein], the latter is a counterpart of PSR J2021+3651 [Abdo et al., 2009c]. This pulsar has a period of 104 ms and a spin-down luminosity of 3.4×10^{36} erg/s [Roberts, 2002]. Due to its high spin-down luminosity, this object could power a PWN scenario, contributing to part of the VHE γ-ray emission. Aliu et al. [2014b] discuss the potential for this PWN to contribute to VHE γ-ray emission in detail.

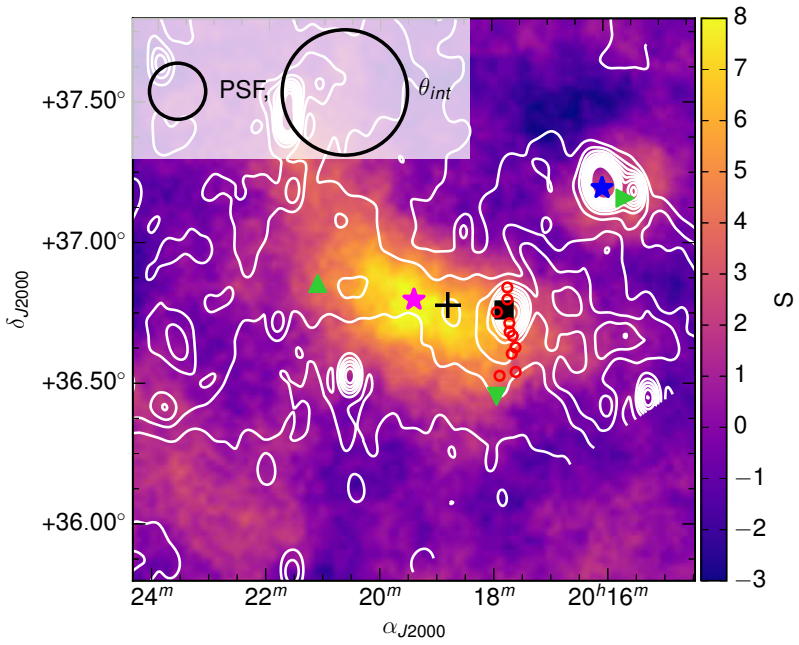

Figure 6.20: VHE γ-ray significance map of the region surrounding VER J2019+368 (magenta star). Overlaid is the radio emission detected from the CGPS at 408 MHz (with 10 logarithmically spaced levels at brightness temperatures from 100 K to 400 K) [Taylor et al., 2003]. Also plotted are the locations of the *NuSTAR* sources [Gotthelf et al., 2016] (red open circles) and the objects mentioned in Figure 6.18.

They state that the majority of the *VERITAS* emission lies to the west of these objects, though the pulsar is moving eastwards with the PWN stretching back towards the VHE emission.

Figure 6.20 shows the *VERITAS* emission of VER J2019+368 overlaid with the radio contours at 408 MHz obtained from the CGPS. The aforementioned sources are the most promising counterparts in the dataset of *Fermi*-LAT. However, neither of them lie close to the centroid of the *VERITAS* source VER J2019+368. It might be plausible that the observed emission is the result of a superposition of several sources, including both 3FGL sources. The hard X-ray transient IGR J20118+3647 [Sguera, 2008] lies near the maximum emission of the VHE γ-ray emission. Although Figure 6.20 clearly shows that VER J2019+368 is spatially correlated with the X-ray source, the extended and diffuse nature of the VHE γ-ray source seems to exclude a physical association. In addition, the HII region *Sh* 2-104 lies at the western edge of VER J2019+368, overlapping the strong radio emission detected during the CGPS. As massive CO clouds are reported to surround this region [Deharveng et al., 2003], this HII region is a perfect candidate to study massive star-formation activity. Torres et al. [2004] reported that γ-rays can be produced from shocks generated by the winds of massive stars which collide with the surrounding material.

Sh 2-104 can contribute to the VHE γ-ray emission due to its proximity to it. It is worth noting that all sources detected by *NuSTAR* [Gotthelf et al., 2016] are positioned close to the HII region inside the area of significant emission. Thus, they can contribute to the γ-ray emission as well, but are unlikely to be the sole contributor. Furthermore, the pulsar PSR J2017+3625 with its spin-down luminosity of 1.2×10^{34} erg/s [Clark et al., 2017], located to the south-east of the *VERITAS* source, could be responsible for part of the VHE emission seen in this region. Gotthelf et al. [2016] argue that due to its approximated age of about 2×10^6 yr and its luminosity, this object might generate a PWN scenario in this region, powering the VHE γ-ray emission.

To conclude, the updated analysis provides no further constraints on the origin of the VHE γ-ray emission from VER J2019+368. Most probably, this emission originates from a combination of multiple objects: the PWN associated with PSR J2021+3651, *Sh* 2-104, and a PWN associated with PSR J2017+3625. Deeper observations of this extended emission by *VERITAS* or future IACT experiments with a lower energy threshold might help to disentangle the VHE γ-ray emission into individual objects.

Results of VER J2016+371

VER J2016+371 was observed for about 68 h (dead-time corrected) at an average zenith angle of 20.4°. Its analysis resulted in 199 events recorded in the source region and 1022 events in the selected background region. This yields a peak-significance of 5.0σ using the integration radius optimised for a point source, $\theta_{int} = 0.09°$. Figure 6.21(a) shows the significance map obtained with a PSF for the analysis of 0.08°. The map is smoothed with a two-dimensional top-hat function with radius 0.09°. In addition, the contours of radio emission at 1420 MHz obtained from the CGPS are shown. The total integral flux of photons above 600 GeV is $(5.67 \pm 0.93_{stat}) \times 10^{-13}/(\mathrm{cm}^2\,\mathrm{s})$, corresponding to about 1 % of the Crab Nebula flux. The significance distribution is shown in Figure 6.21(b), indicating no significant VHE γ-ray emission after exclusion of the sources.

As seen from Figure 6.21(a), the radio emission reveals two sources; one associated with VER J2016+371 and the other locally coincident with the flat spectrum radio quasar QSO J2015+371 [Immer et al., 2011] located at a redshift of 0.859 [Shaw et al., 2013]. Hunt [2016] reported on variability in the GeV energy regime observed from 3FGL J2015.6+3709, hinting for an association with the blazar. Due to the high redshift of the latter, VER J2016+371 is only positionally associated and probably corresponds to a different object other than the blazar. Thus, the discussion of the blazar and its associations are beyond the scope of this thesis and are not considered. The VHE emission of VER J2016+371 is centred on the position that lies within the radio shell of the SNR CTB 87, also called G74.9+1.2. CTB 87 has been identified as a PWN which supports the assumption that the detected emission originates from this source. Observations of the *Chandra X-Ray Observatory* revealed a point source, called CXOU J201609.2+371110

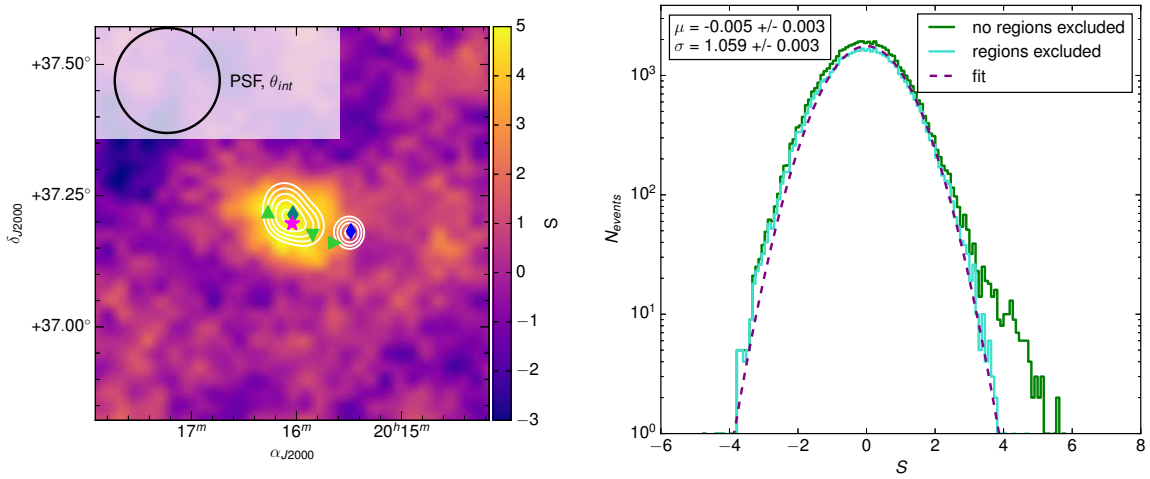

(a) (b)

Figure 6.21: *(a)* VHE γ-ray significance map of the region surrounding VER J2016+371 (magenta star). Overlaid is the radio emission detected from the CGPS at 1420 MHz (with 8 logarithmically spaced levels at brightness temperatures from 20 K to 150 K) [Taylor et al., 2003]. Also plotted are the locations of CTB 87 (teal diamond), QSO J2015+371 (blue diamond), 1FHL J2015.8+3710 (green $\triangledown$), 2FHL J2016.2+3713 (green $\triangle$), and 3FGL J2015.6+3709 (green $\triangleright$). *(b)* The significance distribution of the results obtained from *VERITAS* before (green) and after (cyan) excluding known VHE γ-ray emitters and stars. The dashed magenta line shows the fit of the latter histogram with a normal distribution of mean μ and standard deviation σ

[Matheson et al., 2013], positioned within the emission of the PWN. This source is most likely associated with the location of the pulsar, powering the PWN, with an age of 5 to 28 kyr. However, no pulsed emission is detected to date.

Assuming that the sources detected by *Fermi*-LAT 1FHL J2015.8+3710, 2FHL J2016.2+3713, and 3FGL J2015.6+3709 are associated with VER J2016+371, the emission from MeV to TeV enegies can be explained by an electron spectrum described by a power law and a broken power law [Saha, 2016] of the form

$$\frac{\mathrm{d}n_e}{\mathrm{d}\gamma} = \begin{cases} \gamma^{-\Gamma_1} & \text{for } \gamma < \gamma_{br} \\ \gamma^{-\Gamma_2} \exp\left(-\frac{\gamma}{\gamma_c}\right) & \text{for } \gamma_{br} \leq \gamma \leq \gamma_c \end{cases}, \tag{6.14}$$

with a high-energy cutoff at $E_c = \gamma_c m_e c^2$ with $\gamma_c = 3.3 \times 10^8$, a low-energy cutoff at $E_{min} = \gamma_{min} m_e c^2$ with $\gamma_{min} = 1.0$, the position of the spectral break at $E_{br} = \gamma_{br} m_e c^2$ with $\gamma_{br} = 2.8 \times 10^6$ and spectral indices $\Gamma_1 = 2.0$ and $\Gamma_2 = 3.8$. An additional component to the broken power law distribution is necessary to explain the emission. The Maxwell–Boltzmann

distribution of the electron population assumed here is proportional to $\gamma \exp(-\gamma/\delta\gamma)$ with $\delta\gamma = 1.5 \times 10^5$. These electrons can upscatter low-energy photons to the observed VHE γ-rays. As noted above, 3FGL J2015.6+3709 might be associated with the blazar observed in this field, and not with VER J2016+371.

To summarise, the analysis confirms that the *VERITAS* emission is spatially coincident with the PWN of CTB 87. Observations of future IACT experiments with a better angular resolution than existing ones could dissolve the VHE γ-ray emission from CTB 87 and the QSO J2015+371, yielding to a better understanding of the objects.

6.2.5 Limits on the VHE γ-ray emission

Along with the detected sources in the VHE regime, a number of astrophysical objects, detected at other wavelengths, are investigated. These objects are chosen based on their source class and properties as they are expected to emit VHE γ-ray emission. These sources are,

- 13 SNRs [Green, 2014];
- HMXBs [Liu et al., 2000]: Cygnus X-1, Cygnus X-3, EXO 2030+375, KS 1947+300, XTE J2012+381;
- LMXBs [Liu et al., 2001]: GS 2023+338, XTE J2012+381;
- CWBs [van der Hucht, 2001]: WR140, WR146, WR147;
- pulsar [Manchester et al., 2005]: PSR B1951+32;
- 27 objects of the third catalogue of *Fermi*-LAT [Acero et al., 2015] with a test statistic greater than 20 [Popkow, 2017; VERITAS collaboration, in preparation] and located within the survey region.

An upper limit on the VHE flux for each object is obtained. Of principal interest are those sources for which VHE analyses have been published, such as Cygnus X-1 and Cygnus X-3.

The analysis of the objects is primarily an attempt to fully exploit the available dataset as a potential means of discovery. Except the sources discussed in the previous sections, no significant excess of γ-ray-like events above the background expectation was found. Following this, upper limits on the flux of 50 selected objects were derived (Section 6.1.5). This was done by applying two different cut sets (hard, moderate). The energy threshold differs between the cut sets and depends on the zenith angle of observations. On average, the energy threshold for hard cuts was about 600 GeV and the one for moderate cuts at about 300 GeV.

The upper limits on the flux above the energy threshold, $E_{th} = 600$ GeV, are listed in Table 6.3 and Table 6.4 after applying hard T cuts. Table B.7 and Table B.8 list the results above the energy threshold $E_{th} = 300$ GeV obtained with moderate T cuts. The limits were evaluated under the assumption of an energy spectrum following a power law with index $\Gamma = 2.4$ which is about the average spectral index of Galactic VHE γ-ray sources [Wakely and Horan, 2016].

Table 6.3: Upper limits on the integral flux, Φ^{UL}, above $E_{th} = 0.6\,\mathrm{TeV}$ at 95 % confidence level from objects of interest inside the Cygnus region; calculated with hard cuts and for the search of point-sources. A power-law spectrum with an index of $\Gamma = 2.4$ has been assumed for all sources. The second column indicates the type of the object. The third to sixth column indicate the position in Galactic (longitude, l, and latitude, b) and equatorial (right ascension, α_{J2000}, and declination, δ_{J2000}) coordinates. Time, t, represents the livetime and ϑ the average zenith angle of the observation. N_{ON} represents the total number of events around the source position within a circle of $\theta_{int} = 0.09°$ in the sky, N_{OFF} represents the normalised number of background events. The normalisation factor, α, depends on the observation conditions of the object. The significance is denoted as S and the effective area as A_{eff}. Φ^{UL}_{CU} represents the integral flux in % of the flux of the Crab Nebula [Hillas et al., 1998]. Objects marked with $^{\diamondsuit}$ are associated with the Cygnus cocoon field.

object	type	l	b	α_{J2000}	δ_{J2000}	t	ϑ	N_{ON}	N_{OFF}	α	S	A_{eff}	$\Phi^{UL}_{>0.6\,\mathrm{TeV}}$	Φ^{UL}_{CU}
												m^2	$10^{-13}/(\mathrm{cm}^2\,\mathrm{s})$	%
Cygnus X-1	HMXB	71.34°	+3.07°	$19^h58^m21.7^s$	35.20°	7.20 h	24.4°	4	34	0.17	−0.69	107217	2.46	0.53
Cygnus X-3	HMXB	79.85°	+0.70°	$20^h32^m25.8^s$	40.96°	49.25 h	18.0°	40	242	0.17	−0.07	91294	1.36	0.30
EXO 2030+375	HMXB	77.15°	−1.24°	$20^h32^m15.3^s$	37.64°	6.33 h	21.9°	12	43	0.17	1.50	53666	17.32	3.77
G65.8-0.5	SNR	65.80°	−0.5°	$19^h59^m20.0^s$	28.62°	1.00 h	27.2°	1	6	0.17	0.00	38480	39.73	8.64
G67.8+0.5	SNR	67.80°	+0.50°	$20^h00^m00.0^s$	30.85°	5.90 h	23.1°	3	49	0.17	−1.96	76139	2.88	0.63
GS 2023+338	LMXB	73.12°	−2.09°	$20^h24^m3.8^s$	33.87°	10.20 min	33.9°	0	1	0.17	−0.56	52256	124.38	27.05
3FGL J1951.6+2926	unknown	65.67°	+1.32°	$19^h51^m38.4^s$	29.45°	19.80 min	34.9°	2	2	0.17	1.69	34380	222.35	48.36
3FGL J1958.6+2845	pulsar	65.88°	−0.35°	$19^h58^m38.4^s$	28.76°	40.20 h	26.3°	0	3	0.17	−0.96	40179	35.65	7.75
3FGL J1958.6+3844	unknown	74.41°	+4.85°	$19^h58^m40.8^s$	38.75°	1.65 h	23.6°	1	7	0.17	−0.15	60160	15.03	3.27
3FGL J2014.4+3606	unknown	73.86°	+0.79°	$20^h21^m38.3^s$	36.11°	37.10 h	19.8°	40	188	0.17	1.37	69222	3.97	0.86
3FGL J2018.5+3851	unknown	76.59°	+1.66°	$20^h18^m31.3^s$	38.86°	38.64 h	20.8°	28	186	0.17	−0.51	56731	1.99	0.43
3FGL J2018.6+4213$^{\diamondsuit}$	unknown	79.40°	+3.53°	$20^h18^m40.3^s$	42.23°	18.47 h	24.2°	19	103	0.17	0.40	63381	4.62	1.01
3FGL J2021.5+4026	pulsar	78.23°	+2.08°	$20^h21^m33.5^s$	40.45°	35.96 h	23.8°	50	224	0.17	1.69	73306	4.70	1.02
3FGL J2022.2+3840$^{\diamondsuit}$	unknown	76.86°	+0.96°	$20^h22^m15.1^s$	38.68°	33.28 h	20.9°	32	161	0.17	0.89	61725	3.91	0.85
3FGL J2023.5+4126$^{\diamondsuit}$	unknown	79.25°	+2.34°	$20^h23^m31.1^s$	41.43°	53.29 h	21.9°	42	294	0.17	−0.95	63284	1.28	0.28
3FGL J2024.6+3747	unknown	76.41°	+0.07°	$20^h24^m40.8^s$	37.80°	48.89 h	19.9°	40	205	0.17	0.90	69134	2.64	0.57
3FGL J2025.2+3340	unknown	73.10°	−2.41°	$20^h25^m16.7^s$	33.67°	10.20 min	34.4°	0	1	0.17	−0.56	34793	186.81	40.63
3FGL J2026.8+4003$^{\diamondsuit}$	unknown	78.49°	+1.03°	$20^h26^m52.8^s$	40.05°	40.84 h	20.3°	40	216	0.17	0.60	54144	3.67	0.80
3FGL J2028.5+4040c$^{\diamondsuit}$	unknown	79.19°	+1.13°	$20^h28^m31.1^s$	40.68°	58.94 h	18.9°	43	299	0.17	−0.92	67363	1.11	0.24
3FGL J2030.0+3642	pulsar	76.13°	−1.43°	$20^h30^m0.0^s$	36.70°	16.36 h	18.6°	15	83	0.17	0.29	63913	4.45	0.97
3FGL J2030.8+4416	pulsar	82.35°	+2.89°	$20^h30^m52.8^s$	44.27°	4.61 h	20.9°	5	32	0.18	−0.33	66292	7.61	1.66
3FGL J2032.5+3921$^{\diamondsuit}$	unknown	78.57°	−0.27°	$20^h32^m33.5^s$	39.36°	9.44 h	19.5°	8	50	0.17	−0.11	55424	5.85	1.27
3FGL J2032.5+4032$^{\diamondsuit}$	unknown	79.51°	+0.44°	$20^h32^m31.1^s$	40.53°	50.08 h	17.5°	40	231	0.17	0.22	75964	1.83	0.40

Table 6.3: continued

object	type	l	b	α_{J2000}	δ_{J2000}	t	ϑ	N_{ON}	N_{OFF}	α	S	A_{eff}	$\Phi^{UL}_{>0.6\,\mathrm{TeV}}$	Φ^{UL}_{CU}
												m^2	$10^{-13}/(\mathrm{cm}^2\,\mathrm{s})$	%
3FGL J2033.3+4348c$^\diamondsuit$	unknown	82.24°	+2.26°	$20^h33^m21.5^s$	43.81°	5.45 h	20.7°	9	43	0.17	0.61	65653	11.54	2.51
3FGL J2034.4+3833c$^\diamondsuit$	unknown	78.16°	−1.04°	$20^h34^m28.8^s$	38.56°	5.35 h	17.1°	3	38	0.17	−1.39	50079	5.44	1.18
3FGL J2034.6+4302	unknown	81.77°	+1.60°	$20^h34^m40.8^s$	43.04°	12.29 h	21.3°	17	73	0.17	1.20	57603	9.14	1.99
3FGL J2035.0+3634$^\diamondsuit$	unknown	76.63°	−2.32°	$20^h35^m2.3^s$	36.58°	1.00 h	28.0°	1	10	0.17	−0.52	40470	33.15	7.21
3FGL J2036.8+4234c$^\diamondsuit$	unknown	81.63°	+0.99°	$20^h36^m52.8^s$	42.57°	30.26 h	18.1°	24	126	0.17	0.59	53442	3.91	0.85
3FGL J2037.4+4132c$^\diamondsuit$	unknown	80.87°	+0.29°	$20^h37^m24.0^s$	41.53°	50.61 h	17.9°	55	266	0.17	1.42	72226	3.26	0.71
3FGL J2038.4+4212$^\diamondsuit$	unknown	81.53°	+0.54°	$20^h38^m28.8^s$	42.21°	30.82 h	18.1°	24	146	0.17	−0.06	60377	2.63	0.57
3FGL J2039.4+4111$^\diamondsuit$	unknown	80.83°	−0.21°	$20^h39^m24.0^s$	41.20°	31.93 h	18.7°	25	149	0.17	0.03	68513	2.38	0.52
3FGL J2042.4+4209$^\diamondsuit$	unknown	81.93°	−0.07°	$20^h42^m26.4^s$	42.15°	8.85 h	20.6°	6	55	0.17	−1.04	56172	3.94	0.86
3FGL J2043.1+4350	unknown	83.33°	+0.87°	$20^h43^m7.1^s$	43.84°	1.67 h	23.5°	3	9	0.17	0.98	39595	43.03	9.36
KS 1947+300	HMXB	66.09°	+2.08°	$19^h49^m35.5^s$	30.13°	30.00 min	34.8°	0	5	0.17	−1.24	40405	39.95	8.69
PSR B1951+32	pulsar	68.77°	+2.82°	$19^h52^m58.2^s$	32.87°	59.40 min	26.4°	1	9	0.17	−0.41	51175	26.85	5.84
WR140	CWB	80.93°	+4.18°	$20^h20^m28.0^s$	43.86°	2.00 h	19.8°	1	11	0.17	−0.63	41667	15.44	3.36
WR146	CWB	80.56°	+0.45°	$20^h35^m47.1^s$	41.38°	49.94 h	17.8°	36	202	0.19	−0.37	85349	1.21	0.26
WR147	CWB	79.85°	−0.32°	$20^h36^m43.6^s$	40.36°	35.02 h	18.0°	28	161	0.17	0.21	65149	2.58	0.56
XTE J2012+381	LMXB	75.39°	+2.25°	$20^h12^m37.8^s$	38.19°	23.38 h	22.0°	26	101	0.17	1.89	62471	6.38	1.39

Table 6.4: Upper limits on the integral flux, Φ^{UL}, above $E_{th} = 0.6\,\mathrm{TeV}$ at 95 % confidence level from objects of interest inside the Cygnus region; calculated with hard cuts and for the search of extended-sources. A power-law spectrum with an index of $\Gamma = 2.4$ has been assumed for all sources. The second column indicates the type of the object. The third to sixth column indicate the position in Galactic (longitude, l, and latitude, b) and equatorial (right ascension, α_{J2000}, and declination, δ_{J2000}) coordinates. Time, t, represents the livetime and ϑ the average zenith angle of the observation. N_{ON} represents the total number of events around the source position within a circle of $\theta_{int} = 0.22°$ in the sky, N_{OFF} represents the normalised number of background events. The normalisation factor, α, depends on the observation conditions of the object. The significance is denoted as S and the effective area as A_{eff}. Φ^{UL}_{CU} represents the integral flux in % of the flux of the Crab Nebula [Hillas et al., 1998]. Objects marked with $^{\diamondsuit}$ are associated with the Cygnus cocoon field.

object	type	l	b	α_{J2000}	δ_{J2000}	t	ϑ	N_{ON}	N_{OFF}	α	S	A_{eff}	$\Phi^{UL}_{>0.6\,\mathrm{TeV}}$	Φ^{UL}_{CU}
												m^2	$10^{-13}/(\mathrm{cm}^2\,\mathrm{s})$	%
Cygnus X-1	HMXB	71.34°	+3.07°	$19^h58^m21.7^s$	35.20°	7.36 h	24.6°	44	204	0.21	0.17	142126	6.99	1.52
Cygnus X-3	HMXB	79.85°	+0.70°	$20^h32^m25.8^s$	40.96°	50.55 h	18.2°	273	1002	0.24	1.80	117531	5.03	1.09
EXO 2030+375	HMXB	77.15°	−1.24°	$20^h32^m15.3^s$	37.64°	7.00 h	21.5°	46	226	0.18	0.74	90789	14.54	3.16
G65.7+1.2	SNR	65.70°	+1.20°	$19^h52^m10.0^s$	29.42°	19.80 min	34.5°	5	10	0.17	1.86	70648	168.95	36.75
G65.8-0.5	SNR	65.80°	−0.5°	$19^h59^m20.0^s$	28.62°	1.00 h	26.8°	4	29	0.17	−0.36	77835	27.18	5.91
G66.0-0.0	SNR	66.00°	0.00°	$19^h57^m50.0^s$	29.05°	1.34 h	29.0°	9	38	0.17	0.91	79559	41.94	9.12
G67.6+0.9	SNR	67.60°	+0.90°	$19^h57^m45.0^s$	30.89°	4.30 h	26.8°	33	167	0.17	0.88	97886	19.28	4.19
G67.7+1.8	SNR	67.70°	+1.80°	$19^h54^m32.0^s$	31.44°	3.59 h	26.3°	20	167	0.17	−1.46	100328	7.40	1.61
G68.6-1.2	SNR	68.60°	−1.20°	$20^h08^m40.0^s$	30.62°	2.97 h	21.1°	7	69	0.17	−1.34	85014	7.50	1.63
G69.0+2.7	SNR	69.00°	+2.70°	$19^h53^m20.0^s$	33.02°	1.33 h	26.8°	11	37	0.17	1.59	73623	58.06	12.63
G69.7+1.0	SNR	69.70°	+1.00°	$20^h02^m40.0^s$	32.72°	1.43 h	27.4°	9	54	0.17	0.00	85786	27.28	5.93
G73.9+0.9	SNR	73.90°	+0.90°	$20^h14^m15.0^s$	36.20°	40.40 h	19.6°	169	867	0.17	1.83	86767	6.69	1.46
G76.9+1.0	SNR	76.90°	+1.00°	$20^h22^m20.0^s$	38.74°	37.87 h	21.3°	145	825	0.18	−0.14	88624	3.30	0.72
G83.0-0.3	SNR	83.00°	−0.30°	$20^h46^m55.0^s$	42.85°	3.34 h	24.7°	17	94	0.17	0.31	82702	18.02	3.92
GS 2023+338	LMXB	73.12°	−2.09°	$20^h24^m3.8^s$	33.87°	30.00 min	29.3°	3	4	0.17	1.83	76299	82.61	17.97
3FGL J1951.6+2926	unknown	65.67°	+1.32°	$19^h51^m38.4^s$	29.45°	19.80 min	33.9°	5	6	0.17	2.48	70009	74.54	16.21
3FGL J1958.6+2845	pulsar	65.88°	−0.35°	$19^h58^m38.4^s$	28.76°	1.00 h	26.4°	8	32	0.17	0.98	73783	58.37	12.70
3FGL J1958.6+3844	unknown	74.41°	+4.85°	$19^h58^m40.8^s$	38.75°	1.99 h	26.2°	8	43	0.17	0.28	92758	19.47	4.24
3FGL J2014.4+3606	unknown	73.86°	+0.79°	$20^h21^m38.3^s$	36.11°	40.69 h	20.0°	181	853	0.18	2.11	90847	3.50	0.76
3FGL J2018.5+3851	unknown	76.59°	+1.66°	$20^h18^m31.3^s$	38.86°	45.06 h	21.2°	174	886	0.17	1.72	82940	6.19	1.35
3FGL J2018.6+4213$^{\diamondsuit}$	unknown	79.40°	+3.53°	$20^h18^m40.3^s$	42.23°	22.92 h	23.9°	114	609	0.17	0.89	92754	7.04	1.53
3FGL J2021.5+4026	pulsar	78.23°	+2.08°	$20^h21^m33.5^s$	40.45°	37.21 h	23.6°	244	1247	0.18	1.14	105951	5.99	1.30
3FGL J2022.2+3840$^{\diamondsuit}$	unknown	76.86°	+0.96°	$20^h22^m15.1^s$	38.68°	35.23 h	20.8°	144	912	0.17	−0.86	89660	2.49	0.54

Table 6.4: continued

object	type	l	b	α_{J2000}	δ_{J2000}	t	ϑ	N_{ON}	N_{OFF}	α	S	A_{eff}	$\Phi^{UL}_{>0.6\,\mathrm{TeV}}$	Φ^{UL}_{CU}
												m^2	$10^{-13}/(\mathrm{cm}^2\,\mathrm{s})$	%
3FGL J2023.5+4126$^\diamond$	unknown	79.25°	+2.34°	$20^h23^m31.1^s$	41.43°	56.40 h	21.7°	292	1438	0.18	1.84	92702	5.93	1.29
3FGL J2024.6+3747	unknown	76.41°	+0.07°	$20^h24^m40.8^s$	37.80°	51.01 h	19.7°	242	1326	0.18	0.05	96779	3.13	0.68
3FGL J2025.2+3340	unknown	73.10°	−2.41°	$20^h25^m16.7^s$	33.67°	10.20 min	33.9°	0	4	0.17	−1.11	72473	72.76	15.83
3FGL J2026.8+4003$^\diamond$	unknown	78.49°	+1.03°	$20^h26^m52.8^s$	40.05°	47.27 h	20.5°	208	1188	0.17	0.43	81093	4.40	0.96
3FGL J2028.5+4040c$^\diamond$	unknown	79.19°	+1.13°	$20^h28^m31.1^s$	40.68°	61.87 h	19.1°	286	1441	0.19	0.28	94934	3.16	0.69
3FGL J2030.0+3642	pulsar	76.13°	−1.43°	$20^h30^m0.0^s$	36.70°	18.58 h	18.2°	85	473	0.17	0.63	93371	6.82	1.48
3FGL J2030.8+4416	pulsar	82.35°	+2.89°	$20^h30^m52.8^s$	44.27°	3.28 h	20.3°	19	142	0.17	−0.92	91380	10.48	2.28
3FGL J2032.5+3921$^\diamond$	unknown	78.57°	−0.27°	$20^h32^m33.5^s$	39.36°	11.70 h	18.8°	56	328	0.18	−0.20	87382	6.74	1.47
3FGL J2032.5+4032$^\diamond$	unknown	79.51°	+0.44°	$20^h32^m31.1^s$	40.53°	51.73 h	18.1°	255	1347	0.17	1.60	102520	5.06	1.10
3FGL J2033.3+4348c$^\diamond$	unknown	82.24°	+2.26°	$20^h33^m21.5^s$	43.81°	6.18 h	20.4°	37	166	0.17	1.55	89532	18.49	4.02
3FGL J2034.4+3833c$^\diamond$	unknown	78.16°	−1.04°	$20^h34^m28.8^s$	38.56°	6.02 h	17.5°	38	185	0.17	1.15	87517	17.99	3.91
3FGL J2034.6+4302	unknown	81.77°	+1.60°	$20^h34^m40.8^s$	43.04°	13.97 h	21.2°	82	425	0.17	1.19	91690	10.84	2.36
3FGL J2035.0+3634$^\diamond$	unknown	76.63°	−2.32°	$20^h35^m2.3^s$	36.58°	2.00 h	24.6°	7	41	0.17	0.06	72365	21.47	4.67
3FGL J2036.8+4234c$^\diamond$	unknown	81.63°	+0.99°	$20^h36^m52.8^s$	42.57°	32.70 h	18.2°	117	804	0.17	−1.39	80467	2.17	0.47
3FGL J2037.4+4132c$^\diamond$	unknown	80.87°	+0.29°	$20^h37^m24.0^s$	41.53°	51.61 h	18.2°	249	1074	0.19	2.66	97469	3.75	0.82
3FGL J2038.4+4212$^\diamond$	unknown	81.53°	+0.54°	$20^h38^m28.8^s$	42.21°	33.12 h	18.1°	148	849	0.17	0.39	87029	4.84	1.05
3FGL J2039.4+4111$^\diamond$	unknown	80.83°	−0.21°	$20^h39^m24.0^s$	41.20°	35.54 h	18.4°	170	879	0.17	1.44	96102	6.17	1.34
3FGL J2042.4+4209$^\diamond$	unknown	81.93°	−0.07°	$20^h42^m26.4^s$	42.15°	9.85 h	20.5°	46	263	0.18	−0.29	88640	6.95	1.51
3FGL J2043.1+4350	unknown	83.33°	+0.87°	$20^h43^m7.1^s$	43.84°	2.94 h	21.7°	22	66	0.17	2.65	73439	22.83	4.97
KS 1947+300	HMXB	66.09°	+2.08°	$19^h49^m35.5^s$	30.13°	30.00 min	36.1°	2	18	0.17	−0.57	72244	43.14	9.38
PSR B1951+32	pulsar	68.77°	+2.82°	$19^h52^m58.2^s$	32.87°	2.00 h	21.9°	11	44	0.17	1.15	74769	34.83	7.58
XTE J2012+381	LMXB	75.39°	+2.25°	$20^h12^m37.8^s$	38.19°	27.89 h	22.4°	128	596	0.18	1.75	89601	8.09	1.76

Supernova remnants

VHE γ-rays are the tracers of particle acceleration of cosmic rays in SNRs. Therefore, SNRs are high priority targets in the field of ground-based γ-ray astronomy. Green's catalogue [Green, 2014] lists 13 remnants within the survey region, consistent with the SNR catalogue of Ferrand and Safi-Harb [2012]. Observations of these remnants might be complicated due to their proximity to other extended sources, such as molecular clouds, Wolf-Rayet stars or OB star associations. Except G65.8-0.5 and G67.8+0.5, all objects have an extension larger than 0.09° at energies in the radio regime [Green, 2014]. G65.8-0.5 has an angular size in the radio regime of about $10' \times 6'$ and G67.8+0.5 of about $7' \times 5'$. This is at the limit of the integration radius used for point-source analysis ($\theta_{int} = 0.09°$). Therefore, these objects were analysed with integration radii for both point- and extended-source analyses.

No significant detection was observed of any of the 13 remnants. The objects with the lowest limit on the flux are G67.7+1.8 and G76.9+1.0 with 1.04 % and 0.72 % of the Crab Nebula flux respectively, after applying the extended-source analysis with hard and moderate cuts. It should be noted that two of the 13 SNRs are spatially coincident with objects detected by *Fermi*-LAT, namely G73.9+0.9 associated with 3FGL J2014.4+3606 and G76.9+1.0 associated with 3FGL J2022.2+3840. As both objects, 3FGL J2014.4+3606 and 3FGL J2022.2+3840, were detected at high-energy γ-rays, the measurements of the high-energy γ-ray flux can be extrapolated to estimate the flux at very high energies. Here, an energy spectrum following a power law (Equation 6.10) is assumed. According to Equation 6.12, the integral flux Φ between energies E_1 and E_2 is given as

$$\Phi = N_0 \cdot \frac{1}{1-\Gamma} \cdot \frac{1}{E_0^{-\Gamma}} \cdot \left(E_2^{-\Gamma+1} - E_1^{-\Gamma+1}\right) \approx N_0 \cdot \frac{1}{\Gamma-1} \cdot \frac{1}{E_0^{-\Gamma}} \cdot \left(E_1^{-\Gamma+1}\right). \tag{6.15}$$

The approximation is valid for a spectral index $\Gamma > 1$ and $E_1 \gg E_2$. Following this, the flux in the VHE regime above energy E_{VHE} can be estimated by

$$\Phi_{>E_{VHE}} = \Phi_{>E_{HE}} \cdot \left(\frac{E_{VHE}}{E_{HE}}\right)^{-\Gamma+1}, \tag{6.16}$$

where $\Phi_{>E_{HE}}$ is the flux above energy E_{HE} obtained at high energies with the *Fermi*-LAT instrument. Table 6.5 lists the extrapolation of the flux measurements, obtained from the *Fermi*-LAT instrument, above 600 GeV. Taking the uncertainties of the spectral index in the high-energy regime into account, the flux of 3FGL J2014.4+3606 is extrapolated to $(1.48^{+1.52}_{-0.75}) \times 10^{-13}/(\mathrm{cm}^2\,\mathrm{s})$ above 600 GeV. Following this, the predicted flux of 3FGL J2022.2+3840 is about $(1.25^{+3.69}_{-0.26}) \times 10^{-13}/(\mathrm{cm}^2\,\mathrm{s})$ above 600 GeV. The limits obtained from the *VERITAS* analysis here are listed in Table 6.3 and Table 6.4 and are consistent with the predictions calculated from the extrapolation of the *Fermi*-LAT results. This means that a cutoff of the source spectrum cannot be excluded.

object	Γ_{HE}	$\Phi_{>1\,\mathrm{GeV}_{HE}}$	$\Phi_{>600\,\mathrm{GeV}_{VHE}}$
		$10^{-9}/(\mathrm{cm}^2\,\mathrm{s})$	$10^{-13}/(\mathrm{cm}^2\,\mathrm{s})$
3FGL J2014.4+3606	2.40 ± 0.11	1.13 ± 0.24	$1.48^{+1.52}_{-0.75}$
3FGL J2022.2+3840	2.56 ± 0.25	2.70 ± 0.53	$1.25^{+3.69}_{-0.26}$

Table 6.5: Predictions of the flux at very high energies, Φ_{VHE}, above 600 GeV for 3FGL J2014.4+3606 and 3FGL J2022.2+3840 based on their flux at high energies, Φ_{HE}, above 1 GeV [Acero et al., 2015]. The spectral index of the objects in the high-energy regime is denoted as Γ_{HE}.

High-mass and low-mass X-ray binary systems

Our Galaxy hosts hundreds of binary systems which are known to emit in radio and X-ray wavelengths. However, only a few binaries have been observed that produce VHE γ-rays. Furthermore, the emission mechanisms of VHE γ-rays in the few known sources are not well understood. Thus, any VHE flux measurements, including upper limits, can provide useful information to constrain the emission models of these objects.

The HMXB system Cygnus X-1 contains a blue supergiant variable star orbiting a stellar-mass black hole with a mass of $(14.8 \pm 1.0) M_\odot$ [Orosz et al., 2011]. It is located in the OB3 star association in the Cygnus region. Located at a distance of about 1.86 kpc [Reid et al., 2011; Xiang et al., 2011], this object exhibits episodic γ-ray emission between 100 MeV and 3 GeV [Sabatini et al., 2010]. The *MAGIC* telescope array system observed this source for about 46 h in 2006 and reported an upper limit of 1 % to 2 % of the Crab Nebula flux above 150 GeV [Albert et al., 2007d]. The upper limit on the flux (>600 GeV) derived here ranges between 0.53 % and 1.52 % (between 1.06 % and 1.17 % above 300 GeV) of the flux of the Crab Nebula. In addition, the upper limit above 400 GeV is derived to be $5.8 \times 10^{-13}/(\mathrm{cm}^2\,\mathrm{s})$ after an observation time of 6.8 h. This is more than an order of magnitude lower than the previously published *VERITAS* results of $1.05 \times 10^{-12}/(\mathrm{cm}^2\,\mathrm{s})$ [Guenette, 2009]. From the flux upper limit, the luminosity of the object can be calculated given as

$$L = \Phi \cdot 4\pi d^2, \tag{6.17}$$

where Φ is the calculated upper limit on the flux and d the distance to the object. The luminosity derived here is less than 2.9×10^{36} erg/s above 600 GeV (less than 6.3×10^{36} erg/s above 300 GeV), assuming a distance of 1.86 kpc and isotropic emission. This corresponds to a fraction of about 10^{-3} of the Eddington luminosity of the system, given as

$$L_{edd} = 1.26 \times 10^{38} \left(\frac{M_c}{M_\odot} \right) \mathrm{erg/s}, \tag{6.18}$$

where M_c is the mass of the compact object in units of solar masses $M_\odot$. This is about 10 % of the luminosity obtained from measurements in the X-ray regime of about 2.1×10^{37} erg/s [Orosz et al., 2011].

Cygnus X-3 is an HMXB system, classified as a microquasar and already studied at multiple wavelengths, such as infrared, radio, X-ray, and γ-rays. It consists of a neutron star or a black hole with a mass between 10 and $20 M_\odot$ and a Wolf-Rayet companion star [Tavani et al., 2009]. The object lies at a distance between 8 and 11 kpc [Lauqué et al., 1972]. Its observations included in the dataset used here were studied and upper limits were derived. The upper limit on the flux for E_{th}>600 GeV was set to 0.30 % of the flux of the Crab Nebula or $1.36 \times 10^{-13}/(\mathrm{cm}^2\,\mathrm{s})$, and 0.35 % ($4.56 \times 10^{-13}/(\mathrm{cm}^2\,\mathrm{s})$) above 300 GeV. In order to compare the results derived here with published results by the *VERITAS* [Guenette, 2009; Archambault et al., 2013] and *MAGIC* [Aleksić et al., 2010] collaborations, the upper limits are calculated with the same energy threshold as in previous analyses. The comparison is shown in Table 6.6. The obtained upper limit above 250 GeV is about a third of the one obtained by *MAGIC*, which even used a larger dataset comprising about 70 h of observation. Compared to previously published *VERITAS* results, the upper limits obtained here provide better constraints on the expected flux at VHE γ-rays. The improvement ranges from a factor of six above 400 GeV to a factor of 1.2 above 263 GeV and it depends strongly on the amount of observing time. It should be noted that no systematic uncertainties were considered in this analysis, while the *MAGIC* results include a 30 % systematic uncertainty on flux.

The derived upper limits are equivalent to a luminosity of less than 1.97×10^{33} erg/s above E_{th}>600 GeV (6.60×10^{33} erg/s above E_{th}>300 GeV). This corresponds to a fraction of about 10^{-6} of the Eddington luminosity of the system of 1.26×10^{39} erg/s. This is in contrast to its luminosity in the X-ray regime of about 10^{38} erg/s [Tavani et al., 2009].

The results of EXO 2030+375, KS 1947+300, and XTE J2012+381 can be discussed in the context of previously published results from IACT measurements. First constraints on the flux at VHE γ-rays from these objects were reported by Guenette [2009]. Table 6.7 compares these results with the upper limits derived here. It is obvious from the table that the estimation of the flux depends strongly on the amount of data used in the analysis and the time of observations. The upper limit on the flux decreases slightly for EXO 2030+375, even with a smaller time of observation used for the analysis here. In addition, the dataset available for XTE J2012+381 was studied and upper limits of the flux were set. An increase of the observing time by a factor of about 2 (13.91 h [Guenette, 2009] versus 23.39 h (this work)) resulted in a lower upper limit by more than a factor of 2 for the updated analysis here.

Table 6.8 lists the Eddington luminosity (Equation 6.18) and the upper limits on the γ-ray luminosities above 300 and 600 GeV for EXO 2030+375 and KS1947+300. The results derived here are a fraction of $\approx 10^{-3}$ of its Eddington luminosity for EXO 2030+375, and even smaller for

experiment	t	E_{th}	$\Phi^{UL}_{>E_{th}}$	reference
	h	GeV	$10^{-13}/(\mathrm{cm}^2\,\mathrm{s})$	
MAGIC	70	250	22	Aleksić et al. [2010]
VERITAS	44.70	263	7	Archambault et al. [2013]
	10.35	400	14.2	Guenette [2009]
	44.70	603	2	Archambault et al. [2013]
	≈50	250	6.94	this work
		263	5.62	
		400	2.30	
		603	1.40	

Table 6.6: Upper limits on the flux from Cygnus X-3 obtained from several observations with the IACTs *MAGIC* and *VERITAS*. Time t represents the exposure time of the observation, E_{th} the energy threshold of the analysis and Φ^{UL} the upper limits on the integral flux above E_{th} at 95 % confidence level, assuming a spectral index of 2.4. The last column indicates the corresponding reference. The upper limits were derived with moderate and hard cuts depending on the energy threshold.

object	experiment	t	E_{th}	$\Phi^{UL}_{>E_{th}}$	reference
		h	GeV	$10^{-13}/(\mathrm{cm}^2\,\mathrm{s})$	
EXO 2030+375	*VERITAS*	6.69	400	22.2	Guenette [2009]
		6.67	400	20.05	this work
KS1947+300	*VERITAS*	3.95	400	28.8	Guenette [2009]
		0.50	400	32.78	this work
XTE J2012+381	*VERITAS*	13.91	400	24.5	Guenette [2009]
		25.70	400	9.75	this work

Table 6.7: Upper limits on the flux from EXO 2030+375, KS 1947+300, and XTE J2012+381 obtained from several observations with the IACTs *MAGIC* and *VERITAS*. Time t represents the exposure time of the observation, E_{th} the energy threshold of the analysis and Φ^{UL} the upper limits on the integral flux above E_{th} at 95 % confidence level assuming a spectral index of 2.4. The last column indicates the corresponding reference.

KS1947+300 ($\approx 10^{-4} L_{edd}$). As the distance of the binary system XTE J2012+381 is not known to date no limits on its luminosity at very high energies could be derived.

object	M_c	P_{orb}	d	L_{edd}	$L_{>300\,\mathrm{GeV}}$	$L_{>600\,\mathrm{GeV}}$
	$M_\odot$	d	kpc	10^{38} erg/s	10^{35} erg/s	10^{35} erg/s
EXO 2030+375	1.4	46.02	7.1	1.76	15.86	10.45
KS1947+300	1.4	40.415	≈10	1.76	1.09	0.48
XTE J2012+381	10	3-12	unknown	1.26		

Table 6.8: Upper limits on the γ-ray luminosities from EXO 2030+375, KS 1947+300, and XTE J2012+381 derived here. The mass of the compact objects is denoted as M_c, the orbital period of the system is P_{orb}, the distance is d, its Eddington luminosity is denoted as L_{edd}, and the upper limits on the γ-ray luminosities above an energy E_{VHE} derived here are represented by $L_{>E_{VHE}}$. The parameters characterising the system are obtained from Guenette [2009].

Colliding wind binary systems

The colliding wind binaries (CWBs) WR140, WR146, and WR147 have long been observed at other wavelengths. For current satellite and ground-based instruments at γ-ray energies, the colliding wind zone does not appear to be spatially resolved [Reimer et al., 2006]. This presents individual CWB systems as point sources at these energies and upper limits were derived with point-source analyses here. The results are listed in Table 6.3 and Table B.7 for both hard and moderate cuts. The detection of CWBs in the VHE regime would set constrains on the maximum particle energy reached by such a system.

WR140 is a massive binary system comprising a WC7-type Wolf-Rayet star and an O4-5 companion star [van der Hucht, 2001]. This system exhibits variable emission at radio, IR, optical, radio, and X-ray wavelengths [Setia Gunawan et al., 2001, and references therein], and is one of the brightest non-compact stellar X-ray sources [Pollock, 1987]. The period of this CWB system was estimated to be 7.9 yr [Williams et al., 1987]. The variability of its emission from near-infrared to radio wavelengths seems to be linked to the distance between the two objects, in particular the region where the massive stellar winds collide and accelerate the particles. γ-ray emission at TeV energies is expected to be considerable at certain phases of the orbit of the system; especially at periods close to periastron [Pittard and Dougherty, 2006] as the density of the wind collision region is very high at this point. Thus, the radiation fields are very strong leading to more inverse Compton scattering of electrons and therefore VHE γ-ray emission. The observations of WR140 included in the dataset used here were taken between 2008/09/24 (Modified Julian Day (MJD): 54733) and 2008/11/02 (MJD: 54772). Following Marchenko et al. [2003], the orbital phase of the observations was around periastron between $\Phi_{orb} \sim 0.98 - 0.99$. In addition, upper limits on the flux were obtained, 3.36 % of the Crab Nebula flux for E_{th}>600 GeV and 4.62 % for E_{th}>300 GeV. The derived upper limits are consistent with model predictions obtained from

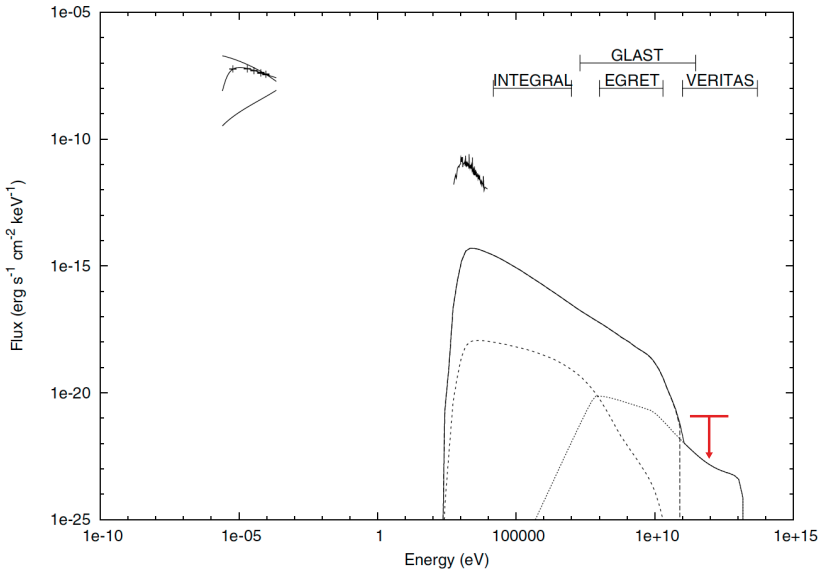

Figure 6.22: The radio (data points), and nonthermal UV, X-ray and γ-ray emissions of WR140. The model inverse Compton scattering (long-dashed line), relativistic bremsstrahlung (short-dashed line), and pion decay (dotted line) emission components are shown, along with the total emission (solid line). The binary separation is assumed to be 3.13×10^{14} cm, the distance to the object 1.85 kpc, the angle of the line of sight into the system 35°. The red line represents the upper limit derived here. Figure adapted from Pittard and Dougherty [2006].

Pittard and Dougherty [2006], as shown Figure 6.22. Additional observations close to periastron will help constraining the models, and to allow better predictions of the flux at TeV energies. The closest distance between the Wolf-Rayet star and its companion is expected to occur again on September 14th, 2024.

WR146 is a binary system, comprising a Wolf-Rayet star and an OB-type star [Dougherty et al., 2000], with variable nonthermal radio emission [van der Hucht et al., 1995]. It is located approximately 0.7° away from the TeV J2032+4130 [Albert et al., 2008b]. The observations of WR146 included in the dataset used here were studied and upper limits were set. Specifically, two values were obtained after an observing time of about 49.94 h, 0.26 % of the Crab Nebula flux for E_{th}>600 GeV or $1.21 \times 10^{-13}/(\mathrm{cm}^2\,\mathrm{s})$, and 0.20 % for E_{th}>300 GeV. The value obtained for E_{th}>600 GeV is about a fifth of the one obtained with *MAGIC* after a similar time of observation (44.5 h) , $\Phi^{UL} = 5.6 \times 10^{-13}/(\mathrm{cm}^2\,\mathrm{s})$ [Aliu et al., 2008].

WR147, located at a distance of 650 pc [Setia Gunawan, 2001, and references therein], is one of the closest systems showing nonthermal radio emission. This system is resolved into a northern nonthermal component (WR147N) and a southern thermal one (WR147S) [Churchwell et al., 1992]. The observations of WR147 included in the dataset here were studied and upper limits were derived. The values derived for hard and moderate cuts after 32.5 h of observation were, 0.56 %

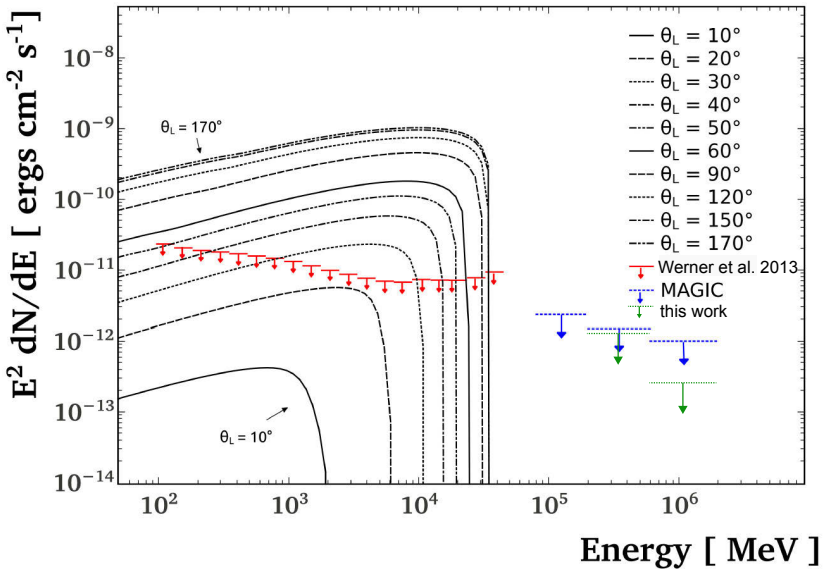

Figure 6.23: Differential flux upper limits (red lines) of WR147 obtained from *Fermi*-LAT [Werner et al., 2013] and from MAGIC measurements (blue dashed lines) [Aliu et al., 2008] compared to models explained in Reimer and Reimer [2009]. The green dotted lines represent the integral upper limits derived here. Figure adapted from Werner et al. [2013].

of the Crab Nebula flux for E_{th}>600 GeV or $2.58 \times 10^{-13}/(\mathrm{cm}^2\,\mathrm{s})$, and 0.36 % for E_{th}>300 GeV. The value obtained for E_{th}>600 GeV is about a factor of 2.8 smaller than the one obtained with *MAGIC* after a similar time of observation (30.3 h) , $\Phi^{UL} = 7.3 \times 10^{-13}/(\mathrm{cm}^2\,\mathrm{s})$ [Aliu et al., 2008]. Figure 6.23 shows the derived *VERITAS* results along with the measurements obtained from *MAGIC* and *Fermi*-LAT [Werner et al., 2013], indicating its consistency with the model predictions. However, it is worth noticing that the upper limits reported in the VHE regime do not pose additional constraints on the assumed models.

Deeper observations of WR140 with improved sensitivity in the energy range between around 50 GeV to 100 GeV, such as with *Fermi*-LAT[1] or the future *CTA*[2] may allow more precise predictions of its flux at GeV to TeV energies and help constraining the models. However, it will be challenging to set constraints on the models of WR147 due to the expected sensitivity of *CTA* below 100 GeV and the model predictions of this system.

Pulsars and unidentified objects

Within the survey region, excluding the four detected VHE γ-ray emitters, 27 objects of the third source catalogue of *Fermi*-LAT were identified. From these sources, 15 are associated

[1] https://www.slac.stanford.edu/exp/glast/groups/canda/lat_Performance.htm
[2] https://web.cta-observatory.org/science/cta-performance/

object 3FGL	S	Γ_{HE}	$\Phi_{>1\,\mathrm{GeV}_{HE}}$	$\Phi_{>300\,\mathrm{GeV}_{VHE}}$
			$10^{-9}/(\mathrm{cm}^2\,\mathrm{s})$	$10^{-13}/(\mathrm{cm}^2\,\mathrm{s})$
J2014.4+3606	4.69	2.40 ± 0.11	1.13 ± 0.24	$3.88^{+4.70}_{-1.46}$
J2023.5+4126	3.75	2.54 ± 0.16	2.51 ± 0.36	$3.86^{+5.71}_{-2.30}$
J2035.0+3634	4.60	1.89 ± 0.22	2.47 ± 0.28	$\left(1.54^{+3.94}_{-1.11}\right) \times 10^2$
J2037.4+4132	4.49	2.18 ± 0.11	1.83 ± 0.34	$0.22^{+1.89}_{-0.02}$
J2039.4+4111	3.97	2.84 ± 0.23	2.88 ± 0.52	$\left(7.78^{+21.45}_{-5.71}\right) \times 10^{-1}$

Table 6.9: Predictions of the flux at very high energies, Φ_{VHE}, above 300 GeV for studied objects of the third *Fermi*-LAT catalogue [Acero et al., 2015] with significance larger 3.5 in this *VERITAS* analysis. The VHE flux is derived based on the flux of the objects at high energies, Φ_{HE}, above 1 GeV [Acero et al., 2015]. The spectral index of the objects in the high-energy regime is denoted as Γ_{HE}.

with the Cygnus cocoon field. Table 6.3, Table 6.4, Table B.7, and Table B.8 list the upper limits on the flux derived here, assuming an energy spectrum following a power law with index 2.4. The pulsar 3FGL J2021.5+4026 is locally coincident with the γ-Cygni pulsar and its analysis resulted in a significance of 7.67σ (Section 6.2.3). No additional object showed significant detection at VHE γ-rays. It is worth noting that the limits on the flux for individual sources associated with the Cygnus cocoon field might reflect poor estimations of the total Cocoon diffuse emission. However, there are five objects whose analysis resulted in a significance larger 3.5σ when using moderate cuts optimised for extended-source searches: 3FGL J2014.4+3606, 3FGL J2023.5+4126, 3FGL J2035.0+3634, 3FGL J2037.4+4132, and 3FGL J2039.4+4111. As these objects were detected in the high-energy regime, the measurements of the high-energy γ-ray flux can be extrapolated to derive the flux in the VHE regime by assuming a power-law spectrum with index Γ_{HE} (Equation 6.16). The results are listed in Table 6.9. The estimated flux at VHE γ-rays is larger than the upper limit on the flux obtained from the *VERITAS* analysis, derived here, except for J2035.0+3634. In this case, the derived upper limit from the *VERITAS* analysis is about a factor two lower than the estimated one. As a power law was assumed to estimate the VHE flux, the real spectrum must follow a power law with a curvature or with a spectral cutoff below 300 GeV. In the cases where the *VERITAS* upper limits were larger than the extrapolated one from *Fermi*-LAT, additional data obtained with the *VERITAS* experiment or future IACTs are necessary in order to set better constraints on their VHE γ-ray emission Previous observations of PSR B1951+32 at very high energies have been carried out by the *MAGIC* experiment [Albert et al., 2007a]. The amount of data available here (2.00 h) is only a fraction of the dataset used by *MAGIC* (30.70 h). Thus, the derived upper limit on the flux is much larger ($103.02 \times 10^{-13}/(\mathrm{cm}^2\,\mathrm{s})$ above 280 GeV) than the one obtained by *MAGIC* ($27 \times 10^{-13}/(\mathrm{cm}^2\,\mathrm{s})$)

above the same energy and not very meaningful. Additional data of this object are needed in order to set better constraints on the VHE γ-ray emission.

Uncertainties

When calculating the flux of an object, sources of uncertainty have to be taken into account. First of all, the shape of the assumed energy spectrum of the object affecting the effective γ-ray collection area has to be considered. For the objects studied here without previous significant detection in the VHE regime, the spectral index and the shape of the spectrum is not known apriori. The presented upper limits on the flux are evaluated under the assumption of a power-law energy spectrum with a spectral index of 2.4. The estimated VHE γ-ray emission strongly depends on the assumed shape of the spectrum of the source, affecting the γ-ray collection area of *VERITAS*. In particular, a harder spectral index of about 2.0 would result in larger effective areas and consequently, more constraining limits are expected (compare with Equation 6.12).

Furthermore, the systematic uncertainty of the energy scale is estimated to about 20 %. Thus, for a spectral index of 2.4, the systematic uncertainty on the energy threshold corresponds to an uncertainty of about 30 % on the integral flux. For a detailed discussion of systematic uncertainty arising from data analysis of the *VERITAS* instrument see Fleischhack [2017]. Hard cuts provide slightly more sensitive limits than moderate cuts for some sources.

7

Summary and conclusions

In this final chapter, the analyses and studies presented in the thesis are summarised and placed in a wider context.

Understanding the origin and acceleration mechanism of cosmic rays in our Galaxy is one of the key questions in the field of γ-ray astronomy. Ground-based γ-ray astronomy offers the possibility to study the underlying high-energy astrophysical processes occurring in the Universe. Multiple objects, such as supernova remnants, pulsar wind nebulae, and binary systems, can accelerate particles up to very high energies above 100 GeV. These particles can in turn produce γ-rays, detectable with ground-based imaging atmospheric Cherenkov telescopes (IACTs). The sensitivity of current instruments is determined by their ability to suppress the contribution of hadron-induced particle showers developed in the Earth's atmosphere while retaining those initiated by γ-rays.

In this thesis, an analysis technique for γ/hadron separation based on Boosted Decision Trees (BDTs) was developed, evaluated, and applied to data collected by the *VERITAS* experiment, an array consisting of four IACTs. The BDTs were trained and tested with Monte-Carlo (MC) simulations of γ-rays and hadron showers from real data collected in observations of γ-ray sources. A number of classifiers were defined, taking into account the different classes of data, with bins in reconstructed energy and zenith angle. The robustness of the new method was shown for a wide variety of γ-ray sources. The consistency of the BDT response was checked by comparing the γ-ray excess and the spectrum from the Crab Nebula to the results obtained with the *VERITAS* standard analysis. Systematic studies showed that this MVA approach is well suited for the analysis of γ-ray data obtained with *VERITAS*. The BDT method was developed to be easily adaptable, such that it can be applied to *VERITAS* data taken with different array configurations and various observing conditions. For this, BDT classifiers are defined for different expected source characteristics, such as intensity and spectral shape. Currently, the optimised cuts based on the BDT response achieve a 20 to 25 % gain in sensitivity for a given observation time compared to the *VERITAS* standard analysis using the box cuts approach.

Possible future improvements of the method include a deeper study of the effect of the geomagnetic field on the shower development with respect to the arrival direction of the initiating particle and further optimisation of the method for data taken with only three telescopes. Beyond the classifying variables used in this work, the inclusion of additional parameters with discrimination potential between hadrons and γ-rays can further improve the performance of the BDTs. These

classifiers describe the properties of the original image in three dimensions and their optimisation potential was shown for other IACT experiments [Becherini et al., 2011]. In addition, there are ongoing campaigns studying the reconstruction of the image parameters by comparing the raw shower image with templates based on predictions from simulations. This template method is currently under development for application to *VERITAS* data [Vincent, 2015]. Combining this approach with the aforementioned three-dimensional shower parameters can further increase the sensitivity of the *VERITAS* data analysis.

In the second part of this thesis, the BDT method was used to analyse γ-ray data obtained from the Cygnus region, an active star-forming region of our Galaxy. The observation of the Cygnus region, and in particular the region of Cygnus X, benefit from the fact that most of the γ-ray sources are located at a close distance of 1 to 2 kpc from the solar system. The analysis presented here uses data taken during approximately 295 h and spanning an area of $15^\circ \times 5^\circ$ in Galactic coordinates. Detailed MC simulations of the survey observations were performed to estimate the trials factor, taking into account the blind search of the sky survey area for a γ-ray signal. After accounting for the trials factor, no new very-high-energy (VHE) γ-ray emission was detected in the survey region. Four known sources were detected in VHE γ-rays: VER J2031+415, VER J2019+407, VER J2019+368, and VER J2016+371. They were analysed in detail and compared to possible counterparts measured at other wavelengths. The spectra of three of the sources were fit to a power law. For VER J2031+415 and VER J2019+368, the spectral indices obtained here are found to be consistent with those obtained in previous measurements. In contrast, the spectrum obtained for VER J2019+407 is significantly softer than the previously published results by *VERITAS*. The additional amount of data available for the present analysis could lead to the softer spectral index. To understand if the VHE γ-rays originated from leptonic or hadronic interactions, the *VERITAS* data should be combined with data from other experiments and detailed modelling of the combined spectral energy distribution is necessary. Further studies of the VHE γ-ray data obtained with *VERITAS*, together with the results obtained from an updated analysis of the *Fermi*-LAT dataset [VERITAS collaboration, in preparation; Popkow, 2017], can help shed light on this. Detailed modelling of the spectral energy distribution from high-energy to VHE γ-rays can help resolve the question of the origin of the γ-rays.

The data of 50 potential γ-ray sources were analysed and, thanks to the greater sensitivity reached with the BDT method, the most stringent upper limits to date were set on the VHE γ-ray emission for all four different source-type scenarios. Further independent observations with *VERITAS* of sources detected by *Fermi*-LAT, specifically those seen to have significances above 3σ, could result in detections of new sources.

Future analyses will benefit from advances in background suppression methodology such as the use of the maximum likelihood approach, as implemented in *ctools* [Knödlseder et al., 2016]. In

this approach, the cosmic-ray background is modelled either from data or MC simulations. This helps to avoid the problem of overestimating the background for very extended sources when using the ring background model, as occurs when the source covers the whole field of view. This is especially important when studying the Cygnus region with the large amount of diffuse emission and potential γ-ray sources. The Cygnus cocoon is a region that would particularly benefit from the maximum likelihood approach, since its γ-ray emission covers the whole field of view of *VERITAS*. It has been associated with the coincident diffuse emission detected by *Milagro* and *ARGO-YBJ*. Analysis of *VERITAS* data using the maximum likelihood approach may help identify the sources which are powering this emission.

The next generation of γ-ray observatories will benefit from the latest technological and methodological developments. The future Cherenkov Telescope Array (*CTA*) [Acharya et al., 2013] will help to understand the physics and the origin of cosmic rays by detecting new γ-ray sources through large-scale survey observations. This experiment will complement and extend observations made by the High Altitude Water Cherenkov Gamma-Ray Observatory (*HAWC*) at higher energies up to 100 TeV. Observations taken with *CTA* and *HAWC* will help face the challenge presented by the Cygnus region with its multiple extended sources overlapping each other. Improvements of the instrument's technology with larger field of views, lower energy thresholds, and better angular resolution with the future *CTA* may contribute to disentangle these sources. In addition, *CTA* can benefit from the use of the BDT method developed here.

Observations taken with *CTA* and *HAWC* will deepen our understanding of the Cygnus cocoon. In addition, *CTA* will help clarify the association between VER J2019+407 and the supernova remnant G78.2+2.1. Additional sources of VHE γ-ray emission associated with VER J2019+368 can be identified and counterparts to the emission seen from VER J2016+371 may be detected. Deep observations of the spatial and spectral morphology of the region of TeV J2032+4130 by *HAWC* and *CTA* will determine whether additional sources exist in this region and whether the γ-ray emission observed from VER J2031+415 originates from the acceleration of protons or electrons.

Understanding the physics processes of the individual objects in the Cygnus region, a small-scale version of the Galaxy, can help expand our understanding of the broader picture of the physics in the Milky Way.

A

Supplementary material for Chapter 4

A.1 Optimized training cut values of the Boosted Decision Trees

E	ϑ	V4		V5	
		moderate	hard	moderate	hard
0.08 TeV to 0.32 TeV	0° to 22.5°	0.64	0.66	0.65	0.67
	22.5° to 32.5°	0.54	0.64	0.54	0.63
	32.5° to 42.5°	0.51	0.60	0.53	0.62
	42.5° to 75°	0.08	0.12	0.23	0.26
0.32 TeV to 0.50 TeV	0° to 22.5°	0.54	0.56	0.54	0.57
	22.5° to 32.5°	0.60	0.62	0.62	0.65
	32.5° to 42.5°	0.62	0.63	0.71	0.73
	42.5° to 75°	0.45	0.47	0.48	0.50
0.50 TeV to 1 TeV	0° to 22.5°	0.16	0.18	0.42	0.45
	22.5° to 32.5°	0.31	0.34	0.53	0.56
	32.5° to 42.5°	0.59	0.62	0.69	0.73
	42.5° to 75°	0.54	0.57	0.39	0.42
1 TeV to 50 TeV	0° to 22.5°	0.01	0.01	0.52	0.52
	22.5° to 32.5°	0.07	0.07	0.46	0.46
	32.5° to 42.5°	0.04	0.04	0.52	0.52
	42.5° to 75°	0.29	0.29	0.32	0.39

Table A.1: Optimized BDT cut values T_{sel} for moderate and hard sources for the different *VERITAS* array configuration epochs for each band of energy, E, and zenith angle, ϑ, as obtained with *eventDisplay* version `v480b`, used in this thesis.

A.2 Response of the Boosted Decision Trees

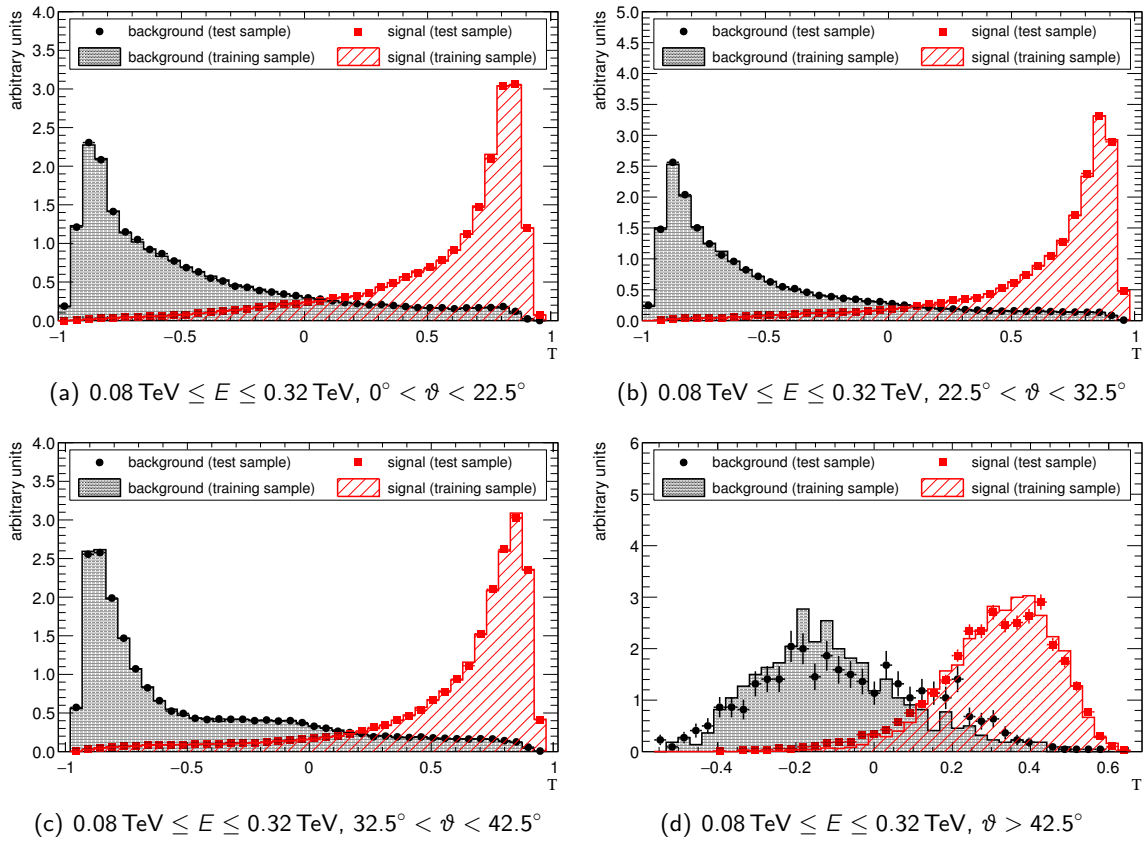

(a) 0.08 TeV $\leq E \leq$ 0.32 TeV, $0^\circ < \vartheta < 22.5^\circ$

(b) 0.08 TeV $\leq E \leq$ 0.32 TeV, $22.5^\circ < \vartheta < 32.5^\circ$

(c) 0.08 TeV $\leq E \leq$ 0.32 TeV, $32.5^\circ < \vartheta < 42.5^\circ$

(d) 0.08 TeV $\leq E \leq$ 0.32 TeV, $\vartheta > 42.5^\circ$

Figure A.1: BDT response, T, for an independent test sample of known signal and background composition for energies, E, between 0.08 TeV and 0.32 TeV, and different ranges of zenith angles, ϑ. Signal events are simulated γ-rays, background events consist of cosmic-ray events from data.

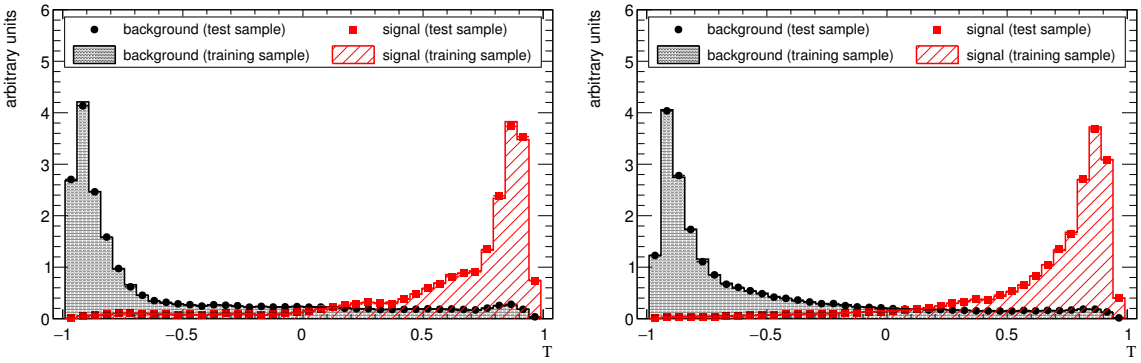

(a) 0.32 TeV $\leq E \leq$ 0.50 TeV, $0^\circ < \vartheta < 22.5^\circ$

(b) 0.32 TeV $\leq E \leq$ 0.50 TeV, $22.5^\circ < \vartheta < 32.5^\circ$

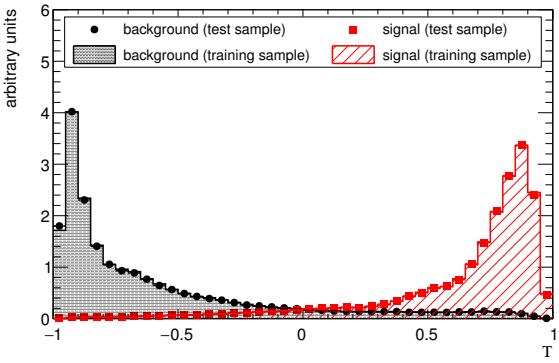

(c) 0.32 TeV $\leq E \leq$ 0.50 TeV, $32.5^\circ < \vartheta < 42.5^\circ$

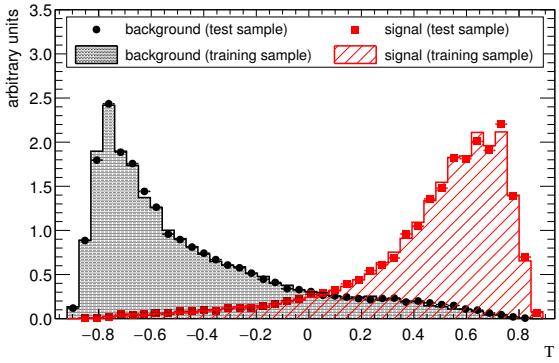

(d) 0.32 TeV $\leq E \leq$ 0.50 TeV, $\vartheta > 42.5^\circ$

Figure A.2: BDT response, T, for an independent test sample of known signal and background composition for energies, E, between 0.32 TeV and 0.50 TeV, and different ranges of zenith angles, ϑ. Signal events are simulated γ-rays, background events consist of cosmic-ray events from data.

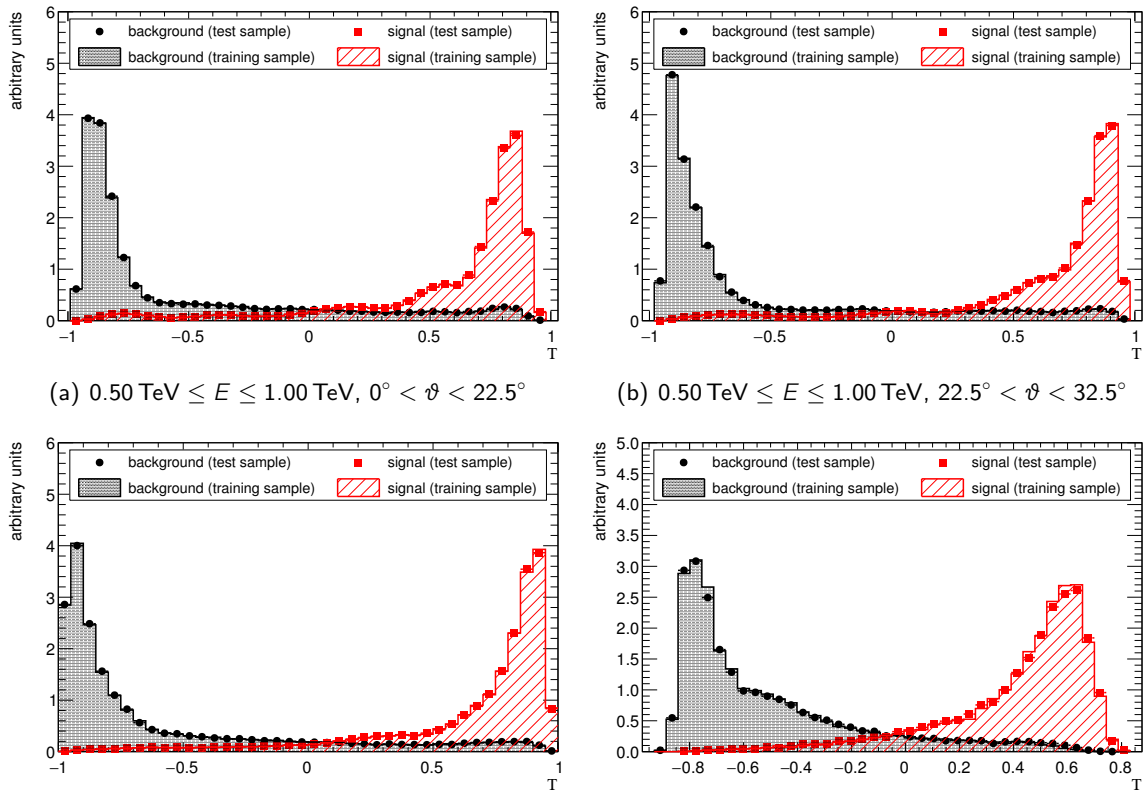

(a) 0.50 TeV $\leq E \leq$ 1.00 TeV, $0^\circ < \vartheta < 22.5^\circ$

(b) 0.50 TeV $\leq E \leq$ 1.00 TeV, $22.5^\circ < \vartheta < 32.5^\circ$

(c) 0.50 TeV $\leq E \leq$ 1.00 TeV, $32.5^\circ < \vartheta < 42.5^\circ$

(d) 0.50 TeV $\leq E \leq$ 1.00 TeV, $\vartheta > 42.5^\circ$

Figure A.3: BDT response, T, for an independent test sample of known signal and background composition for energies, E, between 0.50 TeV and 1.00 TeV, and different ranges of zenith angles, ϑ. Signal events are simulated γ-rays, background events consist of cosmic-ray events from data.

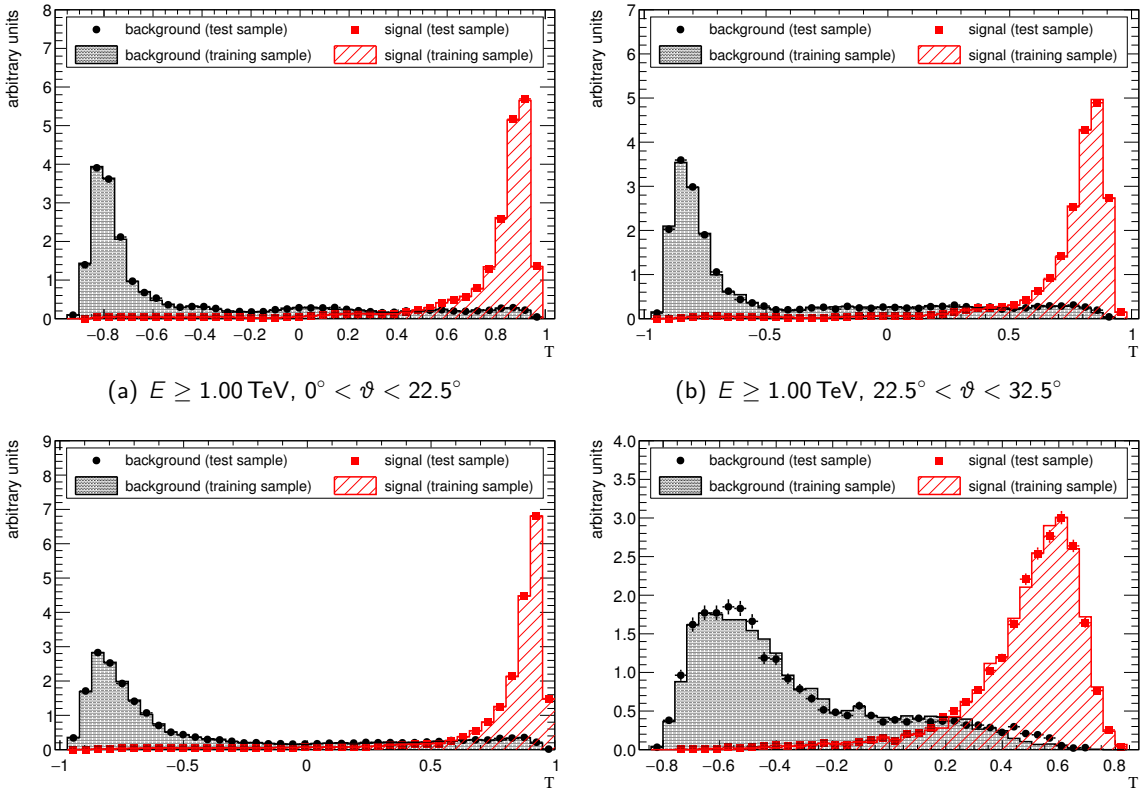

(a) $E \geq 1.00\,\mathrm{TeV}$, $0^\circ < \vartheta < 22.5^\circ$

(b) $E \geq 1.00\,\mathrm{TeV}$, $22.5^\circ < \vartheta < 32.5^\circ$

(c) $E \geq 1.00\,\mathrm{TeV}$, $32.5^\circ < \vartheta < 42.5^\circ$

(d) $E \geq 1.00\,\mathrm{TeV}$, $\vartheta > 42.5^\circ$

Figure A.4: BDT response, T, for an independent test sample of known signal and background composition for energies, E, larger than 1.00 TeV and different ranges of zenith angles, ϑ. Signal events are simulated γ-rays, background events consist of cosmic-ray events from data.

A.3 Signal and background efficiencies after applying T and box cuts

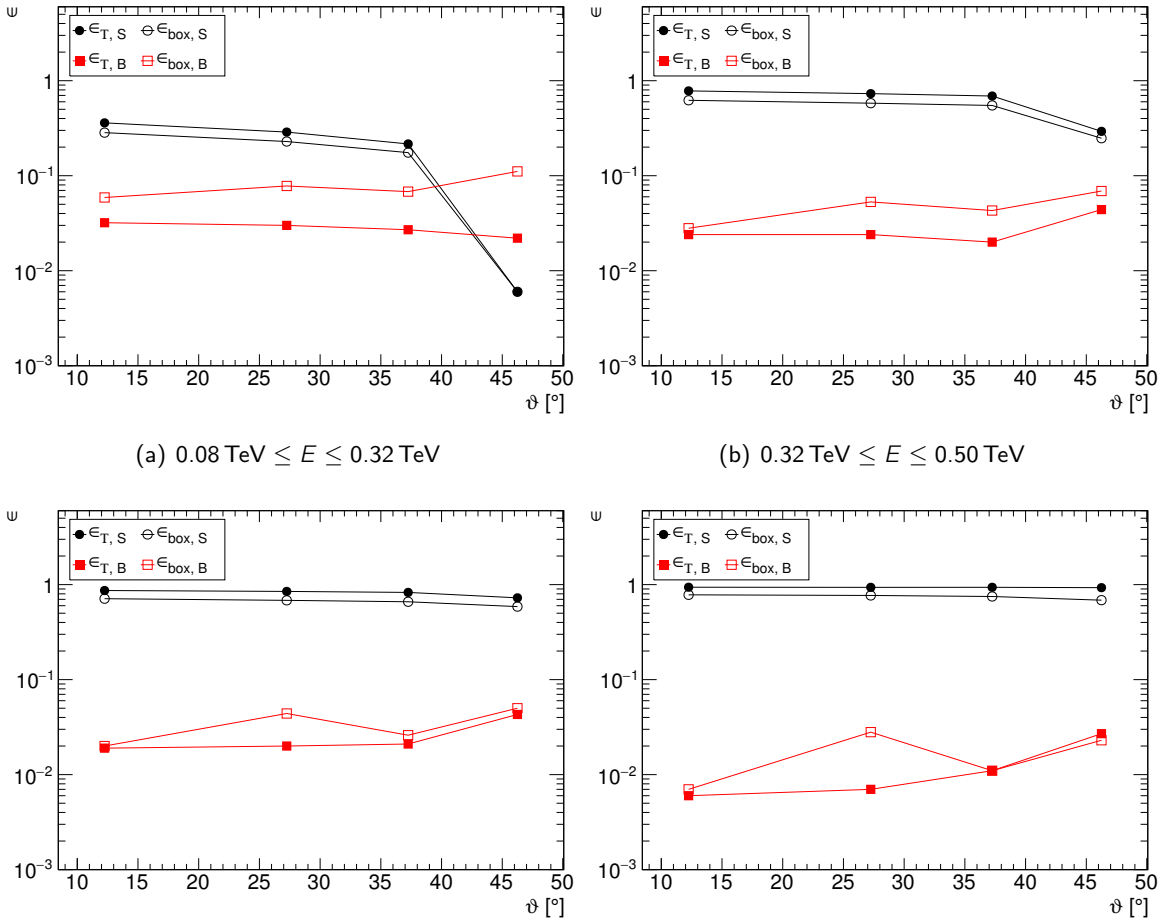

(a) 0.08 TeV $\leq E \leq$ 0.32 TeV

(b) 0.32 TeV $\leq E \leq$ 0.50 TeV

(c) 0.50 TeV $\leq E \leq$ 1.00 TeV

(d) $E \geq$ 1.00 TeV

Figure A.5: Signal (black circles) and background (red squares) efficiency, ϵ, as a function of zenith angle, ϑ, after applying the optimal selection T_{sel} (filled symbols) and the box cuts (open symbols) for all bands of energy, E. The uncertainties of the efficiency are smaller than the size of the symbols.

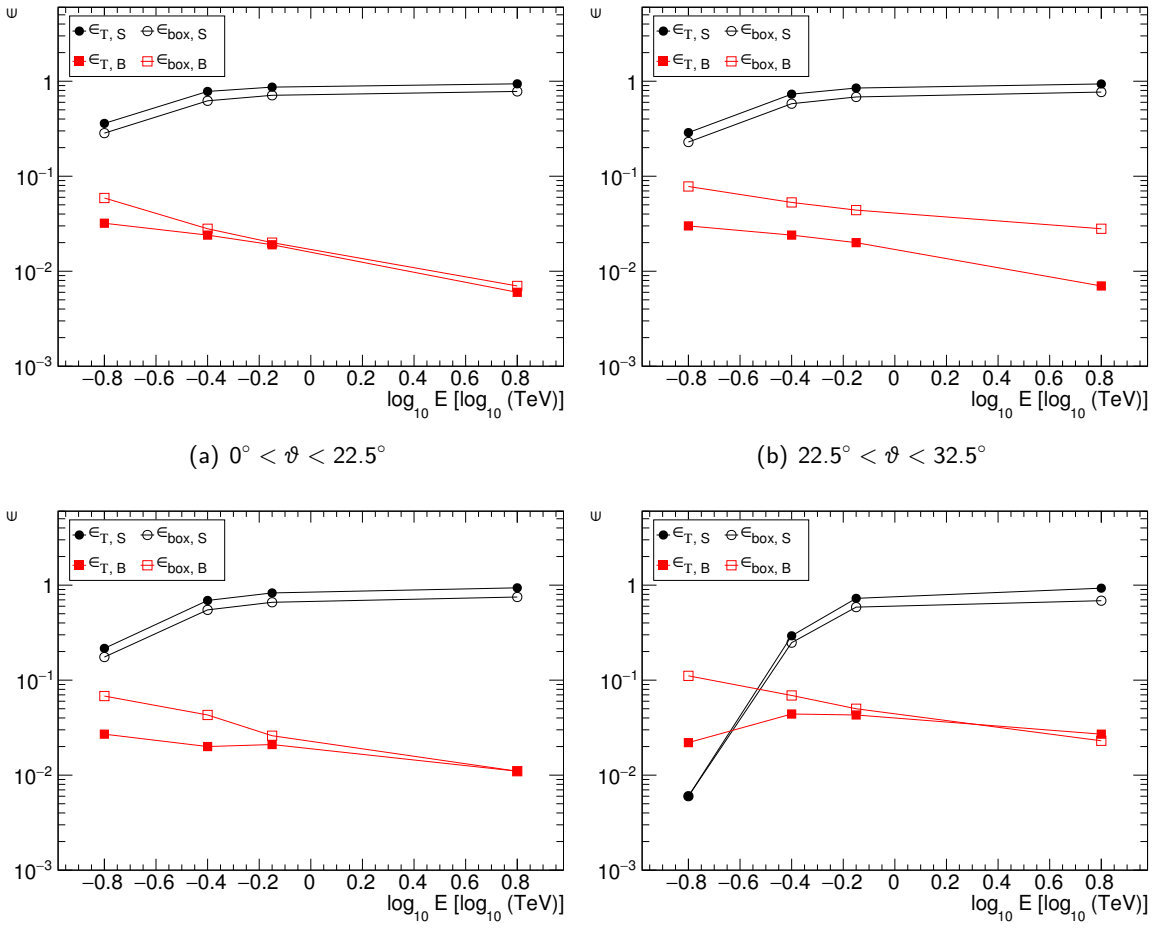

(a) $0^\circ < \vartheta < 22.5^\circ$

(b) $22.5^\circ < \vartheta < 32.5^\circ$

(c) $32.5^\circ < \vartheta < 42.5^\circ$

(d) $\vartheta > 42.5^\circ$

Figure A.6: Signal (black circles) and background (red squares) efficiency, ϵ, as a function of energy, E, after applying the optimal selection T_{sel} (filled symbols) and the box cuts (open symbols) for all bands of zenith angle, ϑ. The uncertainties of the efficiency are smaller than the size of the symbols.

A.4 Sensitivity of moderate cut configuration

array configuration	$\Phi(E)$	t_{box}	t_{T}
	C.U.		
V4	1	2.00 min	1.90 min
	0.30	10.00 min	8.00 min
	0.10	56.90 min	42.40 min
	0.05	3.20 h	2.30 h
	0.03	8.20 h	5.60 h
	0.01	67.00 h	44.70 h
V5	1	1.40 min	1.40 min
	0.30	6.50 min	5.40 min
	0.10	36.60 min	27.20 min
	0.05	2.00 h	1.40 h
	0.03	5.00 h	3.50 h
	0.01	41.50 h	27.20 h
V6	1	1.20 min	1.20 min
	0.30	5.80 min	4.90 min
	0.10	32.10 min	24.80 min
	0.05	1.80 h	1.30 h
	0.03	4.40 h	3.10 h
	0.01	36.10 h	24.30 h

Table A.2: Observation time required for a detection of a point-like VHE γ-ray source with a flux between 1 % and 100 % of the flux of the Crab Nebula in Crab Units (C.U.) for a moderate spectrum source with index $\Gamma = 2.4$ and different *VERITAS* array configurations. The uncertainties of observation time are about 2 to 4 %.

B

Supplementary material for Chapter 6

B.1 Division of the region of the Cygnus sky survey

field N_{ID}	longitude l	latitude b	right ascension α_{J2000}		declination δ_{J2000}
0	$-2°$	$67°$	$301.94°$	$20^h7^m45.5^s$	$+28.84°$
1	$-2°$	$70°$	$303.84°$	$20^h15^m21.5^s$	$+31.35°$
2	$-2°$	$73°$	$305.84°$	$20^h23^m21.5^s$	$+33.82°$
3	$-2°$	$76°$	$307.98°$	$20^h31^m55.2^s$	$+36.26°$
4	$-2°$	$79°$	$310.25°$	$20^h41^m0^s$	$+38.66°$
5	$-2°$	$82°$	$312.68°$	$20^h50^m43.2^s$	$+40.99°$
6	$+1°$	$67°$	$299.01°$	$19^h56^m2.3^s$	$+30.43°$
7	$+1°$	$70°$	$300.86°$	$20^h3^m26.4^s$	$+32.98°$
8	$+1°$	$73°$	$302.82°$	$20^h11^m16.7^s$	$+35.20°$
9	$+1°$	$76°$	$304.91°$	$20^h19^m38.4^s$	$+37.99°$
10	$+1°$	$79°$	$307.13°$	$20^h28^m31.1^s$	$+40.45°$
11	$+1°$	$82°$	$309.52°$	$20^h38^m4.7^s$	$+42.86°$
12	$+4°$	$67°$	$295.99°$	$19^h43^m57.6^s$	$+31.95°$
13	$+4°$	$70°$	$297.78°$	$19^h51^m7.1^s$	$+34.54°$
14	$+4°$	$73°$	$299.68°$	$19^h58^m43.2^s$	$+37.11°$
15	$+4°$	$76°$	$301.69°$	$20^h6^m45.5^s$	$+39.65°$
16	$+4°$	$79°$	$303.85°$	$20^h15^m24^s$	$+42.16°$
17	$+4°$	$82°$	$306.17°$	$20^h24^m40.8^s$	$+44.63°$

Table B.1: Central positions of the fields in Galactic (longitude, l, and latitude, b) and equatorial (right ascension, α_{J2000}, and declination, δ_{J2000}) coordinates as used for the analysis of the Cygnus region observed with *VERITAS*. Each field contains a size of $6° \times 6°$.

B.2 List of exclusion regions of the Cygnus sky survey

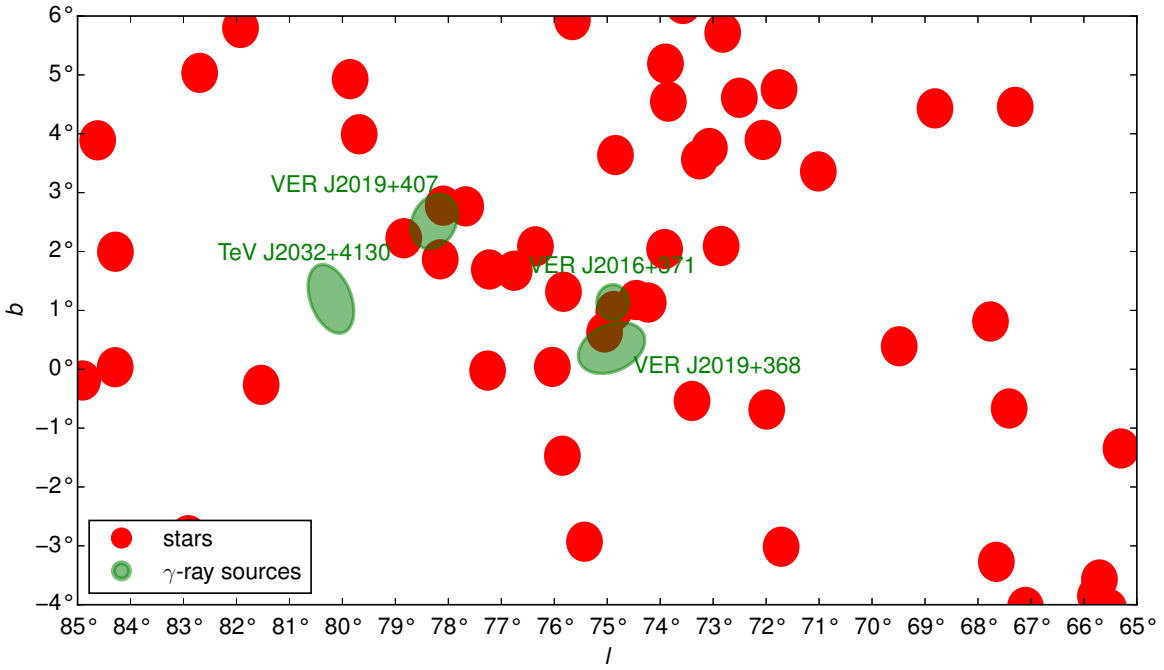

Figure B.1: Position of exclusion regions in Galactic (longitude, l, and latitude, b) coordinates as used for the analysis of the Cygnus region observed with *VERITAS*. The red circles represent stars with a magnitude in the visual band smaller than 6.5, whereas the green symbols depict the positions and approximated extensions of known VHE γ-ray sources.

source	longitude l	latitude b	right ascension α_{J2000}	declination δ_{J2000}	extension
VER J2031+415	80.22°	+1.19°	307.91°	41.56°	$0.62° \times 0.38°$ $\theta_{rot} = 65°$
VER J2019+407	78.27°	+2.51°	304.95°	40.72°	$0.50° \times 0.40°$ $\theta_{rot} = 128°$
VER J2019+368	74.92°	+0.36°	304.86°	37.16°	$0.65° \times 0.40°$ $\theta_{rot} = -19°$
VER J2016+371	74.89°	+1.14°	303.98°	37.16°	$0.30° \times 0.30°$

Table B.2: List of known γ-ray emitters excluded in the analysis of the Cygnus region. For each object, the position in Galactic (longitude, l, and latitude, b) and equatorial (right ascension, α_{J2000}, and declination, δ_{J2000}) coordinates, and their extension used for the exclusion is given. The angle θ_{rot} indicates the orientation of the source from west to north in the Galactic coordinate system.

Table B.3: List of stars excluded in the analysis of the Cygnus region observed with *VERITAS*. For each object, the identifier according to the Hipparcos catalogue [Perryman et al., 1997], HIP ID, the position in Galactic (longitude, l, and latitude, b) and equatorial (right ascension, α_{J2000}, and declination, δ_{J2000}) coordinates is given.

HIP ID	longitude l	latitude b	right ascension α_{J2000}	declination δ_{J2000}
96977	67.30°	+4.46°	295.69°	+32.43°
97118	71.76°	+6.60°	296.07°	+37.35°
97295	68.81°	+4.43°	296.61°	+33.73°
97376	73.00°	+6.57°	296.87°	+38.41°
97630	73.57°	+6.20°	297.64°	+38.72°
97651	72.82°	+5.72°	297.70°	+37.83°
97789	71.76°	+4.76°	298.07°	+36.43°
97985	72.51°	+4.61°	298.70°	+37.00°
98068	73.90°	+5.19°	298.97°	+38.49°
98110	71.01°	+3.36°	299.08°	+35.08°
98143	72.06°	+3.90°	299.18°	+36.25°
98194	75.66°	+5.93°	299.31°	+40.37°
98253	77.36°	+6.79°	299.48°	+42.26°
98320	73.85°	+4.55°	299.64°	+38.11°
98325	67.76°	+0.81°	299.66°	+30.98°
98425	73.07°	+3.76°	299.98°	+37.04°
98543	65.30°	−1.35°	300.28°	+27.75°
98563	73.26°	+3.57°	300.31°	+37.10°
98767	67.41°	−0.67°	300.90°	+29.90°
98863	69.49°	+0.39°	301.15°	+32.22°
98921	74.84°	+3.64°	301.29°	+38.48°
99031	72.85°	+2.09°	301.59°	+35.97°
99303	73.92°	+2.04°	302.36°	+36.84°
99404	65.71°	−3.57°	302.64°	+26.90°
99518	65.78°	−3.85°	302.95°	+26.81°
99531	65.53°	−4.07°	303.00°	+26.48°
99639	82.71°	+6.86°	303.33°	+46.82°
99675	82.68°	+6.77°	303.41°	+46.74°
99685	79.85°	+4.93°	303.43°	+43.38°
99719	74.23°	+1.13°	303.52°	+36.60°
99738	67.65°	−3.27°	303.56°	+28.69°
99770	74.45°	+1.18°	303.63°	+36.81°

Table B.3: continued

HIP ID	longitude l	latitude b	right ascension α_{J2000}	declination δ_{J2000}
99841	71.99°	−0.68°	303.85°	+33.73°
99874	67.10°	−4.04°	303.94°	+27.81°
99889	81.92°	+5.80°	304.00°	+45.58°
99893	76.35°	+2.09°	304.01°	+38.90°
99929	74.88°	+0.99°	304.12°	+37.06°
99968	77.67°	+2.77°	304.23°	+40.37°
100016	79.68°	+3.99°	304.37°	+42.72°
100044	75.83°	+1.32°	304.45°	+38.03°
100069	78.10°	+2.78°	304.53°	+40.73°
100108	75.05°	+0.63°	304.62°	+37.00°
100122	73.40°	−0.54°	304.66°	+34.98°
100155	76.76°	+1.67°	304.74°	+39.00°
100268	77.23°	+1.69°	305.06°	+39.40°
100437	82.69°	+5.03°	305.52°	+45.79°
100453	78.15°	+1.87°	305.56°	+40.26°
100501	78.84°	+2.23°	305.69°	+41.03°
100574	76.04°	+0.04°	305.93°	+37.48°
100587	71.72°	−3.01°	305.96°	+32.19°
100907	77.26°	−0.02°	306.89°	+38.44°
101067	75.85°	−1.47°	307.33°	+36.45°
101474	75.43°	−2.93°	308.48°	+35.25°
101475	84.62°	+3.89°	308.48°	+46.69°
102098	84.29°	+2.00°	310.36°	+45.28°
102155	81.53°	−0.26°	310.49°	+41.72°
102589	78.08°	−4.34°	311.85°	+36.49°
102843	84.29°	+0.03°	312.52°	+44.06°
103089	84.90°	−0.19°	313.31°	+44.39°
103413	82.91°	−2.82°	314.29°	+41.17°

B.3 Trial simulations

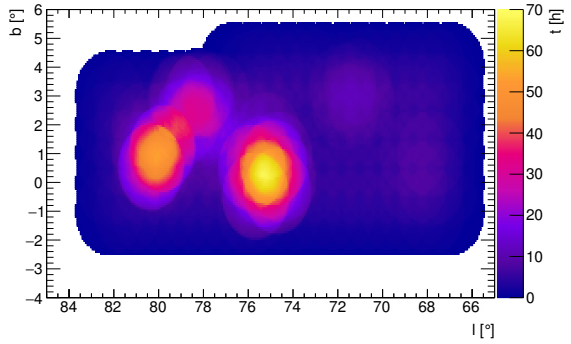

(a) Acceptance-corrected, accumulated observation time, t, in hours.

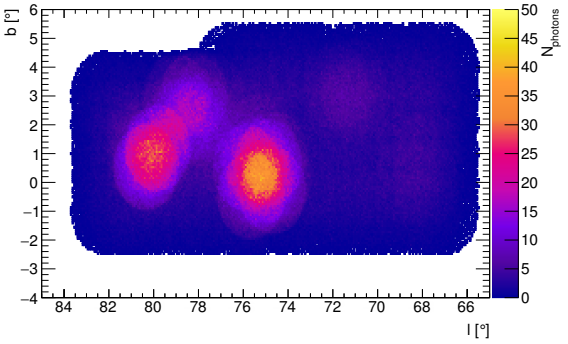

(b) Number of γ-ray-like events, $N_{photons}$.

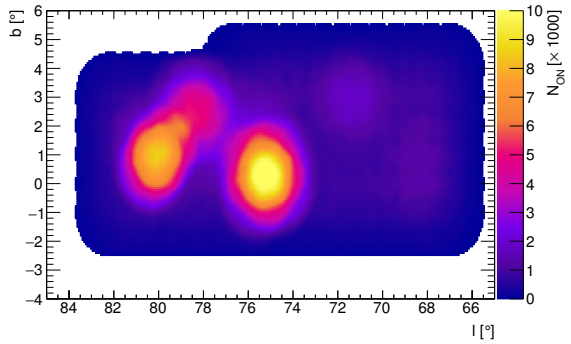

(c) Number of ON events, N_{ON}, summed over a circle of radius θ_{int}.

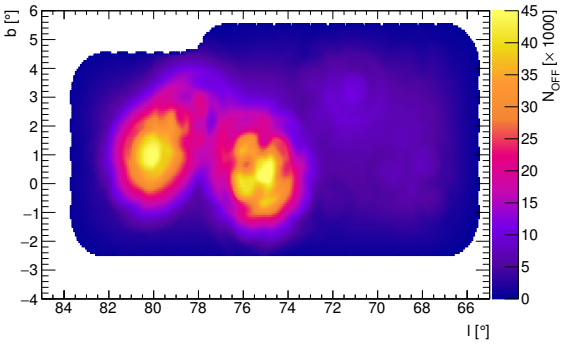

(d) Number of OFF events, N_{OFF}, estimated from a ring with mean radius of $(r_{in} + r_{out})/2$ and an area κ times as large as the ON source region.

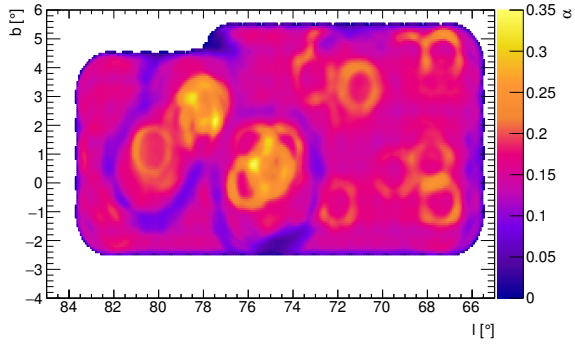

(e) Correction factor, α, estimated from Equation 3.7.

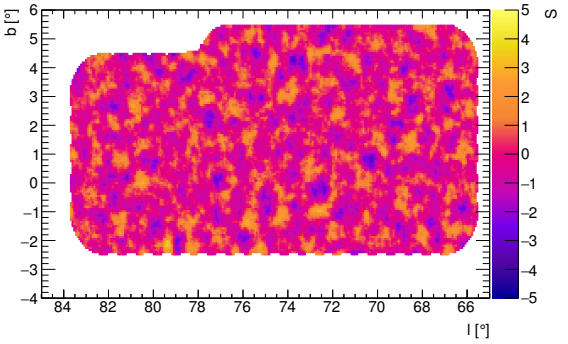

(f) Significance, S, calculated from Equation 3.8.

Figure B.2: Maps used to simulate the trial factor for the analysis. Each maps spans an area of $20° \times 10°$ in Galactic coordinates (longitude, l, and latitude, b). The parameters corresponding to the point- and extended-source analysis are listed in Table 6.1.

B.4 Skymaps of the Cygnus region

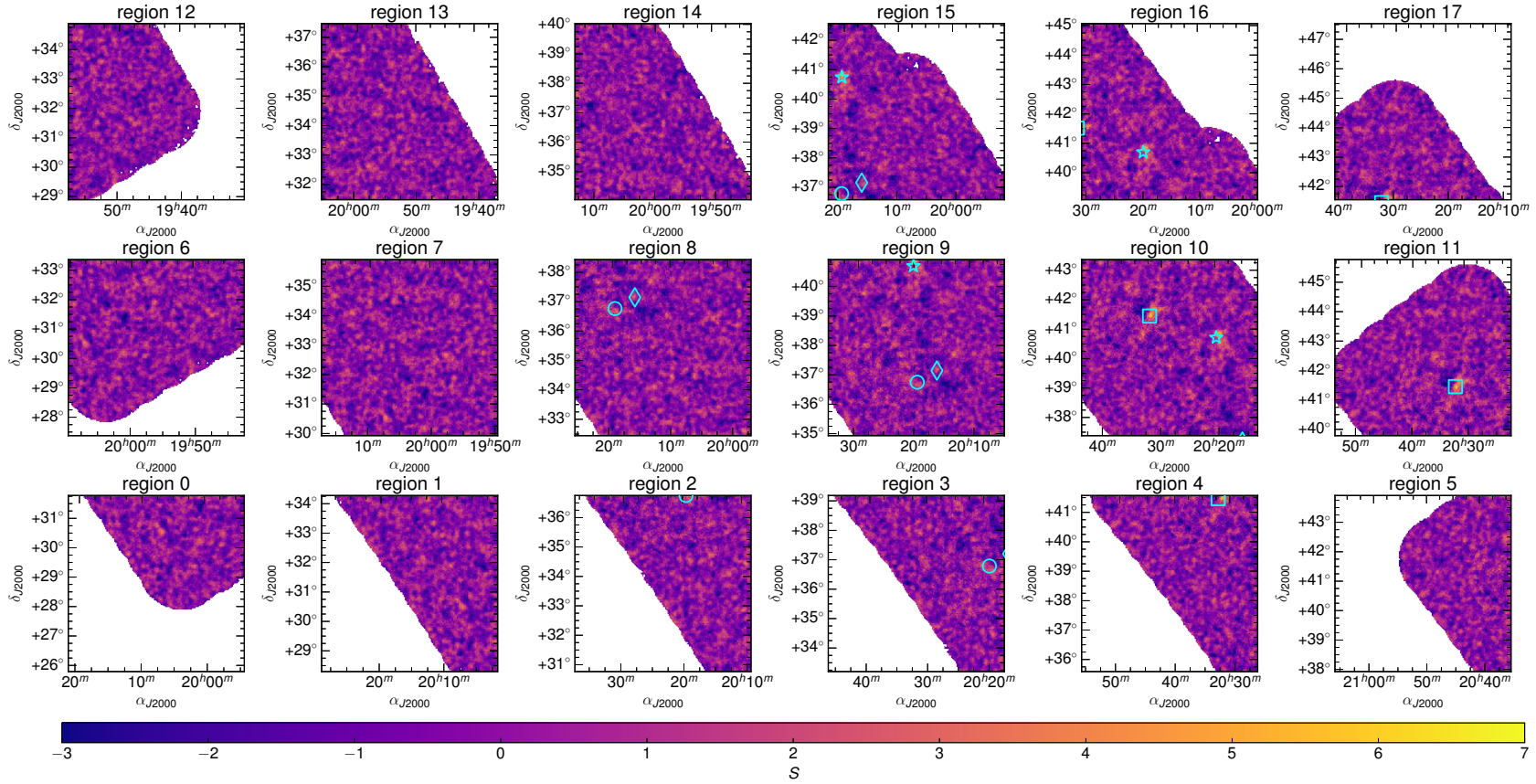

Figure B.3: Significance maps of the *VERITAS* Cygnus sky survey region for the search of point sources. The counts of the ON region are summed from a circle of radius $\theta_{int} = 0.22°$ around each bin. The γ/hadron separation was done using moderate T cuts. The colour scale is saturated at 7σ for visibility. The following objects are also plotted: VER J2031+415 (square), VER J2019+407 (star), VER J2016+371 (diamond), VER J2019+368 (circle).

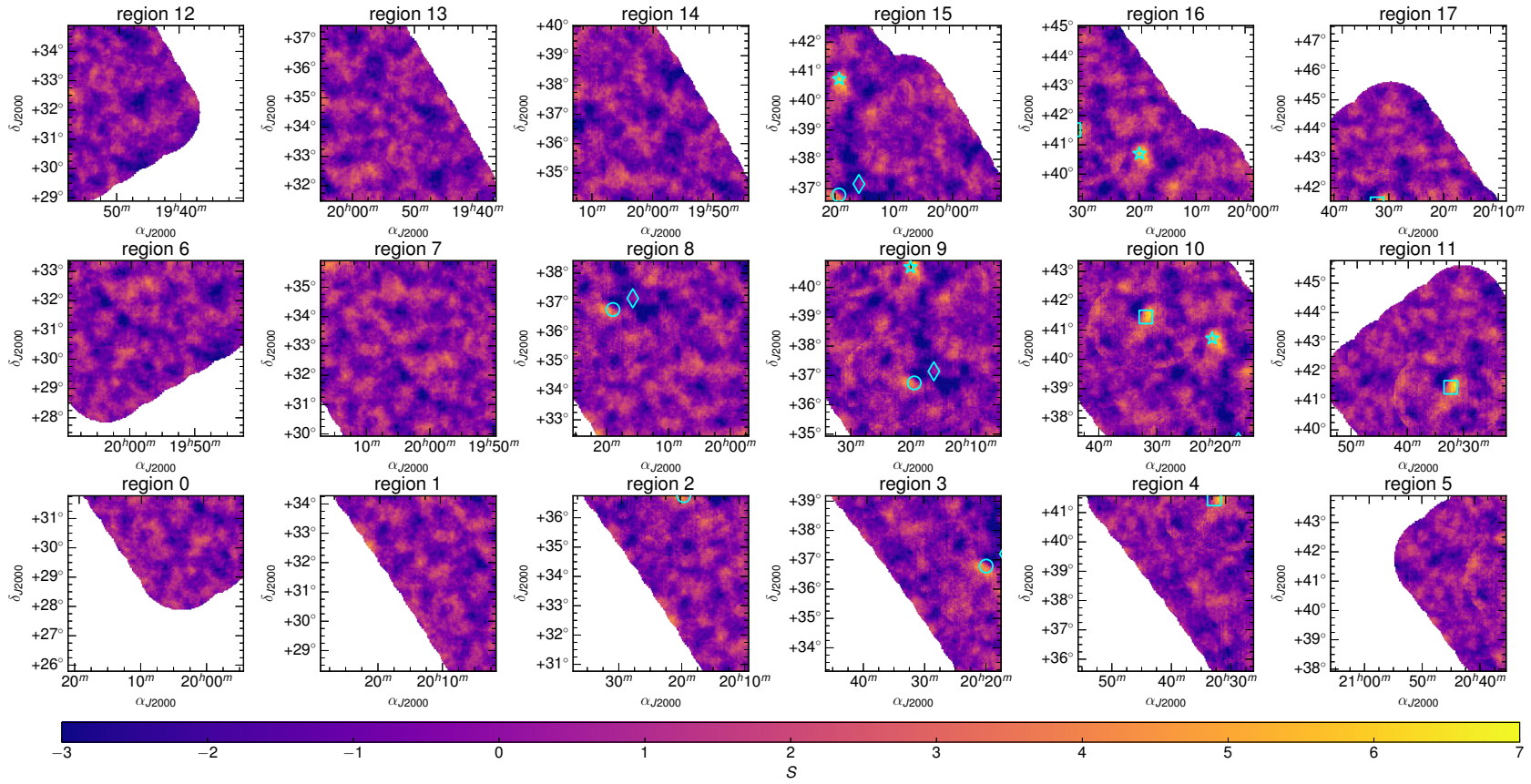

Figure B.4: Significance maps of the *VERITAS* Cygnus sky survey region for the search of extended sources. The counts of the ON region are summed from a circle of radius $\theta_{int} = 0.22°$ around each bin. The γ/hadron separation was done using moderate T cuts. The colour scale is saturated at 7σ for visibility. The following objects are also plotted: VER J2031+415 (square), VER J2019+407 (star), VER J2016+371 (diamond), VER J2019+368 (circle).

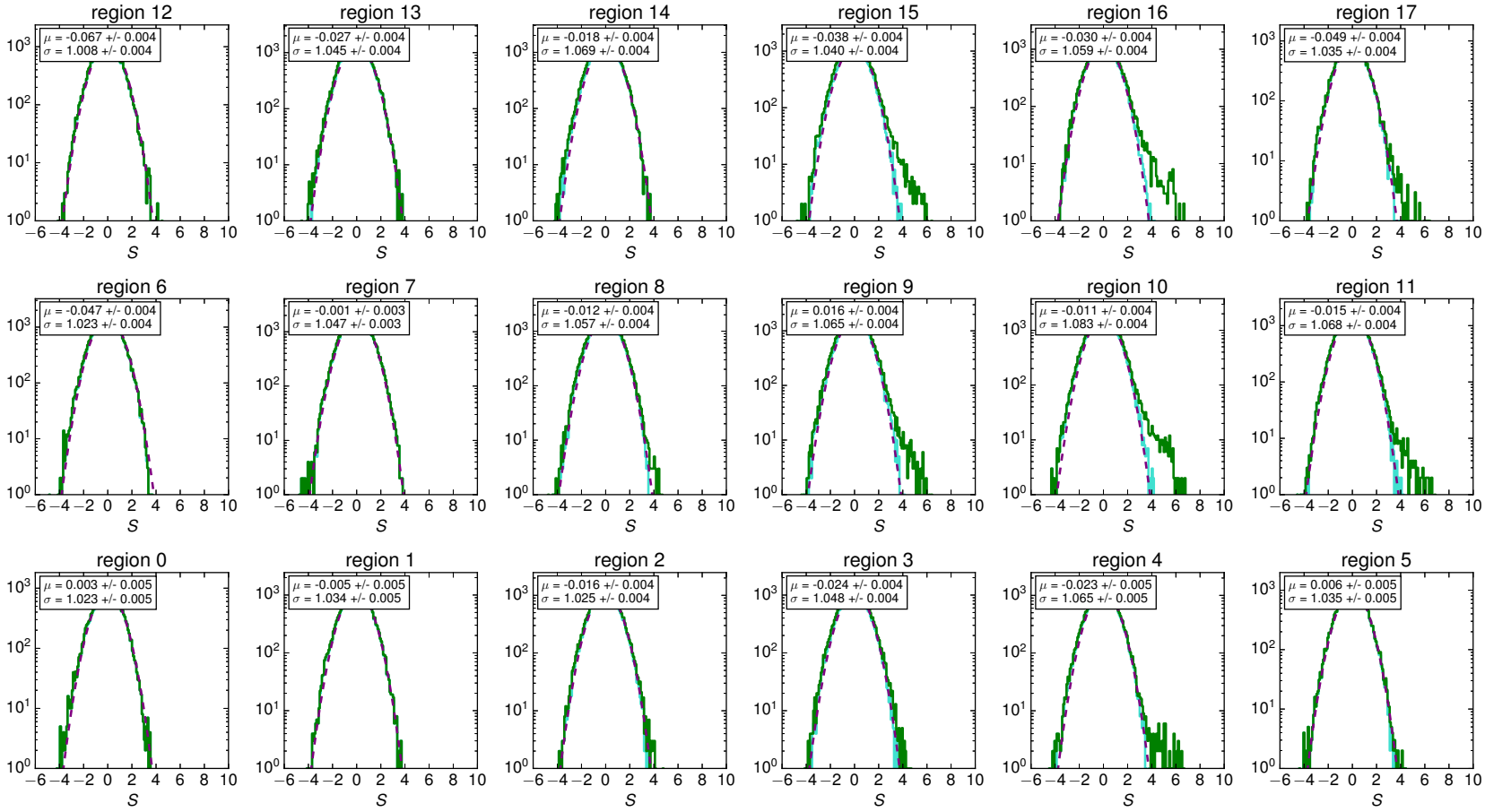

Figure B.5: Distributions of the significances, S, of the bins. The eighteen histograms correspond to each region of Figure 6.8 generated with moderate cuts and an integration radius of $\theta_{int} = 0.09°$. The green histogram represents the distribution of the significances without any exclusion regions. The cyan histogram shows the distribution after removal of known VHE γ-ray emitters and bright stars with a magnitude in the visual band smaller than 6.5 (Section B.2). The dashed magenta line shows the fit of the latter histogram with a normal distribution of mean μ and standard deviation σ, denoted in the upper left box of each canvas.

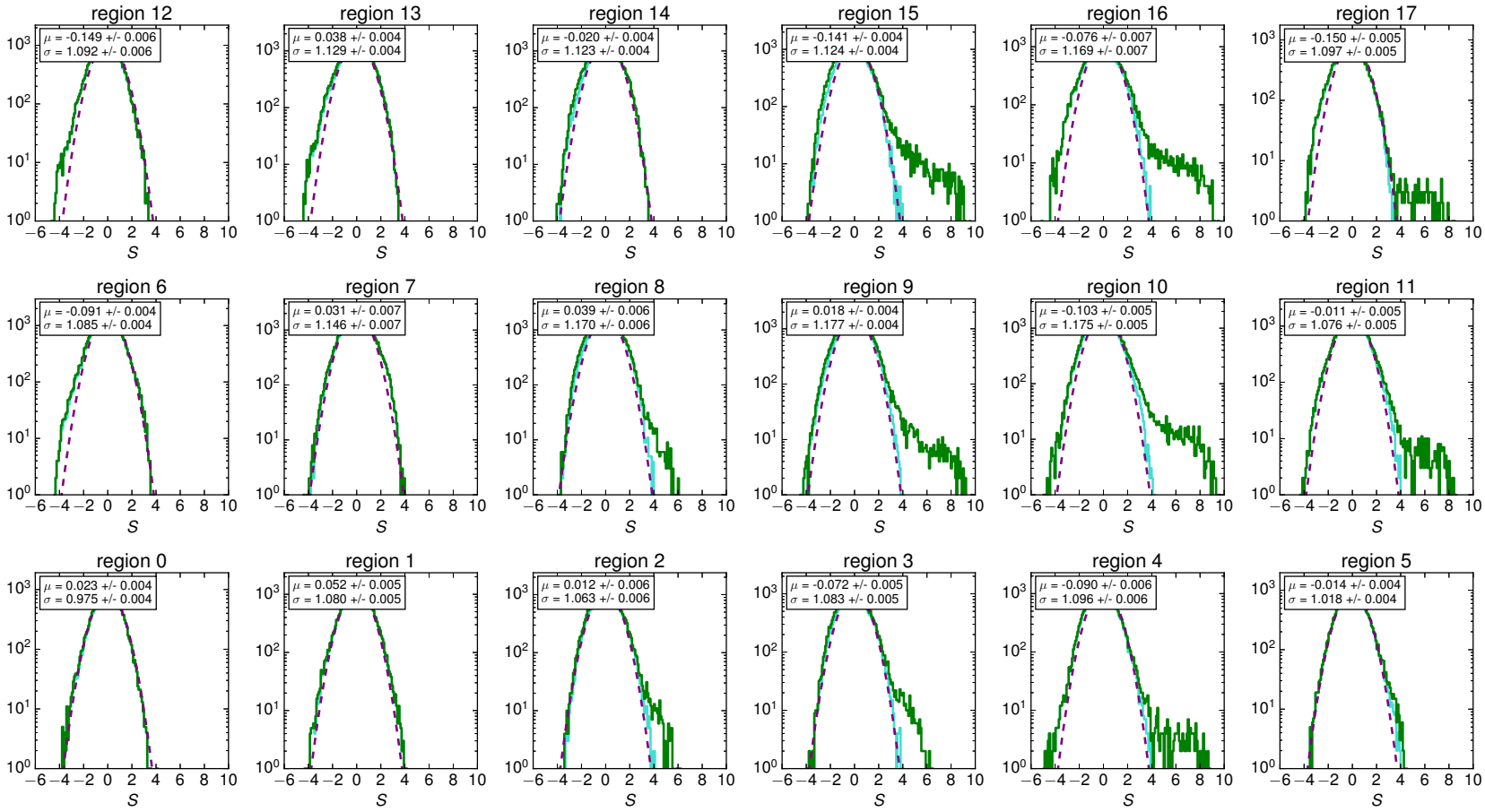

Figure B.6: Distributions of the significances, S, of the bins. The eighteen histograms correspond to each region of Figure 6.8 generated with moderate cuts and an integration radius of $\theta_{int} = 0.22°$. The green histogram represents the distribution of the significances without any exclusion regions. The cyan histogram shows the distribution after removal of known VHE γ-ray emitters and bright stars with a magnitude in the visual band smaller than 6.5 (Section B.2). The dashed magenta line shows the fit of the latter histogram with a normal distribution of mean μ and standard deviation σ, denoted in the upper left box of each canvas.

B.5 Spectral points

The differential flux, Φ, and its uncertainties, $\Delta\Phi$ of VER J2031+415, VER J2019+407, and VER J2019+368 are listed below. E_{min} and E_{max} represent the lower and upper boundary of the energy bin, whereas E_c corresponds to the logarithmic centre of the bin. N_{ON} and N_{OFF} are the number of events in the ON region and the OFF region after applying the analysis cuts, respectively. The significance per bin is indicated as S. If the significance is lower than 2σ, an upper limit of the flux is plotted. The flux is estimated following the algorithm of Rolke et al. [2005] (method 4) at 95 % confidence level.

VER J2031+451

E_{min}	E_{max}	E_c	N_{ON}	N_{OFF}	S	Φ	$\Delta\Phi$	
TeV	TeV	TeV				$10^{-13}/(\mathrm{cm}^2\,\mathrm{s\,TeV})$	$10^{-13}/(\mathrm{cm}^2\,\mathrm{s\,TeV})$	
0.398	0.708	0.531	229	905	1.1	9.12		
0.708	1.259	0.944	204	609	4.3	7.74	+1.85	-1.82
1.259	2.239	1.679	81	195	4.2	1.81	+0.49	-0.47
2.239	3.981	2.985	52	99	4.5	0.69	+0.18	-0.17
3.981	7.079	5.309	24	33	4.0	0.19	+0.06	-0.06
7.079	12.589	9.441	5	5	2	0.02	+0.01	-0.01
12.589	22.387	16.788	3	1	2	0.01	+0.005	-0.004

Table B.4: Spectral points of VER J2031+451.

VER J2019+407

E_{min}	E_{max}	E_c	N_{ON}	N_{OFF}	S	Φ	$\Delta\Phi$	
TeV	TeV	TeV				$10^{-13}/(\mathrm{cm}^2\,\mathrm{s\,TeV})$	$10^{-13}/(\mathrm{cm}^2\,\mathrm{s\,TeV})$	
0.398	0.708	0.531	107	242	6.3	106.90	+20.06	-19.52
0.708	1.259	0.944	156	377	7.0	15.09	+2.50	-2.44
1.259	2.239	1.679	81	134	7.2	4.13	+0.72	-0.69
2.239	3.981	2.985	30	70	3.2	0.56	+0.20	-0.19
3.981	7.079	5.309	9	22	1.7	0.08		
7.079	12.589	9.441	0	11	-2.0	0.006		
12.589	22.387	16.788	0	5	-1.4	0.004		

Table B.5: Spectral points of VER J2019+407.

VER J2019+368

E_{min}	E_{max}	E_c	N_{ON}	N_{OFF}	S	Φ	$\Delta\Phi$	
TeV	TeV	TeV				$10^{-13}/(\mathrm{cm}^2\,\mathrm{s}\,\mathrm{TeV})$	$10^{-13}/(\mathrm{cm}^2\,\mathrm{s}\,\mathrm{TeV})$	
0.316	0.501	0.398	46	134	3.2	136.80	+48.29	-46.35
0.501	0.794	0.631	298	1078	5.3	24.09	+4.88	-4.81
0.794	1.259	1.000	191	584	6.1	7.95	+1.47	-1.45
1.259	1.995	1.585	99	207	7.0	3.05	+0.53	-0.52
1.995	3.162	2.512	75	136	6.8	1.36	+0.25	-0.24
3.162	5.012	3.981	48	65	6.6	0.55	+0.11	-0.10
5.012	7.943	6.310	26	27	5.6	0.18	+0.05	-0.04
7.943	12.589	10.000	15	11	4.8	0.07	+0.02	-0.02
12.589	19.953	15.849	12	3	5.5	0.03	+0.01	-0.01

Table B.6: Spectral points of VER J2019+368.

B.6 Upper limits on the flux

The tables below list the pper limits on the integral flux, Φ^{UL}, above 0.3 TeV at 95 % confidence level from objects of interest inside the Cygnus region; calculated with moderate cuts. A power-law spectrum with an index of $\Gamma = 2.4$ has been assumed for all sources. The second column indicates the type of the object. The third to sixth column indicate the position in Galactic (longitude, l, and latitude, b) and equatorial (right ascension, α_{J2000}, and declination, δ_{J2000}) coordinates. Time, t, represents the livetime and ϑ the average zenith angle of the observation. N_{ON} represents the total number of events around the source position within a circle of θ_{int} in the sky, N_{OFF} represents the normalised number of background events. The normalisation factor, α, depends on the observation conditions of the object. The significance is denoted as S and the effective area as A_{eff}. Φ^{UL}_{CU} represents the integral flux in % of the flux of the Crab Nebula [Hillas et al., 1998]. Objects marked with $^{\diamondsuit}$ are associated with the Cygnus cocoon field.

Table B.7: Upper limits on the integral flux, Φ^{UL}, above 0.3 TeV using an integration radius of $\theta_{int} = 0.09°$ for the search of point-sources; calculated with moderate cuts.

object	type	l	b	α_{J2000}	δ_{J2000}	t	ϑ	N_{ON}	N_{OFF}	α	S	A_{eff}	$\Phi^{UL}_{>0.3\,\mathrm{TeV}}$	Φ^{UL}_{CU}
												m^2	$10^{-13}/(\mathrm{cm}^2\,\mathrm{s})$	%
Cygnus X-1	HMXB	71.34°	+3.07°	$19^h58^m21.7^s$	35.20°	7.36 h	24.6°	39	213	0.17	0.53	205135	13.72	1.06
Cygnus X-3	HMXB	79.85°	+0.70°	$20^h32^m25.8^s$	40.96°	51.18 h	18.4°	217	1270	0.17	0.28	180611	4.56	0.35
EXO 2030+375	HMXB	77.15°	-1.24°	$20^h32^m15.3^s$	37.64°	6.67 h	22.3°	41	235	0.17	0.27	110760	26.29	2.04
G65.8-0.5	SNR	65.80°	−0.5°	$19^h59^m20.0^s$	28.62°	1.00 h	27.2°	4	24	0.17	0.00	77464	82.28	6.37
G67.8+0.5	SNR	67.80°	+0.50°	$20^h00^m00.0^s$	30.85°	6.07 h	23.4°	41	224	0.17	0.55	147384	23.90	1.85
GS 2023+338	LMXB	73.12°	−2.09°	$20^h24^m3.8^s$	33.87°	30.00 min	19.4°	1	4	0.17	0.35	76750	115.30	8.93
3FGL J1951.6+2926	unknown	65.67°	+1.32°	$19^h51^m38.4^s$	29.45°	19.80 min	34.9°	2	7	0.17	0.64	64271	271.58	21.03
3FGL J1958.6+2845	pulsar	65.88°	−0.35°	$19^h58^m38.4^s$	28.76°	1.00 h	27.4°	3	24	0.17	−0.49	82545	58.79	4.55
3FGL J1958.6+3844	unknown	74.41°	+4.85°	$19^h58^m40.8^s$	38.75°	1.65 h	24.0°	9	49	0.17	0.26	115518	51.93	4.02
3FGL J2014.4+3606	unknown	73.86°	+0.79°	$20^h21^m38.3^s$	36.11°	41.82 h	20.4°	163	934	0.17	0.45	126385	7.57	0.59
3FGL J2018.5+3851	unknown	76.59°	+1.66°	$20^h18^m31.3^s$	38.86°	42.97 h	20.8°	136	840	0.17	−0.49	104746	5.31	0.41
3FGL J2018.6+4213$^\diamond$	unknown	79.40°	+3.53°	$20^h18^m40.3^s$	42.23°	19.27 h	24.1°	80	519	0.17	−0.66	120966	7.46	0.58
3FGL J2021.5+4026	pulsar	78.23°	+2.08°	$20^h21^m33.5^s$	40.45°	37.61 h	23.8°	215	1024	0.18	1.97	141032	13.75	1.06
3FGL J2022.2+3840$^\diamond$	unknown	76.86°	+0.96°	$20^h22^m15.1^s$	38.68°	35.69 h	20.8°	135	802	0.17	0.11	117980	7.48	0.58
3FGL J2023.5+4126$^\diamond$	unknown	79.25°	+2.34°	$20^h23^m31.1^s$	41.43°	55.10 h	21.7°	228	1410	0.17	−0.43	120056	4.75	0.37
3FGL J2024.6+3747	unknown	76.41°	+0.07°	$20^h24^m40.8^s$	37.80°	51.18 h	19.8°	193	1156	0.17	0.02	134097	5.23	0.41
3FGL J2025.2+3340	unknown	73.10°	−2.41°	$20^h25^m16.7^s$	33.67°	10.20 min	33.2°	1	2	0.17	0.83	63244	448.19	34.71
3FGL J2026.8+4003$^\diamond$	unknown	78.49°	+1.03°	$20^h26^m52.8^s$	40.05°	44.74 h	20.1°	163	944	0.17	0.42	101177	8.66	0.67
3FGL J2028.5+4040c$^\diamond$	unknown	79.19°	+1.13°	$20^h28^m31.1^s$	40.68°	61.18 h	19.2°	211	1341	0.17	−0.78	128838	3.23	0.25
3FGL J2030.0+3642	pulsar	76.13°	−1.43°	$20^h30^m0.0^s$	36.70°	17.98 h	18.4°	70	398	0.17	0.41	123020	11.86	0.92
3FGL J2030.8+4416	pulsar	82.35°	+2.89°	$20^h30^m52.8^s$	44.27°	4.61 h	20.9°	26	126	0.18	0.55	133931	28.07	2.17
3FGL J2032.5+3921$^\diamond$	unknown	78.57°	−0.27°	$20^h32^m33.5^s$	39.36°	9.77 h	19.0°	33	263	0.17	−1.59	113962	7.43	0.58
3FGL J2032.5+4032$^\diamond$	unknown	79.51°	+0.44°	$20^h32^m31.1^s$	40.53°	51.98 h	17.6°	189	1168	0.17	−0.38	147888	3.77	0.29
3FGL J2033.3+4348c$^\diamond$	unknown	82.24°	+2.26°	$20^h33^m21.5^s$	43.81°	5.95 h	20.8°	40	182	0.17	1.54	129231	36.52	2.83
3FGL J2034.4+3833c$^\diamond$	unknown	78.16°	−1.04°	$20^h34^m28.8^s$	38.56°	6.02 h	18.2°	24	146	0.17	−0.06	100402	21.85	1.69
3FGL J2034.6+4302	unknown	81.77°	+1.60°	$20^h34^m40.8^s$	43.04°	13.30 h	21.3°	72	309	0.17	2.47	113375	15.93	1.23
3FGL J2035.0+3634$^\diamond$	unknown	76.63°	−2.32°	$20^h35^m2.3^s$	36.58°	2.00 h	27.2°	7	34	0.17	0.50	71383	66.53	5.15
3FGL J2036.8+4234c$^\diamond$	unknown	81.63°	+0.99°	$20^h36^m52.8^s$	42.57°	33.60 h	18.5°	80	651	0.17	−2.68	101417	2.53	0.20
3FGL J2037.4+4132c$^\diamond$	unknown	80.87°	+0.29°	$20^h37^m24.0^s$	41.53°	53.26 h	18.3°	211	1173	0.17	1.01	137816	7.40	0.57
3FGL J2038.4+4212$^\diamond$	unknown	81.53°	+0.54°	$20^h38^m28.8^s$	42.21°	32.11 h	18.3°	111	670	0.17	−0.06	114289	7.15	0.55
3FGL J2039.4+4111$^\diamond$	unknown	80.83°	−0.21°	$20^h39^m24.0^s$	41.20°	33.70 h	18.4°	133	688	0.17	1.54	132020	11.32	0.88

Table B.7: continued

object	type	l	b	α_{J2000}	δ_{J2000}	t	ϑ	N_{ON}	N_{OFF}	α	S	A_{eff}	$\Phi^{UL}_{>0.3\,\mathrm{TeV}}$	Φ^{UL}_{CU}
												m^2	$10^{-13}/(\mathrm{cm}^2\,\mathrm{s})$	%
3FGL J2042.4+4209$^{\diamondsuit}$	unknown	81.93°	−0.07°	$20^h42^m26.4^s$	42.15°	8.85 h	20.8°	36	266	0.17	−1.20	110898	9.94	0.77
3FGL J2043.1+4350	unknown	83.33°	+0.87°	$20^h43^m7.1^s$	43.84°	2.00 h	22.6°	12	58	0.17	0.67	83563	76.02	5.89
KS 1947+300	HMXB	66.09°	2.08°	$19^h49^m35.5^s$	30.13°	30.00 min	35.8°	1	13	0.17	−0.83	73100	88.44	6.85
PSR B1951+32	pulsar	68.77°	+2.82°	$19^h52^m58.2^s$	32.87°	2.00 h	24.3°	10	29	0.17	1.86	82852	90.71	7.02
WR140	CWB	80.93°	+4.18°	$20^h20^m28.0^s$	43.86°	2.00 h	19.8°	9	46	0.17	0.43	85615	59.61	4.62
WR146	CWB	80.56°	+0.45°	$20^h35^m47.1^s$	41.38°	52.04 h	18.1°	185	1043	0.19	−0.89	167527	2.63	0.20
WR147	CWB	79.85°	−0.32°	$20^h36^m43.6^s$	40.36°	40.65 h	18.0°	119	743	0.17	−0.41	120992	4.67	0.36
XTE J2012+381	LMXB	75.39°	+2.25°	$20^h12^m37.8^s$	38.19°	25.70 h	22.5°	110	581	0.17	1.21	116966	14.21	1.10

Table B.8: Upper limits on the integral flux, Φ^{UL}, above 0.3 TeV using an integration radius of $\theta_{int} = 0.22°$ for the search of extended-sources; calculated with moderate cuts.

object	type	l	b	α_{J2000}	δ_{J2000}	t	ϑ	N_{ON}	N_{OFF}	α	S	A_{eff}	$\Phi^{UL}_{>0.3\,\mathrm{TeV}}$	Φ^{UL}_{CU}
												m^2	$10^{-13}/(\mathrm{cm}^2\,\mathrm{s})$	%
Cygnus X-1	HMXB	71.34°	+3.07°	$19^h58^m21.7^s$	35.20°	7.36 h	24.6°	230	882	0.27	−0.23	320493	15.17	1.17
Cygnus X-3	HMXB	79.85°	+0.70°	$20^h32^m25.8^s$	40.96°	51.55 h	18.3°	1309	5063	0.24	2.30	268769	7.52	0.58
EXO 2030+375	HMXB	77.15°	−1.24°	$20^h32^m15.3^s$	37.64°	8.00 h	19.9°	208	1104	0.19	0.23	200714	25.91	2.01
G65.7+1.2	SNR	65.70°	+1.20°	$19^h52^m10.0^s$	29.42°	19.80 min	34.1°	14	51	0.17	1.57	158746	312.81	24.22
G65.8-0.5	SNR	65.80°	−0.5°	$19^h59^m20.0^s$	28.62°	1.00 h	27.3°	26	154	0.17	0.06	172818	82.69	6.40
G66.0-0.0	SNR	66.00°	0.00°	$19^h57^m50.0^s$	29.05°	1.34 h	29.3°	28	173	0.17	−0.14	177330	56.78	4.40
G67.6+0.9	SNR	67.60°	+0.90°	$19^h57^m45.0^s$	30.89°	4.30 h	26.6°	125	860	0.17	−1.45	218320	16.32	1.26
G67.7+1.8	SNR	67.70°	+1.80°	$19^h54^m32.0^s$	31.44°	3.59 h	26.3°	96	726	0.17	−2.19	222803	13.37	1.04
G68.6-1.2	SNR	68.60°	−1.20°	$20^h08^m40.0^s$	30.62°	3.30 h	22.0°	58	342	0.17	0.12	188603	34.22	2.65
G69.0+2.7	SNR	69.00°	+2.70°	$19^h53^m20.0^s$	33.02°	1.33 h	26.7°	33	166	0.17	0.91	156096	103.92	8.05
G69.7+1.0	SNR	69.70°	+1.00°	$20^h02^m40.0^s$	32.72°	1.43 h	27.3°	46	218	0.17	1.42	188930	108.25	8.38
G73.9+0.9	SNR	73.90°	+0.90°	$20^h14^m15.0^s$	36.20°	47.76 h	20.0°	794	3815	0.19	2.95	179095	11.95	0.93
G76.9+1.0	SNR	76.90°	+1.00°	$20^h22^m20.0^s$	38.74°	40.99 h	21.3°	755	3778	0.19	1.43	189952	15.24	1.18
G83.0-0.3	SNR	83.00°	−0.30°	$20^h46^m55.0^s$	42.85°	3.34 h	24.7°	79	428	0.17	0.82	195542	49.43	3.83
GS 2023+338	LMXB	73.12°	−2.09°	$20^h24^m3.8^s$	33.87°	50.40 min	22.7°	6	28	0.17	0.54	158813	67.90	5.26
3FGL J1951.6+2926	unknown	65.67°	+1.32°	$19^h51^m38.4^s$	29.45°	30.00 min	35.8°	15	46	0.17	2.12	151866	111.05	8.60
3FGL J1958.6+2845	pulsar	65.88°	−0.35°	$19^h58^m38.4^s$	28.76°	1.00 h	27.4°	26	168	0.17	−0.35	171069	69.48	5.38
3FGL J1958.6+3844	unknown	74.41°	+4.85°	$19^h58^m40.8^s$	38.75°	2.32 h	25.7°	50	248	0.18	0.77	192534	57.80	4.48
3FGL J2014.4+3606	unknown	73.86°	+0.79°	$20^h21^m38.3^s$	36.11°	49.61 h	20.5°	862	3502	0.21	4.69	184867	18.29	1.42
3FGL J2018.5+3851	unknown	76.59°	+1.66°	$20^h18^m31.3^s$	38.86°	50.21 h	21.7°	801	4143	0.18	2.28	174520	9.09	0.70
3FGL J2018.6+4213$^\diamondsuit$	unknown	79.40°	+3.53°	$20^h18^m40.3^s$	42.23°	25.35 h	23.5°	586	2731	0.19	2.35	201620	13.85	1.07
3FGL J2021.5+4026	pulsar	78.23°	+2.08°	$20^h21^m33.5^s$	40.45°	38.63 h	23.7°	1210	4807	0.20	7.67	235309	34.97	2.71
3FGL J2022.2+3840$^\diamondsuit$	unknown	76.86°	+0.96°	$20^h22^m15.1^s$	38.68°	36.54 h	20.6°	725	3743	0.18	1.57	194663	16.94	1.31
3FGL J2023.5+4126$^\diamondsuit$	unknown	79.25°	+2.34°	$20^h23^m31.1^s$	41.43°	57.73 h	21.8°	1409	6849	0.18	3.75	203329	14.72	1.14
3FGL J2024.6+3747	unknown	76.41°	+0.07°	$20^h24^m40.8^s$	37.80°	53.27 h	19.7°	1137	5674	0.21	−0.72	214268	5.29	0.41
3FGL J2025.2+3340	unknown	73.10°	−2.41°	$20^h25^m16.7^s$	33.67°	10.2 min	33.6°	2	17	0.17	−0.49	149515	169.99	13.16
3FGL J2026.8+4003$^\diamondsuit$	unknown	78.49°	+1.03°	$20^h26^m52.8^s$	40.05°	48.70 h	20.5°	910	5055	0.17	1.23	174454	14.32	1.11
3FGL J2028.5+4040c$^\diamondsuit$	unknown	79.19°	+1.13°	$20^h28^m31.1^s$	40.68°	63.87 h	19.2°	1365	6739	0.20	1.14	206683	11.02	0.85
3FGL J2030.0+3642	pulsar	76.13°	−1.43°	$20^h30^m0.0^s$	36.70°	21.57 h	18.9°	452	2304	0.17	2.81	199314	16.82	1.30
3FGL J2030.8+4416	pulsar	82.35°	+2.89°	$20^h30^m52.8^s$	44.27°	3.28 h	20.3°	105	601	0.17	0.44	209669	46.88	3.63
3FGL J2032.5+3921$^\diamondsuit$	unknown	78.57°	−0.27°	$20^h32^m33.5^s$	39.36°	12.36 h	18.8°	285	1475	0.18	1.45	196847	30.03	2.33

Table B.8: continued

object	type	l	b	α_{J2000}	δ_{J2000}	t	ϑ	N_{ON}	N_{OFF}	α	S	A_{eff}	$\Phi^{UL}_{>0.3\,\mathrm{TeV}}$	Φ^{UL}_{CU}
												m^2	$10^{-13}/(\mathrm{cm}^2\,\mathrm{s})$	%
3FGL J2032.5+4032$^{\diamondsuit}$	unknown	79.51°	+0.44°	$20^h32^m31.1^s$	40.53°	53.40 h	18.0°	1205	6390	0.17	3.37	227639	11.60	0.90
3FGL J2033.3+4348c$^{\diamondsuit}$	unknown	82.24°	+2.26°	$20^h33^m21.5^s$	43.81°	6.51 h	21.2°	153	777	0.17	1.85	202023	44.78	3.47
3FGL J2034.4+3833c$^{\diamondsuit}$	unknown	78.16°	−1.04°	$20^h34^m28.8^s$	38.56°	6.68 h	18.8°	172	833	0.17	2.50	195128	29.96	2.32
3FGL J2034.6+4302	unknown	81.77°	+1.60°	$20^h34^m40.8^s$	43.04°	16.63 h	20.8°	386	2030	0.17	2.34	196929	17.03	1.32
3FGL J2035.0+3634$^{\diamondsuit}$	unknown	76.63°	−2.32°	$20^h35^m2.3^s$	36.58°	3.66 h	25.9°	63	185	0.17	4.60	152321	67.98	5.26
3FGL J2036.8+4234c$^{\diamondsuit}$	unknown	81.63°	+0.99°	$20^h36^m52.8^s$	42.57°	33.63 h	18.5°	527	3572	0.17	−2.65	172403	3.44	0.27
3FGL J2037.4+4132c$^{\diamondsuit}$	unknown	80.87°	+0.29°	$20^h37^m24.0^s$	41.53°	52.60 h	18.4°	1097	4893	0.19	4.49	215826	15.72	1.22
3FGL J2038.4+4212$^{\diamondsuit}$	unknown	81.53°	+0.54°	$20^h38^m28.8^s$	42.21°	35.06 h	18.4°	685	3851	0.17	1.24	189800	15.76	1.22
3FGL J2039.4+4111$^{\diamondsuit}$	unknown	80.83°	−0.21°	$20^h39^m24.0^s$	41.20°	38.48 h	19.1°	844	4208	0.17	3.97	209127	17.13	1.33
3FGL J2042.4+4209$^{\diamondsuit}$	unknown	81.93°	−0.07°	$20^h42^m26.4^s$	42.15°	10.52 h	20.8°	243	1202	0.19	1.20	201005	29.93	2.32
3FGL J2043.1+4350	unknown	83.33°	+0.87°	$20^h43^m7.1^s$	43.84°	2.94 h	22.0°	73	309	0.17	2.58	166599	51.90	4.02
KS 1947+300	HMXB	66.09°	+2.08°	$19^h49^m35.5^s$	30.13°	30.00 min	35.3°	9	73	0.17	−0.89	165236	74.66	5.78
PSR B1951+32	pulsar	68.77°	+2.82°	$19^h52^m58.2^s$	32.87°	2.33 h	22.9°	43	181	0.17	2.01	168676	38.11	2.95
XTE J2012+381	LMXB	75.39°	+2.25°	$20^h12^m37.8^s$	38.19°	32.83 h	22.1°	666	2742	0.20	4.96	187754	24.95	1.93

List of Figures

1.1 The energy spectrum of cosmic rays. 1

2.1 The entire γ-ray sky at energies above 50 GeV based on six years of data from the *Fermi*-LAT instrument. 7
2.2 Schematic view of the acceleration of particles in the vicinity of a shock front. . . 9
2.3 Sketch of the sites and various radiation mechanisms of nonthermal emission associated with PWNe. 16
2.4 Models for VHE γ-rays from microquasars and binary pulsars. 17
2.5 Sketch of the longitudinal development of an extensive air shower induced by a primary particle. 21
2.6 Air shower simulations initiated by a primary particle of 100 GeV. 22
2.7 Geometry of Cherenkov radiation. 24
2.8 Detection principle of γ-rays using the imaging atmospheric Cherenkov technique. 25
2.9 Skymap of sources of VHE γ-rays. 26

3.1 The *VERITAS* array layout before and after the summer 2009. 29
3.2 Single *VERITAS* telescope with the different telescope components indicated. . . 31
3.3 Schematic view of the trigger and data acquisition system as used in *VERITAS*. . 32
3.4 Example of a *VERITAS* bias curve taken under dark sky conditions. 33
3.5 Typical FADC traces as recoded by the *VERITAS* PMTs. 37
3.6 Basic image parameters for a single telescope. 38
3.7 Lookup table for the energy estimation of the reconstructed event. 40
3.8 Event distribution of the mean reduced scaled width and length. 42
3.9 Background analysis methods: reflected region and ring background method. . . 44
3.10 Acceptance curve of the *VERITAS* camera. 45

4.1 Sketch of the development of a decision tree. 49
4.2 Comparison of the parameter distributions: *MRSL*, *MRSW*, and emission height. 51
4.3 Distribution of the classifying variables with γ/hadron classification potential. . . 52
4.4 Energy dependence of classification parameters with γ/hadron separation potential. 54
4.5 Zenith angle dependence of classification parameters with γ/hadron identification potential. 55
4.6 Distribution of the classifying variables with γ/hadron classification potential for showers arriving from north and south. 59
4.7 Relative importance of the training parameters as a function of energy and zenith angle. 62

4.8 BDT response, T, for an independent test sample for two different energies. . . . 63
4.9 Significance as a function of T; signal and background efficiencies as a function of energy. . . . 64
4.10 BDT response for MC γ-ray events and real γ-ray data from the Crab Nebula. . 66
4.11 Angular resolution and energy bias for T and box cuts. . . . 67
4.12 Effective areas for true and reconstructed energy for T and box cuts. . . . 68
4.13 Effective areas for different azimuth and zenith angles for T selection cuts. . . . 70
4.14 Effective areas for different selection cuts using T and box cuts. . . . 71
4.15 Effective area ratios for different selection cuts using T and box cuts. . . . 72
4.16 Improvement of quality factor as a function of zenith angle and reconstructed energy. 73
4.17 Classification of events after applying the T and box cuts. . . . 74
4.18 Signal efficiency and purity for T analysis and box cuts analysis. . . . 74
4.19 Differential flux sensitivity of T and box cuts. . . . 76
4.20 Differential energy spectrum of the Crab Nebula as obtained with T and box cuts. 79

5.1 Map of the Cygnus region in Galactic coordinates. . . . 83
5.2 Infrared image of the star-forming region Cygnus X as seen by the *Herschel Space Observatory*. . . . 87
5.3 Regions around TeV J2032+4130 and SNR G78.2+2.1. . . . 88
5.4 Cygnus region as seen by the *Milagro* experiment. . . . 90

6.1 Time of observation of the region of the Cygnus sky survey including the central positions of the *eventDisplay* fields. . . . 91
6.2 Distribution of observation time for different periods of time and different ranges of zenith angle. . . . 92
6.3 Distribution of spectral indices and extensions of sources in the Galactic Plane. . 94
6.4 Schematic description of the correlation between adjacent grid points. . . . 97
6.5 Pseudo-random raw γ-ray counts map and significance map obtained from the MC simulations. . . . 97
6.6 Distributions of significances from the survey simulations for point and extended analyses. . . . 99
6.7 Trial factor as a function of pre-trial significance, and post-trial significance as a function of pre-trial significance. . . . 100
6.8 Significance maps of the *VERITAS* Cygnus sky survey region for hard spectrum, point-source analysis. . . . 103
6.9 Significance maps of the *VERITAS* Cygnus sky survey region for hard spectrum, extended-source analysis. . . . 104
6.10 Distribution of significances for hard spectrum, point-source analysis. . . . 105
6.11 Distribution of significances for hard spectrum, extended-source analysis. . . . 106

6.12 Significance map of the Cygnus sky survey region using *VEGAS*. 107
6.13 Significance map and significance distribution for VER J2031+415. 108
6.14 Differential energy spectrum of VER J2031+415. 109
6.15 Multiwavelength images obtained from infrared and radio measurements for VER J2031+415. 110
6.16 Significance map and significance distribution for VER J2019+407. 112
6.17 Differential energy spectrum of VER J2019+407. 113
6.18 Significance map and significance distribution for VER J2019+368. 115
6.19 Differential energy spectrum of VER J2019+368. 116
6.20 Multiwavelength view of VER J2019+368. 117
6.21 Significance map and significance distribution for VER J2016+371. 119
6.22 Upper limits on the flux of WR140 compared to previous measurements. 130
6.23 Upper limits on the flux of WR147 compared to previous measurements. 131

A.1 BDT response, T, for an independent test sample for energies between 0.08 TeV and 0.32 TeV. 140
A.2 BDT response, T, for an independent test sample for energies between 0.32 TeV and 0.50 TeV. 141
A.3 BDT response, T, for an independent test sample for energies between 0.50 TeV and 1.00 TeV. 142
A.4 BDT response, T, for an independent test sample for energies larger than 1.00 TeV. 143
A.5 Signal and background efficiency dependent on zenith angle for all energy bands. 144
A.6 Signal and background efficiency dependent on energy for all zenith angle bands. 145

B.1 Position of exclusion regions, including stars and known VHE γ-ray sources, in Galactic coordinates. 148
B.2 Maps used for trial simulations. 151
B.3 Significance maps of the *VERITAS* Cygnus sky survey region for moderate spectrum, point-source analysis. 153
B.4 Significance maps of the *VERITAS* Cygnus sky survey region for moderate spectrum, extended-source analysis. 154
B.5 Distribution of significances for moderate spectrum, point-source analysis. 155
B.6 Distribution of significances for moderate spectrum, extended-source analysis. . . 156

List of Tables

3.1 Definition of image shape parameters. 38

4.1 Different values of the parameters used to construct the architecture of the BDTs. 60
4.2 Parameters used to construct the architecture of the BDTs. 61
4.3 Energy threshold of the T analysis for different cut configurations and zenith angles 69
4.4 Observation time required for a detection of a point-like VHE γ-ray source using the hard configuration. 76
4.5 Performance of the applied cuts on some *VERITAS* sources. 77
4.6 Sensitivity of T analysis for different wobble offsets and telescope configurations. 80

6.1 Analysis parameters for significance maps. 94
6.2 Fit results to the distributions of significances from the survey simulations for point and extended analyses. 99
6.3 Upper limits on the integral flux: hard spectrum, point-source analysis. 121
6.4 Upper limits on the integral flux: hard spectrum, extended-source analysis. . . . 123
6.5 Predictions of the flux at very high energies for 3FGL J2014.4+3606 and 3FGL J2022.2+3840. 126
6.6 Results of upper limits on the flux from Cygnus X-3. 128
6.7 Results of upper limits on the flux from EXO 2030+375, KS 1947+300, and XTE J2012+381. 128
6.8 Results of γ-ray luminosities from EXO 2030+375, KS 1947+300, and XTE J2012+381. 129
6.9 Predictions of the flux at very high energies for studied objects of the third *Fermi*-LAT catalogue with significance larger 3.5 in this *VERITAS* analysis. 132

A.1 Optimized cut values T_{sel}. 139
A.2 Observation time required for a detection of a point-like VHE γ-ray source using the moderate configuration. 146

B.1 Central positions of the fields used for the analysis of the Cygnus region. 147
B.2 List of known γ-ray emitters excluded in the analysis of the Cygnus region. . . . 148
B.3 List of stars excluded in the analysis of the Cygnus region. 149
B.4 Spectral points of VER J2031+451. 157
B.5 Spectral points of VER J2019+407. 157
B.6 Spectral points of VER J2019+368. 158
B.7 Upper limits on the integral flux: moderate spectrum, point-source analysis. . . . 159

B.8 Upper limits on the integral flux: moderate spectrum, extended-source analysis. . 161

List of Abbreviations

AdaBoost	adaptive boosting
AGN	active galactic nuclei
BDT	Boosted Decision Tree
C.U.	Crab Units
CF	confidence level
CFD	constant fraction discriminator
CGPS	Canadian Galactic Plane Survey
CTA	Cherenkov Telescope Array
CWB	colliding wind binary
DAQ	data acquisition
dc	digital counts
EAS	extensive air shower
EGRET	Energetic Gamma Ray Experiment Telescope
FADC	flash analog-to-digital converter
H.E.S.S.	High Energy Stereoscopic System
HAWC	High Altitude Water Cherenkov Gamma-Ray Observatory
HEGRA	High Energy Gamma Ray Astronomy Experiment
IACT	Imaging Atmospheric Cherenkov Telescope
ISM	interstellar medium
KS	Kolmogorov-Smirnov
MAGIC	Major Atmospheric Gamma Imaging Cherenkov Telescopes
MC	Monte-Carlo
MJD	Modified Julian Day

MRSL	mean reduced scaled length
MRSW	mean reduced scaled width
MVA	multivariate classification algorithm
NSB	night sky background
OSS	optical support structure
PDF	probability density function
PMT	photomultiplier tube
PSF	point spread function
PWN	pulsar wind nebula
RF	Random Forest
SNR	supernova remnant
VERITAS	Very Energetic Radiation Imaging Telescope Array System
VHE	very-high-energy

Bibliography

Aartsen, M.G. et al. (2013a). Evidence for High-Energy Extraterrestrial Neutrinos at the IceCube Detector. *Science*, 342(6161):1242856, doi:10.1126/science.1242856.

Aartsen, M.G. et al. (2013b). First observation of PeV-energy neutrinos with IceCube. *Phys. Rev. Lett.*, 111:021103, doi:10.1103/PhysRevLett.111.021103.

Aartsen, M.G. et al. (2014). Observation of High-Energy Astrophysical Neutrinos in Three Years of IceCube Data. *Phys. Rev. Lett.*, 113(10):101101, doi:10.1103/PhysRevLett.113.101101.

Abbasi, R.U. et al. (2008). First Observation of the Greisen-Zatsepin-Kuzmin Suppression. *Phys. Rev. Lett.*, 100(10):101101–1 – 101101–5, doi:10.1103/PhysRevLett.100.101101.

Abdo, A.A. et al. (2007a). Discovery of TeV Gamma-Ray Emission from the Cygnus Region of the Galaxy. *Astrophys.J.*, 658(1):L33–L36, doi:10.1086/513696.

Abdo, A.A. et al. (2007b). TeV Gamma-Ray Sources from a Survey of the Galactic Plane with Milagro. *Astrophys.J.*, 664(2):L91–L94, doi:10.1086/520717.

Abdo, A.A. et al. (2009a). Detection of 16 Gamma-Ray Pulsars Through Blind Frequency Searches Using the Fermi LAT. *Science*, 325(5942):840–844, doi:10.1126/science.1175558.

Abdo, A.A. et al. (2009b). Modulated High-Energy Gamma-Ray Emission from the Microquasar Cygnus X-3. *Science*, 326(5959):1512–1516, doi:10.1126/science.1182174.

Abdo, A.A. et al. (2009c). Pulsed Gamma-rays from PSR J2021+3651 with the Fermi Large Area Telescope. *Astrophys. J.*, 700(2):1059–1066, doi:10.1088/0004-637X/700/2/1059.

Abdo, A.A. et al. (2009d). *FERMI*/Large Area Telescope Bright Gamma-Ray Source List. *Astrophys. J. Suppl. S.*, 183(1):46–66, doi:10.1088/0067-0049/183/1/46.

Abdo, A.A. et al. (2010a). Fermi Large Area Telescope First Source Catalog. *Astrophys. J. Suppl. S.*, 188(2):405–436, doi:10.1088/0067-0049/188/2/405.

Abdo, A.A. et al. (2010b). The First Fermi Large Area Telescope Catalog of Gamma-ray Pulsars. *Astron. Astrophys. Suppl. Ser.*, 187(2):460–494, doi:10.1088/0067-0049/187/2/460.

Abdo, A.A. et al. (2012). Spectrum and Morphology of the Two Brightest Milagro Sources in the Cygnus Region: MGRO J2019+37 and MGRO J2031+41. *Astrophys. J.*, 753(2):8pp., doi:10.1088/0004-637X/753/2/159.

Abdo, A.A. et al. (2013). The Second Fermi Large Area Telescope Catalog of Gamma-Ray Pulsars. *Astrophys. J. Suppl. S.*, 208(2):17–76, doi:10.1088/0067-0049/208/2/17.

Abramowski, A. et al. (2012a). Discovery of extended VHE γ-ray emission from the vicinity of the young massive stellar cluster Westerlund 1. *Astron. Astrophys.*, 537(A114):11pp, doi:10.1051/0004-6361/201117928.

Abramowski, A. et al. (2012b). HESS observations of the Carina nebula and its enigmatic colliding wind binary Eta Carinae. *Mon. Not. R. Astron. Soc.*, 424(1):128–135, doi:10.111/j.1365-2966.2012.21180.x.

Abramowski, A. et al. (2014). Discovery of the VHE gamma-ray source HESS J1832-093 in the vicinity of SNR G22.7-0.2. *Mon. Not. R. Astron. Soc.*, 446(2):1163–1169, doi:10.1093/mnras/stu2148.

Abramowski, A. et al. (2015). Discovery of variable VHE gamma-ray emission from the binary system 1FGLJ1018.6-5856. *Astron. Astrophys.*, 577(A131):6pp, doi:10.1051/0004-6361/201525699.

Abramowski, A. et al. (2016). Acceleration of petaelectronvolt protons in the Galactic Centre. *Nature*, 531(7595):476–479, doi:10.1038/nature17147.

Acciari, V.A. et al. (2008). VERITAS Observations of the gamma-Ray Binary LS I +61 303. *Astrophys. J.*, 679(2):1427–1432, doi:10.1086/587736.

Acciari, V.A. et al. (2009). Observation of Extended VHE Emission from the Supernova Remnant IC 443 with VERITAS. *Astrophys. J. Lett.*, 698(2):133–137, doi:10.1088/0004-637X/698/2/L133.

Acciari, V.A. et al. (2010). Observations of the shell-type SNR Cassiopeia A at TeV energies with VERITAS. *Astrophys. J.*, 714(1):163–169, doi:10.1088/0004-637X/714/1/163.

Acciari, V.A. et al. (2011). Discovery of TeV gamma-ray emission from Tycho's supernova remnant. *Astrophys. J. Lett.*, 730(2):L20–L25, doi:10.1088/2041-8205/730/2/L20.

Acero, F. et al. (2015). Fermi Large Area Telescope Third Source Catalog. *Astrophys. J. Suppl. S.*, 218(23):41pp, doi:10.1088/0067-0049/218/2/23.

Acharya, B.S. et al. (2013). Introducing the CTA concept. *Astropart. Phys.*, 43:3–18, doi:10.1016/j.astropartphys.2013.01.007.

Ackermann, M. et al. (2011). A Cocoon of Freshly Accelerated Cosmic Rays Detected by Fermi in the Cygnus Superbubble. *Science*, 334(6059):1103–1107, doi:10.1126/science.1210311.

Ackermann, M. et al. (2012a). The cosmic-ray and gas content of the Cygnus region as measured in gamma rays by the Fermi Large Area Telescope. *Astron.Astrophys.*, 538(A71):15pp, doi:10.1051/0004-6361/201117539.

Ackermann, M. et al. (2012b). Periodic emission from the gamma-ray binary 1FGLJ1018.6-5856. *Science*, 335(6065):189–193, doi:10.1126/science.1213974.

Ackermann, M. et al. (2013). Detection of the Characteristic Pion-Decay Signature in Supernova Remnants. *Science*, 339(6121):807–811, doi:10.1126/science.1231160.

Ackermann, M. et al. (2016). 2FHL: The Second Catalog of Hard Fermi-LAT Sources. *Astrophys. J. Suppl. S.*, 222(1):5–23, doi:10.3847/0067-0049/222/1/5.

Adriani, O. et al. (2011). PAMELA Measurements of Cosmic-Ray Proton and Helium Spectra. *Science*, 332(6025):69–72, doi:10.1126/science.1199172.

Aharonian, F. (2005). Discovery of Very High Energy Gamma Rays Associated with an X-ray Binary. *Science*, 309(5735):746–749, doi:10.1126/science.113764.

Aharonian, F. et al. (2001). Evidence for TeV gamma-ray emission from Cassiopeia A. *Astron. Astrophys.*, 370(1):112–120, doi:10.1051/0004-6361:20010243.

Aharonian, F. et al. (2002a). An Unidentified TeV source in the vicinity of Cygnus OB2. *Astron.Astrophys.*, 393:L37–L40, doi:10.1051/0004-6361:20021171.

Aharonian, F. et al. (2004). Observations of 54 Active Galactic Nuclei with the HEGRA system of Cherenkov Telescopes. *Astron.Astrophys.*, 421:529–537, doi:10.1051/0004-6361:20035764.

Aharonian, F. et al. (2005a). Discovery of the binary pulsar PSR B1259-63 in very-high-energy gamma rays around periastron with HESS. *Astron. Astrophys.*, 442(1):1–10, doi:10.1051/0004-6361:20052983.

Aharonian, F. et al. (2005b). A new population of very high-energy gamma-ray sources in the Milky Way. *Science*, 307(5717):1938–1942, doi:10.1126/science.1108643.

Aharonian, F. et al. (2005c). The unidentified TeV source (TeV J2032+4130) and surrounding field: Final HEGRA IACT-System results. *Astronomy and Astrophysics*, 431(2):197–202, doi:10.1051/0004-6361:20041552.

Aharonian, F. et al. (2006a). The H.E.S.S. survey of the Inner Galaxy in very high-energy gamma-rays. *Astrophys. J.*, 636(2):777–797, doi:10.1086/498013.

Aharonian, F. et al. (2006b). Observations of the Crab nebula with HESS. *Astron. Astrophys.*, 457(3):899–915, doi:10.1051/0004-6361:20065351.

Aharonian, F. et al. (2007a). Detection of extended very-high-energy γ-ray emission towards the young stellar cluster Westerlund 2. *Astron. Astrophys.*, 467(3):1075–1080, doi:10.1051/0004-6361:20066950.

Aharonian, F. et al. (2008). High energy astrophysics with ground-based gamma ray detectors. *Rep. Prog. Phys.*, 71(9):096901, doi:10.1088/0034-4885/71/9/096901.

Aharonian, F.A. (2004). *Very High Energy Cosmic Gamma Radiation - A Crucial Window on the Extreme Universe*. World Scientific Publishing Co., Singapore.

Aharonian, F.A. and Atoyan, A.M. (1981). Compton scattering of relativistic electrons in compact X-ray sources. *Astrophys. Space Sci.*, 79(2):321–336, doi:10.1007/BF00649428.

Aharonian, F.A. and Bogovalov, S. (2003). Exploring physics of rotation powered pulsars with sub-10 GeV imaging atmospheric Cherenkov telescopes. *New Astron.*, 8(2):85–103, doi:10.1016/S1384-1076(02)00200-2.

Aharonian, F.A. et al. (1997). The potential of ground based arrays of imaging atmospheric Cherenkov telescopes. I. Determination of shower parameters. *Astropart. Phys.*, 6(3):343–368, doi:10.1016/S0927-6505(96)00069-2.

Aharonian, F.A. et al. (2002b). A Search for TeV gamma-ray emission from SNRs, pulsars and unidentified GeV sources in the galactic plane in the longitude range between -2 deg and 85 deg. *Astron. Astrophys.*, 395(3):803–811, doi:10.1051/0004-6361:20021347.

Aharonian, F.A. et al. (2007b). Discovery of a point-like very-high-energy γ-ray source in Monoceros. *Astron. Astrophys.*, 469(1):L1–L4, doi:10.1051/0004-6361:20077299.

Albert, J. et al. (2006). Variable Very-High-Energy Gamma-Ray Emission from the Microquasar LS I +61 303. *Science*, 312(5781):1771–1773, doi:10.1126/science.1128177.

Albert, J. et al. (2007a). Constraints on the steady and pulsed VHE gamma-ray emission from observation of PSR B1951+32/CTB 80 with the MAGIC Telescope. *Astrophys. J.*, 669(2):1143–1149, doi:10.1086/521807.

Albert, J. et al. (2007b). Discovery of Very High Energy Gamma Radiation from IC 443 with the MAGIC Telescope. *Astrophys. J. Lett.*, 664(2):87–90, doi:10.1086/520957.

Albert, J. et al. (2007c). Observations of VHE gamma-rays from Cassiopeia A with the MAGIC telescope. *Astron. Astrophys.*, 474(3):937–940, doi:10.1051/0004-6361:20078168.

Albert, J. et al. (2007d). Very High Energy Gamma-ray Radiation from the Stellar-mass Black Hole Cygnus X-1. *Astrophys. J.*, 665(a):L51–L54, doi:10.1086/521145.

Albert, J. et al. (2008a). Implementation of the Random Forest method for the Imaging Atmospheric Cherenkov Telescope MAGIC. *Nucl. Instrum. Meth. A*, 588(3):424–432, doi:10.1016/j.nima.2007.11.068.

Albert, J. et al. (2008b). MAGIC Observations of the Unidentified γ-Ray Source TeV J2032+4130. *Astrophys. J.*, 675(1):L25–L28, doi:10.1086/529520.

Aleksić, J. et al. (2010). MAGIC constraints on Gamma-ray emission from Cygnus X-3. *Astrophys. J.*, 721(1):843–855, doi:10.1088/0004-637X/721/1/843.

Aleksić, J. et al. (2012). Performance of the MAGIC stereo system obtained with Crab Nebula data. *Astroparticle Physics*, 35(7):435–448, doi:10.1016/j.astropartphys.2011.11.007.

Aleksić, J. et al. (2016a). The major upgrade of the MAGIC telescopes, Part I: The hardware improvements and the commissioning of the system. *Astropart. Phys.*, 72:61–75, doi:10.1016/j.astropartphys.2015.04.004.

Aleksić, J. et al. (2016b). The major upgrade of the MAGIC telescopes, Part II: The achieved physics performance using the Crab Nebula observations. *Astropart. Phys.*, 72:76–94, doi:10.1016/j.astropartphys.2015.02.005.

Aliu, E. et al. (2008). First bounds on the high-energy emission from isolated Wolf-Rayet binary systems. *Astrophys. J.*, 685(1):L71–L74, doi:10.1086/592433.

Aliu, E. et al. (2011). Detection of Pulsed Gamma Rays Above 100 GeV from the Crab Pulsar. *Science*, 334(6052):69–72, doi:10.1126/science.1208192.

Aliu, E. et al. (2013). Discovery of TeV Gamma-ray Emission Toward Supernova Remnant SNR G78.2+2.1. *Astrophys.J.*, 770(2):93–99, doi:10.1088/0004-637X/770/2/93.

Aliu, E. et al. (2014a). Observations of the unidentified gamma-ray source TeV J2032+4130 by VERITAS. *Astrophys.J.*, 783(1):16–25, doi:10.1088/0004-637X/783/1/16.

Aliu, E. et al. (2014b). Spatially Resolving the Very High Energy emission from MGRO J2019+37 with VERITAS. *Astrophys. J.*, 788(1):78–87, doi:10.1088/0004-637X/788/1/78.

Amenomori, M. et al. (2007). Study on TeV γ Ray Emission from Cygnus Region Using the Tibet Air Shower Array. In Caballero, R. et al., editors, *Proceedings of the 30th International Cosmic Ray Conference (ICRC2007)*, volume 2, pages 695–698, Merida, Yucatan, Mexico.

Amenomori, M. et al. (2008). The All-particle spectrum of primary cosmic rays in the wide energy range from 10^{14} to 10^{17} eV observed with the Tibet-III air-shower array. *Astrophys. J.*, 678(2):1165–1179, doi:10.1086/529514.

Anderson, D.P., Christensen, C. and Allen, B. (2006). Designing a Runtime System for Volunteer Computing. In *SC '06: Proceedings of the 2006 ACM/IEEE Conference on Supercomputing*, pages 1–33, New York, U.S. IEEE.

Apel, W.D. et al. (2012). The spectrum of high-energy cosmic rays measured with KASCADE-Grande. *Astropart. Phys.*, 36(1):183–194, doi:10.1016/j.astropartphys.2012.05.023.

Archambault, S. et al. (2013). VERITAS Observations of the Microquasar Cygnus X-3. *Astrophys. J.*, 779(2):150–159, doi:10.1088/0004-637X/779/2/150.

Baade, W. and Zwicky, F. (1934). Remarks on Super-Novae and Cosmic Rays. *Phys. Rev.*, 46(1):76, doi:10.1103/PhysRev.46.76.2.

Bartoli, B. et al. (2012). Observation of TeV gamma rays from the Cygnus region with the ARGO-YBJ experiment. *Astrophys.J.*, 745(2):L22, doi:10.1088/2041-8205/745/2/L22.

Bartoli, B. et al. (2014). Identification of the TeV Gamma-ray Source ARGO J2031+4157 with the Cygnus Cocoon. *Astrophys. J.*, 790(2):152, doi:10.1088/0004-637X/790/2/152.

Becherini, Y. et al. (2011). A new analysis strategy for detection of faint gamma-ray sources with Imaging Atmospheric Cherenkov Telescopes. *Astropart.Phys.*, 34:858–970, doi:10.1016/j.astropartphys.2011.03.005.

Bednarek, W. (2007). Gamma-ray production in young open clusters: Berk 87, Cyg OB2 and Westerlund 2. *Mon. Not. R. Astron. Soc.*, 382(1):367–376, doi:10.1111/j.1365-2966.2007.12373.x.

Beerer, I.M. et al. (2010). A Spitzer View of Star Formation in the Cygnus X North Complex. *Astrophys. J.*, 720(1):679–693, doi:10.1088/0004-637X/720/1/679.

Behnke, O. et al., editors (2013). *Data Analysis in High Energy Physics - A Practical Guide to Statistical Methods*. WILEY-VCH, Weinheim, Germany.

Bell, A.R. (1978a). The acceleration of cosmic rays in shock fronts. I. *Mon. Not. R. Astron. Soc.*, 182(2):147–156, doi:10.1093/mnras/182.2.147.

Bell, A.R. (1978b). The acceleration of cosmic rays in shock fronts. II. *Mon. Not. R. Astron. Soc.*, 182(3):443–455, doi:10.1093/mnras/182.3.443.

Benjamin, R.A. et al. (2003). GLIMPSE: 1. An SIRTF Legacy Project to Map the Inner Galaxy. *Publ. Astron. Soc. Pac.*, 115:953–964, doi:10.1086/376696.

Bethe, H. and Heitler, W. (1934). On the Stopping of Fast Particles and on the Creation of Positive Electrons. In *Proceedings of the Royal Society of London*, volume 146 of *A*, pages 83–112.

Blandford, R. and Eichler, D. (1987). Particle acceleration at astrophysical shocks: A theory of cosmic ray origin. *Phys. Rep.*, 154(1):1–75, doi:10.1016/0370-1573(87)90134-7.

Blandford, R.D. and Ostriker, J.P. (1978). Particle acceleration by astrophysical shocks. *Astrophys. J. Lett.*, 221:L29–L32, doi:10.1086/182658.

Blumenthal, G.R. and Gould, R.J. (1970). Bremsstrahlung, Synchrotron Radiation, and Compton Scattering of High-Energy Electrons Traversing Dilute Gases. *Rev. Mod. Phys.*, 42(2):237–271, doi:10.1103/RevModPhys.42.237.

Bond, I.H., Hillas, A.M. and Bradbury, S.M. (2003). An island method of image cleaning for near threshold events from atmospheric Čerenkov telescopes. *Astropart. Phys.*, 20(3):311–321, doi:10.1016/S0927-6505(03)00193-2.

Breiman, L. et al. (1984). *Classification and Regression Trees*. The Wadsworth and Brooks-Cole statistics-probability series Wadsworth statistics/probability series. Taylor & Francis, Belmont, California.

Brun, R. and Rademakers, F. (1997). ROOT - An Object Oriented Data Analysis Framework. In *Proceedings AIHENP'96 Workshop*, volume 389, pages 81–86, Lausanne, Switzerland. Nucl. Instrum. Meth. A.

Bugayov, V.V. et al. (2002). On the application of differences in intrinsic fluctuations of Cherenkov light images for separation of air showers. *Astropart. Phys.*, 17(1):41–50, doi:10.1016/S0927-6505(01)00128-1.

Butt, Y. et al. (2003). Chandra/VLA follow-up of TeV J2032+4131: The only unidentified TeV gamma-ray source. *Astrophys. J.*, 597(1):494–512, doi:10.1086/378121.

Butt, Y. et al. (2006). Deeper Chandra follow-up of Cygnus TeV source perpetuates mystery. *Astrophys. J.*, 643(1):238–244, doi:10.1086/502642.

Cassé, M. and Paul, J. (1980). Local Gamma Rays and Cosmic-ray Acceleration by Supersonic Stellar Winds. *Astrophys. J.*, 237(1):236–243, doi:10.1086/157863.

Chaves, R.C.G. (2011). *The extended H.E.S.S. Galactic Plane survey: Discovering and identifying new sources of VHE gamma-rays*. PhD thesis, Ruprecht-Karls-Universität Heidelberg, Heidelberg, Germany.

Cherenkov, P.A. (1934). Visible Emission of Clear Liquids by Action of γ Radiation. *Dokl. Akad. Nauk SSSR+*, 2:451.

Churchwell, E. et al. (1992). The Wolf-Rayet system WR 147 - A binary radio source with thermal and nonthermal components. *Astrophys. J.*, 393(1):329–340, doi:10.1086/171508.

Churchwell, E. et al. (2009). The Spitzer/GLIMPSE Surveys: A New View of the Milky Way. *Publ. Astron. Soc. Pac.*, 121:213–230, doi:10.1086/597811.

Clark, C.J. et al. (2017). The Einstein@Home Gamma-ray Pulsar Survey I: Search Methods, Sensitivity and Discovery of New Young Gamma-ray Pulsars. *Astrophys. J.*, 834(2):106–124, doi:10.3847/1538-4357/834/2/106.

Cogan, P. (2007). VEGAS, the VERITAS Gamma-ray Analysis Suite. In Caballero, R. et al., editors, *Proceedings of the 30th International Cosmic Ray Conference (ICRC2007)*, volume 3, pages 1385–1388, Merida, Yucatan, Mexico.

Comerón, F. and Pasquali, A. (2012). New members of the massive stellar population in Cygnus. *Astron. Astrophys.*, 543(A101):23pp, doi:10.1051/0004-6361/201219022.

Comerón, F. et al. (2002). On the massive star contents of Cygnus OB2. *Astron. Astrophys.*, 389(3):874–888, doi:10.1051/0004-6361:20020648.

Corbel, S. et al. (2005). Large-Scale, Decelerating, Relativistic X-ray Jets from the Microquasar XTE J1550-564. *Science*, 298(5591):196–199, doi:10.1126/science.1075857.

Daniel, M.K. (2007). The VERITAS standard data analysis. In Caballero, R. et al., editors, *Proceedings of the 30th International Cosmic Ray Conference (ICRC2007)*, volume 3, pages 1325–1328, Merida, Yucatan, Mexico.

Davies, J.M. and Cotton, E.S. (1957). Design of the quartermaster solar furnace. *Sol. Energy*, 1(2-3):16–22, doi:10.1016/0038-092X(57)90116-0.

de Naurois, M. and Rolland, L. (2009). A high performance likelihood reconstruction of γ-rays fro imaging atmospheric Cherenkov telescopes. *Astropart. Phys.*, 32(5):231–252, doi:10.1016/j.astropartphys/2009.09.001.

Degrange, B. and Fontaine, G. (2015). Introduction to high-energy gamma-ray astronomy. *C. R. Phys.*, 16(6-7):587–599, doi:10.1016/j.crhy.2015.07.003.

Deharveng, L. et al. (2003). Triggered massive-star formation at the border of the H II Region Sh 104. *Astron. Astrophys.*, 408(3):L25–L28, doi:10.1051/0004-6361:20031157.

Deil, C. et al. (2015). The H.E.S.S. Galactic Plane Survey. In *Proceedings of the 34th International Cosmic Ray Conference (ICRC2015)*, The Hague, The Netherlands. Proceedings of Science. PoS(ICRC2015)773.

Dougherty, S.M., Williams, P.M. and Pollacco, D.L. (2000). WR 146 - observing the OB-type companion. *Mon. Not. R. Astron. Soc.*, 316(1):143–151, doi:10.1046/j.1365-8711.2000.03504.x.

Draine, B.T. (2011). *Physics of the Interstellar and Intergalactic Medium*. Princeton University Press.

Drury, L.O., Aharonian, F.A. and Völk, H.J. (1994). The gamma-ray visibility of supernova remnants. A test of cosmic ray origin. *Astron. Astrophys.*, 287:959–971.

Eger, P. et al. (2016). Discovery of a variable X-ray counterpart to HESS J1832-093: a new gamma-ray binary? *Mon. Not. R. Astron. Soc.*, 547(2):1753–1758, doi:10.1093/mnras/stw125.

Fegan, D.J. (1997). γ/hadron separation at TeV energies. *J. Phys. G: Nucl. Part. Phys.*, 23(9):1013–1060, doi:doi:10.1088/0954-3899/23/9/004.

Feinstein, A. (1995). Open Clusters in the Carina Nebula. In *Revista Mexicana de Astronomia y Astrofisica Serie de Conferencias*, volume 2, pages 57–67, La Plata, Argentina.

Fermi, E. (1949). On the Origin of the Cosmic Radiation. *Phys. Rev.*, 75(8):1169–1174, doi:10.1103/PhysRev.75.1169.

Ferrand, G. and Safi-Harb, S. (2012). A census of high-energy observations of Galactic supernova remnants. *Adv. Space Res.*, 49(1):1313–1319, doi:10.1016/j.asr.2012.02.004. http://www.physics.umanitoba.ca/snr/SNRcat/.

Fichtel, C.E. et al. (1983). EGRET - The high energy gamma ray telescope for NASA's Gamma Ray Observatory. In *Proceedings of the 18th International Cosmic Ray Conference (ICRC1983)*, volume 8, pages 19–22, Bangalore, India.

Fleischhack, H. (2017). *Measurement of the Iron Spectrum in Cosmic Rays with the VERITAS Experiment*. PhD thesis, Humboldt-Universität zu Berlin, Berlin, Germany.

Fraija, N. and Araya, M. (2016). The GeV counterpart of VER J2019+407 in the northern shell of the supernova remnant G78.2+2.1 (γ Cygni). *Astrophys. J.*, 826(1):31–38, doi:10.3847/0004-637X/826/1/31.

Freund, Y. (1995). Boosting a weak learning algorithm by majority. *Inform. Comput.*, 121(2):256–285, doi:10.1006/inco.1995.1136.

Freund, Y. and Schapire, R.E. (1997). A Decision-Theoretic Generalization of On-Line Learning and an Application to Boosting. *J. Comput. Syst. Sci.*, 55(1):119–139, doi:10.1006/jcss.1997.1504.

Freund, Y. and Schapire, R.E. (1999). A Short Introduction to Boosting. *J. Jpn. Soc. Artif. Intell.*, 14(5):771–780.

Funk, S. (2005). *A new population of very high-energy gamma-ray sources detected with H.E.S.S. in the inner part of the Milky Way*. PhD thesis, Ruprecht-Karls-Universität Heidelberg, Heidelberg, Germany.

Gaensler, B.M. and Slane, P.O. (2006). The Evolution and Structure of Pulsar Wind Nebulae. *Annu. Rev. Astron. Astr.*, 44:17–47, doi:10.1146/annurev.astro.44.051905.092528.

Gaisser, T.K. (1990). *Cosmic Rays and Particle Physics*. Cambridge University Press, 1st edition.

Galbraith, W. and Jelley, J. (1953). Light Pulses from the Night Sky associated with Cosmic Rays. *Nature*, 171:349–350, doi:10.1038/171349a0.

Gallo, E. et al. (2005). A dark jet dominates the power output of the stellar black hole Cygnus X-1. *Nature*, 436(7052):819–821, doi:10.1038/nature03879.

Ginzburg, V.L. and Syravatskii, S.I. (1964). *The Origin of Cosmic Rays*. Macmillan, New York, U.S.

Gotthelf, E.V. et al. (2016). Hard X-ray Emission from Sh2-104: A NuSTAR search for Gamma-ray Counterparts. *Astrophys. J.*, 826(1):25–31, doi:10.3847/0004-637X/826/1/25.

Green, D.A. (2014). A catalogue of 294 Galactic supernova remnants. *Bull. Astron. Soc. India*, 42:47–58.

Grieder, P.K.F. (2010). *Extensive Air Showers*, volume 1+2. Springer-Verlag Berlin Heidelberg.

Gross, E. and Vitells, O. (2010). Trial factors or the look elsewhere effect in high energy physics. *Eur. Phys. J.*, C70:525–530, doi:10.1140/epjc/s10052-010-1470-8.

Guenette, R. (2009). VERITAS Observations of X-ray Binaries. In *Proceedings of the 31st International Cosmic Ray Conference (ICRC2009)*, Łódź, Poland.

Guenette, R. (2010). *VERITAS observations of galactic compact objects*. PhD thesis, McGill University, Montreal, Quebec.

Hall, J. et al. (2003). VERITAS CFDs. In Kajita, T. et al., editors, *Proceedings of the 28th International Cosmic Ray Conference (ICRC2003)*, pages 2851–2854, Trukuba, Japan.

Hanna, D. (2007). Calibration Techniques for VERITAS. In Caballero, R. et al., editors, *Proceedings of the 30th International Cosmic Ray Conference (ICRC2007)*, volume 3, pages 1417–1420, Merida, Yucatan, Mexico.

Hanna, D. et al. (2010). An LED-based flasher system for VERITAS. *Nucl. Instrum. Meth. A*, 612(2):278–287, doi:doi:10.1016/j.nima.2009.10.107.

Hartman, R.C. et al. (1999). The Third EGRET Catalog of High-Energy Gamma-Ray Sources. *Astrophys. J. Suppl. S.*, 123(1):79–202, doi:10.1086/313231.

Hays, E. (2007). VERITAS Data Acquisition. In Caballero, R. et al., editors, *Proceedings of the 30th International Cosmic Ray Conference (ICRC2007)*, volume 3, pages 1543–1546, Merida, Yucatan, Mexico.

Heck, D. (2016). CORSIKA - an Air Shower Simulation Program. `https://www.ikp.kit.edu/corsika/index.php`. Retrieved July 29, 2016.

Heck, D. et al. (1998). CORSIKA: A Monte Carlo Code to Simulate Extensive Air Showers. Technical Report FZKA 6019, Forschungszentrum Karlsruhe.

Heitler, W. (1954). *The Quantum Theory of Radiation*. Oxford University Press, London, 3rd edition.

Hess, V.F. (1912). Über Beobachtungen der durchdringenden Strahlung bei sieben Freiballonfahrten. *Phys. Z.*, 13:1084–1091.

Higgs, L.A., Landecker, T.L. and Roger, R.S. (1977). The true extent of the Gamma Cygni supernova remnant. *Astron. J.*, 82(9):718–724, doi:10.1086/112114.

Hillas, A.M. (1982). The sensitivity of Cerenkov radiation pulses to the longitudinal development of cosmic-ray showers. *J. Phys. G: Nucl. Part. Phys.*, 8(10):1475–1492, doi:10.1088/0305-4616/8/10/017.

Hillas, A.M. (1984). The Origin of Ultra-High-Energy Cosmic Rays. *Annu. Rev. Astron. Astr.*, 22:425–444, doi:10.1146/annurev.aa.22.090184.002233.

Hillas, A.M. (1985). Cerenkov light images of EAS produced by primary gamma. In *Proceedings of the 19th International Cosmic Ray Conference (ICRC1985)*, volume 3, pages 445–448, La Jolla, U.S.A.

Hillas, A.M. (1996). Differences between Gamma-Ray and Hadronic Showers. *Space Sci. Rev.*, 75(1-2):17–30, doi:10.1007/BF00195021.

Hillas, A.M. et al. (1998). The Spectrum of TeV Gamma Rays from the Crab Nebula. *Astron. Astrophys.*, 503(2):744–759, doi:10.1086/306005.

Hinton, J.A. and Hofmann, W. (2009). Teraelectronvolt Astronomy. *Annu. Rev. Astron. Astr.*, 47:523–565, doi:10.1146/annurev-astro-082708-101816.

Ho, W.C.G. et al. (2017). Multiwavelength monitoring and X-ray brightening of Be X-ray binary PSR J2032+4127/MT91 213 on its approach to periastron. *Mon. Not. R. Astron. Soc.*, 464(1):1211–1219, doi:10.1093/mnras/stw2420.

Hoecker, A. et al. (2007). Toolkit for Multivariate Data Analysis. In *Proceedings of XI International Workshop on Advanced Computing and Analysis Techniques in Physics Research*, Nikhef, Amsterdam, The Netherlands. Proceedings of Science. PoS(ACAT)040.

Hofmann, W. et al. (1999). Comparison of techniques to reconstruct vhe gamma-ray showers from multiple stereoscopic Cherenkov images. *Astropart. Phys.*, 12(3):135–143, doi:10.1016/S0927-6505(99)00084-5.

Holder, J. (2005). Exploiting VERITAS Timing Information. In *Proceedings of the 29th International Cosmic Ray Conference (ICRC2005)*, volume 5, pages 383–386, Pune, India.

Holder, J. et al. (2006). The first VERITAS telescope. *Astropart. Phys.*, 25(6):391–401, doi:10.1016/j.astropartphys.2006.04.002.

Holder, J. et al. (2009). Status of the VERITAS Observatory. In Aharonian, F.A., Hofmann, W. and Rieger, F., editors, *Proceedings of the 4th Heidelberg International Symposium on High Energy Gamma-Ray Astronomy*, volume 1085 of *AIP Conf. Proc.*, pages 657–660, Heidelberg, Germany. American Institute of Physics.

Horns, D. et al. (2007). XMM-Newton observations of the first unidentified TeV gamma-ray source TeV J2032+4130. *Astron. Astrophys.*, 469(1):L17–L21, doi:10.1051/0004-6361:20066836.

Hughes, E.B. et al. (1980). Characteristics of the telescope for high energy gamma-ray astronomy selected for definition studies on the Gamma Ray Observatory. *IEEE T. Nucl. Sci.*, 27(1):363–369, doi:10.1109/TNS.1980.4330853.

Hunt, Q. (2016). The Dual Associations of Fermi Source 3FGL J2015.6+3709. Presentation at the American Astronomical Society, AAS Meeting #227, id.238.09.

Immer, K. et al. (2011). The VLBA Calibrator Search for the BeSSeL Survey. *Astrophys. J. Suppl. S.*, 194(2):25, doi:10.1088/0067-0049/194/2/25.

Jelley, J.V. and Porter, N.A. (1963). Cerenkov Radiation from the Night Sky, and its Application to γ-Ray Astronomy. *Q. J. Roy. Astron. Soc.*, 4:275–293.

Jordan, P. and Krennrich, F. (2004). The Design of Light Concentrators for a 12m Cherenkov Telescope. http://cherenkov.physics.iastate.edu/research/memos/LightconeStudies-collector_optimization.pdf.

Jourdain, E., Roques, J.P. and Malzac, J. (2011). The Emission of Cygnus X-1: Observations with INTEGRAL SPI from 20 keV to 2 MeV. *Astrophys. J.*, 744(1):64, doi:10.1088/0004-637X/744/1/64.

Kieda, D. (2011). Status of the VERITAS Upgrade. In *Proceedings of the 32nd International Cosmic Ray Conference (ICRC2011)*, Beijing, China.

Kieda, D.B. (2013). The Gamma Ray Detection sensitivity of the upgraded VERITAS Observatory. In *Proceedings of the 33rd International Cosmic Ray Conference (ICRC2013)*, Rio de Janeiro, Brazil.

Knödlseder, J. (2000). Cygnus OB2 - a young globular cluster in the Milky Way. *Astron. Astrophys.*, 360:539–548.

Knödlseder, J. et al. (2016). GammaLib and ctools: A software framework for the analysis of astronomical gamma-ray data. *Astron. Astrophys.*, 593(A1):19, doi:10.1051/0004-6361/201628822.

Kohnle, A. et al. (1996). Stereoscopic imaging of air showers with the first two HEGRA Cherenkov telescopes. *Astropart. Phys.*, 5(2):119–131, doi:10.1016/0927-6505(96)00011-4.

Konopelko, A. et al. (2007). Observations of the Unidentified TeV γ-Ray Source TeV J2032+4130 with the Whipple Observatory 10 m Telescope. *Astrophys. J.*, 658(2):1062–1068, doi:10.1086/511262.

Kraemer, K.E. et al. (2010). Circumstellar Structure Around Evolved Stars in the Cygnus-X Star Formation Region. *Astron. J.*, 139(6):2319–2329, doi:10.1088/0004-6256/139/6/2319.

Krause, M. (2011). *Studies of the influence of the geomagnetic fiels on the sensitivity of gamma-ray observatories*. Master's thesis, Brandenburg University of Technology Cottbus and Poznan University of Techology, Cottbus, Germany and Poznan, Poland.

Krawczynski, H. et al. (2006). Gamma-Hadron Separation Methods for the VERITAS Array of Four Imaging Atmospheric Cherenkov Telescopes. *Astropart. Phys.*, 25(6):380–390, doi:10.1016/j.astropartphys.2006.03.011.

Krivonos, R. et al. (2012). INTEGRAL/IBIS nine-year Galactic hard X-ray survey. *Astron. Astrophys.*, 545(A27):7, doi:10.1051/0004-6361/201219617.

Lafebre, S. (2008). *From Cosmic Particle to Radio Pulse*. PhD thesis, Radboud University Nijmegen, Nijmegen, The Netherlands.

Lande, J. et al. (2012). Search for Spatially Extended Fermi-LAT Sources Using Two Years of Data. *Astrophys. J.*, 756(1):26pp, doi:10.1088/0004-637X/756/1/5.

Lauqué, R., Lequeux, J. and Nguyen-Quang-Rieu (1972). Determination of the Distance of Cygnus X-3 by 21-cm Absorption. *Nature*, 239:119–120, doi:10.1038/physci239119a0.

Lemoine-Goumard, M., Degrange, B. and Tluczykont, M. (2006). Selection and 3D-Reconstruction of Gamma-Ray-induced Air Showers with a Stereoscopic System of Atmospheric Cherenkov Telescopes. *Astropart. Phys.*, 25(3):195–211, doi:10.1016/j.astropartphys.2006.01.005.

Leo, W.R. (1994). *Techniques for Nuclear and Particle Physics Experiments*. Springer-Verlag Berlin Heidelberg, 2nd edition.

Leroy, C. and Rancoita, P.G. (2016). *Principles of Radiation Interaction in Matter and Detection*. World Scientific Publishing Co., Singapore, 4th edition.

Li, T.P. and Ma, Y.Q. (1983). Analysis method for results in gamma-ray astronomy. *Astrophys. J.*, 272:317–324, doi:10.1086/161295.

Lin, T.T.Y. (2015). Bias Curve Study. VERITAS Internal Publication.

Liu, Q.Z., van Paradijs, J. and van den Heuvel, E.P.J. (2000). A catalogue of high-mass X-ray binaries. *Astron. Astrophys. Suppl. Ser.*, 147(1):25–49, doi:10.1051/aas:2000288.

Liu, Q.Z., van Paradijs, J. and van den Heuvel, E.P.J. (2001). A catalogue of low-mass X-ray binaries. *Astron. Astrophys.*, 368(3):1021–1054, doi:10.1051/0004-6361:20010075.

Liu, Q.Z., van Paradijs, J. and van den Heuvel, E.P.J. (2006). Catalogue of high-mass X-ray binaries in the Galaxy (4th edition). *Astron. Astrophys.*, 455(3):1165–1168, doi:10.1051/0004-6361:20064987.

Liu, Q.Z., van Paradijs, J. and van den Heuvel, E.P.J. (2007). A catalogue of low-mass X-ray binaries in the Galaxy, LMC, and SMC (Fourth edition). *Astron. Astrophys.*, 469(2):807–810, doi:10.1051/0004-6361:20077303.

Longair, M.S. (2011). *High Energy Astrophysics*. Cambridge University Press, New York, U.S., 3rd edition.

Lozinskaya, T.A., Pravdikova, V.V. and Finoguenov, A. (2002). Searches for the shell swept up by the stellar wind from Cyg OB2. *Astron. Lett.*, 28(4):223–236, doi:10.1134/1.1467257.

Lozinskaya, T.A., Pravdikova, V.V. and Finoguenov, A.V. (2000). The Supernova Remnant G78.2+2.1: New Optical and X-ray Observations. *Astron. Lett.*, 26(2):77–87, doi:10.1134/1.20371.

Lyne, A. and Graham-Smith, F. (2012). *Pulsar Astronomy*. Cambridge Astrophysics. Cambridge University Press, 4th edition.

Lyne, A. et al. (2015). The Binary Nature of PSR J2032+4127. *Mon. Not. R. Astron. Soc.*, 451(1):581–587, doi:10.1093/mnras/stv236.

Maier, G. (2007). Monte Carlo studies of the VERITAS array of Cherenkov telescopes. In Caballero, R. et al., editors, *Proceedings of the 30th International Cosmic Ray Conference (ICRC2007)*, volume 3, pages 1413–1416, Merida, Yucatan, Mexico.

Maier, G. and Knapp, J. (2007). Cosmic-Ray Events as Background in Imaging Atmospheric Cherenkov Telescopes. *Astropart.Phys.*, 28(1):72–81, doi:10.1016/j.astropartphys.2007.04.009.

Manchester, R.N. et al. (2005). The Australia Telescope National Facility Pulsar Catalogue. *Astron. J.*, 129(4):1993–2006, doi:10.1086/428488.

Marchenko, S.V. et al. (2003). The Unusual 2001 Periastron Passage in the "Clockwork" Colliding-Wind Binary WR 140. *Astrophys. J.*, 596(2):1295–1304, doi:10.1086/378154.

Matheson, H., Safi-Harb, S. and Kothes, R. (2013). X-ray Observations of the Supernova Remnant CTB 87 (G74.9+1.2): An Evolved Pulsar Wind Nebula. *Astrophys. J.*, 774(1):33–42, doi:10.1088/0004-637X/774/1/33.

Matthews, J. (2005). A Heitler model of extensive air showers. *Astropart. Phys.*, 22(5-6):387–397, doi:10.1016/j.astropartphys.2004.09.003.

Max Planck Institute for Nuclear Physics (2014). First results from H.E.S.S. II announced: Detection of pulsed gamma-ray emission from Vela in the 30 GeV energy range. press release. http://www.nanowerk.com/news2/space/newsid=36373.php.

McCann, A. et al. (2010). A new mirror alignment system for the VERITAS telescopes. *Astropart. Phys.*, 32(6):325–329, doi:10.1016/j.astropartphys.2009.10.001.

Mirabel, I.F. (2006). Very Energetic Gamma-Rays from Microquasars and Binary Pulsars. *Science*, 312(5781):1759–1760, doi:10.1126/science.1129815.

Mirabel, I.F. (2007). Microquasars. *C. R. Phys.*, 8(1):7–15, doi:10.1016/j.crhy.2006.12.001.

Mirabel, I.F. and Rodríguez, L.F. (1994). A superluminal source in the Galaxy. *Nature*, 371(6492):46–48, doi:10.1038/371046a0.

Mirabel, I.F. and Rodríguez, L.F. (1999). Source of relativistic jetz in the galaxy. *Annu. Rev. Astron. Astr.*, 37:409–443, doi:10.1146/annurev.astro.37.7.409.

Mitchell, T.M. (1997). *Machine Learning*. The McGraw-Hill Companies, Inc., International edition.

Montmerle, T. (1979). On gamma-ray sources, supernova remnants, OB associations, and the origin of cosmic rays. *Astrophys. J.*, 231(1):95–110, doi:10.1086/157166.

Murakami, H. et al. (2011). Detection of X-Ray Emission from the Unidentified TeV Gamma-Ray Source TeV J2032+4130. *Publ. Astron. Soc. Jpn.*, 63(SP3):S873–S878, doi:10.1093/pasj/63.sp3.S873.

Nagai, T. et al. (2007). Focal Plane Instrumentation of VERITAS. In Caballero, R. et al., editors, *Proceedings of the 30th International Cosmic Ray Conference (ICRC2007)*, volume 3, pages 1437–1440, Merida, Yucatan, Mexico.

Ohm, S., van Eldik, C. and Egberts, K. (2009). Gamma-Hadron Separation in Very-High-Energy gamma-ray astronomy using a multivariate analysis method. *Astroparticle Physics*, 31(5):383–391, doi:10.1016/j.astropartphys.2009.04.001.

Orosz, J.A. et al. (2011). The mass of the black hole in Cygnus X-1. *Astrophys. J.*, 742(2):84–93, doi:10.1088/0004-637X/742/2/84.

Otte, A.N. (2011). The Upgrade of VERITAS with High Efficiency Photomultipliers. In *Proceedings of the 32nd International Cosmic Ray Conference (ICRC2011)*, Beijing, China.

Panov, A.D. et al. (2007). Elemental energy spectra of cosmic rays from the data of the ATIC-2 experiment. *B. Russ. Acad. Sci. Phys.*, 71(4):494–497, doi:10.3103/S1062873807040168.

Paredes, J.M. et al. (2007). The population of radio sources in the field of the unidentified gamma-ray source TeV J2032+4130. *Astrophys. J.*, 654(2):L135–L138, doi:10.1086/511178.

Parizot, E. et al. (2004). Superbubbles and energetic particles in the Galaxy. I. Collective effects of particle acceleration. *Astron. Astrophys.*, 424:747–760, doi:10.1051/0004-6361:20041269.

Park, N. (2015). Performance of the VERITAS experiment. In *Proceedings of the 34th International Cosmic Ray Conference (ICRC2015)*, The Hague, The Netherlands. Proceedings of Science. PoS(ICRC2015)771.

Parsons, R.D. and Hinton, J.A. (2014). A Monte Carlo template based analysis for air-Cherenkov arrays. *Astropart. Phys.*, 56:26–34, doi:10.1016/j.astropartphys.2014.03.002.

Perkins, J. and Maier, G. (2009). VERITAS Telescope 1 Relocation: Details and Improvements. In *Proceedings of the 2nd Fermi Symposium*, Washington D.C., U.S.A.

Perryman, M.A.C. et al. (1997). The HIPPARCOS Catalogue. *Astron. Astrophys.*, 323:L49–L52.

Pittard, J.M. and Dougherty, S.M. (2006). Radio, X-ray, and γ-ray emission models of the colliding-wind binary WR140. *Mon. Not. R. Astron. Soc.*, 372(2):801–826, doi:10.111/j.1365-2966.2006.10888.x.

Pollock, A.M.T. (1987). The Einstein view of the Wolf-Rayet stars. *Astrophys. J.*, 320:283–295, doi:10.1086/165539.

Popkow, A. (2017). *Very-High-Energy Astrophysical Processes in the Cygnus region of the Milky Way*. PhD thesis, University of California Los Angeles, Los Angeles, USA.

Prialnik, D. (2010). *An Introduction to the Theory of Stellar Structure and Evolution*. Cambridge University Press, UK, 2nd edition.

Prokoph, H. (2013). *Observations and modeling of the active galactic nucleus B2 1215+30 together with performance studies of the ground-based gamma-ray observatories VERITAS and CTA*. PhD thesis, Humboldt-Universität zu Berlin, Berlin, Germany.

Reid, M.J. et al. (2011). The Trigonometric Parallax of Cygnus X-1. *Astrophys. J.*, 742(2):83–87, doi:10.1088/0004-637X/742/2/83.

Reimer, A., Pohl, M. and Reimer, O. (2006). Nonthermal High-Energy Emission from Colliding Winds of Massive Stars. *Astrophys. J.*, 644(2):1118–1144, doi:10.1086/503598.

Reimer, A. and Reimer, O. (2009). Parameter constraints for high-energy models of colliding winds of massive stars: the case WR 147. *Astrophys. J.*, 694(2):1139–1146, doi:10.1088/0004-637X/694/2/1139.

Reipurth, B. and Schneider, N. (2008). *Handbook of Star Forming Regions, Volume I: The Northern Sky*, volume 4, chapter Star Formation and Yound Clusters in Cygnus, pages 36–89. ASP Monograph Publications, San Francisco, CA, US.

Reynolds, S.P. (2008). Supernova Remnants at High Energy. *Annu. Rev. Astron. Astr.*, 46(1):89–126, doi:10.1146/annurev.astro.46.060407.145237.

Rieke, G.H. et al. (2004). The Multiband Imaging Photometer For Spitzer (MIPS). *Astrophys. J. Suppl. S.*, 154:25–29.

Roache, E. et al. (2007). Mirror Facets for the VERITAS Telescopes. In Caballero, R. et al., editors, *Proceedings of the 30th International Cosmic Ray Conference (ICRC2007)*, volume 3, pages 1397–1400, Merida, Yucatan, Mexico.

Roberts, M.S.E. (2002). PSR J2021+3651: A Young Radio Pulsar Coincident with an Unidentified EGRET γ-Ray Source. *Astrophys. J.*, 577(1):L19–L22, doi:10.1086/344082.

Rolke, W.A., Lopez, A.M. and Conrad, J. (2005). Limits and confidence intervals in the presence of nuisance parameters. *Nucl. Instrum. Meth. A*, 551(2-3):493–503, doi:10.1016/j.nima.2005.05.068.

Rossi, B. and Greisen, K. (1941). Cosmic-Ray Theory. *Rev. Mod. Phys.*, 13:240–315, doi:10.1103/RevModPhys.13.240.

Sabatini, S. et al. (2010). Episodic Transient Gamma-Ray Emission from the Microquasar Cygnus X-1. *Astrophys. J.*, 712(1):L10–L15, doi:10.1088/2041-8205/712/1/L10.

Saha, L. (2016). Implications of the pulsar wind nebula scenario for a TeV gamma-ray source VER J2016+371. *Mon. Not. R. Astron. Soc.*, 460(4), doi:10.1093/mnras/stw1255.

Schapire, R.E. (1990). The strength of weak learnabilty. *Mach. Learn.*, 5(2):197–227, doi:10.1007/BF00116037.

Schapire, R.E. and Singer, Y. (1990). Improved Boosting Algorithms Using Confidence-rated Predictions. *Mach. Learn. - The Eleventh Annual Conference on computational Learning Theory*, 37(3):297–336, doi:10.1023/A:1007614523901.

Schellart, P. (2015). *Measuring radio emission from air showers with LOFAR*. PhD thesis, Radboud University Nijmegen, Nijmegen, The Netherlands.

Schmidt, F. (2005). CORSIKA Shower Images. `http://www.ast.leeds.ac.uk/~fs/showerimages.html`. Retrieved June 9th, 2016.

Schneider, N. et al. (2006). A new view of the Cygnus X region. *Astron. Astrophys.*, 458(3):855–871, doi:10.1051/0004-6361:20065088.

Schneider, N. et al. (2016). Globules and Pillars in Cygnus X I. Herschel Far-infrared imaging of the Cyg OB2 environment. *Astron. Astrophys.*, 591(A40):21, doi:10.1051/0004-6361/201628328.

Schulz, A. (2013). The measurement of the energy spectrum of cosmic rays above 3×10^{17} eV with the Pierre Auger Observatory. In *Proceedings of the 33rd International Cosmic Ray Conference (ICRC2013)*, Rio de Janeiro, Brazil.

Setia Gunawan, D.Y.A. (2001). WSRT 1.4 and 5-GHz light curves for WR 147 (AS 431, WN8(h)+OB). *Astron. Astrophys.*, 368(2):484–496, doi:10.1051/0004-6361:20000561.

Setia Gunawan, D.Y.A. et al. (2001). Multi-frequency variations of the Wolf-Rayet system HD 193793 (WC7pd+O4-5). *Astron. Astrophys.*, 376(2):460–475, doi:10.1051/0004-6361:20010879.

Sguera, V. (2008). Fast X-ray transients as counterparts of unidentified MeV/TeV sources. In *Proceedings of the 7th INTEGRAL Workshop - An INTEGRAL View of Compact Objects*, number 082 in PoS Integral08. Proceedings of Science, Copenhagen, Denmark. PoS(Integral08)082.

Shaw, M.S. et al. (2013). Spectroscopy of The Largest Ever Gamma-ray Selected BL Lac Sample. *Astrophys. J.*, 764(2):135, doi:10.1088/0004-637X/764/2/135.

Smith, N. (2006). A census of the Carina Nebula. 1. Cumulative energy input from massive stars. *Mon. Not. R. Astron. Soc.*, 367:763–772, doi:10.1111/j.1365-2966.2006.10007.x. [Erratum: Mon. Not. Roy. Astron. Soc.368,1983(2006), doi:10.1111/j.1365-2966.2006.10428.x].

Sommers, P. and Elbert, J.W. (1987). Ultra-high-energy gamma-ray astronomy using atmospheric Cerenkov detectors at large zenith angles. *J. Phys. G: Nucl. Partic.*, 13(4):553–566, doi:10.1088/0305-4616/13/4/019.

Stanev, T. (2010). *High Energy Cosmic Rays*. Astronomy and Planetary Sciences. Springer-Verlag Berlin Heidelberg, 2nd edition.

Stegmann, C. (2014). H.E.S.S. Highlights. Presentation at Astroparticle Physics 2014 - A joing TeVPa/IDM conference.

Tamm, I.E. and Frank, I.M. (1937). Coherent Radiation of Fast Electrons in Medium. *Dokl. Akad. Nauk SSSR+*, 14:107.

Tavani, M. et al. (2004). Sciene with AGILE. AGILE Document AP-27. from http://agile.mi.iasf.cnr.it/.

Tavani, M. et al. (2009). Extreme particle acceleration in the microquasar Cygnus X-3. *Nature*, 462:620–623, doi:10.1038/nature08578.

Taylor, A.R. et al. (2003). The Canadian Galactic Plane Survey. *Astrophys. J.*, 125(6):3145–3164.

Thompson, D.J. et al. (1995). The Second EGRET Catalog of High-Energy Gamma-Ray Sources. *Astrophys. J. Suppl. S.*, 101:259–286, doi:10.1086/192240.

Toner, J.A. et al. (2007). Bias Alignment of the VERITAS Telescope. In Caballero, R. et al., editors, *Proceedings of the 30th International Cosmic Ray Conference (ICRC2007)*, volume 3, pages 1401–1404, Merida, Yucatan, Mexico.

Torres, D.F., Domingo-Santamaria, E. and Romero, G.E. (2004). High-Energy Gamma Rays from Stellar Associations. *Astrophys. J.*, 601(1):L75–L78, doi:10.1086/381803.

Tsai, Y.S. (1974). Pair production and bremsstrahlung of charged leptons. *Rev. Mod. Phys.*, 46(4):815–851, doi:10.1103/RevModPhys.46.815.

Uyaniker, B. et al. (2001). The Cygnus superbubble revisited. *Astron. Astrophys.*, 371:675–697, doi:10.1051/0004-6361:20010387.

van der Hucht, K.A. (2001). The VIIth catalogue of galactic Wolf-Rayet stars. *New Astron. Rev.*, 45(3):135–232, doi:10.1016/S1387-6473(00)00112-3.

van der Hucht, K.A. et al. (1995). Radio Monitoring of the Non-Thermal Wolf-Rayet Objects WR125, WR146 and WR147. In van der Hucht, K.A. and Williams, P.M., editors, *Wolf-Rayet Stars: Binaries, Colliding Winds, Evolution - Proceedings of the 163rd Symposium of the International Astronomical Union*, volume 163 of *International Astronomical Union / Union Astronomique Internationale*, pages 559–561, La Biodola, Elba, Italy. Springer Netherlands.

VERITAS collaboration (in preparation). A Very High Energy Survey of the Cygnus Region of the Galaxy.

Vincent, S. (2015). A Monte Carlo template-based analysis for very high definition imaging atmospheric Cherenkov telescopes as applied to the VERITAS telescope array. In *Proceedings of the 34th International Cosmic Ray Conference (ICRC2015)*, The Hague, The Netherlands.

Proceedings of Science. Pos(ICRC2015)844.

Voelk, H.J. and Forman, M. (1982). Cosmic rays and gamma-rays from OB stars. *Astrophys. J.*, 253(1):188–198, doi:10.1086/159623.

Wakely, S.P. and Horan, D. (2008). TeVCat: An online catalog for Very High Energy Gamma-Ray Astronomy. In Caballero, R. et al., editors, *Proceedings of the 30th International Cosmic Ray Conference (ICRC2007)*, volume 3, pages 1341–1344, Merida, Yucatan, Mexico.

Wakely, S.P. and Horan, D. (2016). TeVCat: An online catalog for Very High Energy Gamma-Ray Astronomy. http://tevcat.uchicago.edu. Retrieved September 30, 2016.

Ward, J.E. (2010). *VERITAS Survey of the Cygnus Region of the Galactic Plane*. PhD thesis, University College Dublin, Dublin, Ireland.

Wdowczyk, J. and Wolfendale, A.W. (1989). Highest energy cosmic rays. *Annu. Rev. Nucl. Part. S.*, 39:43–71, doi:10.1146/annurev.ns.39.120189.000355.

Weekes, T.C. (1988). Very high energy gamma-ray astronomy. *Phys. Rep.*, 160(1-2):1–121, doi:10.1016/0370-1573(88)90177-9.

Weekes, T.C. (2003). *Very High Energy Gamma-Ray Astronomy*. Series in Astronomy and Astrophysics. Institute of Physics Publishing, Bristol and Philadelphia.

Weekes, T.C. et al. (1989). Observation of TeV gamma rays from the Crab nebula using the atmospheric Cerenkov imaging technique. *Astrophys. J.*, 342:379–395, doi:10.1086/167599.

Weinstein, A. (2007). The VERITAS Trigger System. In Caballero, R. et al., editors, *Proceedings of the 30th International Cosmic Ray Conference (ICRC2007)*, volume 3, pages 1539–1542, Merida, Yucatan, Mexico.

Weinstein, A. (2009a). The VERITAS Survey of the Cygnus Region of the Galactic Plane. In *Proceedings of the 31st International Cosmic Ray Conference (ICRC2009)*, Łódź, Poland.

Weinstein, A. (2009b). The VERITAS Survey of the Cygnus Region of the Galactic Plane. In *Proceedings of the 2nd Fermi Symposium*, Washington D.C.,.

Werner, M. et al. (2013). Fermi-LAT upper limits on gamma-ray emission from colliding wind binaries. *Astron. Astrophys.*, 555(A102):9pp, doi:10.1051/0004-6361/201220502.

Williams, P.M. et al. (1987). *Instabilities in Luminous Early Type Stars*, volume 136 of *Astrophysics and Space Science Library*, chapter Episodic Distortion and Dust Formation in the Wind of WR 140, pages 221–226. Springer Netherlands.

Wright, N.J. and Drake, J.J. (2009). The Massive Star-Forming Region Cygnus OB2. I. Chandra Catalog of Association Members. *Astrophys. J.*, 184(1):84–99, doi:10.1088/0067-0049/184/1/84.

Wright, N.J. et al. (2010). The Massive Star-Forming Region Cygnus OB2. II. Integrated Stellar Properties and the Star Formation History. *Astrophys. J.*, 713(2):871–882, doi:10.1088/0004-637X/713/2/871.

Xiang, J. et al. (2011). Using the X-ray Dust Scattering Halo of Cygnus X-1 to determine distance and dust distributions. *Astrophys. J.*, 738(1):78–87, doi:10.1088/0004-637X/738/1/78.

Yoon, Y.S. et al. (2011). Cosmic-ray Proton and Helium Spectra from the First CREAM Flight. *Astrophys. J.*, 728(2):122–127, doi:10.1088/0004-637X/728/2/122.

Zitzer, B. (2013). The VERITAS Upgraded Telescope-Level Trigger Systems: Technical Details and Performance Characterization. In *Proceedings of the 33rd International Cosmic Ray Conference (ICRC2013)*, Rio de Janeiro, Brazil.

Zwicky, F. (1939). Production of Atomic Rays and of Cosmic Rays in Supernovae. In *Proceedings of the National Academy of Sciences of the United States of America*, volume 25, pages 338–344. National Academy of Sciences.

Acknowledgement

There have been many people who have walked alongside me during the last three years. They have guided me, placed opportunities in front of me and showed me the doors that might be useful to open. I would like to thank each and every one of them.

First of all my supervisor Gernot Maier for all the invested time in the supervision, for sharing his broad knowledge of astroparticle physics and astrophysics, and for his readiness for scientific discussion. Thank you for the opportunity to work on such an interesting research topic, which was for sure never boring. I appreciate all the support and discussions during the last three years. I learned many new things and got in touch with many interesting people. Thank you for all the opportunities you created during this time. I also thank Prof. Thomas Lohse, Prof. Marek Kowalski, Prof. Petra Huentemeyer and Prof. Beate Röder for joining my PhD committee.

Without Heike Prokoph, Gareth Hughes, and Stefan Schlenstedt I probably wouldn't have started my PhD in Zeuthen. Together with Gernot Maier they got me excited about γ-ray astronomy during my summer student project at DESY in 2010. They encouraged me to return as a PhD student; I have never regretted doing so.

It was an honour to be part of the *VERITAS* group in Zeuthen and would like to thank Henrike Fleischhack, Galo Gallardo, Lucie Gerárd, Orel Gueta, Nathan Kelley-Hoskins, Moritz Hütten, Anna O'Faoláin de Bhróithe, Iftach Sadeh, Stefan Schlenstedt, Stephane Vincent, and Roman Welsing. Working so close together with them was special in many aspects and for sure never boring. Without their encouragement the road would have seems a lonely place. Thank you for the fruitful discussions and advice. I am grateful to Henrike for many inspiring discussions during tea and lunch; and to Nathan for his help to efficiently code in *bash*.

Special thanks goes to Stephane for the laid-back discussions during coffee, tea, and lunch, in our office or in the S-Bahn about physics and other topics of daily life. It has been a pleasure sharing the office with you. I really much appreciated your continuous support, motivation, and patience during the whole time. Thank you for your help and friendship over the past three years.

The very friendly atmosphere within the *VERITAS* collaboration set up the framework for many fruitful discussions with colleagues from all over the world. One of the great advantages of being an astrophysicist, if only for a little while, is that you get to travel and meet many interesting people from places all over the world. Thanks to all of you, I feel lucky and privileged to have met you. There are several people with those I worked close together. They deserve special

appreciation: Taylor Aune, Ralph Bird, Rene Ong, and Alexis Popkow. Thank you for the great collaboration, even in busy times!

My closest foreign collaborator Elisa Pueschel I would like to thank for all the inspiring discussions and teamwork, and for becoming a friend during many hours of scientific conversations and travels to either Germany, Ireland, Denmark or the U.S.A. It has been a great pleasure to work with you. I am looking forward to meet you wherever we are.

I am grateful to Ralph Bird, Henrike Fleischhack, Orel Gueta, Elisa Pueschel, Iftach Sadeh, and Stephane Vincent, for proof-reading and discussing this dissertation, or parts thereof.

This journey would have been impossible without the support of my family and friends, who helped me to be able to make it to this point. Thanks for the incredible support during the most difficult times and for never doubting that there is sunshine after the rain. Thank you for listening, offering me advice, supporting me, and for being there whenever I needed a friend.

Ein ganz besonderer Dank geht an meine Eltern, die mich immer bedingungslos unterstützt haben. Wenn ich mit dem Kopf nicht zu Hause, sondern bei der Arbeit war, sind sie es gewesen, die mich wachgerüttelt, immer unterstützt und motiviert haben. Danke für alles!

Selbständigkeitserklärung

Ich erkläre, dass ich die Dissertation selbstständig und nur unter Verwendung der von mir gemäß §7 Abs. 3 der Promotionsordnung der Mathematisch-Naturwissenschaftlichen Fakultät, veröffentlicht im Amtlichen Mitteilungsblatt der Humboldt-Universität zu Berlin Nr. 126/2014 am 18.11.2014 angegebenen Hilfsmittel angefertigt habe.

Berlin, den 9. November 2016 Maria Krause